UNIVERSITÀ
DEGLI STUDI
DI PADOVA

Sede Amministrativa: Università degli Studi di Padova

Dipartimento di Scienze Chimiche

CORSO DI DOTTORATO DI RICERCA IN: Scienze Molecolari

CURRICOLO: Scienze Chimiche

CICLO XXXII

THERMOMETERS AT THE NANOSCALE:

A MOLECULAR APPROACH TO DESIGN AND DEVELOP FUNCTIONAL LANTHANOID-BASED LUMINESCENT MATERIALS

Coordinatore: Ch.mo Prof. Leonard J. Prins

Supervisore: Ch.ma Prof. Lidia Armelao

Dottorando: Luca Bellucci

Riassunto

Questo lavoro è volto allo sviluppo di termometri molecolari a base di ioni lantanoidei ed allo studio delle correlazioni tra proprietà termometriche ed i diversi *building blocks* che compongono i sistemi. In particolare, usando cationi lantanoidei, β-dichetoni (H(β-dike)= dibenzoilmetano, Hdbm; benzoiltrifluoroacetone, Hbta; esafluoroacetilacetone, Hhfac; tenoiltrifluoroacetone, Htta), e leganti divergenti (4,4'-bipiridina, bipy; 4,4'-bipiridina-*N*-ossido, bipyMO; pirazina-*N*-ossido, pyrzMO; 2,5-diidrossi-1,4-dicarbossilato, H_2DHT^{2-}) sono stati preparati sistemi molecolari con diversa dimensionalità: i) complessi dinucleari (0D), polimeri di coordinazione (CPs, 1D) e Metal Organic Frameworks (MOFs, 3D).

Nei complessi dinucleari di europio $[Eu_2(\beta\text{-dike})_6(L\text{-}MO)_x]$ (x=3 per hfac, x=2 per dbm, bta, and tta) le proprietà elettroniche e steriche del β-dichetonato sono state modulate sostituendo i gruppi $-CF_3$ di hfac con anelli fenilici (uno nel bta, due nel dbm) o con un anello tienilico (tta). Il diverso ingombro sterico dei leganti bipyMO e pyrzMO influenzarono invece la disposizione spaziale dei leganti β-dichetonato e le loro interazioni inter- ed intra-molecolari. I complessi mostrarono valori di sensibilità termica relativa (S_r) maggiori di 1 (valore generalmente usato come criterio di qualità per questi termometri) dipendenti dalla natura dei leganti β-dike e L-MO nell'intervallo di temperatura -50 ÷ 100 °C. I leganti β-dichetonato influenzarono i valori di S_r, l'intervallo applicativo di temperature e la fotostabilità dei complessi. I composti contenenti pyrzMO mostrarono performances migliori (S_r massimo da 4.6 a 8.1 % $°C^{-1}$ a seconda del β-dike) rispetto agli analoghi con bipyMO (S_r massimo da 3.4 a 5.1 % $°C^{-1}$).

Successivamente è stata ottenuta una serie di termometri luminescenti raziometrici a base di Eu^{3+} e Tb^{3+} miscelando diverse quantità dei due polimeri di coordinazione 1D $[Ln(hfac)_3(bipy)]_n$ (Ln^{3+}= Eu^{3+} e Tb^{3+}) in KBr (inerte dal punto di vista spettroscopico). In questo caso è stato studiato l'effetto su S_r della quantità relativa

dei due ioni metallici e della lunghezza d'onda di eccitazione nell'intervallo -190 ÷ 110 °C. Per tutti i campioni i valori di S_r risultarono non influenzati dal rapporto molare Tb/Eu e dalla lunghezza d'onda di eccitazione. Ciascun campione mostrò un peculiare colore emesso (dal verde al rosso) in funzione della temperatura. Ciò è stato sfruttato per sviluppare termometri basati su codici di colori capaci di distinguere intervalli di temperatura di 10/ 20 °C.

È stata inoltre sviluppata una procedura basata su condizioni blande per attuare la modifica post-sintetica da cristallo singolo a cristallo singolo del MOF $\{[Eu_2(H_2DHT)_3(DMF)_4]\cdot 2DMF\}_n$ (DMF= *N*,*N*-dimetilformamide) sostituendo la DMF nei canali con diverse molecole ($CHCl_3$, imidazolo, piridina e tetraidrofurano) per studiare la modulazione di S_r. A seconda della molecola ospitata, la temperatura alla quale si raggiunge il massimo di S_r e il suo valore variarono da 2.5 a -90 °C a 4.2 % $°C^{-1}$ a -10 °C.

Composti molecolari come complessi, CPs e MOFs sono ideali per lo studio delle correlazioni tra struttura, composizione (nel senso di funzionalizzazione molecolare) e proprietà funzionali in quanto facilmente modificabili tramite processi chimici. Tuttavia, è necessario integrare questi sistemi in dispositivi per sfruttare le loro proprietà in strumenti di uso comune. La funzionalizzazione di superfici è una procedura comunemente usata per questo scopo. In questo caso tuttavia, non è semplice mantenere il controllo sulla disposizione dei vari *building blocks* e caratterizzare la superficie funzionalizzata così che è fondamentale sviluppare un adeguato protocollo sintetico. In questo contesto, è stata messa a punto una procedura sintetica per la funzionalizzazione di superfici. Per questo scopo è stata sfruttata la reattività degli *N*,*N*-dialchilcarbammati lantanoidei per creare una sequenza eterobimetallica Eu^{3+}-Tb^{3+} ordinata aggraffata su silice amorfa, usando l'acido tereftalico come legante divergente per connettere i due centri metallici. La fotoluminescenza è stata qui utilizzata per determinare la distribuzione spaziale dei due ioni metallici sulla silice. In particolare, fenomeni di trasferimento energetico dal

Tb^{3+} all'Eu^{3+} sono stati usati come righello molecolare per determinare la distribuzione e le distanze intermetalliche ottenendo dati a supporto della formazione della sequenza desiderata.

Parole chiave: *lantanidi, leganti eterotopici, leganti β-dichetonati, polimeri di coordinazione, lanthanide organic frameworks, modifiche post-sintetiche, fotoluminescenza, termometri luminescenti, materiali funzionali, aggraffaggio, complessi N,N- dialchilcarbammici.*

Abstract

The present work is devoted to the development of lanthanoid-based luminescent thermometers and to the study of the correlations between the thermometric properties and the different building blocks composing the systems. In particular, using rare earth cations, β-diketones (H(β-dike)= dibenzoylmethane, Hdbm; benzoyltrifluoroacetone, Hbta; hexafluoroacetylacetone, Hhfac; thenoyltrifluoroacetone, Htta), and divergent ligands (4,4'-bipyridine, bipy; 4,4'-bipyridine-*N*-oxide, bipyMO; pyrazine-*N*-oxide, pyrzMO; 2,5-dihydroxy-1,4-dicarboxylate, H_2DHT^{2-}) we prepared molecular systems with different dimensionality: *i*) dinuclear complexes (0D), *ii*) Coordination Polymers (CPs, 1D), and Metal Organic Frameworks (MOFs, 3D).

We started with europium β-dike dinuclear compounds with molecular formula $[Eu_2(\beta\text{-dike})_6(L\text{-}MO)_x]$ (x=3 for hfac, x=2 for dbm, bta, and tta). Substituting the hfac -CF_3 groups with phenyl rings (one in bta, two in dbm) or with a thienyl ring (tta) the β-dike electronic and steric properties were modulated. Conversely, the different steric hindrance of bipyMO and pyrzMO influenced the spatial disposition of the β-dike ligands and the inter- and intra-molecular interactions. In the -50 ÷ 100 °C temperature range, the complexes showed relative thermal sensitivity (S_r) values higher than 1 (generally assumed as quality criterion for these thermometers) that depended on the nature of both the β-dike and L-MO ligands. The β-diketonates influenced S_r values, thermal operative range, and photostability of the system, while pyrzMO-containing compounds showed improved performances (S_r maximum from 4.6 to 8.1 % $°C^{-1}$ depending of the β-dike ligand) compared to that based on bipyMO (S_r maximum from 3.4 to 5.1 % $°C^{-1}$).

In the second part, a series of ratiometric Eu^{3+}/ Tb^{3+} luminescent thermometers were obtained by mixing different quantities of the two homometallic $[Ln(hfac)_3(bipy)]_n$ 1D-CPs (Ln^{3+}= Eu^{3+} and Tb^{3+}) in spectroscopically inert KBr. Here, we studied the effect of the relative metal amounts and of the excitation wavelength on the S_r. For

all the samples, S_r values almost independent from the Tb/Eu molar ratio and the excitation wavelength were found between -190 and 110 °C. Each sample showed a peculiar temperature-dependent emission colour, from green to red, that was exploited to develop colour-coded thermometers able to distinguish temperature intervals in the order of 10/ 20 °C.

Then we developed a mild-condition synthetic procedure to obtain *single crystal to single crystal* post-synthesis modifications of the 3D-MOF $\{[Eu_2(H_2DHT)_3(DMF)_4]\cdot 2DMF\}_n$ (DMF= *N*,*N*-dimethylformamide) to substitute DMF in the channels with different organic molecules (*i.e.* $CHCl_3$, imidazole, pyridine, and tetrahydrofuran) and to study the S_r modulation. Depending on the guest molecule, the temperature at which S_r reaches the maximum and its value varied from 2.5 at -90 °C to 4.2 % $°C^{-1}$ at -10 °C.

Molecular compounds like complexes, CPs and MOFs are ideal systems to study the correlations between structure, composition (in the meaning of molecular functionalization) and functional properties because they can be easily modified through chemical processes. Nevertheless, to exploit the unique properties of these compounds in commonly used tools and instruments they need to be integrated into a device. Surface functionalization is a recurrent way to achieve this target. However, maintaining the control on the arrangement of the various building blocks and characterize the functionalized surface is not straightforward, so that the development of *"ad hoc"* synthetic protocols and methods is required. In this context, we developed a general procedure for surface functionalization. We exploited the reactivity of lanthanoid *N*,*N*-dialkylcarbamate complexes to create an ordered Eu^{3+}-Tb^{3+} heterobimetallic sequence grafted on amorphous silica using terephthalic acid as divergent ligand to connect the two Ln^{3+} ions. Photoluminescence was here used to determine the spatial disposition of the two metal ions on silica. In particular, Tb^{3+}-to-Eu^{3+} energy transfer was used as molecular ruler to study the Ln^{3+} ions spatial

distribution and intermetal distances that allow us to obtain data supporting the formation of the desired sequence.

Keywords: *lanthanides, heterotopic ligands, β-diketonato ligands, coordination polymers, lanthanide organic frameworks, post-synthesis modifications, photoluminescence, luminescent thermometers, functional materials, smart-grafting, N,N- dialkylcarbamato complexes.*

Contents

List of abbreviations

- $(H_2NBu_2)(HT)$= Butylammonium monoacid terephthalate
- $(H_2NBu_2)_2(T)$= Di-dibutylammonium terephthalate
- ATR= Attenuated Total Reflectance
- BBR= Building Block Replacement
- BEnT= Back-Energy Transfer
- bipy=4,4'-bipyridine
- bipyMO= 4,4'-bipyridine-*N*-oxide
- C.F.= Crystalline Field
- CCD= Charge Coupled Device
- $CHCl_3$= Chloroform
- CN= Coordination Number
- CP= Coordination Polymer
- CSE= Coordinating Solvent Exchange
- CT= Charge transfer
- d= day
- DMF= *N*,*N*-dimethylformamide
- DMSO= Dimethylsulfoxide
- DR= Diffuse reflectance
- E.C.= Energetic configuration
- E.R.: Electronic repulsion
- ET= Energy transfer
- h= hour
- H_2T= Benzene-1,4-dicarboxylic acid/ terephthalic acid
- H_4DHT= 2,5-Dihydroxybenzene-1,4-dicarboxylic acid
- Hbta= 4,4,4-Trifluoro-1-phenyl-1,3-butanedione/ benzoyltrifluoroacetone
- Hdbm= 1,3-Diphenylpropane-1,3-dione/ dibenzoylmethane
- Hhfac= 1,1,1,5,5,5-Hexafluoro-2,4-pentanedione/ hexafluoroacetylacetone
- $HNBu_2$= Dibutylamine
- $HNMe_2$= Dimethylamine
- Htta= 4,4,4-Trifluoro-1-(2-thienyl)-1,3-butanedione/ 2-thenoyltrifluoroacetone
- Im= Imidazole
- ^{i}Pr= Iso-propyl group
- IR= Infrared
- *ISC*= Intersystem crossing

- IUPAC= International Union of Pure and Applied Chemistry
- LMCT= Ligand-to-Metal Charge Transfer
- L-MO= Generic *N*-oxide ligand
- Ln^{3+}= Lanthanoid tripositive ion
- MOF/LOF= Metal/ Lanthanoid Organic Framework
- MS= Mott-Seitz
- PSM= Post-Synthesis Modification
- Py= Pyridine
- pyrzMO= pyrazine-*N*-oxide
- Q= Pyrrolidine
- S.O.C.= Spin-Orbit Coupling
- S_1= Excited singlet state
- SALE= Solvent Assisted Ligand Exchange
- SBU= Secondary Building Unit
- SCSC= Single Crystal-to-Single Crystal
- SME= Solvent-Mediated Extraction
- Sr= Relative thermal sensitivity
- T= Temperature
- T= Triplet level
- THF= Tetrahydrofuran
- TSP= Temperature Sensitive Painting
- UV/Vis= Ultraviolet/ visible
- XRD= X-Ray Diffraction
- Δ= Thermometric parameter
- $\Delta E_{T\text{-}Ln}$= Triplet level- metal emissive level energy gap
- Φ= Intrinsic Quantum Yield
- β-dike= generic β-diketonate ligand
- λ_{em}= emission wavelength
- λ_{exc}= excitation wavelength
- η_{ET}= Energy transfer efficiency
- τ_{obs}= Experimental lifetime
- τ_{rad}= Radiative lifetime

1. General introduction

1.1. Lanthanoid chemistry and luminescent properties

According to IUPAC, the name Lanthanoids (commonly named Lanthanides) defines the fifteen elements with atomic number from 57 (lanthanum) to 71 (lutetium) which present, except lanthanum, partially or totally filled 4f orbitals. The general electronic configuration of these elements is [Xe] $4f^n$ $6s^2$ (n= 1 to 14) except for few cases like La, Ce, Gd, and Lu where the configuration [Xe] $4f^n$ $5d^1$ $6s^2$ (n= 0, 1, 7, and 14 respectively) is favoured. Lanthanoid elements usually exist in their trivalent state (Ln^{3+}) assuming a [Xe] $4f^n$ configuration (n= 1 to 14) since the sum of the first three ionization energies is relatively low ($I_1+I_2+I_3 \approx 3000 - 4000$ KJ mol^{-1}), except in that cases where a stable empty, half-filled, or totally filled 4f subshell is reached (Ce^{4+}, Tb^{4+}, Eu^{2+}, Yb^{2+}).[1]

The peculiar properties of lanthanoid elements derive from the unique characteristics of the 4f orbitals. Indeed, increasing the atomic number, the 4f orbitals contract rapidly and become more stable than the 5d and 6s orbitals. This appreciable penetration of the "xenon core" by 4f orbitals generates the peculiar chemical and electronic properties that distinguish the lanthanoid elements from all the rest of the periodic table.[1]

The inner nature of the 4f orbitals indeed prevents their overlap with the ligand orbitals and participation in the bonding. For this reason, lanthanoid reactivity is greater than that of *d* transition metals, akin to group II metals.

Lanthanoids generally form labile "ionic" complexes that undergo ligands exchange assuming very wide coordination numbers, generally from 6 to 12, and coordination geometries often depending by the ligand steric hindrance.[1,2]

Moreover, these ions are strong Lewis acids due to their high charge/ radius ratio. This feature is reflected in their coordination chemistry characterized by a strong affinity towards ligands presenting "hard" electronegative donor atoms (e.g. O and

F). In particular, a huge number of lanthanoid complexes based on anionic β-diketonate, carboxylate or phosphonate ligands is reported in the literature.[3–7] Moreover, the complex formation is entropically favoured by the use of chelating ligands which present stabilizing properties.

The inner nature of 4f orbitals generates also the unique luminescent properties of lanthanoid ions (Ln^{3+}). Indeed, the shielding of the 4f orbitals determines a crystal-field perturbation (10^2 cm^{-1}) significantly lower than the spin-orbit coupling (10^3 cm^{-1}).[8] This weak overlap between the lanthanoid 4f and ligands orbitals reflects in the moderate coupling between the electronic and molecular (vibrational and rotational) transitions generating narrow lines (up to few nanometers) in their absorption and emission spectra, with emissions which cover a large range in the electromagnetic spectrum from the visible (Pr^{3+}, Sm^{3+}, Eu^{3+}, Tb^{3+}, Dy^{3+}, Ho^{3+}, and Tm^{3+})[9–13] to the near infrared (Pr^{3+}, Nd^{3+}, Ho^{3+}, Er^{3+}, and Yb^{3+}).[14] The influence of principal physical interactions on the development of the energy level structure of a trivalent europium ion when introduced into a solid is illustrated in **Figure 1.1**.

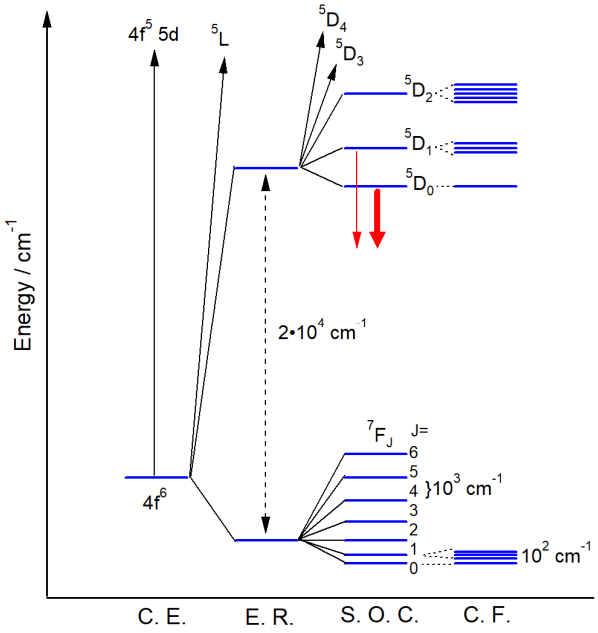

Figure 1.1: Energy diagram of Eu^{3+} $4f^6$ configuration (E.C.) showing the relative magnitude of the interelectronic repulsion (E.R.), spin–orbit coupling (S.O.C.) and crystal-field effects (C.F.). The downward arrows indicate the excited states $^5D_0$ and $^5D_1$ from which luminescence occurs. Readapted from ref. [15].

However, 4f-4f transitions are parity-forbidden according to Laporte's rule presenting weak intensities due to the low molar absorption coefficient in the near UV/Vis region ($\varepsilon < 10\ M^{-1}\ cm^{-1}$) and long excited states lifetimes (up to milliseconds). Nevertheless, π-conjugated organic chromophore with high molar absorption coefficient ($\varepsilon \approx 10^4$- $10^5\ M^{-1}\ cm^{-1}$) can be used to sensitize indirectly the lanthanoid luminescence. This phenomenon, also called *antenna effect*, was deeply studied by Crosby and Whan[16–18] and it can be summarized in the following steps (**Figure 1.2**): *a*) absorption of light with population of the first excited singlet state (S_1) of the organic ligand, (*b*) intersystem crossing (*ISC*) from the singlet to the triplet (*T*) level, and (*c*) energy transfer (E.T.) from the chromophore to the lanthanoid cation. In this way, by choosing the proper organic ligand, lanthanoid luminescence can be enhanced of several orders of magnitude.[19–23]

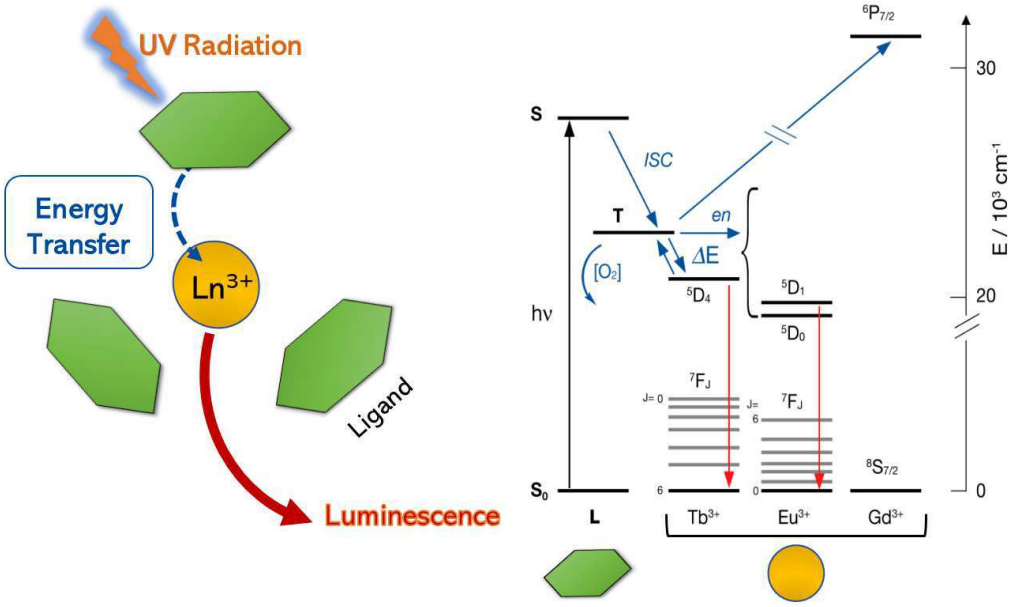

Figure 1.2: Schematization of the "*antenna effect*".

The total sensitization efficiency (Φ_{SE}) is determined by the *ISC* (Φ_{ISC}), the E.T. efficiency (Φ_{ET}), and by the Ln^{3+} photoluminescence quantum yield (Φ_{Ln}) according to the equation **(1.1)**:

$$\Phi_{SE} = \Phi_{ISC} \cdot \Phi_{ET} \cdot \Phi_{Ln} \qquad \textbf{(1.1)}$$

The energy transfer processes from the ligand to the lanthanoid ion are strongly influenced by the energy gap between the triplet excited state level of the chromophore and the emitting level of the metal cation ($\Delta E_{T\text{-}Ln}$).

Three main situations can be discussed:[24,25]

- if $\Delta E_{T\text{-}Ln} \leq 1{,}850$ cm^{-1}, low Φ_{ET} values are expected because back energy transfer from the metal to the ligand is effective;
- if $1{,}850$ cm^{-1} $< \Delta E_{T\text{-}Ln} <$ $5{,}000$ cm^{-1}, in this situation the energy transfer efficiency is optimised;
- if $\Delta E_{T\text{-}Ln} >> 5{,}000$ cm^{-1}, the energy gap between the ligand and the metal ion energy levels is too high, and no energy transfer processes are present. The energy is then dissipated through non-radiative processes.

Two non-radiative processes that influence the lanthanoid luminescence are *i)* the multiphonon emission and *ii)* the crossover from the $4f^n$ configuration to low-energy charge transfer (CT) state.

In the case of multiphonon emission, the non-radiative relaxation transition occurs from the excited state to the nearest lower electronic level of the metal ion (e.g. $^5D_0 \rightarrow {}^7F_6$ transition in Eu^{3+}). The energy difference between the two electronic states is converted in vibrational energy in the complex. In lanthanoid compounds, the vibrational energies are usually localized on the ligand which possess high-energy vibrational quenchers such as -OH, -NH, and -CH groups coordinated or spatially close to the lanthanoid ion. These groups can bridge large energy gaps with only a few phonons.[24,26] For example, in the case of Eu^{3+} $^5D_0 \rightarrow {}^7F_6$ energy gap ($12{,}000$ cm^{-1}) the third or the fourth vibrational overtone of proximate -OH oscillators (νOH $\approx$ $3{,}300 - 3{,}700$ cm^{-1}) is sufficient to bridge the energy gap.

The crossover from the $4f^n$ configuration to low-energy charge transfer state, or metal-to-ligand charge transfer state (LMCT), derives from the orbital overlap between the ligand and Ln^{3+} energy levels which can favour the electron transfer from the metal ion to the organic ligand with the formal reduction of the metal ion to

Ln^{2+}.[8] LMCT are often present in Eu^{3+} complexes since Eu^{3+} is the most oxidising trivalent rare-earth ions (Eu^{2+} achieves a stable half-filled configuration like Gd^{3+}). Charge transfer bands can sensitize or quench the Ln^{3+} luminescence depending on their energy: the closer the LMCT state is to Ln^{3+} emitting level, the higher will be the quenching probability.

Finally, also temperature is an important factor which regulates the luminescence of these systems. The sensitivity of lanthanoid complexes towards temperature variation is due to the fact that thermal energy allows the activation of quenching processes (e.g. metal-to-ligand back energy transfer, LMCT, or multiphonon processes) that influence the non-radiative deactivation of the excited states. This phenomenon is mainly due to the coupling between electronic and vibrational energy levels.[27,28]

After this overview on lanthanoid luminescent properties, it easy to understand why they are of great interest in the development of molecular and functional materials endowed with luminescent properties.

1.2. Molecular and functional materials

Functional materials play a pivotal role in our society. Indeed, they are the basis of a wide range of technologies such as computation, communication, storage and displaying of information making them essential for the entire technology sector.[29–31] The same is true for the generation and the storage of energy, for mobility and for sensing.[32,33] The term functional materials covers different material classes ranging from semiconductors, over polymers and molecular crystals, to nanoparticles. Their special electrical, optical and magnetic properties make functional materials so important. As concern luminescent materials, such as luminescent thin films, polymeric optical amplifiers, lasers, OLEDs, and luminescent chemical sensors, lanthanoid ions and their complexes play a key role due to their unique luminescent properties.[34] In particular, two types of lanthanoid coordination compounds can be distinguished in the context of molecular materials (**Figure 1.3**): *i*) discrete systems

based on Ln^{3+}- ligand complexes, and *ii*) extended systems as lanthanoid coordination polymers (CPs) and lanthanoid metal-organic frameworks (LOFs).

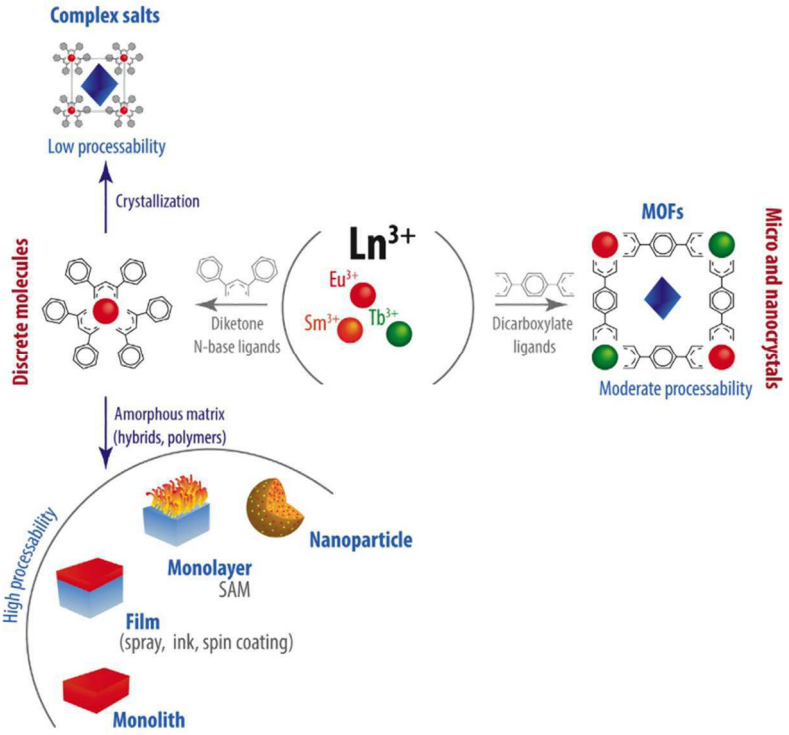

Figure 1.3: Different routes to design functionalized materials based on Ln^{3+} complexes. Adapted from ref. [35].

Molecular systems, often based on β-diketonate ligands, are generally soluble in organic solvents presenting a good processability through dispersion in matrices as films, monoliths or nanoparticles, or grafted on surfaces.[3,36] It is important to emphasize that a good processability is the key point to exploit in the daily life the properties of what is synthesized in a chemistry laboratory. For example, the integration of a metal complex in a support matrix allows to create materials characterized by completely new properties (optical, magnetic, *etc.*) or to develop electronic devices which exploit the properties of the metal complex.

On the other hand, CPs and LOFs, often based on carboxylate ligands,[5,37] are generally characterized by a moderate processability. However, they often show a higher thermal stability (> 250 °C) than discrete systems, which is important in material molding or solder dissolution processes,[38] and the possibility of a fine tuning of their properties.

Beside the numerous applications of lanthanoid luminescent complexes and materials in photonics, chemical sensing, lasers, and OLEDs, over the last few years a growing interest has been posed on their possible use as luminescent molecular thermometers due to their temperature dependent luminescent properties.

1.3. Luminescent thermometers

The concept of temperature rises from the observation that a physical state change can occur when two objects are in contact with each other, for example when an incandescent metal is immersed in water generating the boiling of water. This state change derives from an energy flow as heat form an object to another one. Temperature (T) is the physical property which indicates the direction of this heat flow. If two bodies are in contact with each other through a diathermic wall and no state change is observed, the two bodies are in thermic equilibrium according to the zeroth law of thermodynamics:[39]

"If a body C is in thermal equilibrium with two other bodies, A and B, then A and B are in thermal equilibrium with one another"

The zeroth law justify the concept of temperature and the use of the thermometers, *i.e.* devices for temperature measurements.

Nowadays, thermometry is a very explored field due to its high relevance to societal needs. Indeed, temperature measurements are required in countless technological and industrial fields, such as microelectronics, microoptics, photonics, microfluidics, and nanomedicine (e.g. in intracellular temperature measurement, or microcircuit thermal map), and in scientific research bring to a rapid increase in the development of temperature sensors which actually represents about the 80 % of the sensor market throughout the world (the global market is likely to grow to $ 6.13 billion in 2020).[40,41]

Over the time, several techniques have been developed to satisfy the different technological needs. These are based on different physical phenomena such as the

thermal expansion of mercury or alcohol, changes in the metal conductibility, shifts in infrared reflections and so on. For this reason, a classification based on the type of the interaction between the sample and the thermometer is more suitable rather than the one based on the physical phenomenon behind the measure:[42]

- *Contact*. The monitoring device is in direct contact with the interested medium (e.g. mercury or alcohol thermometers, and thermocouples).
- *Semi-invasive*. The sample of interest is treated in some manner to perform a remote observation (e.g. superficial coating with thermal paints, and imaging with the use of a contrast agent).
- *Non-invasive*. A remote and contactless observation of the sample (e.g. infrared thermography).

Contact techniques are generally characterized by a good temperature sensitivity and they are commonly used in everyday applications. However, contact methods are generally useless for temperature measurements in systems below 10 μm because they often present device intrinsic miniaturization limit. Moreover, since they require the reaching of the thermal equilibrium between the sensor and the object, the heat transfer can significantly alter the object temperature if it is too small.[43] The contact between sensor and sample can be also disadvantageous in moving systems. Other limitations for contact methods arise when the measurement conditions or the system itself can damage the thermometric probe or alter its sensitivity (e.g. the use of a thermo-resistor in a strong magnetic field).[43] For this reason, new classes of thermometers often based on non-contact methods (semi-, or non-invasive) have been developed reaching a proper sub-micrometric spatial resolution.[35,44]

Luminescent thermometry is a semi-/ non-invasive non-contact method which can overcome the operative limits which affect the abovementioned contact thermometers. It is regarded as one of the most promising techniques in temperature measurements because it combines high spatial resolution (< 10 μm) and short acquisition times (in the order of microseconds).[45]

In luminescence thermometry, temperature is associated to a variation of a luminescent property of an emitter species. This luminescent property, which is temperature-dependent, is also called *thermometric parameter* (Δ) Generally, three main thermometric parameters are used (**Figure 1.4**):[46]

a) the peak position spectral shift;

b) emission intensity, integrated intensity of one or two transitions;

c) excited state lifetime.

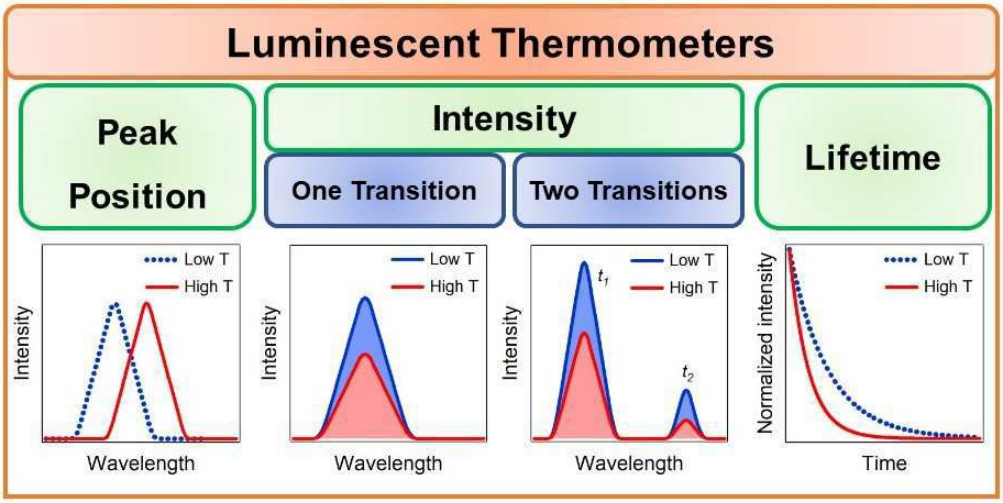

Figure 1.4: Luminescent thermometers classification.

Lifetime measurements are the most reliable because lifetime is directly related to temperature.[44] For example, they are often used in life-science where fluorescence lifetimes microscopy is largely employed.[47–49] However, lifetime measurements generally require long acquisition times, a post-processing techniques, and a more complex and demanding instrumentation by shortening the decay time.[50] For this reason, lifetime based luminescent thermometers are not useful for temperature measurements on large systems characterized by extended surfaces.

Also the emission intensity of a given fluorophore is directly correlated with temperature since it diminishes by increasing temperature.[44] Emission intensity-based luminescent thermometers are more practical to use than the lifetime-based one especially for temperature measurements on large systems.

For example, by dispersing a luminescent dye and a polymer binder in a solvent it is possible to create the so-called "temperature sensitive paintings" (TSPs)[51,52] which can be spread over a large surface area. By illuminating the threated object and using a CCD detector it is possible to collect a 2D map in which colours with different intensities are related to different temperatures.[41,42] However, intensity-based luminescent thermometers are affected by a variety of phenomena which alter the correlation between temperature and intensity such as the emitter local concentration, photodegradation phenomena, or instrumental conditions such as fluctuations of the excitation source.[35,53] These limitations can be overcome by using the intensities of two transitions: a transition whose intensity is temperature dependent and acts as thermometric probe, and a second transition which is unaffected by temperature and is used as internal standard. In this case, temperature is associated to the intensity ratio between the two transitions creating a self-calibrated luminescent thermometer which does not suffer the problems caused by changes in the experimental measurement conditions.[44,45,54,55]

Luminescent thermometric probes can be developed using several emitters such as organic compounds,[56–59] or polymers,[60–62] organic-inorganic hybrid materials,[63] semiconductor nanoparticles (quantum dots, QDs),[64,65] and lanthanoid ions (Ln^{3+}) dispersed in inorganic matrices[54,66–74] or as coordination compounds.[50,53,75–80]
Historically, organic dies played a pivotal role in this research field because of their well-known temperature-dependent luminescent properties around room temperature. For this reason, luminescent thermometers based on organic molecules are extensively employed for several applications, especially in biology and biomedicine, still today.[56–59]

However, during last years, luminescent thermometers based on QDs and Ln^{3+} ions spread up due to their high photostability. In particular, as described in **Section 1.1**, lanthanoid-based systems are particularly promising in virtue of their peculiar spectroscopic properties.

Since luminescence thermometry is based on different emitters and thermometric parameters (Δ, e.g. lifetimes, peak position, emission intensity), it is convenient to introduce the concept of *relative thermal sensitivity* (S_r) which is commonly used to compare the performances of different thermometers independently from their nature.[35] S_r is defined as the percentage variation of the thermometric parameter (Δ) per temperature degree:

$$S_r = \frac{1}{\Delta} \cdot \left|\frac{\partial \Delta}{\partial T}\right| \qquad [S_r] = \%\,°C^{-1} \text{ or } \%\,K^{-1} \tag{1.2}$$

For a certain temperature, the higher is the S_r value, the better are the thermometric properties of the system at that temperature. As depicted in **Figure 1.5**, where are reported the temperature dependent S_r trends of Ln^{3+}-Metal Organic Frameworks (LOFs) luminescent thermometers,[55] it can be seen that it is difficult for a single compound to cover wide temperature ranges. Generally, if a given system presents good S_r values in a cryogenic temperature range (< 100 K) it will not be effective in a physiological range (298-323 K) and *"vice versa"*.

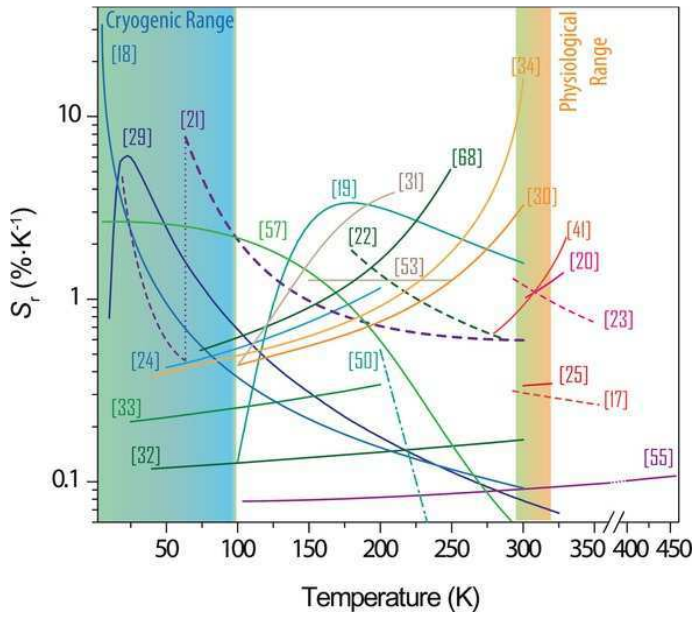

Figure 1.5: Temperature dependence of the relative thermal sensitivity of a series of Ln^{3+}-LOFs. Thermometers based on the intensity ratio between: (straight lines) two Ln^{3+} transitions, (dotted lines) Ln^{3+} transition and ligand transition. Reproduced from ref. [55].

The working range of a lanthanoid luminescent thermometer is mainly governed by the energy gap between the ligand triplet state (T) and Ln^{3+} emissive level ($\Delta E_{T\text{-}Ln}$). In particular, the smaller is this energy gap, the lower will be the operative temperature range of the luminescent thermometer because of the easier activation of metal-to-ligand energy back transfer processes. For example, considering the two [HQ][Ln(bta)$_4$] β-diketonate complexes (Ln^{3+}= Eu^{3+} and Tb^{3+}, Q= pyrrolidine, and Hbta= 4,4,4-trifluoro-1-phenyl-1,3-butanedione, T= 21,450 cm^{-1})[81] the luminescent properties of the Tb^{3+} complex are sensitive to temperature variation around -100 °C while the Eu^{3+} derivative only after room temperature. This difference is explained considering that Tb^{3+} $^5D_4$ emissive level (20,500 cm^{-1})[82] is much closer in energy to the ligand T level than Eu^{3+} $^5D_0$ level (17,220 cm^{-1})[8] so metal-to-ligand energy transfer occurs at lower temperature in the terbium derivative.

Nowadays, beside the synthesis of new luminescent thermometers with extended applicative temperature range, other challenges are investigated in this research field.[43],[45] One of the most interesting concerns the study of the correlations between the thermometric properties of a given system and the molecular fragments which compose it. The importance of this topic lies in the possibility to modulate at will the properties of the system by selectively varying the components that make it up. Moreover, once understood the parameters that influence the thermometric properties, it will be possible to create a theoretical model for the "*a priori*" design of complexes with the desired thermometric properties.

As concerns lanthanoid-based luminescent thermometers, there are three main interactions that influence the temperature dependence of the luminescent properties. The first, discussed before, is the ligand-to-metal energy transfer and the corresponding metal-to-ligand back donation (**Figure 1.6 a**). This interaction can be modulated changing the energy gap between the ligand triplet state and the lanthanoid emissive level modifying the nature of the antenna ligand or of the Ln^{3+} metal ion.

The second interaction, typical of ratiometric thermometers which are based on two different emitting ions, concerns the relative amount of the two emitting ions (generally Eu^{3+} and Tb^{3+}). Indeed, each metal ion will contribute to the overall thermometric properties of the system according to its specific thermometric response. Moreover, the eventual presence of energy transfer processes between them can provide an additional modulation of the thermometric properties (**Figure 1.6 b**).[82,83]

Finally, in 3D porous structures (e.g. Lanthanoid Organic Frameworks, LOFs) where guest molecules usually fill the LOF cavities, there can be a third mechanism. Indeed, in this case, the interaction between the guest molecule and the metal ion provides thermally-activated guest-to-ion and ion-to-guest energy transfer processes which can be effective in the modulation of the compound thermometric properties (**Figure 1.6 c**).

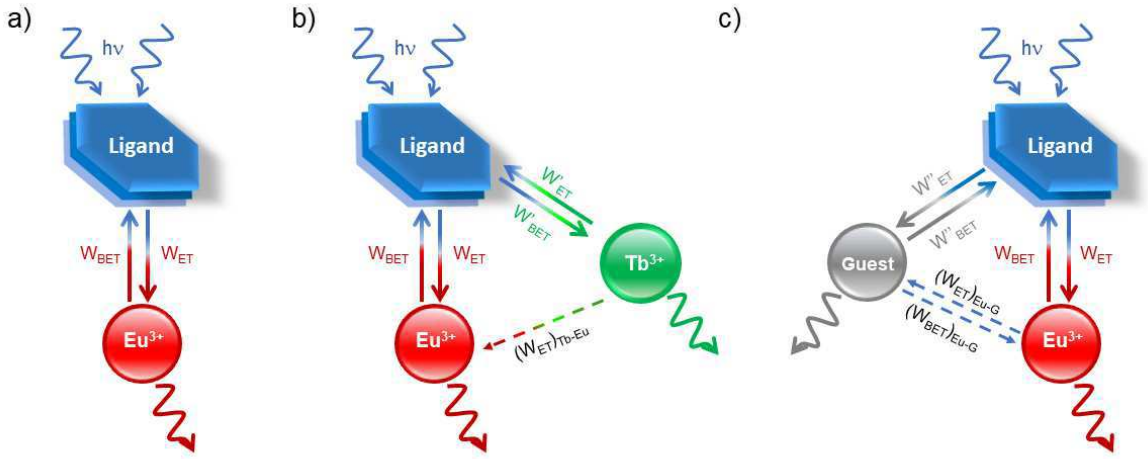

Figure 1.6: The three main mechanisms that influence the thermometric response in a Ln-based luminescence thermometer: **a**) ligand-to-ion, **b**) ion-to-ion, and **c**) guest-to-ion energy and back-energy transfer.

1.4. Thesis outline

In this PhD thesis the synthesis of new lanthanoid luminescent complexes of various dimensionality has been associated to the study of their thermometric properties. Starting from different points of interest in the lanthanoid chemistry, three different

systems have been designed *"ad hoc"* for the selective study of each of the three interactions that contribute to the modulation of the thermometric response (**Figure 1.6**): the ligand-to-ion energy transfer, the relative amount of two emitting ions, and the guest-ion interactions.

Relatively to the ligand-to-metal energy transfer, a series of europium dinuclear compounds based on four different commercial β-diketonate ligands and two *N*-oxides molecules with molecular formula $[Eu_2(\beta\text{-dike})_6(L\text{-}MO)_x]$ (x=2 or 3 depending by the nature of the β-diketonate ligand) was chosen (**Chapter 2**). Here it was investigated the correlation between the thermometric properties and the metal/β-diketonate ligand interactions.

As concerns the modulation of the thermometric properties due to the different amount of the two emitting metal ions, we studied a series of ratiometric thermometers based on two 1D zig-zag coordination polymers with chemical formula $[Ln(hfac)_3(bipy)]_n$ (where Ln^{3+} were Eu^{3+} and Tb^{3+} and bipy was 4,4'-bipyridine) in which the relative Eu^{3+}/Tb^{3+} amount was gradually changed (**Chapter 3**).

Finally, the system investigated for the study of the guest-metal ion interaction was the porous 3D-LOF $[Eu_2(H_2DHT)_3(DMF)_4 \cdot 2DMF]_n$ (where H_2DHT was the dianion of the 2,5-dihydroxytherephtalic acid) (**Chapter 4**). In this case, DMF was substituted with different organic molecules to study how the thermometric properties of the resulting LOFs were modulated depending on the molecules hosted in the structure.

As previously discussed, to exploit the properties of molecular compounds in commonly used tools and instruments they need to be integrated into a device. Surface functionalization (e.g. *via* dispersion or chemical grafting) is a recurrent way to achieve this target. For this reason, it has been also investigated the possibility to develop a general synthetic protocol for the functionalization of an inorganic matrix (e.g. amorphous silica), by exploiting the reactivity of lanthanoid *N*,*N*-dialkylcarbamate complexes for the creation of luminescent materials (**Chapter 5**).

In this case, lanthanoid luminescence properties were also used as a tool for the material characterization.

In the following chapters, each topic and the idea behind will be discussed in detail.

2. Eu^{3+}-dinuclear compounds

2.1. Introduction

As described in **Chapter 1**, organic ligands are commonly used to sensitize the lanthanoid ion luminescence *via* the "*antenna effect*". β-diketonate ligands[84] (**Figure 2.1**) are a class of commercial and inexpensive monoanionic bidentate oxygen donor ligands commonly used in lanthanoid coordination chemistry for the development of luminescent compounds[3,85–89] thanks to the strong $n \rightarrow \pi^*$ molecular transition centred in the near UV which often presents suitable energy for the luminescence sensitization of many lanthanoid ions.[3]

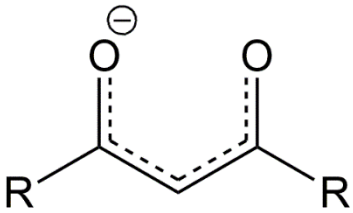

Figure 2.1: Representation of a β-diketonate ligand.

Moreover, β-diketonate spectroscopic properties can be finely tuned simply varying the nature the R- substituent groups.[3] Different R- substituents modulate the energy of the ligand triplet state (T) which can move from the UV towards the visible range of the electromagnetic spectrum increasing the aromaticity of the substituents (**Figure 2.2**). Depending on the energy of the triplet level, the sensitized emission of several lanthanoid ions can be achieved both in the visible (Eu^{3+}, Tb^{3+})[90,91] and in the near-infrared.[92,93]

As previously described in **Chapter 1** (pages 5-6 and 14), the energy gap between the ligand triplet level and the lanthanoid ion emissive level ($\Delta E_{T\text{-}Ln}$) is one of the parameters that regulates the thermometric response in a lanthanoid-based luminescence thermometer. In a pioneering work of Sato and Wada,[81] the correlation between $\Delta E_{T\text{-}Ln}$ and the temperature dependence of the excited state lifetime in a series of Tb^{3+} and Eu^{3+} chelate compounds with composition [HQ][Ln(β-dike)$_4$] (Q=

pyrrolidine) was showed. It was assessed that the smaller is the $\Delta E_{T\text{-}Ln}$, the lower is the temperature at which metal-to-ligand back energy transfer becomes operative.

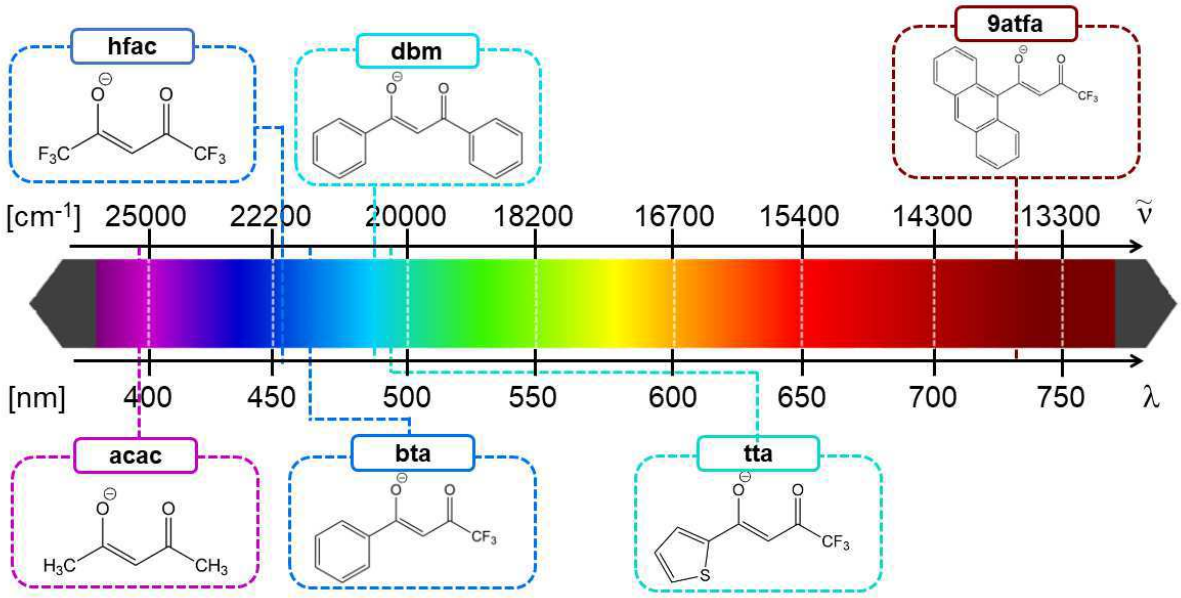

Figure 2.2: Triplet energy levels of some β-diketonate ligands. Acetylacetonate (acac, 25,200 cm^{-1}),[94] hexafluoroacetilacetonate (hfac, 21,900 cm^{-1}),[95] benzoyltrifluoroacetonate (bta, 21,450 cm^{-1}),[96] dibenzoylmethide (dbm, 20,500 cm^{-1}),[97] 2-thenoyltrifluoroacetonate (tta, 20,400 cm^{-1}),[97] and 9-anthroyltrifluoroacetonate (9atfa, 13,600 cm^{-1}).[81]

In lanthanoid β-diketonate complexes both anionic *tetrakis*-(β-diketonate) complexes (Ln^{3+}:β-dike = 1:4), in which the Ln^{3+} is octacoordinated, and neutral *tris*-(β-diketonate) complexes (Ln^{3+}:β-dike = 1:3) can be prepared by modulating the β-diketonate ligand/ Ln^{3+} molar ratio. However, *tris*-(β-diketonate) complexes, in which the Ln^{3+} is hexacoordinated, tend to a coordination number eight, binding basic Lewis species as water or organic molecules. This behaviour can be often exploited to rationalize and forecast the composition and the nuclearity of the resulting products through a careful choice of the Lewis base ligand (or ancillary ligand). As depicted in **Figure 2.3**, from the [Ln(tta)$_3$] moiety (Ln= Eu^{3+} or Gd^{3+}) it is possible to obtain mononuclear (**a**),[98] dinuclear complexes (**b**),[99] or Coordination Polymers (**c**)[100] using three different *N*-donor ligands.

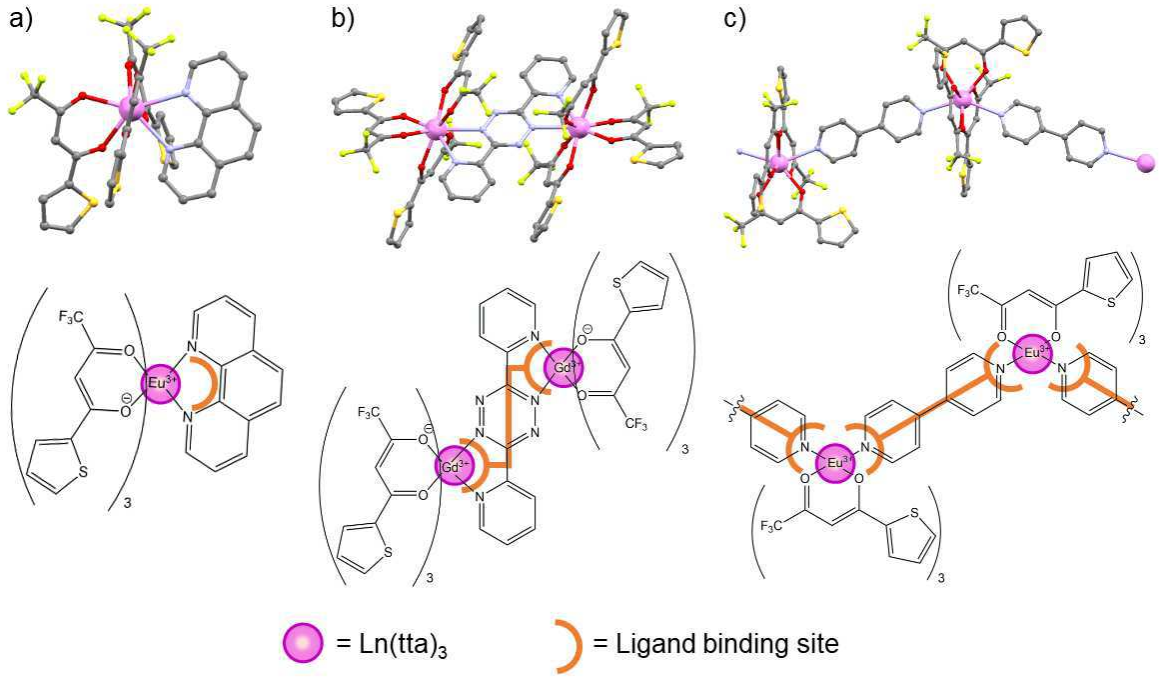

Figure 2.3: Lanthanoid complexes with various nuclearity depending on the nature of the ancillary ligand: **a**) mononuclear [Eu(tta)$_3$(phen)], **b**) dinuclear [Gd(tta)$_3$]$_2$(bpta)], and **c**) multinuclear [Eu(tta)$_3$(bipy)]$_n$.

With the aim of studying the correlations between structural modifications and the luminescent and thermometric properties modulation of a certain system, we selected lanthanoid *tris*-β-diketonate moieties that are useful for this kind of investigation. Indeed, the ancillary ligand is able to define the nuclearity of the metal compounds and a series of isostructural complexes can be obtained using β-diketonate ligands with different R- groups.[100]

The design of a new family of molecular metal complexes allows a better synthetic control and a higher solubility that may lead to an easier characterization and purification respect to extended structure Coordination Polymers (CPs) or Metal Organic Frameworks (MOFs). To this purpose, *N*-oxide molecules were an interesting class of organic ligand to be used as ancillary ligands in the synthesis of *tris*-(β-diketonate) complexes.

2.1.1. *N*-oxide ligands: 4,4'-bipyridine-*N*-oxide e pyrazine-*N*-oxide

N-oxide ligands are a class of organic molecules scarcely used in lanthanoid coordination chemistry despite the strong affinity between Ln^{3+} ions and O-donor ligands. They can be obtained from the partial or total oxidation of an *N*-heterocyclic aromatic ring (e.g. pyridine, pyrazine, bipyridine) generally with H_2O_2[101] or 2-Bromo-6-chloroperbenzoic acid.[102]

The most used *N*-oxide is the 4,4'-bipyridine-*N*,*N*'-dioxide (bipyDO) which was also employed in the synthesis of lanthanoid Coordination Polymers (CPs).[103–105] BipyDO is a rigid divergent ligand able to coordinate two or more metal centers in different ways (**Figure 2.4**).[106]

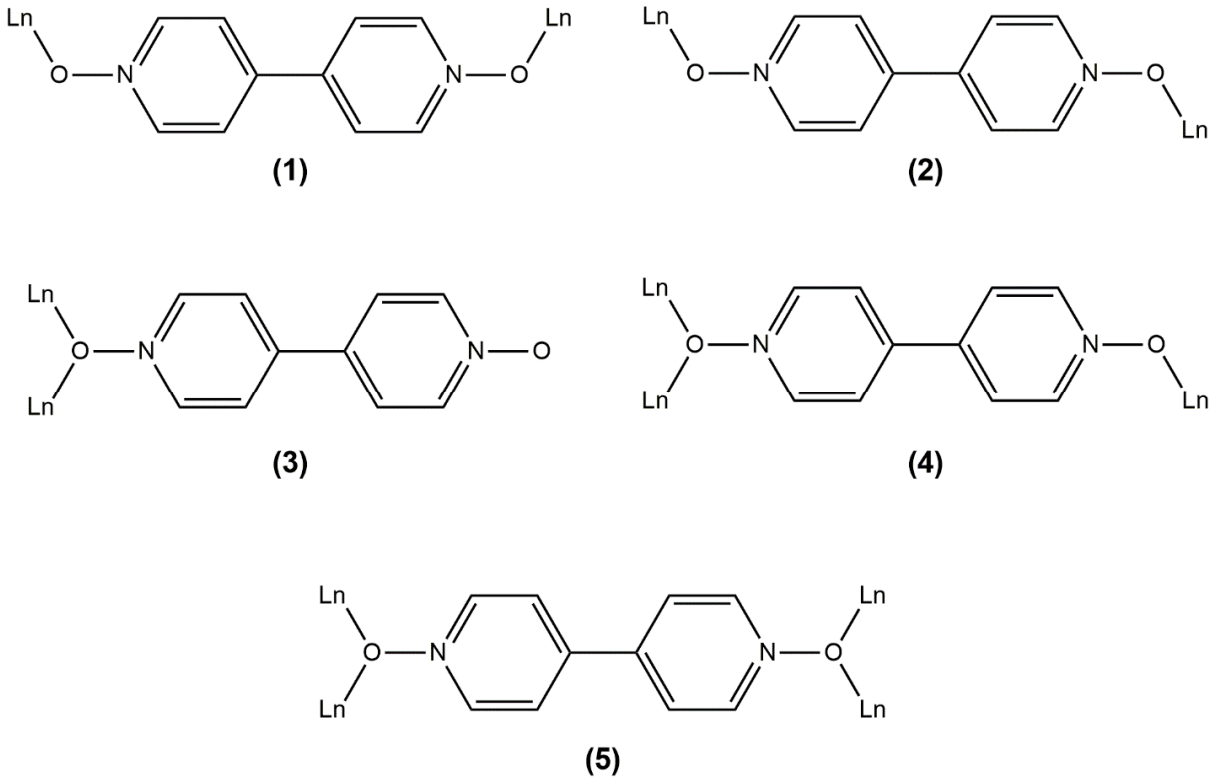

Figure 2.4: Different coordination modes of the bipyDO ligand.

According to **Figure 2.4**, bipyDO can bind one or two Ln^{3+} ions per each *N*-oxide group with a total number of coordinated metal ions which vary from two up to four. Two different coordination modes can be discussed:

1. bridging two different metal centers with *cis* **(1)** or *trans* **(2)** geometries respect to the N-N axis; [107]

2. as μ-ligand between two metal centers coordinated to the same *N*-oxide group as in **(3)** and **(5)**. [108–110]

It is worth to note that the two binding modes can be also present at the same time as in **(4)**. The factors that favour coordination modes **1** and **2** over **3** and **5** are not completely clear yet, but probably they depend on both steric and electronic factors.

When lanthanoid inorganic salts are reacted with bipyDO the choice of the solvent can be crucial for the synthetic purposes. For example, keeping constant the experimental Tb^{3+}/ bipyDO molar ratio (1:1.5) Long and co-workers synthesized five different compounds based on $Tb(NO_3)_3$ and bipyDO simply varying the ratio between the solvents (CH_3OH, CH_2Cl_2, and H_2O) in the reaction mixture (**Figure 2.5**).[104]

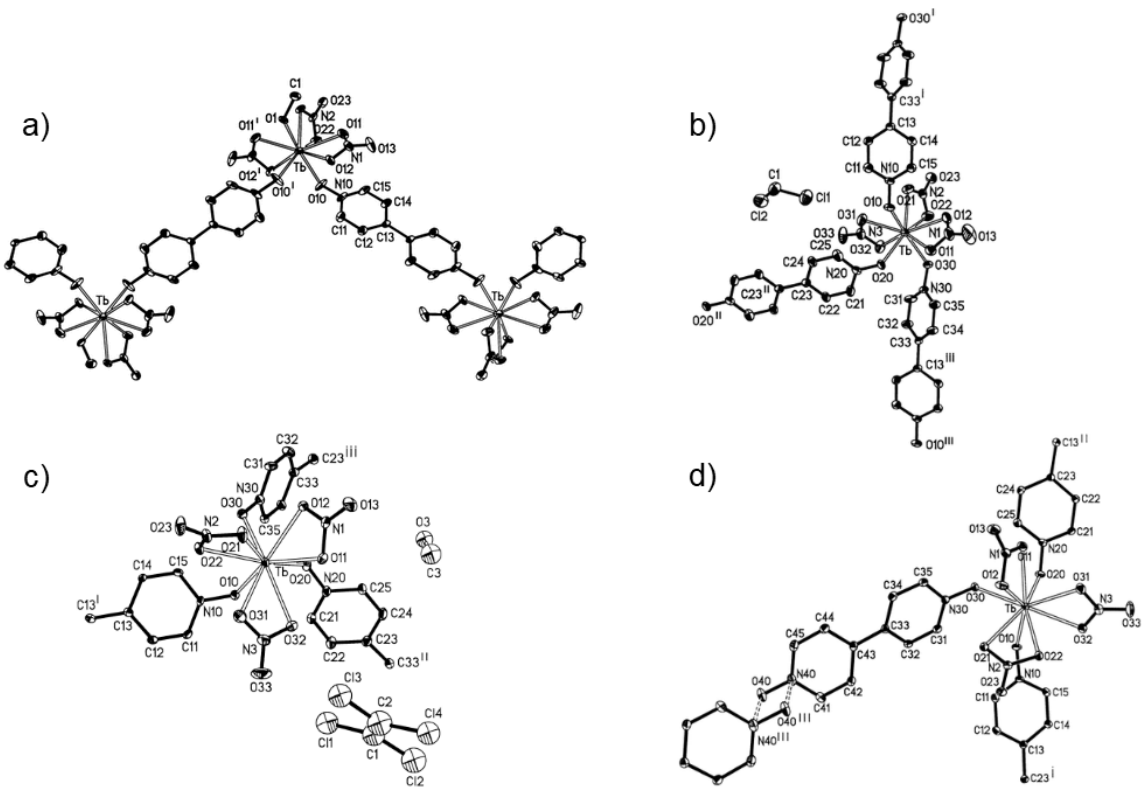

Figure 2.5: XRD-crystallographic structures of four of the five Tb^{3+}-CPs synthetized using $Tb(NO_3)_3$ and bipyDO: **a**) $[Tb(bipyDO)(CH_3OH)(NO_3)_3]_n$, **b**)$\{[Tb(bipyDO)_{1.5}(NO_3)_3] \cdot CH_2Cl_2\}_n$, **c**)$\{[Tb(bipyDO)_{1.5}(NO_3)_3] \cdot 0.4CH_2Cl_2 \cdot 0.8CH_3OH\}_n$, **d**)$[Tb(bipyDO)_2(NO_3)_3]_n$. Adapted from ref [104].

However, for lanthanoid *tris*-β-diketonate complexes Bernot and co-workers obtained the 2D-CPs $\{[Ln(hfac)_3]_2[bipyDO]_{1.5}\}_n$ (where Ln = Eu, Gd, Dy and hfac= hexafluoroacetilacetonate) employing different reaction conditions.[109] In these compounds the metal center is nonacoordinate with six oxygen atoms deriving from three hfac ligands and three oxygen atoms from three bipyDO ligands that bridge two different metal centers forming dinuclear metal units (**Figure 2.6**).

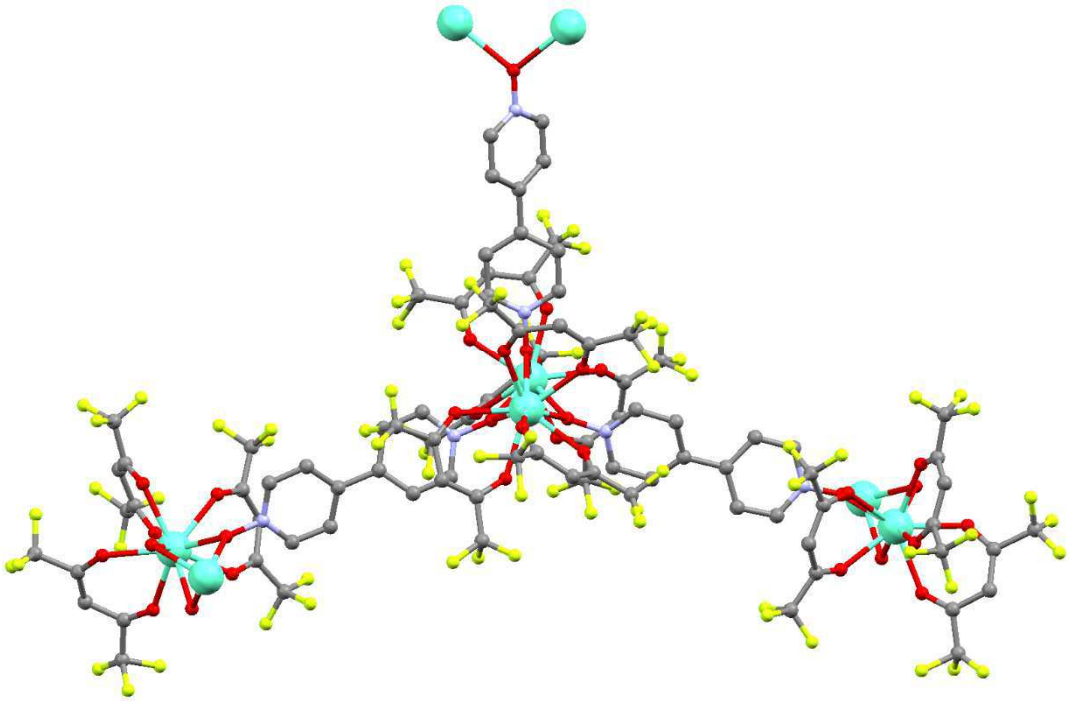

Figure 2.6: Crystal structure of the 3D-CP $\{[Ln(hfac)_3]_2[bipyDO]_{1.5}\}_n$ obtained by Bernot and co-workers. Ref [109].

The same authors reported similar molecular systems based on the $[Ln(hfac)_3]$ (Ln= Eu, Gd, Tb, Dy) in which also the pyridine-*N*-oxide ligand showed a coordination mode similar to that of the bipyDO originating the same lanthanoid dinuclear unit with the bridging *N*-oxide.[28,29] Moreover, also the 3D-CP $\{[La_2(bta)_6(bipyDO)_{1.5}\cdot H_2O]\}$ (bta= benzoyltrifluoroacetonate) reported by Ma and collaborators[108] showed the same lanthanoid dinuclear unit with three bridging bipyDO ligands.

These reports suggest that the $[Ln_2(\beta\text{-dike})_6(bipyDO)_{1.5}]$ dinuclear unit can be assumed independent from the nature of the employed β-diketonate and *N*-oxide

ligands and that it could be possible to synthesize a series of compounds based on this unit with different anionic and ancillary ligands.

By substituting bipyDO with a ligand bearing only an *N*-oxide moiety, discrete metal complexes can be synthesized.[110] The scarcely used heterotopic ligands 4,4′-bipyridine-*N*-oxide (bipyMO) and pyrazine-*N*-oxide (pyrzMO) were employed for the synthesis of discrete lanthanoid complexes because Ln^{3+} ions present a higher affinity towards O-donor ligands than to nitrogen donors. Indeed, the lanthanoid ion is able to distinguish the two ligand binding sites preferring the oxygen one, as we recently showed by synthesizing a series of alternating *d-f* heterobimetallic 1D-CPs with composition $[Ln(hfac)_3M(hfac)_2(bipyMO)_2]_n$ (Ln^{3+}= Eu^{3+}, Dy^{3+} while M^{2+}= Co^{2+}, Cu^{2+}, and Zn^{2+}) in which the Ln^{3+} ion is selectively bound to the ligand oxygen site while the M^{2+} *d* metal to the N site of the ligand (**Figure 2.7**).[111]

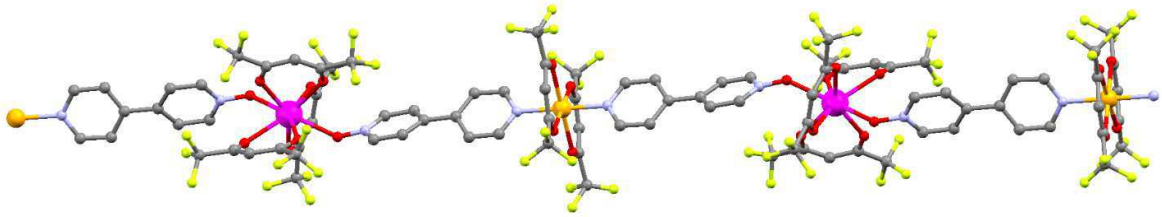

Figure 2.7: Structure of the 1D-CPs $[Ln(hfac)_3M(hfac)_2(bipyMO)_2]_n$ (Ln^{3+}= Eu^{3+}, Dy^{3+} while M^{2+}= Co^{2+}, Cu^{2+}, and Zn^{2+}) adapted from ref [111].

2.1.2. Topic outline

Four different commercial β-diketonate ligands (hexafluoroacetilacetonate, hfac; benzoyltrifluoroacetonate, bta; dibenzoylmethide, dbm; and 2-thenoyltrifluoroacetonate, tta) and the two *N*-oxide ligands 4,4′-bipyridine-*N*-Oxide (bipyMO) and pyrazine-*N*-oxide (pyrzMO) were employed to synthesize two series of lanthanoid dinuclear β-diketonate complexes with composition $[Eu_2(\beta\text{-dike})_3(L\text{-}MO)_x]$ (x=2 for β-dike= dbm, bta, and tta, while x=3 for β-dike= hfac) that were fully characterized. We will discuss here how the two building blocks (β-dike and *N*-oxide)

influence the room temperature and temperature-dependent luminescent properties of the system.

The chosen β-diketonate ligands have different electronic properties and steric hindrance due to the gradual substitution of the -CF_3 groups of hfac with aromatic rings: one or two phenyl rings in the case of bta and dbm or with the thienyl ring in tta. In this way, also the energy of the ligand triplet level and the ligand-to-metal (and metal-to-ligand) energy transfer processes are modulated. Conversely, the different steric hindrance of bipyMO and pyrzMO (two and one aromatic rings) can influence the spatial disposition of the other ligands and the inter- and intra-molecular interactions.

2.3. Results and discussion

2.3.1. Synthesis and characterizations

The dinuclear compound $[Eu_2(hfac)_3(bipyMO)_3]$ was synthesized by reacting the two precursors $[Eu(hfac)_3]$ and bipyMO in anhydrous toluene using a metal/ ligand molar ratio of 2:3.[109] The yellow solution was refluxed for two hours and then cooled at -20 °C recovering a colorless precipitate. The elemental analysis performed on the dried powder confirmed the correct composition. The solid was recrystallized from hot toluene obtaining single crystals suitable for single crystal XRD analysis. As shown in **Figure 2.8**, the compound is characterized by the Eu^{3+} dinuclear unit in which each Eu^{3+} ion is surrounded by three hfac ligand and three μ-bipyMO moieties assuming a coordination number (CN) of nine and a tricapped trigonal prismatic geometry. The two Eu^{3+} sites are crystallographycally independent. As expected, the bipyMO is coordinated to the metal centers only through its oxygen atom leaving the nitrogen site uncoordinated. Three toluene molecules were found in the crystalline structure. Crystals loose solvent in the drying process producing an amorphous powder.

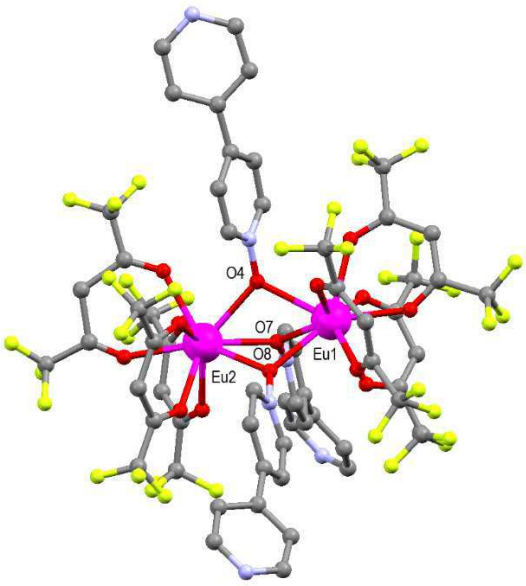

Figure 2.8: Structure of the Eu^{3+} dinuclear compound $[Eu_2(hfac)_6(bipyMO)_3 \cdot 3toluene]$. Solvent molecules were omitted for clarity.

Hhfac is often used as electron density acceptor (Hhfac $pK_a = 4.35$)[112] to increase the acidic behaviour of the metal center which becomes able to react also with poor basic

ligands.[113–115] Conversely, dibenzoylmethane (1,3-diphenylpropane-1,3-dione, Hdbm) has significantly different electronic properties (Hdbm pK_a= 8.95)[116] and a higher steric hindrance due to the two phenyl rings as substituents.

The reaction between [Tb(dbm)$_3$] and bipyMO in a 2:3 molar ratio in hot toluene led to a yellow solution from which yellow crystals can be recovered at low temperature (-20 °C).[117] Single crystal X-ray diffraction study established that the product was formed by [Tb_2(dbm)$_6$(bipyMO)$_2$] dinuclear molecules (**Figure 2.9**).[117,118]

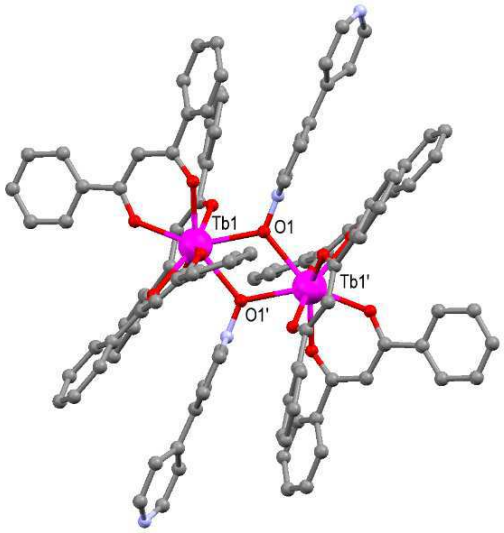

Figure 2.9: Structure of the Tb^{3+} dinuclear compound [Tb_2(dbm)$_6$(bipyMO)$_2$]. Solvent molecules were omitted for clarity.

In this case, the obtained complex is centrosymmetric with the inversion center located between the two oxygen atoms of the bipyMO molecules (O1 and O1' in **Figure 2.9**). Each Tb^{3+} ion is coordinated to eight oxygen atoms: six from the three dibenzoylmethide ligands and two from the two bridging (μ_2-O) bipyMO ligands. Tb^{3+} assumes a trigonal dodecahedron coordination geometry commonly found in octacoordinated lanthanoid complexes. Also in this complex, the nitrogen atoms of the bipyMO ligand resulted uncoordinated pointing at about 180° from each other.

The crystals of the solvated product collapsed in air or under vacuum with loss of crystallization solvent. The infrared spectrum collected on the resulting powder showed signals attributable to the coordinated bipyMO at 1594, 1023, and 810 cm^{-1}

while no signals related to free bipyMO were present since the ligand excess was well soluble in toluene.

The synthesis was repeated to prepare the corresponding Eu^{3+} analogue using $[Eu(dbm)_3]$ and bipyMO in a 1:1 stoichiometry obtaining $[Eu_2(dbm)_6(bipyMO)_2]$ in good yields. The elemental analysis and the IR spectrum superimposable to that of $[Tb_2(dbm)_6(bipyMO)_2]$ confirmed the synthesis of the desired Eu^{3+} compound structurally similar to the Tb^{3+} derivative.[118]

From the reaction in toluene between $[Eu(bta)_3]$ (Hbta= 4,4,4-Trifluoro-1-phenyl-1,3-butanedione or benzoyltrifluoroacetone) and bipyMO in a 1:1 molar ratio, performed in the same conditions of the previous synthesis, a microcrystalline product was recovered at -20 °C with analytical composition $[Eu_2(bta)_6(bipyMO)_2]$. From a recrystallization through pentane vapours diffusion in a toluene solution of the product, single crystals suitable for XRD analysis were obtained (**Figure 2.10 a**). A toluene molecule, present in the crystal structure, is lost exposing the compound to air. Despite the different nature of the β-diketonate ligands, the structure of $[Eu_2(bta)_6(bipyMO)_2]$ is similar to that of $[Eu_2(dbm)_6(bipyMO)_2]$ with the two bipyMO ligands laying on the same plane and an inversion center located between their oxygen atoms. Eu^{3+} ions present coordination number eight and a trigonal dodecahedral geometry.

Similar results were also obtained using the $[Eu(tta)_3]$ derivative (Htta= 4,4,4-trifluoro-1-(2-thienyl)-1,3-butanedione or 2-thenoyltrifluoroacetone) whereby the compound $[Eu_2(tta)_6(bipyMO)_2]$ was synthesized in good yields. Its molecular structure is analogue to that already found in the case of dbm and bta with the same inversion centre and coordination geometry (**Figure 2.10 b**). In this case no toluene molecules are present in the complex structure and the crystals do not lose their crystalline habit if exposed to air or under reduced pressure.

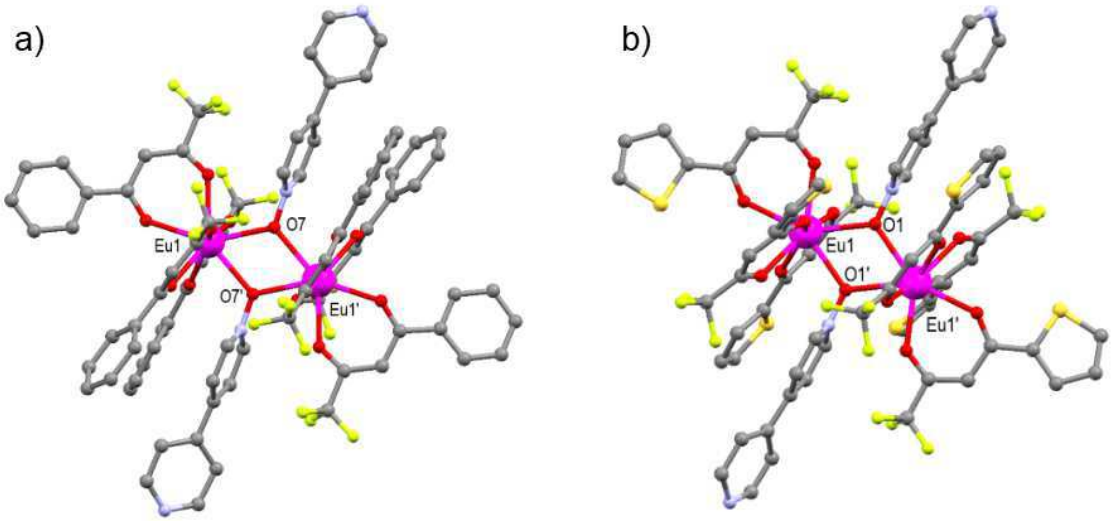

Figure 2.10: Structure of the Eu^{3+} dinuclear compound $[Eu_2(bta)_6(bipyMO)_2]$ (**a**) and $[Eu_2(tta)_6(bipyMO)_2]$ (**b**). In (**a**) solvent molecules were omitted for clarity.

These $[Ln_2(\beta\text{-diketonate})_6(bipyMO)_x]$ (x= 2, 3) species confirmed the preference of lanthanoid ions towards the oxygen atom of the ancillary ligand directing the assembly of the dinuclear derivatives with a hypodentate bipyMO. In principle, the uncoordinated nitrogen atom could be used as H^+ acceptor for the creation of supramolecular structures based on H-bond, or as a coordination site for a different metal center (such as *d* metals) to obtain extended structures.[119] These $[Eu_2(\beta\text{-dike})_6(bipyMO)_x]$ (x = 2, 3) compounds showed the μ^2-O coordination type for the bipyMO in analogy to that observed with the homotopic bipyDO.

The different number of coordinated bipyMO ligands in the hfac complex compared to the dbm, bta, and tta derivatives can be related both to steric or electronic reasons. Indeed, three bipyMO ligands are necessary to fulfil Eu^{3+} electronic demand considering the hfac behaviour as electron density acceptor. Conversely, aromatic rings (phenyl and thienyl) of the dbm, bta, and tta ligands provide a greater steric hindrance than the $-CF_3$ group thus preventing the coordination of the third bipyMO molecule.

The synthesis of the analogue Eu^{3+} compounds based on pyrzMO confirmed that, for an europium center, solely the nature of the β-diketonate ligand determines the

reaction stoichiometry. Indeed, four dinuclear compounds with the same composition and coordination geometry of the corresponding bipyMO derivatives were obtained: $[Eu_2(hfac)_6(pyrzMO)_3]$, $[Eu_2(dbm)_6(pyrzMO)_2]$, $[Eu_2(bta)_6(pyrzMO)_2]$, and $[Eu_2(tta)_6(pyrzMO)_2]$ (**Figure 2.11**). As previously, Eu^{3+} coordination number is nine only in the hfac derivative while it is eight for the other three complexes.

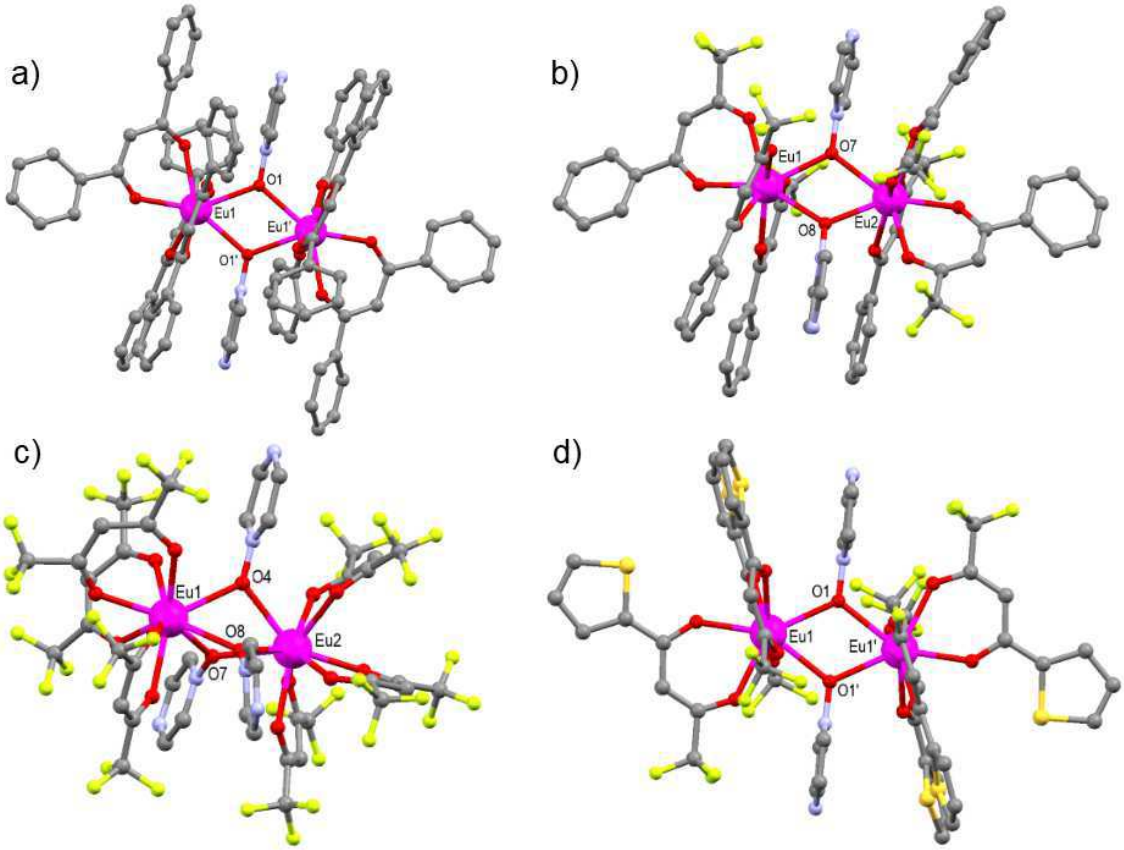

Figure 2.11: Structures of the Eu^{3+} dinuclear compounds $[Eu_2(dbm)_6(pyrzMO)_2]$ (**a**), $[Eu_2(bta)_6(pyrzMO)_2]$ (**b**), $[Eu_2(hfac)_6(pyrzMO)_3]$ (**c**), and $[Eu_2(tta)_6(pyrzMO)_2]$ (**d**). Solvent molecules were omitted for clarity.

However, comparing the four pyrzMO compounds to their bipyMO analogues, small differences in the distribution of the ligands around the metal center can be observed. These differences are probably related to the smaller steric hindrance of the pyrzMO ligand which allows a different spatial disposition of the ligands. As an example, in **Table 2.1** the values of the O_x-Eu_y-O_z angles formed by the oxygen atoms of the *N*-oxide ligands and each crystallographycally non-equivalent Eu^{3+} center are compared. Moreover, the spatial packing of the complexes is more compact using pyrzMO instead of bipyMO because the shorter length of the ancillary ligand allows a better

approach between different asymmetric units as also visible in **Figure 2.12** where the packing of $[Eu_2(bta)_6(bipyMO)_2]$ and $[Eu_2(bta)_6(pyrzMO)_2]$ complexes is reported as example.

β-diketonate ligand	bipyMO	Angles	pyrzMO
hfac	61.78°	O_4-Eu_1-O_7	62.20°
	62.79°	O_4-Eu_1-O_8	61.01°
	67.27°	O_7-Eu_1-O_8	67.79°
	61.69°	O_4-Eu_2-O_7	62.31°
	62.79°	O_4-Eu_2-O_8	61.86°
	68.21°	O_7-Eu_2-O_8	67.50°
dbm	62.19°	O_1-Eu-O_1'	62.02°
bta	61.26°	O_7-Eu-O_7'	61.95° + 62.88°
tta	61.77°	O_1-Eu-O_1'	63.11°

Table 2.1: Values of the O_x-Eu_y-O_z angles in the eight Eu^{3+} dinuclear compounds. For compound $[Eu_2(bta)_6(pyrzMO)_2]$ are reported the values of the O_7-Eu_1-O_8 and O_7-Eu_2-O_8 angles.

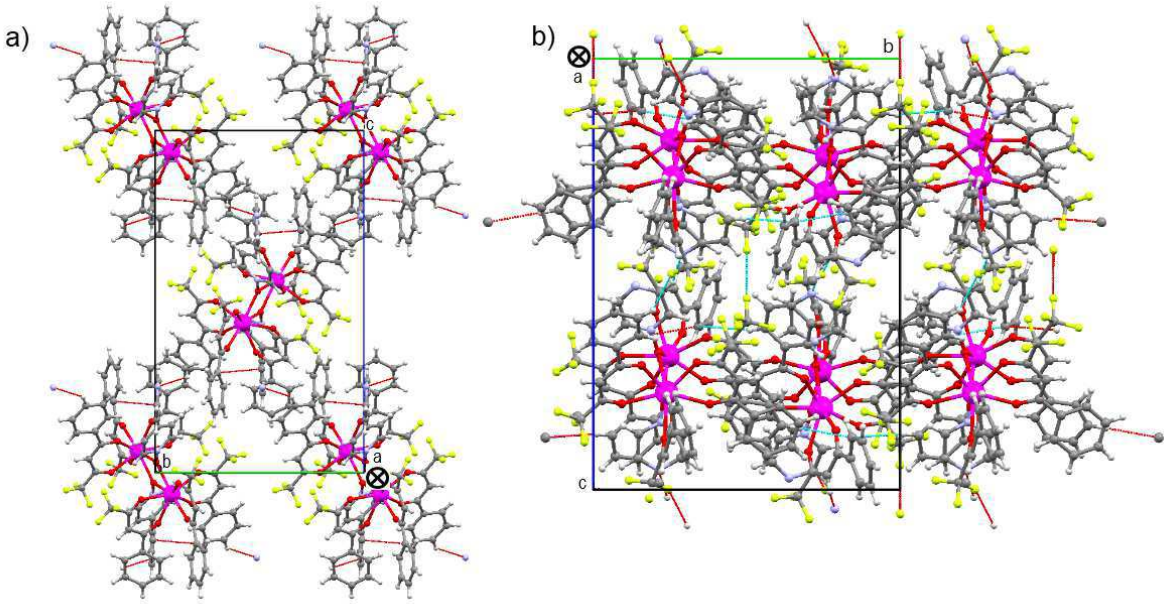

Figure 2.12: Different packing of (**a**) $[Eu_2(bta)_6(bipyMO)_2]$ and (**b**) $[Eu_2(bta)_6(pyrzMO)_2]$ complexes along the *a* crystallographic axes.

It is worth to note that the compound $[Eu_2(bta)_6(pyrzMO)_2]$ is the only octacoordinated compound not presenting an inversion center. This absence is related to the different spatial distribution of the β-diketonate substituents which surround the two Eu^{3+} centers. Referring to **Figure 2.11 b,** if we image a plane passing through the two europium centers, the three bta ligands coordinated to Eu1 disposed

their phenyl rings on the same side of the plane in a pseudo-*fac* disposition while the three bta ligands coordinated to Eu2 center showed an alternate disposition of their substituents.

Henceforth, the studied complexes will be labelled according to the nature of the β-diketonate and the ancillary ligands as depicted in **Table 2.2**.

Compound	Acronym	Compound	Acronym
$[Eu_2(dbm)_6(bipyMO)_2]$	**b-dbm**	$[Eu_2(dbm)_6(pyrzMO)_2]$	**p-dbm**
$[Eu_2(bta)_6(bipyMO)_2]$	**b-bta**	$[Eu_2(bta)_6(pyrzMO)_2]$	**p-bta**
$[Eu_2(hfac)_6(bipyMO)_3]$	**b-hfac**	$[Eu_2(hfac)_6(pyrzMO)_3]$	**p-hfac**
$[Eu_2(tta)_6(bipyMO)_2]$	**b-tta**	$[Eu_2(tta)_6(pyrzMO)_2]$	**p-tta**

Table 2.2: List of acronyms for the identification of the studied Eu^{3+} dinuclear compounds.

2.3.2. Luminescence studies

The eight Eu^{3+}-based dinuclear complexes can be classified considering the number of divergent bipyMO ligands connecting two europium centers, as well as the Eu^{3+} coordination number (CN). This is sketched in **Figure 2.13**; these drawings serve as a quick eye guide to correlate the dimers structure with their luminescence properties.

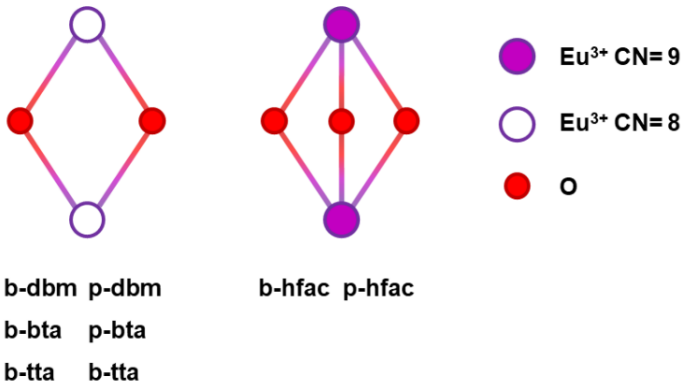

Figure 2.13: Schematic representation of the connections between two Eu^{3+} ions in the eight dinuclear complexes.

Upon irradiation, all compounds emit bright red light also detectable at the naked eye. Europium emission can be excited in a wide wavelength range, from UV to the visible, up to 450 - 490 nm depending on the nature of the β-diketonate ligand (**Figure 2.14**). As well known in the literature,[120] an increasing of the number of

phenyl groups on the β-diketonate ligand shifts the excitation range towards the visible due to an higher aromaticity; a similar result can be obtained with the thienyl ring of the tta ligand. The spectra in **Figure 2.14** evidence that the excitation range of the bipyMO derivatives is generally broader than their corresponding pyrzMO analogues. These differences can be related to the absorption properties of the bipyMO whose solid state absorption spectrum extends in the visible up to 480 nm.[121,122]

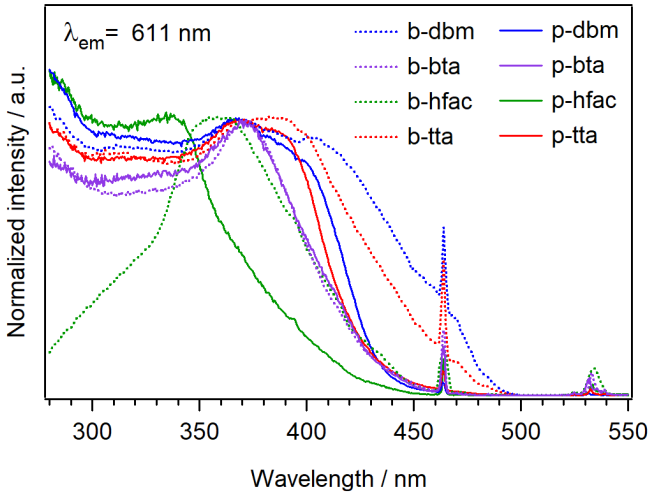

Figure 2.14: Excitation spectra of the compounds monitored at 611 nm.

The photoluminescence (PL) spectra of the compounds show the Eu^{3+} sharp bands associated to the $^5D_0 \rightarrow {}^7F_J$ (J= 0-4) transitions in the 570 -720 nm range (**Figure 2.15**).[8] As usual for Eu^{3+} β-diketonate complexes, all spectra present a strong hypersensitive $^5D_0 \rightarrow {}^7F_2$ transition which is about one order of magnitude more intense than the other $^5D_0 \rightarrow {}^7F_J$ (J= 0, 1, 3, and 4) emission lines.

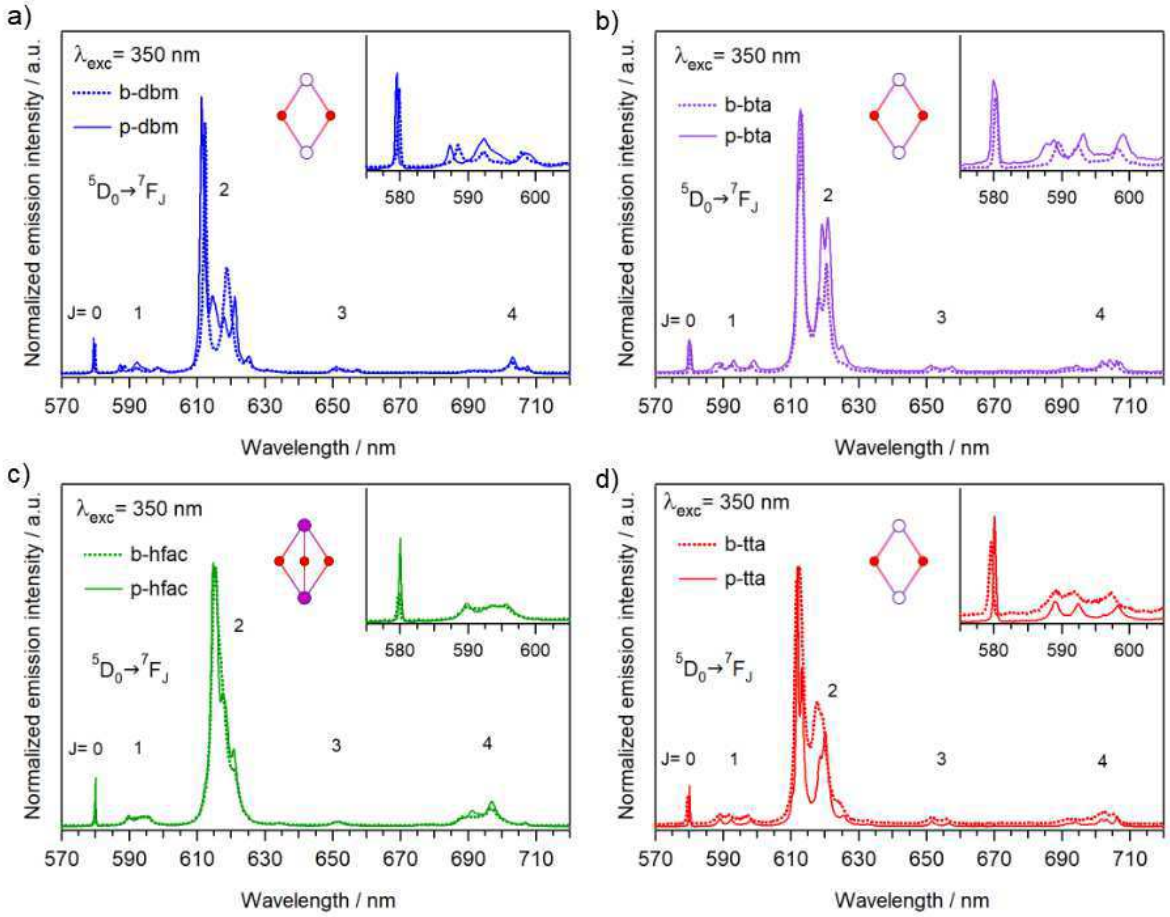

Figure 2.15: Room temperature emission spectra of the Eu^{3+} dinuclear compounds excited at 350 nm. In the insets the region of the $^5D_0 \rightarrow {}^7F_0$ and $^5D_0 \rightarrow {}^7F_1$ transitions is zoomed.

Compounds with the same coordination polyhedron in the crystallographic structure have emission spectra with similar band shape.[8] For example, the $^5D_0 \rightarrow {}^7F_2$ transition of the octacoordinated compounds based on dbm, bta, and tta ligands (**Figure 2.15 a**, **b**, and **d**) has similar shape and it is well splitted in all the samples. The small differences in the shape of $^5D_0 \rightarrow {}^7F_2$ transition in each couple of samples with the same β-diketonate ligand are related to the small variation in the Eu^{3+} coordination polyhedron caused by the different ancillary ligand. Similar considerations can be done for the $^5D_0 \rightarrow {}^7F_1$ transition (**Figure 2.15 a**, **b**, **d** insets) whose degeneration is completely removed due to the low symmetry of the Eu^{3+} coordination polyhedra.[8] Conversely, the nonacoordinated complexes **b-hfac** and **p-hfac** are characterized by a $^5D_0 \rightarrow {}^7F_2$ transition with a single sharp peak at 612 nm with a shoulder at longer wavelengths (**Figure 2.15 c**). Also for these two samples, small differences in the shape of the Eu^{3+} transitions due to the different *N*-oxide ligand are detectable.

Changing the nature of the β-diketonate ligand in the order dbm - tta - bta - hfac, $^5D_0$ lifetimes (τ_{obs}) progressively increased from 0.45 to 0.67 ms in the bipyMO series and from 0.58 to 0.70 ms in the pyrzMO one (**Table 2.3**). Indeed, the introduction of an increasing number of -CF_3 groups diminishes the probability of a non-radiative deactivation of the excited state as also reported in the literature.[3]

Compound	CN	τ_{obs} (ms)	τ_{rad} (ms)	Φ(%)
b-dbm	8	0.58	1.29	45
b-bta	8	0.67	1.16	58
b-hfac	9	0.70	1.08	60
b-tta	8	0.59	1.22	48
p-dbm	8	0.45	0.95	48
p-bta	8	0.60	0.97	62
p-hfac	9	0.65	1.08	63
p-tta	8	0.58	1.06	55

Table 2.3: Experimental lifetimes (τ_{obs}), radiative lifetimes (τ_{rad}), and intrinsic quantum yields (Φ) for the europium dinuclear compounds excited at 350 nm. In the second column the europium coordination number (CN) is reported.

From europium emission spectra it is possible to calculate the radiative lifetimes (τ_{rad}) (**2.1**) which corresponds to the luminescence lifetime of the $^5D_0$ level in the absence of non-radiative processes:[8]

$$\frac{1}{\tau_{rad}} = A_{MD,0} n^3 \left(\frac{I_{tot}}{I_{MD}}\right) \qquad \textbf{(2.1)}$$

In **(2.1)**, $A_{MD,0}$ is the spontaneous emission probability in vacuo of the $^5D_0 \rightarrow {}^7F_1$ transition and its value is 14.65 s^{-1}. I_{tot} and I_{MD} are the integrated areas of the whole emission spectrum and the $^5D_0 \rightarrow {}^7F_1$ transition, and n is the refractive index ($n \approx 1.55$ at the solid state).[8]

The lifetime of an excited state depends on the balance between the probability for radiative and non-radiative deactivation processes. Since the non-radiative relaxations can not be directly observed, the information about them can be achieved only by comparing the experimental excited state lifetimes (τ_{obs}) and the radiative lifetimes

(τ_{rad}). The difference between their values is attributed to the occurrence of non-radiative relaxations phenomena.

Radiative lifetimes can be used to calculate the intrinsic quantum yield (Φ, **Table 2.3**) which gives the ratio between the radiative and the experimental lifetimes (**Equation (2.2)**):

$$\Phi = \frac{\tau_{obs}}{\tau_{rad}} \quad (2.2)$$

It is possible to see that, in each series, the Φ values increase with the same order of τ_{obs} (dbm < tta < bta < hfac). As already found for the experimental excited state lifetimes (τ_{obs}), the Φ trend is related to the substitution of the dbm phenyl rings with an increasing number of the -CF_3 groups which prevents the non-radiative decay of Eu^{3+} excited state.

2.3.3. Thermometric studies

As described in **Chapter 1**, the thermometric properties of a lanthanoid complex usually depend on the energy gap between the ligand triplet state (T) and Eu^{3+} $^5D_0$ emissive level ($\Delta E_{T\text{-}Eu}$) and on the presence of vibrational quenchers coordinated to the Eu^{3+} ion such as -OH, -NH, or -CH groups.

In β-diketonate complexes, Eu^{3+} luminescent properties are sensitive to temperature variations around room temperature.[81,123] Indeed, when the $\Delta E_{T\text{-}Eu}$ energy gap is higher than 1,800 cm^{-1}, as in the case of our Eu^{3+} β-diketonate complexes ($\Delta E_{T\text{-}Eu}$ = 4700 – 3200 cm^{-1} from hfac to tta), back energy transfer processes from the metal center to the ligand T level are effective only around room or higher temperature. For example, below room temperature Eu^{3+} $^5D_0 \rightarrow {}^7F_2$ transition in [Eu(hfac)$_3$] moieties shows constant intensity and it is commonly used as reference transition in ratiometric luminescent thermometers working in cryogenic temperature ranges.[82] In this case, the high $\Delta E_{T\text{-}Eu}$ value makes ineffective metal-to-ligand back energy transfer processes in that temperature region and Eu^{3+} $^5D_0 \rightarrow {}^7F_2$ transition intensity remains almost constant (see also **Chapter 3**). In addition, our complexes do not have high-

frequency vibrational groups (e.g. -OH or -NH) directly coordinated to the Eu^{3+} ion which can modulate the Eu^{3+} luminescent properties at low temperatures.

As stated above, the temperature range between -50 to 100 °C seemed suitable to study the thermometric properties of our dinuclear compounds since only scarce responses are expected below room temperature for the high $\Delta E_{T\text{-}Eu}$ values. For the same reason, they would be good luminescent thermometers beyond room temperature. Moreover, in the perspective to disperse the Eu^{3+} dinuclear compounds in polymeric matrices to develop functionalized materials, this temperature range is suitable for the most commonly used organic polymers.[123]

In the -50 to 100 °C temperature range, Eu^{3+} emitted intensity decreases as temperature increase. Since the $^5D_0 \rightarrow {}^7F_2$ transition is about one order of magnitude more intense than the other transitions and it is the main contribution to the total Eu^{3+} emission, its integrated intensity was chosen as thermometric parameter (Δ, **Figure 2.16**).

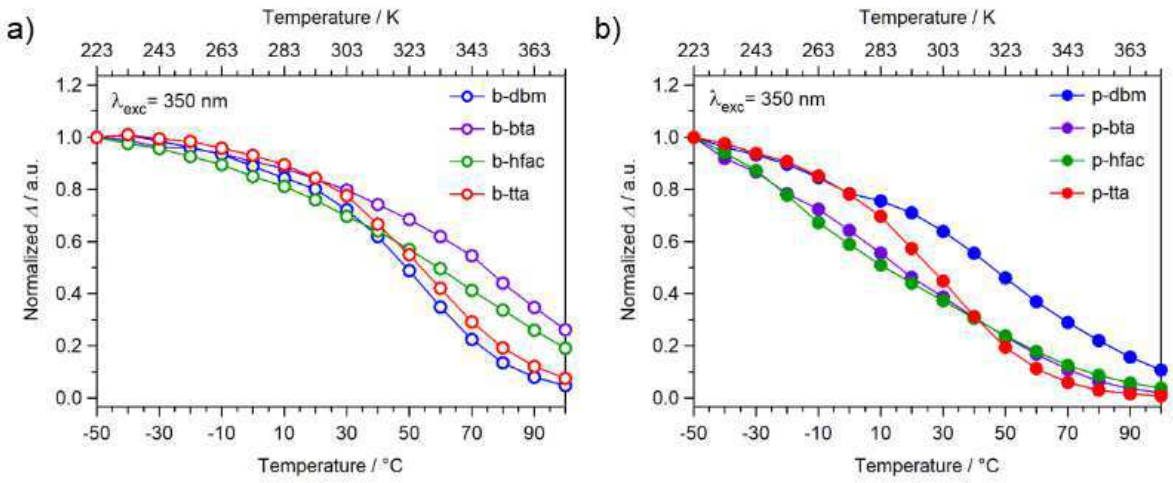

Figure 2.16: Normalized Δ curves of the Eu^{3+} dinuclear bipyMO (**a**) and pyrzMO (**b**) compounds. λ_{exc}= 350 nm.

The shape of the Δ curves depends on the nature of both the β-diketonate and the *N*-oxide ligands. In the bipyMO series (**Figure 2.16 a**), **b-tta** and **b-dbm** are characterized by a similar S-shape curve while in the case of **b-hfac** and **b-bta** the curves do not reach a lower plateau in the studied temperature range. In the pyrzMO

series instead, the differences between the different Δ curves are more pronounced also at lower temperatures (**Figure 2.16 b**). Indeed, only **p-tta** showed a S-shaped curve while **p-dbm**, **p-bta**, and **p-hfac** Δ curves are very squashed in the studied temperature range. Moreover, **p-hfac** and **p-bta** Δ curves are almost completely overlapped.

Comparing the bipyMO compounds with their pyrzMO analogues, it is possible to see that the shape of the Δ curves changes significantly (**Figure 2.17**): in particular, in pyrzMO derivatives Δ starts to vary earlier and in a more pronounced way respect to the corresponding bipyMO analogues. According to the Δ curves, it is fair to think that pyrzMO derivatives have better thermometric responses than bipyMO compounds corresponding to higher S_r values already at lower temperature.

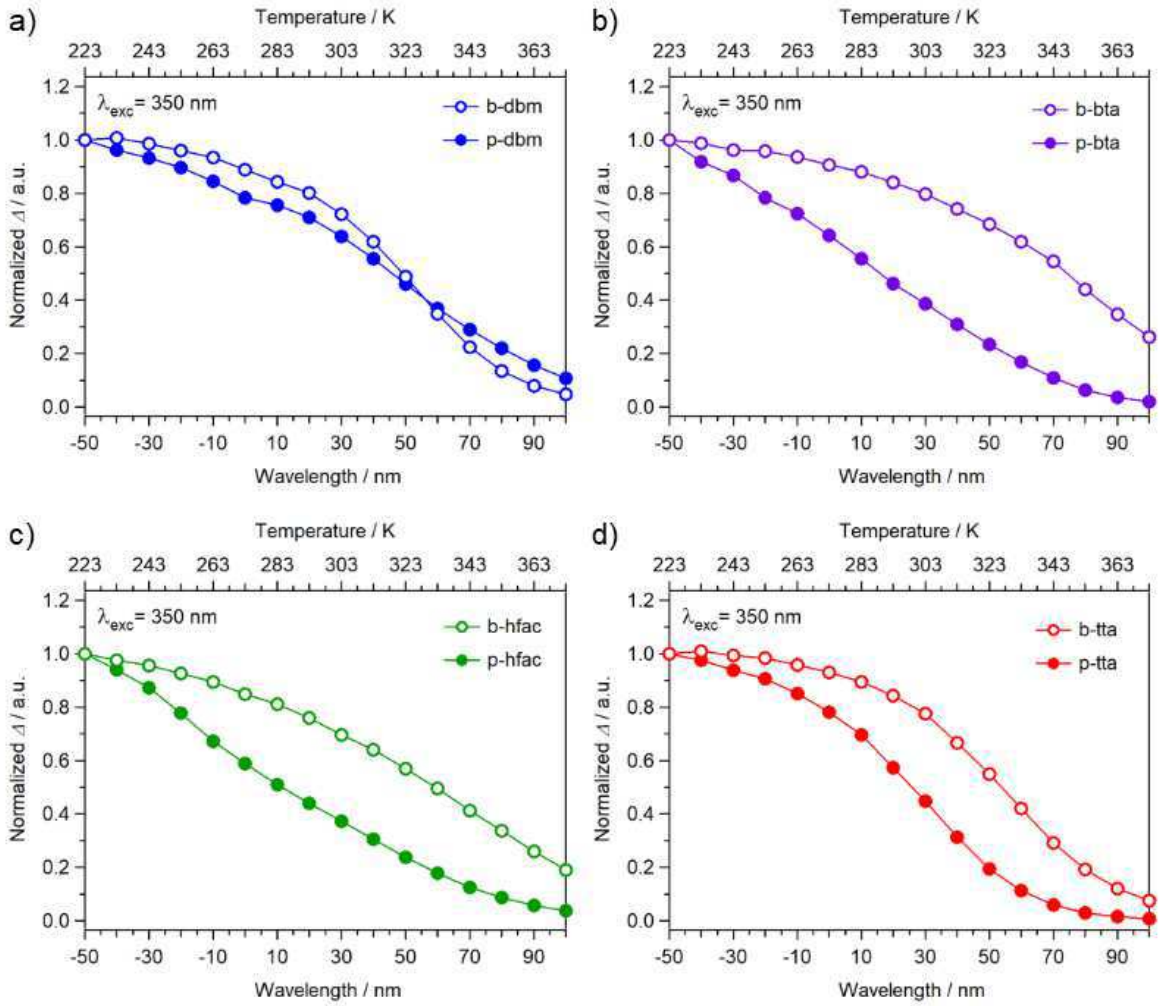

Figure 2.17: Comparison between the Δ curves of the bipyMO and the pyrzMO derivatives.

The relative thermal sensitivity parameter (S_r, see **Chapter 1**) allows us to compare the thermometric properties of the different systems. We choose $S_r \geq 1$ as quality criterion to determine the operational temperature range of the complexes (**Figure 2.18**). As concerns the bipyMO series, $S_r \geq 1$ values are found around room or higher temperature (**Figure 2.18 a** and **Table 2.4**): above 10 °C for **b-dbm**, 50 °C for **b-bta**, 40 °C for **b-hfac**, and 30 °C **b-tta**. The S_r curves of compounds **b-dbm** and **b-tta** reach a maximum in the studied temperature range at 70 and 90 °C of 5.1 and 4.8 respectively while **b-bta** and **b-hfac** curves do not.

Compound	**Applicative range / °C ($S_r \geq 1$)**	**S_r max (T/ °C)**	**Compound**	**Applicative range / °C ($S_r \geq 1$)**	**S_r max (T/ °C)**
b-dbm	10 – 100	5.1 (70)	**b-dbm**	20 – 100	4.6 (100)
b-bta	50 - 100	3.7 (100)	**b-bta**	-10 - 100	8.1 (100)
b-hfac	40 - 100	3.4 (100)	**b-hfac**	-30 – 100	5.3 (100)
b-tta	30 - 100	4.8 (90)	**b-tta**	0 - 100	7.0 (80)

Table 2.4: Comparison between the applicative range and the maximum relative thermal sensitivity of the europium dinuclear compounds.

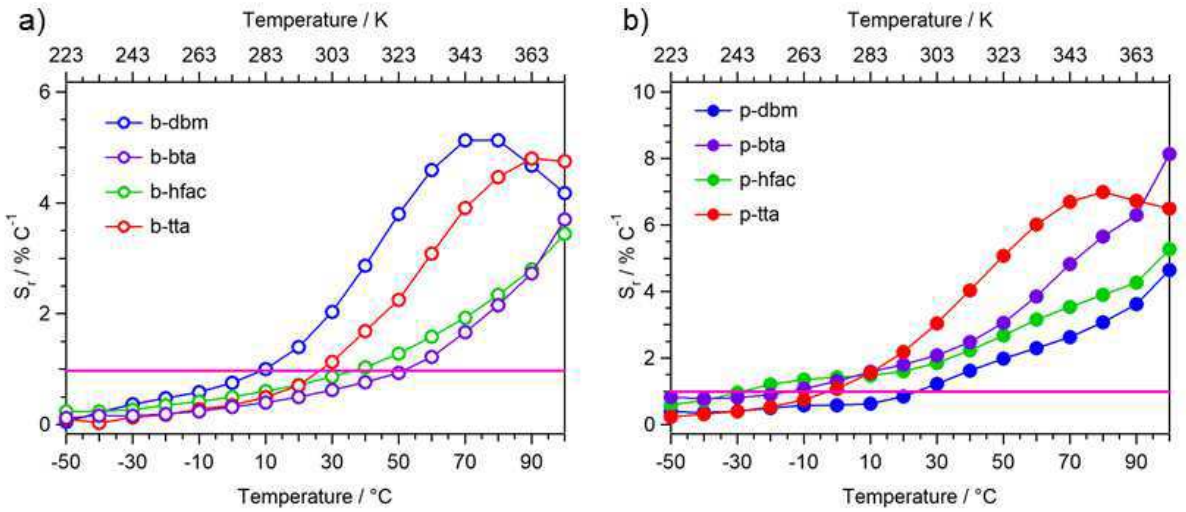

Figure 2.18: Relative thermal sensitivity of the **a**) bipyMO and **b**) pyrzMO compounds; $S_r = 1$ is highlighted with the fuchsia line.

Conversely, the pyrzMO derivatives showed S_r curves significantly different from their bipyMO analogues (**Figure 2.18 b**). S_r values of the pyrzMO compounds are generally higher than 1 at lower temperature than their bipyMO as expected from

the respective Δ curves (see **Figure 2.17**). For example, in **p-hfac** S_r is equal to 1 at -30 °C versus the 40 °C of the **b-hfac** complex. Moreover, pyrzMO derivatives showed higher S_r maximum values than their corresponding bipyMO compounds confirming that the Eu^{3+} $^5D_0 \rightarrow {}^7F_2$ transition in that complexes is more sensitive to a temperature variation (**Table 2.4**). In this case, only **p-tta** reaches the S_r maximum (7.0 at 80 °C) while the curves of the other three complexes do not reach their maximum in the studied temperature range.

The Mott-Seitz equation (see **Appendix 1**)[124,125] can be used to determine the number of non-radiative deactivation pathways able to modulate the Eu^{3+} luminescent properties in the studied compounds:

$$\Delta = \Delta_0 \frac{1}{1+\sum_{i=1}^{n} \alpha_i \cdot exp\left(\frac{-\Delta E_i}{k_b \cdot T}\right)} \quad \textbf{(2.3)}$$

Δ_0 is the extrapolated value of the thermometric parameter at 0 K, ΔE_i the energy required for the activation of i-th non-radiative deactivation pathways, α_i the ratio between the non-radiative and radiative deactivation probabilities of the considered deactivation channel, k_b the Boltzmann constant, and T the absolute temperature.[80,126,127]

The three main mechanisms that can affect the thermometric behaviour of the complexes are the metal-to-ligand triplet level back energy transfer (BEnT) processes, influenced by the $\Delta E_{T\text{-}Eu}$, ligand-to-metal charge transfer (LMCT) and multiphonon processes.[26]

Considering only the contribution due to the BEnT processes in the MS equation, given the absence of groups with high-energy vibrations coordinated to the europium ions, good fitting curves were found only in the case of **b-dbm**, **b-tta**, and **p-tta**. For the other samples, two deactivation pathways are required to fit the experimental Δ curves (**Table 2.5**).

Compound	ΔE_1 (cm^{-1})	α_1	ΔE_2 (cm^{-1})	α_2	R^2
b-dbm	3,285 ± 246	$5.25 \cdot 10^6$	//	//	0.994
b-bta	4,680 ± 835	$1.52 \cdot 10^8$	1,219 ± 345	81.7	0.999
b-hfac	4,838 ± 490	$3.33 \cdot 10^8$	1,560 ± 155	67.9	0.999
b-tta	3,644 ± 200	$9.96 \cdot 10^6$	//	//	0.997
p-dbm	3,800 ± 410	$2.00 \cdot 10^7$	595 ± 386	11.5	0.999
p-bta	4,497 ± 426	$6.81 \cdot 10^8$	1,285 ± 201	902.3	0.999
p-hfac	5,001 ± 856	$9.25 \cdot 10^9$	1,187 ± 188	452.5	0.999
p-tta	3,411 ± 276	$1.57 \cdot 10^7$	//	//	0.994

Table 2.5: ΔE_1, α_1, ΔE_2, and α_2 Mott-Seitz parameters for the europium dinuclear compounds and the respective coefficient of determination (R^2).

In all the complexes ΔE_1 energies are close to the $\Delta E_{T\text{-}Eu}$ energy difference (see **Figure 2.19**) indicating that back energy transfer processes from Eu^{3+} $^5D_0$ level to the ligand triplet state are effective in the modulation of the luminescent properties. This is the predominant factor that influences the thermometric response in compounds **b-dbm**, **b-tta**, and **p-tta**.

For the other compounds, a second term characterized by lower activation energy shall be used to reproduce the experimental curves. This term can be related to low-energy LMCT states or to multiphonon processes. Both mechanisms can not be "*a priori*" excluded with the information currently available. Indeed, all the complexes show an absorption at the wavelengths corresponding to the ΔE_2 energy which could be related to the presence LMCT states (**Figure 2.20**). Conversely, even if no groups with high-frequency vibration are directly coordinated to the Eu^{3+} ions, the crystallographic data showed that the C-H groups adjacent to the ligand N-O moiety are close enough to Eu^{3+} to promote multiphonon processes ($d < 4$ Å).

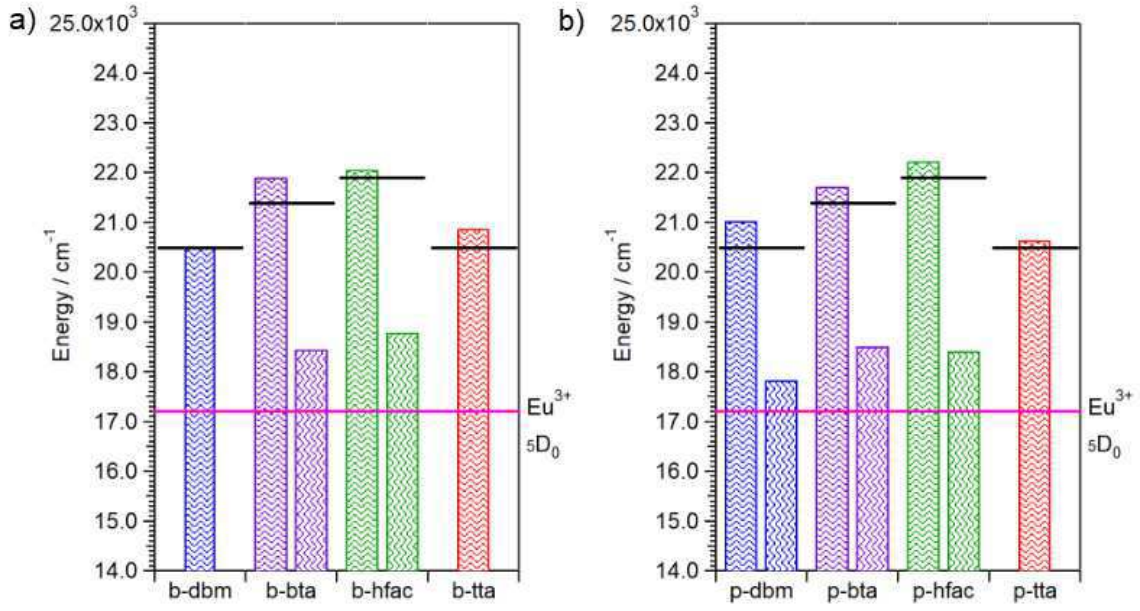

Figure 2.19: E_1 (horizontal checkering) and E_2 (vertical checkering) energies for the Eu^{3+} dinuclear compounds compared with Eu^{3+} $^5D_0$ level (fuchsia line) and the respective β-diketonate triplet energy (black line) in the case of **a)** bipyMO and **b)** pyrzMO derivatives.

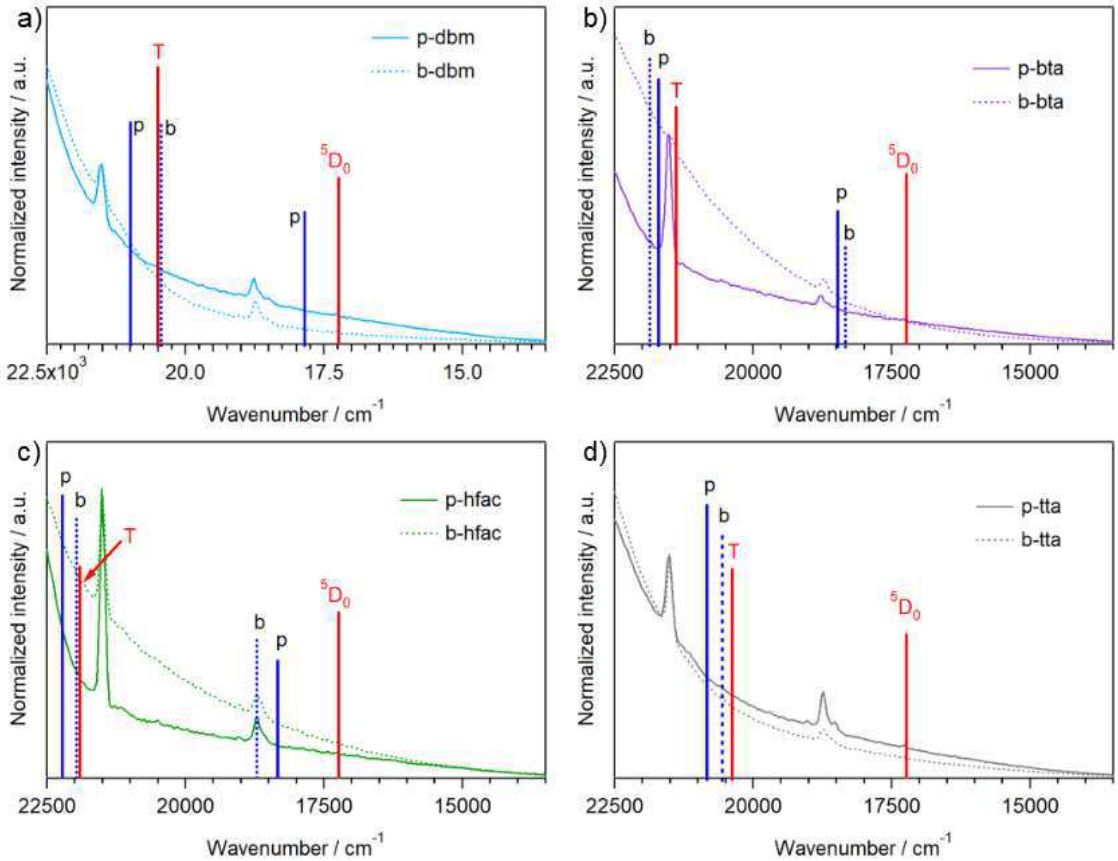

Figure 2.20: Comparison between the absorption spectra of the Eu^{3+} dinuclear compounds, the energies derived from the MS equation (dashed and full blue lines for the bipyMO and the pyrzMO derivative, respectively), and the values of Eu^{3+} $^5D_0$ and the β-diketonate ligand triplet (T) energy levels (red lines).

Beside a good thermometric response in the studied temperature range, thermal and photochemical stabilities are two important parameters to be evaluated for luminescent thermometers. Indeed, since Δ is the integrated intensity of the $^5D_0 \rightarrow {}^7F_2$ transition (no reference transitions are used) all phenomena that can modulate the intensity of Eu^{3+} emission, excluding temperature, are potential sources of error.

The thermal stability was evaluated through thermogravimetric analysis (TGA) in air performed between 20 and 800 °C. For all the compounds no weight loss was recorded below 100 °C indicating that the complexes are thermally stable in the temperature range considered in the thermometric studies.

Photodegradation involves the organic part of the metal compound and it occurs because organic molecules are not kinetically stable towards oxidation in their excited state in presence of oxygen.[128] We tested the photostability in air of the samples during long expositions times through sample continuous irradiation at 350 nm for 2 hours and recording the integrated intensity of Eu^{3+} $^5D_0 \rightarrow {}^7F_2$ transition every 5 minutes. The power of the excitation beam was 60 μW.

Different *N*-oxide molecules do not influence the overall photostability of the compounds which is instead affected by the nature of the β-diketonate ligand (**Figure 2.21 b** as example). In particular, hfac derivatives showed no photodegradation phenomena during the exposition time as it can be seen from the constant intensity of the $^5D_0 \rightarrow {}^7F_2$ transition (**Figure 2.21 a**). This characteristic is attributable to the high resistance of C-F bonds towards photodegradation which occurs only at lower wavelength ($\lambda_{exc} < 300$ nm).[129]

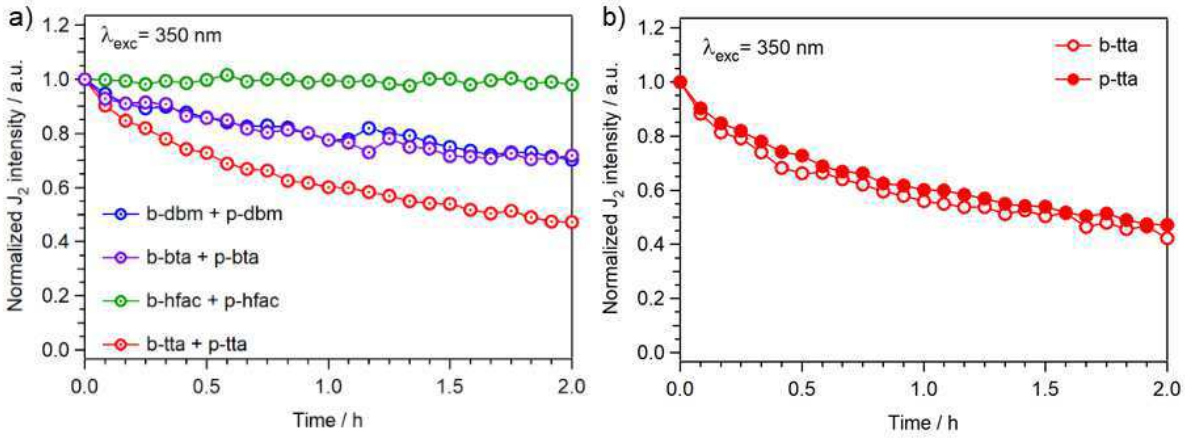

Figure 2.21: **a**) Photostability of the eight Eu^{3+} complexes during 2 h. **b**) Comparison between the photostability of **b-tta** and **p-tta**.

By reducing the number of -CF_3 groups with the introduction of one (bta) or two (dbm) phenyl rings, the complexes showed analogous photodegradation curves independently from the ancillary *N*-oxide ligand. Also in this case the photostability of the complexes is quite good since the intensity of the $^5D_0 \rightarrow {}^7F_2$ transition decreases only by 30 % of the initial intensity after two hours. Finally, the two tta compounds showed the highest fading tendency keeping only 50 % of the initial intensity after two hours. In this case, the lower stability can be attributed to the ligand thienyl ring which can be easily oxidized into the corresponding sulfone and other photo-oxidation products as reported in the literature.[130]

In conclusion, all the studied compounds have wide ranges of applicability with S_r values higher than 1 which slightly depend by the nature of both the β-diketonate and *N*-oxide ligands. All complexes were also thermally stable below 100 °C degree and have good/ excellent photostability properties depending on the nature of the β-diketonate moiety. The data suggest a possible use of these complexes as luminescent molecular thermometers in the daily life.

2.5. Conclusions

The heterotopic ligand 4,4-bipyridine-*N*-oxide (bipyMO) and pyrazine-*N*-oxide (pyrzMO) were used for the synthesis of a series of Eu^{3+} dinuclear compounds with composition $[Eu_2(\beta\text{-dike})_6(\text{L-MO})_x]$, where x is two or three depending on the nature of the β-diketonate ligand (3 for hfac, 2 for dbm, bta, and tta). In all compounds, the Eu^{3+} ion ignores the N-donor site of the ancillary ligand coordinating to the oxygen atom of the N-O moiety highlighting the different affinity of a lanthanoid ion towards ligands with oxygen and nitrogen donor sites. The *N*-oxide ligand is always coordinated in a hypodentate mode bridging two Eu^{3+} ions. Photoluminescence studies showed the typical Eu^{3+} intense red emission.

Thermometric studies performed in the -50 to 100 °C temperature range showed good thermometric properties for all complexes and different thermometric behaviours depending on the nature of the β-diketonate and *N*-oxide ligands. PyrzMO derivatives generally showed higher S_r values and a more extended application range than the respective bipyMO analogues. The **p-hfac** complex showed the widest application range ($S_r \geq 1$) from -30 up to 100 °C.

The Mott-Seitz equation, used to rationalize the experimental results, showed that in all complexes back-energy transfer processes from the Eu^{3+} $^5D_0$ emissive level to the ligand triplet are effective in the modulation of the thermometric properties. A second mechanism with a lower activation energy is also present in samples **b-bta**, **b-hfac**, **p-dbm**, **p-bta**, and **p-hfac**. Even if the current experimental data do not allow us to clearly identify the nature of this second mechanism, it reasonably can be attributed to a LMCT or a multiphonon deactivation process.

The nature of the β-diketonate ligand influences also the photostability of the Eu^{3+} dinuclear complexes. In this case hfac derivatives resulted to be the most photostable compounds since they did not show relevant photobleaching phenomena after two hours of continuous irradiation.

All the studied complexes appeared to be good luminescent thermometers with the possibility to selectively modulate the thermometric response varying the nature of the β-diketonate and *N*-oxide ligand. The importance to study the correlation between the molecular fragment and the thermometric response of the overall system is here highlighted. The overall properties can be easily varied and improved consistently with the goal to be achieved (e.g. higher S_r values, extended applicative range *etc.*).

In the future it will be interesting to study the processability of the presented compounds to develop functional materials (e.g. polymeric films) that can be used in the everyday life.

Another interesting aspect that is at present investigated in our laboratories is the synthesis of *d-f* heterobimetallic compounds based on these dinuclear complexes[119] through a self-assembling process. Indeed, the uncoordinated nitrogen binding site of the *N*-oxide ligand can be potentially used as a good donor site towards *d*-metals complexes.[111] Choosing the proper Eu^{3+} dinuclear compound and varying the nature of the *d*-metal complex it is possible to vary the coordination geometry and the dimensionality of the resulting *d-f* metal compound from linear or triangular discrete complexes to mono- or multidimensional mixed *d-f* coordination polymers. In this case, it will be interesting to study how the *d* metal moiety influences the physical and photophysical properties of Eu^{3+} ion and the resulting thermometric response.

3. Eu^{3+}-Tb^{3+} Coordination Polymers

3.1. Introduction

As discussed in **Chapter 1** and **2**, luminescent thermometers based on the emission intensity of a single transition are particularly useful for many applications.[41,42,51,52] However, errors in temperature readout can be due to light source fluctuations or to changes in the emitter local concentration.[35,53] The often required periodic calibration procedure is not compatible with an end-user application.

These limitations can be overcome using as thermometric parameter (Δ) the absolute intensity ratio of different emission bands of a luminescent material creating in this way a self-referencing system.[53,54,79,131–133] Generally, the intensity of one transition is almost temperature independent and it is used as internal reference, while the second transition is the "real" thermometric probe.

Ratiometric luminescent thermometers can be obtained with a great versatility using a variety of probes of different materials[44,53,55] and exploiting the emissions of a single chromophore or two different emissive centers. Concerning lanthanoid ions, ratiometric luminescent thermometers based on a single emitter generally exploit the intensity ratio between Eu^{3+} $^5D_0 \rightarrow {}^7F_2$ and $^5D_0 \rightarrow {}^7F_4$ transitions. Conversely, in multi-centers thermometers, Eu^{3+} $^5D_0 \rightarrow {}^7F_2$ and Tb^{3+} $^5D_4 \rightarrow {}^7F_5$ transitions are commonly used for Δ determination. In the latter example, Eu^{3+} is the reference while Tb^{3+} (which emits green light) is the thermometric probe for the easier activation of metal-to-ligand back energy transfer processes (cfr. **Chapter 1**, page 14).

Moreover, in Ln^{3+}-based two center thermometers, temperature is associated to different emitted colours because the intensity ratio of the two transitions changes with temperature. For example, in the $[Tb_{0.9}Eu_{0.1}PIA]$[134] (PIA= 5-(pyridin-4-yl)isophthalate) thermometer, the emitted colour varies from green at low temperature (where Tb^{3+} emission is predominant) to yellow, because at higher temperature Tb^{3+} emission intensity diminishes (see **Figure 3.1**).

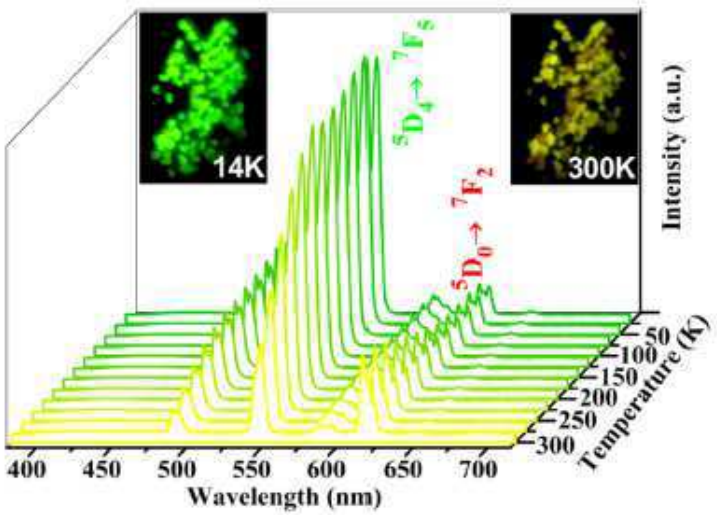

Figure 3.1: Example of temperature-induced colour variation in the [$Tb_{0.9}Eu_{0.1}$PIA] two centers ratiometric thermometer. Reprinted from ref [134].

This feature is particularly interesting from a practical point of view because it is possible to uniquely associate a given colour to a certain temperature using these systems as colorimetric temperature sensors.[135] For example, this feature is particularly exploited in bio-imaging allowing the use of a simple experimental instrumentation for temperature measurements.[136]

Lanthanoid Metal Organic Frameworks (LOFs) and Coordination Polymers (CPs) immediately generated great attention in the development of ratiometric lanthanoid-based luminescent thermometers, due to their peculiar structural properties. These two classes of compounds are hybrid inorganic-organic systems where centers containing metal ions (*nodes*) are connected by organic ligands (*spacers*) via coordinative interactions. Depending on the nodes and spacers nature, 1D,[95,100,137] 2D[109] or 3D[37,138] extended structures, with cavities able to host small guest molecules can be synthesized.

Since the final structure of these compounds depends only by the bonding symmetry coordination geometry of the *node* and the *spacer* and not by the employed Ln^{3+} ion, heterometallic LOFs and CPs can be easily synthesized creating a system which exploits the functional properties of different metal centers.[139,140] Both the spacer and the guest molecules can be emitters increasing therefore the possibility to modulate

the thermometric properties of the system. Lastly, it is possible to design compounds in which the ion-to-ion energy transfer is modulated through the use of spacers with different length that are able to impose different intermetallic distances.[83] The great flexibility of LOFs and CPs allows to study all these possible modulations.

While a large number of examples based on lanthanoid carboxylates[55,78] such as terephthalate,[77,83,141] dipicolinate[135] or isophthalate[134,142–145] are reported, ratiometric luminescent thermometers based on LOFs or CPs containing lanthanoid *tris*-β-diketonate complexes as nodes have been only scarcely explored.

Among commercial β-diketonate ligands, hexafluoroacetylacetonate (hfac) is a good choice for the development of Eu^{3+} and Tb^{3+}-based ratiometric luminescent thermometers. Indeed, its excited triplet level at about 21,900 cm^{-1} [82,95] is sufficiently high to sensitize both Eu^{3+} and Tb^{3+} luminescence. Moreover, the energy gap between the ligand triplet level and the metal ion emissive level it is quite small for Tb^{3+} ($\Delta E_{T\text{-}Tb} \approx$ 1,400 cm^{-1}) but high enough for Eu^{3+} ($\Delta E_{T\text{-}Eu} \approx$ 4,700 cm^{-1}) thus providing a good probe/reference pair for the development of a ratiometric thermometer.

Recently, Hasegawa and co-workers showed this possibility developing a series of Ln^{3+} 1D-CPs with composition $[Tb_{0.99}Eu_{0.01}(hfac)_3(linker)]_n$ based on different bis-phosphane oxide ligands (**Figure 3.2**).[82,146] These CPs are characterized by a high thermal stability, favoured by the CH/F and CH/π interaction present in the systems,[137] and good thermometric properties in the -170 to 180 °C temperature range which can be modulated changing the nature of the bis-phosphane oxide ligand.[146]

Given the scarcity of lanthanoid CPs based on β-diketonate ligand used as ratiometric luminescent thermometers, it appeared interesting to develop new systems to enlarge the knowledge in this research area.

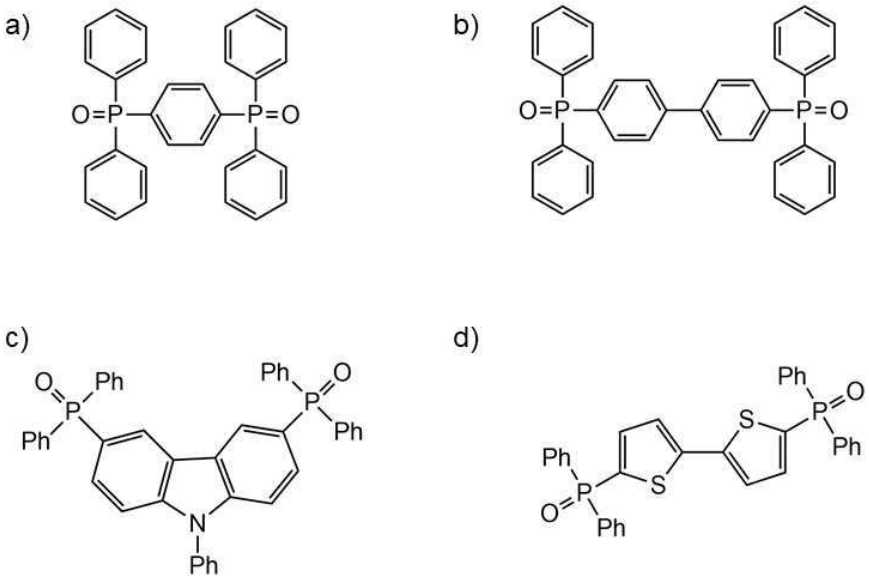

Figure 3.2: Bis-phosphane ligands used by Hasegawa and co-workers for the synthesis of $[Ln(hfac)_3(linker)]_n$ 1D-CPs.

3.1.1. Ln^{3+}-CPs based on *N*-donor ligands as spacer

During the last years, my research group focused the attention on the synthesis of lanthanoid CPs based on 4,4'-bipyridine (bipy, **Figure 3.3**) as *N*-donor spacer. This classic divergent ligand has been used to prepare a very large amount of CPs containing *d* transition metals with several topologies ranging from one- to three-dimensional frameworks.[106,147]

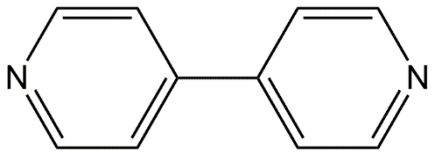

Figure 3.3: The *N*-donor divergent ligand 4,4'-bipyridine.

Conversely, a limited number of structures in which bipy was used in Ln^{3+} coordination chemistry are reported in the CSD (Cambridge Structural Database)[1].[90,148–150] Among these, only in few cases bipy is present as a single bridging

[1] The Cambridge Structural Database (CSD) is the largest and the most commonly used database containing the structure of inorganic complexes, Coordination Polymers, and Metal-Organic Frameworks.

ligand[151–155] and only once it happens in a compound with an extended structure: the $\{[LnCl_3(bipy)(Py)_2]_n \cdot Py\}$ 1D-CP (Ln^{3+}= Gd^{3+}, Er^{3+}, and Yb^{3+}; Py= pyridine; **Figure 3.4**).[156] The synthesis of this CP was carried out using anhydrous metal chlorides with bipy and Py in solvothermal conditions in a sealed evacuated glass ampoule at 220 °C controlling both the reaction temperature and the pyridine amount to avoid the formation of undesired products.[153]

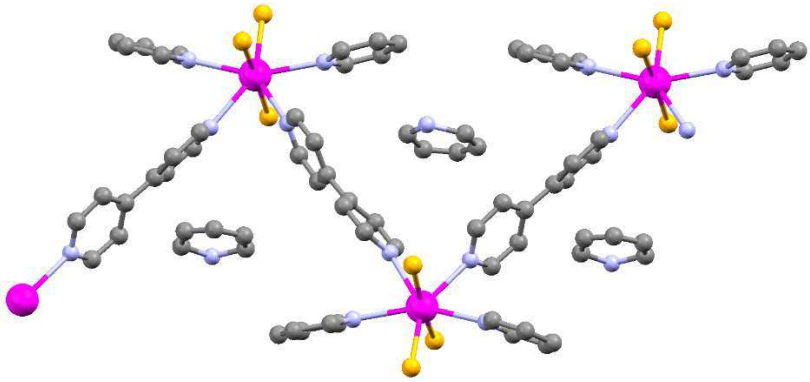

Figure 3.4: Crystal structure of $\{[LnCl_3(bipy)(Py)_2]_n \cdot Py\}$: Ln (magenta), C (dark grey), N (light blue), Cl (orange). Adapted from ref. [156].

The scarcity of examples of Ln^{3+}-CPs based on N-donor spacers is related to the high oxophilicity of lanthanoid ions towards "hard" O-donor ligands (see **Chapter 1** pages 3-4). Indeed, the preparation of lanthanoid extended networks with N-donor ligands requires anhydrous conditions and exclusion of potential ligands or solvents bearing oxygen atoms for two reason:[156]

1. if anhydrous conditions are not guaranteed, N-donor ligands, usually more basic than oxygen ones, can favour the deprotonation of water molecules, with the formation of undesired sub-products as hydroxo- or oxo-lanthanoid derivatives;[157,158]
2. the presence of O-donor species (e.g. water, alcohols *etc.*) drives the reaction towards the formation of dimers and/or low molecular weight oligomers instead of the desired coordination polymers.[150]

Recently, we developed a generical and practical synthetic strategy for the synthesis of monodimensional Eu-CPs based on bipy as single connector between lanthanoid *tris*-β-diketonate complexes [Eu(β-dike)$_3$] as nodes (β-dike= 1,3-diphenylpropane-1,3-dione, Hdbm; 4,4,4-Trifluoro-1-(2-thienyl)-1,3-butanedione, Htta, and Hhfac).[100] The key-point of this procedure is the use of [Eu(β-dike)$_3$] moieties as metal precursors for the CPs synthesis. In a [Eu(β-dike)$_3$] moiety, the europium ion is coordinatively unsaturated (coordination number (CN) of 6) and it has two available binding sites (see also **Chapter 2**, page 18).

Using anhydrous toluene as solvent and a [Eu(β-dike)$_3$]:bipy molar ratio of 1:1, each metal center is able to coordinate two N-groups of two different bipy molecules forming a low soluble monodimensional chain (**Figure 3.5**).

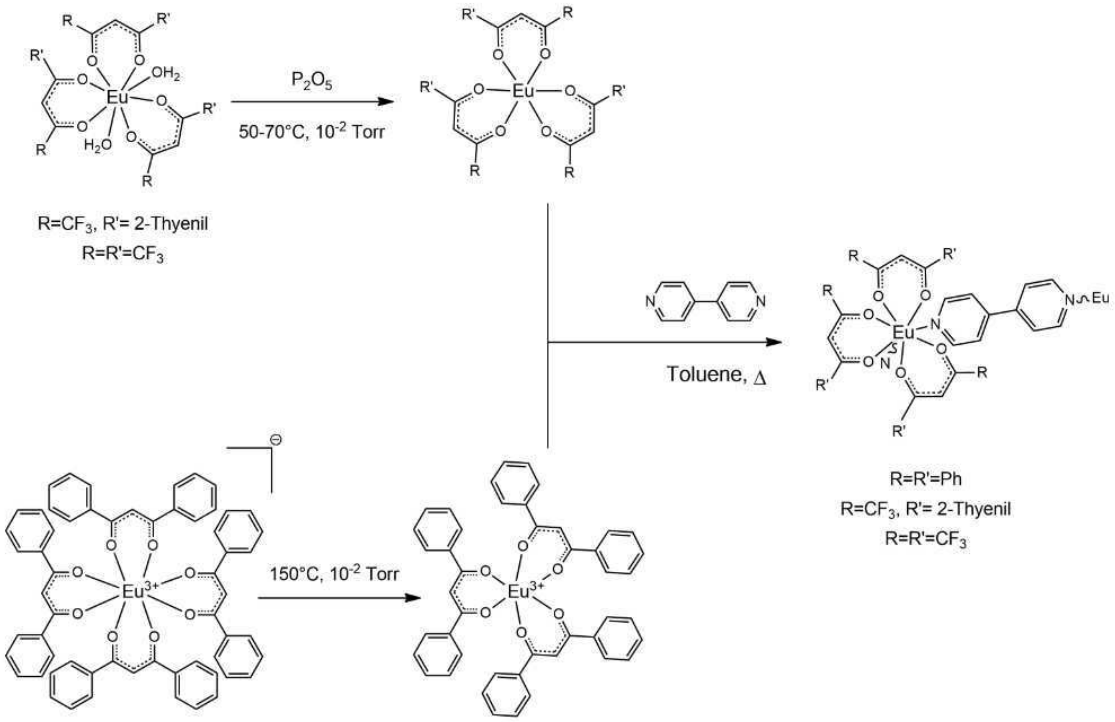

Figure 3.5: General procedure for the synthesis of a [Eu(β-dike)$_3$(bipy)]$_n$ CPs.

3.1.2. Topic outline

Two isostructural homometallic polymers with composition [Ln(hfac)$_3$(bipy)]$_n$ (Ln^{3+}= Eu^{3+} and Tb^{3+}) were used for the development of a series of intensity-based luminescent thermometers. The synthetic procedure already employed for the

synthesis of $[Eu(hfac)_3(bipy)]_n$[100] was extended to the $[Tb(hfac)_3(bipy)]_n$ derivative which was fully characterized. Room temperature photoluminescent studies were conducted on the two compounds measuring also the thermometric properties.

A series of ratiometric luminescent thermometers containing different Eu^{3+}/ Tb^{3+} molar ratio was obtained by mixing together the two homometallic compounds. Two main aspects have been here studied:

1. the modulation of the thermometric properties changing the Eu^{3+}/ Tb^{3+} molar ratio;
2. the sample behaviour using two different excitation wavelengths.

3.2. Results and Discussion

3.2.1. Synthesis and photoluminescence studies

The synthesis of the $[Tb(hfac)_3(bipy)]_n$ CP performed according to the literature protocol for the europium compound is discussed below (**Figure 3.6**).[100]

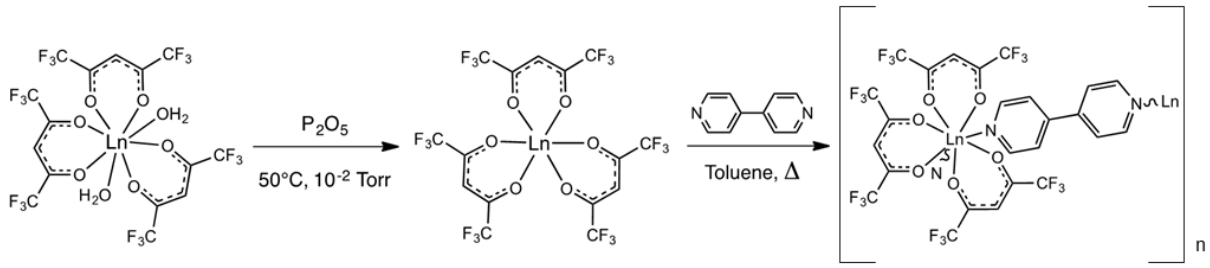

Figure 3.6: General synthetic procedure for the synthesis of a $[Ln(hfac)_3(bipy)]_n$ coordination polymer.

Treating $[Tb(hfac)_3(H_2O)_2]$ at 50 °C under reduced pressure (10^{-2} mmHg) over P_2O_5, coordinated water can be quantitatively removed obtaining the corresponding anhydrous $[Tb(hfac)_3]$ in a quantitative way.

$[Tb(hfac)_3]$ and 4,4'-bipyridine were mixed in a 1:1 molar ratio in anhydrous toluene under Ar atmosphere. The suspension was refluxed for one hour obtaining a yellow solution which was then cooled to room temperature obtaining a microcrystalline solid. The obtained product loses solvent under reduced pressure yielding an amorphous colourless powder with an elemental analysis in good agreement with the $[Tb(hfac)_3(bipy)]_n$ composition. The ATR-IR spectrum was completely superimposable to that of the corresponding Eu^{3+} analogue. As for the Eu^{3+} derivative, the unsolvated terbium compound resulted stable in air.

The structure of the two Ln^{3+}-CPs consists of 1D zig-zag chains which extend along the crystallographic *b*-axis (**Figure 3.7**). Each Ln^{3+} center is coordinated to six oxygen atoms from three hfac ligands and to two N atoms of two different bipy in distorted square antiprismatic geometry. The chains are distorted from linearity since the Ln···Ln···Ln angle between three different metal centers is about 148°. One crystallization molecule of toluene is close to each bipy ligand so that the formula of the crystallized compound is $[Ln(hfac)_3(bipy)\cdot toluene]_n$.

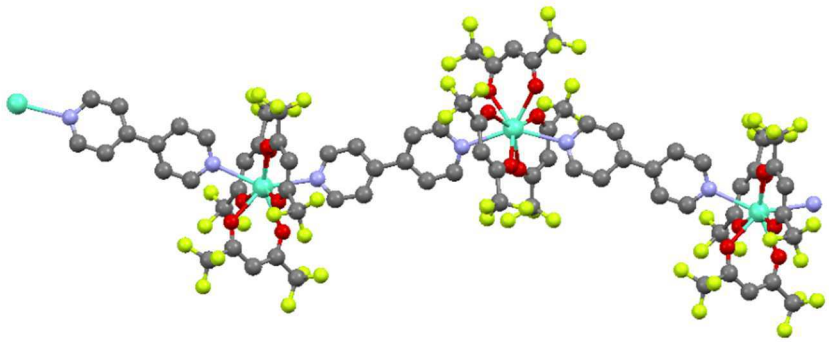

Figure 3.7: Structure of a portion of the chain of $[Ln(hfac)_{3(}bipy)\cdot toluene]_n$. Only the most populated positions of the disordered CF_3 groups are represented; toluene was omitted for clarity. Adapted from ref [100].

The two CPs can be excited in a wide temperature range, from UV to visible, up to ≈500 nm in the case of the Eu^{3+} compound and ≈400 nm for the Tb^{3+} analogue (**Figure 3.8**). The sensitized emission is achieved thanks to the light absorption of both bipy and β-diketonate ligands, although their different contributions cannot be separated due to spectral overlap.

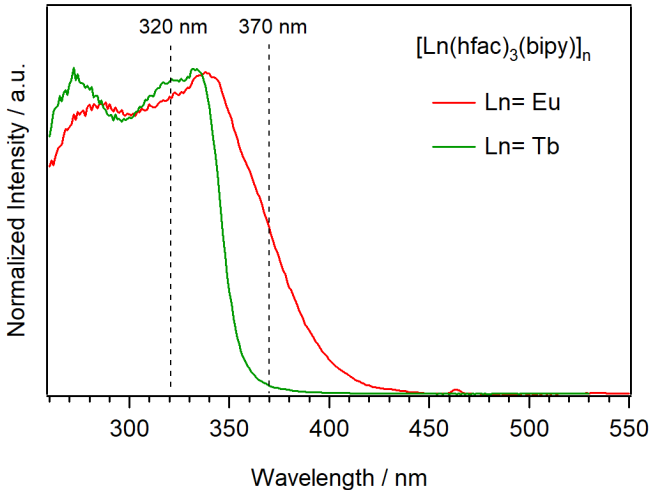

Figure 3.8: Excitation spectra of Eu^{3+} and Tb^{3+} CPs. λ_{em}= 614 nm for Eu^{3+}, 543 nm for Tb^{3+}.

Both $[Ln(hfac)_3(bipy)]_n$ complexes present intense light emission also visible to the naked eye: red for Eu^{3+} and green for Tb^{3+} derivative. In particular, the europium emission spectrum (**Figure 3.9 a**) showed the typical Eu^{3+} $^5D_0 \rightarrow {}^7F_J$ (J= 0-4) transitions corresponding to the lines centred at 587, 595, 614. 652, and 693 nm. Conversely, the emission spectrum of the terbium analogue (**Figure 3.9 b**) showed Tb^{3+} lines centred at 490, 543, 583, and 619 nm corresponding to Tb^{3+} $^5D_4 \rightarrow {}^7F_{6\text{-}3}$

transitions. The shape of both Eu^{3+} and Tb^{3+} transitions is independent from the excitation wavelength. As clearly visible in **Figure 3.9**, Eu^{3+} $^5D_0 \rightarrow {}^7F_2$ and Tb^{3+} $^5D_4 \rightarrow {}^7F_5$ transitions are one order of magnitude more intense than the other transitions.

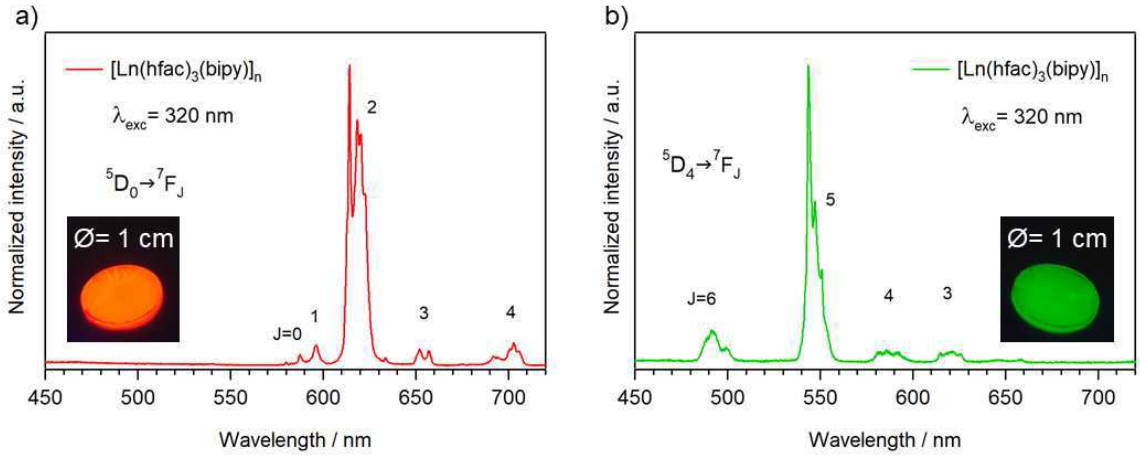

Figure 3.9: Emission spectra of **a)** $[Eu(hfac)_3(bipy)]_n$ and **b)** $[Tb(hfac)_3(bipy)]_n$, λ_{exc}= 320 nm.

3.2.2. Thermometric studies

As previously discussed (**Chapter 1** and **Chapter 2**), the energy gap between the ligand triplet state (T) and Ln^{3+} emissive level ($\Delta E_{T\text{-}Ln}$) is the main contribution which determines the operative temperature region of a lanthanoid luminescent thermometer. The hfac T level is located at about 21,900 cm^{-1} [95] and it can sensitize both Eu^{3+} and Tb^{3+} emission. In Eu^{3+}-based hfac complexes the $\Delta E_{T\text{-}Eu}$ is about 4,700 cm^{-1} meaning that Eu^{3+} emission will be constant below room temperature[81] so that it can be used as a reference in a ratiometric thermometer. Conversely, Tb^{3+} emission is expected to be sensitive to temperature variations also below room temperature because the $\Delta E_{T\text{-}Tb}$ is about 1,400 cm^{-1} (Tb^{3+} $^5D_4$ emissive level ≈20,500 cm^{-1}).[81,82]

The thermometric properties of the two compounds were studied in the -190 to 110 °C temperature range. Two different excitation wavelengths (320 and 370 nm) were used to study the influence of λ_{exc} on the thermometric response of the system. Such a choice relies on the availability of commercial LEDs working at these wavelengths.

Moreover, 370 nm is compatible with glass and plastic materials which absorb radiation below 350 nm.

Since the Eu^{3+} $^5D_0 \rightarrow {}^7F_2$ and Tb^{3+} $^5D_4 \rightarrow {}^7F_5$ transitions are, among all, the most intense transitions and they mainly contribute to the total Eu^{3+} and Tb^{3+} emissions, their integrated intensity was chosen as the thermometric parameter (Δ) for $[Eu(hfac)_3(bipy)]_n$ and $[Tb(hfac)_3(bipy)]_n$ respectively (**Figure 3.10**).

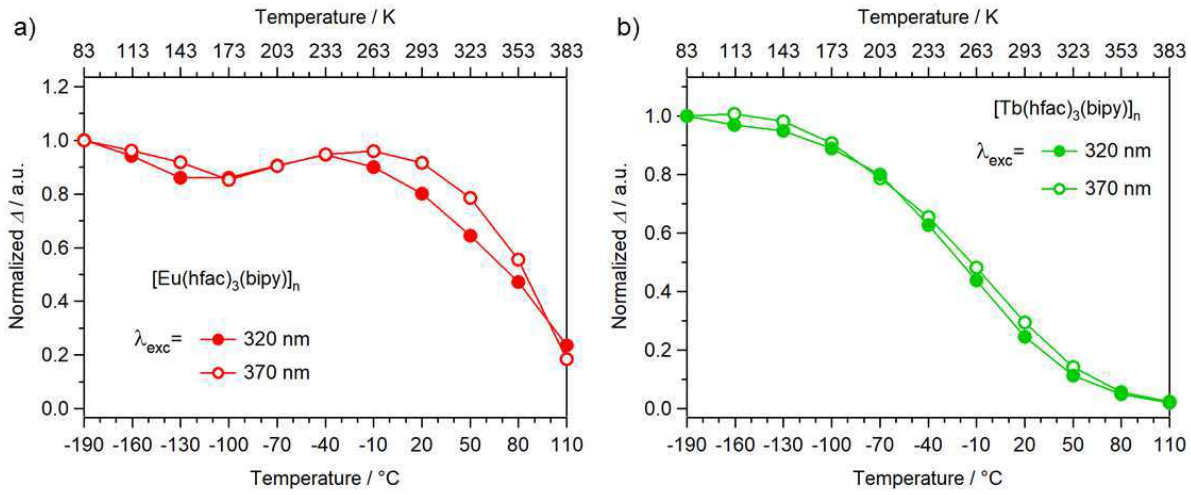

Figure 3.10: Normalized Δ curves of the $[Ln(hfac)_3(bipy)]_n$ CPs; λ_{exc}= 320 and 370 nm. **a**) Δ_{Eu}= $^5D_0 \rightarrow {}^7F_2$ integrated intensity; **b**) Δ_{Tb}= $^5D_4 \rightarrow {}^7F_5$ integrated intensity.

The shape of the Δ curves depends on the used Ln^{3+} ion but they do not change with the excitation wavelengths. In the Eu^{3+} compound (**Figure 3.10 a**) the thermometric parameter Δ remains almost constant up to about -10 °C, while it gradually decreases at higher temperatures without reaching a lower plateau. Conversely, the Δ parameter of the terbium compound (**Figure 3.10 b**) shows a well-defined S-shaped curve gradually decreasing beyond -160 °C. As expected, these differences are related to the different $\Delta E_{T\text{-}Ln}$ value: for the terbium compound with a $\Delta E_{T\text{-}Ln}$ value smaller than 1,800 cm^{-1}, back energy transfer processes are effective at lower temperatures compared to the europium derivative.

To better compare the thermometric response of the two systems and to determine their applicative temperature range, the relative thermal sensitivity parameter (S_r, see **Chapter 1**) was used. As explained in **Chapter 2**, a value of $S_r \geq 1$ identifies

the optimal operative temperature ranges for the two compounds. As showed in **Figure 3.11**, the two compounds show $S_r \geq 1$ in different temperature ranges. The Eu^{3+} species is not sensitive towards temperature variations below -10°C ($Sr = 0$), while S_r values higher than 1 were found only in the 50 ÷ 110 °C temperature range. Conversely, Tb^{3+} derivative is sensitive to temperature in all the studied temperature range (Sr is always ≠ 0) and it shows an extended applicative range from -40 °C to 110 °C. In both compounds, the temperature where $S_r \geq 1$ does not depend on the excitation wavelength (see **Figure 3.11**).

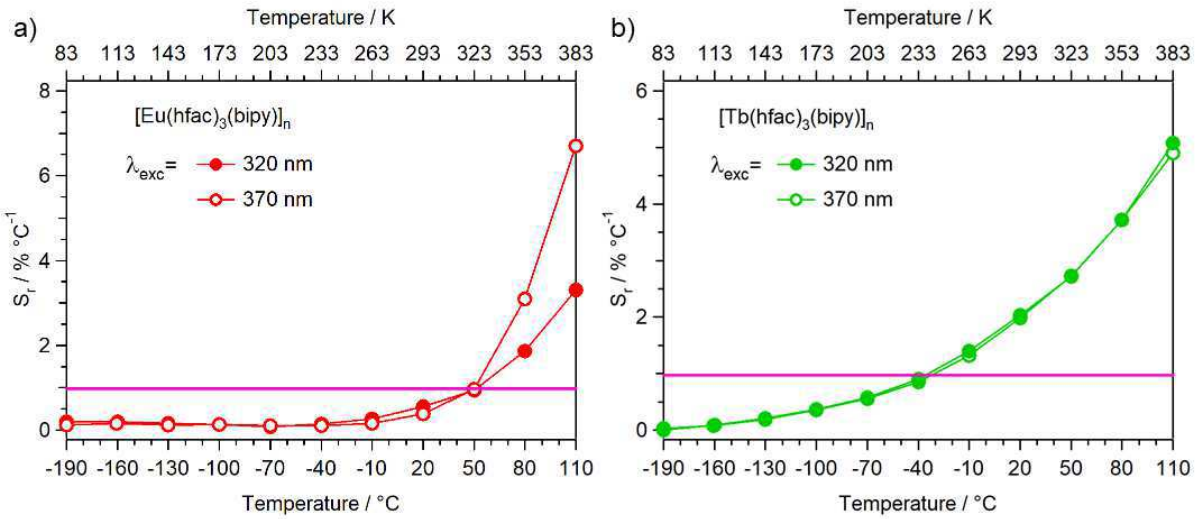

Figure 3.11: Relative thermal sensitivity of the **a)** Eu^{3+} and **b)** Tb^{3+} CPs at the two different λ_{exc} (320 and 370 nm).

These data encouraged us to use the Eu^{3+} and Tb^{3+} homometallic coordination polymers to develop a series of ratiometric luminescent thermometers obtained by mixing the two Ln^{3+}-CPs at the solid state in which Tb^{3+} $^5D_4 \rightarrow {}^7F_5$ transition acts as thermometric probe while the Eu^{3+} $^5D_0 \rightarrow {}^7F_2$ one is the reference. It appeared interesting to study the effect of different molar ratios between the two metals on the thermometric properties of the system.

3.2.3. Eu^{3+}-Tb^{3+} ratiometric thermometers

Known amounts of the two homometallic CPs were mixed in KBr to obtain homogeneous dispersions. The mixtures were finely grinded in an agate mortar

adding few drops of *n*-pentane to facilitate the milling process. The organic solvent was removed drying the KBr powders under a slight N_2 flow. Finally, the resulting mixtures were pressed forming pellets easy to handle. KBr was chosen because it is spectroscopically inert, and it gives non-friable pellets.

Four samples with different europium/terbium molar ratio **Eu1Tb1**, **Eu1Tb3**, **Eu1Tb5**, and **Eu1Tb10,** and constant Ln^{3+}/KBr molar ratio (Ln^{3+}= Eu^{3+}+ Tb^{3+}) were prepared (see **Table 3.1**). In these conditions, the CPs chains are far enough to prevent any possible Tb^{3+}-to-Eu^{3+} energy transfer processes.

Sample	$[Eu(hfac)_3(bipy)]_n$		$[Tb(hfac)_3(bipy)]_n$		KBr	
	mg	mmol	mg	mmol	mg	mmol
Eu1Tb1	1.05	$1.13 \cdot 10^{-3}$	1.04	$1.12 \cdot 10^{-3}$	209.6	1.76
Eu1Tb3	0.55	$0.59 \cdot 10^{-3}$	1.65	$1.77 \cdot 10^{-3}$	222.8	1.87
Eu1Tb5	0.59	$0.64 \cdot 10^{-3}$	2.99	$3.20 \cdot 10^{-3}$	362.1	3.04
Eu1Tb10	0.28	$0.31 \cdot 10^{-3}$	2.90	$3.10 \cdot 10^{-3}$	325.3	2.73

Table 3.1: Composition of the Eu^{3+}/ Tb^{3+} mixed samples.

As anticipated in the introduction of this chapter, the intensity ratio between Tb^{3+} $^5D_4 \rightarrow {}^7F_5$ and Eu^{3+} $^5D_0 \rightarrow {}^7F_2$ transitions is used as thermometric parameter for ratiometric thermometers. Therefore, the presence of single metal (Eu^{3+} or Tb^{3+}) CP local aggregates is a source of error in the determination of the thermometric properties. For this reason, the sample homogeneity and reproducibility were tested. At room temperature (λ_{exc}= 320 nm), the samples showed a bright emission characterized by a homogeneous colour variation from orange to green upon increasing the Tb^{3+} amount (see **Figure 3.12**).

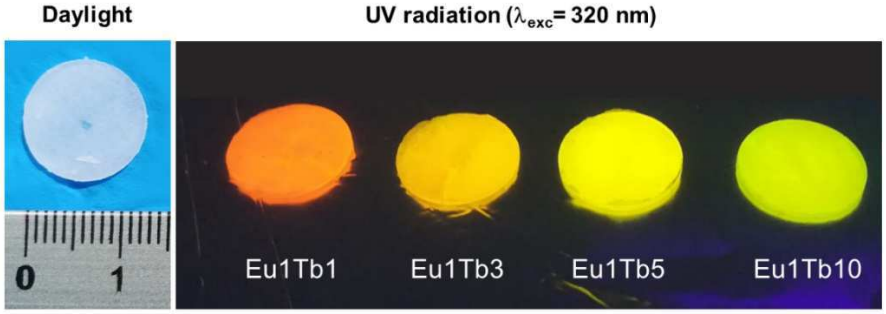

Figure 3.12: Dimension in cm (left) and room temperature emitted colour of the studied Eu-Tb mixed samples (right). λ_{exc}=320 nm.

Sampling different spots on the sample, no significant differences between the relative intensity of Tb^{3+} $^5D_4 \rightarrow {}^7F_5$ and Eu^{3+} $^5D_0 \rightarrow {}^7F_2$ transitions were observed confirming the homogeneous dispersion of the two metal centers inside all the samples. The method reproducibility was determined on three replicates of the sample **Eu1Tb3** comparing the relative intensity of Tb^{3+} $^5D_4 \rightarrow {}^7F_5$ and Eu^{3+} $^5D_0 \rightarrow {}^7F_2$ transitions as before. In different samples, the small differences of Tb^{3+}/Eu^{3+} intensity ratio (about 10 %) can be used as experimental error.

The emission spectra of the mixed samples are characterized by terbium and europium bright emissions clearly visible also at the naked eye. The relative intensity of green (Tb^{3+}) and red (Eu^{3+}) depends on the terbium amount and on the excitation wavelength (**Figure 3.13** as example).

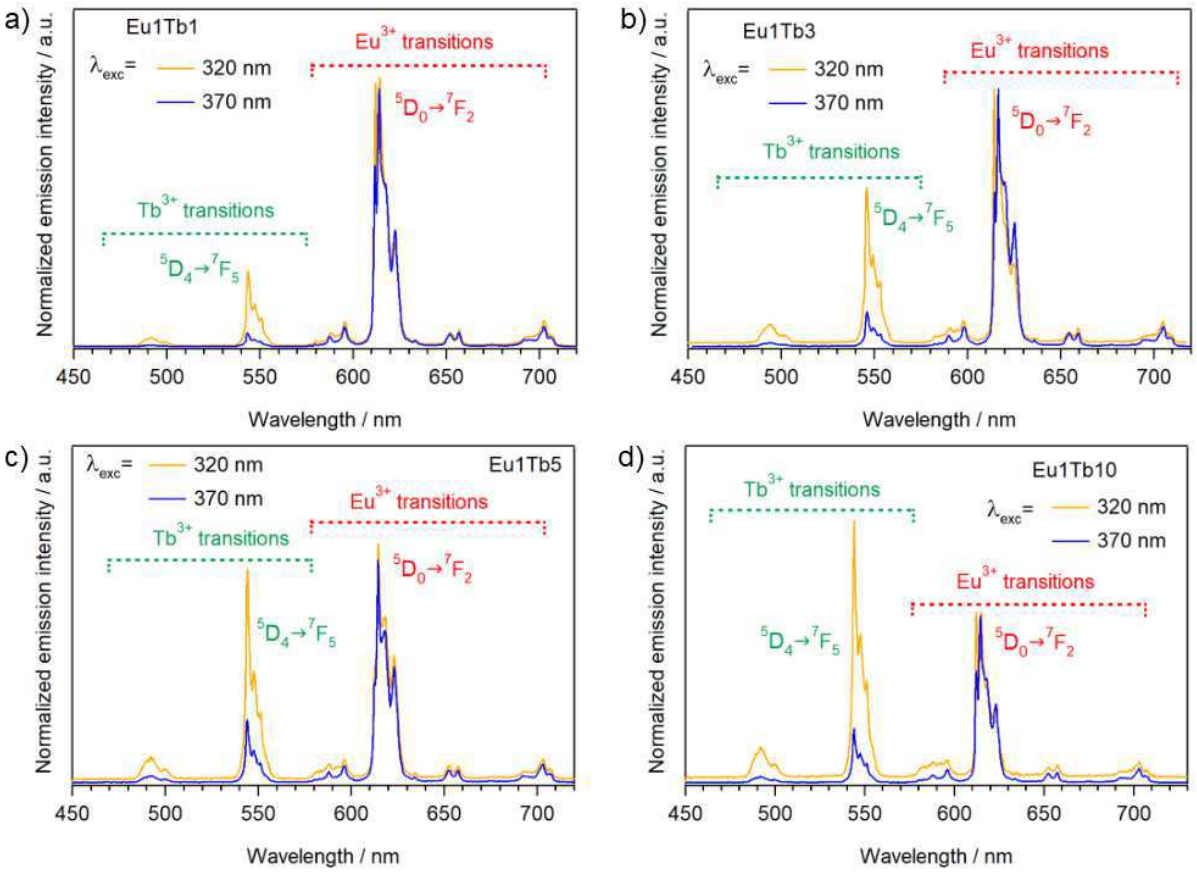

Figure 3.13: Room temperature emission spectra of the Eu^{3+}/Tb^{3+} mixed samples normalized at 614 nm.

The shape of Eu^{3+} and Tb^{3+} transitions does not change in the studied temperature range as showed in **Figure 3.14** reporting the temperature dependent PL emission spectra (λ_{exc}= 320 and 370) of the sample **Eu1Tb3** as example.

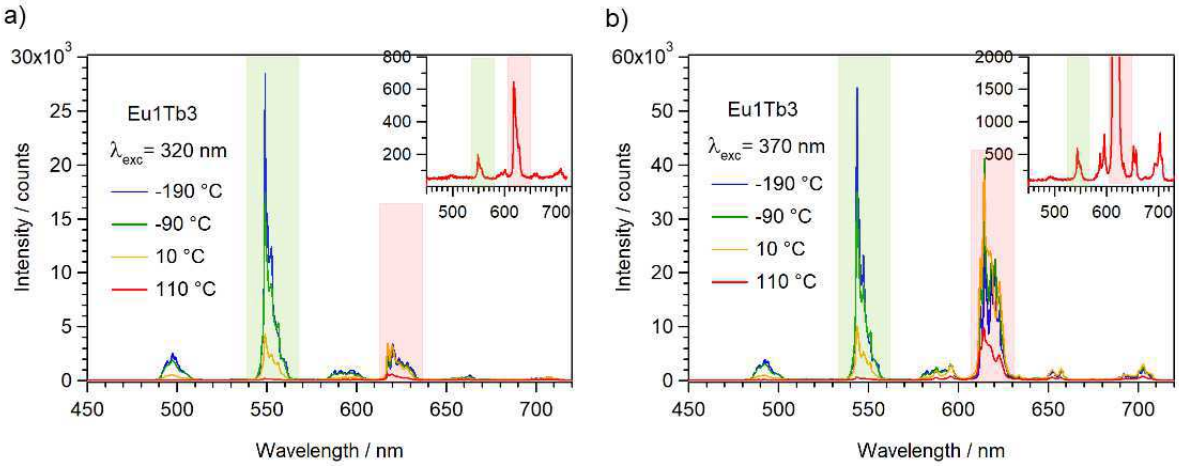

Figure 3.14: Temperature dependent photoluminescent properties of compound **Eu1Tb3** excited at **a)** 320 nm and **b)** 370 nm; in the inset the spectrum at 110 °C is highlighted.

The corresponding Δ curves (I_{Tb}/I_{Eu}) have a well-defined S-shape. The Δ values depend on the relative Tb^{3+}/Eu^{3+} amount so that they have been normalized at -190 °C to have qualitative information.

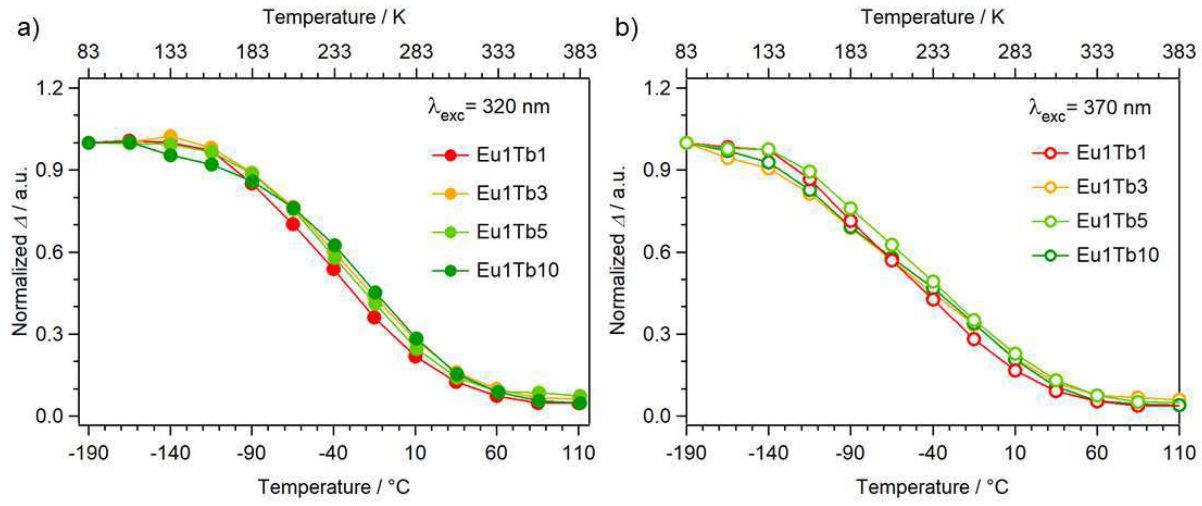

Figure 3.15: Mixed samples normalized Δ curves at the two different λ_{exc}.

Since the normalized Δ curves (**Figure 3.15**) have basically the same shape we expected samples to have similar thermometric properties. Indeed, the derived S_r

curves (**Figure 3.16**) are almost independent from the relative Tb^{3+}/Eu^{3+} amount and by the excitation wavelength.

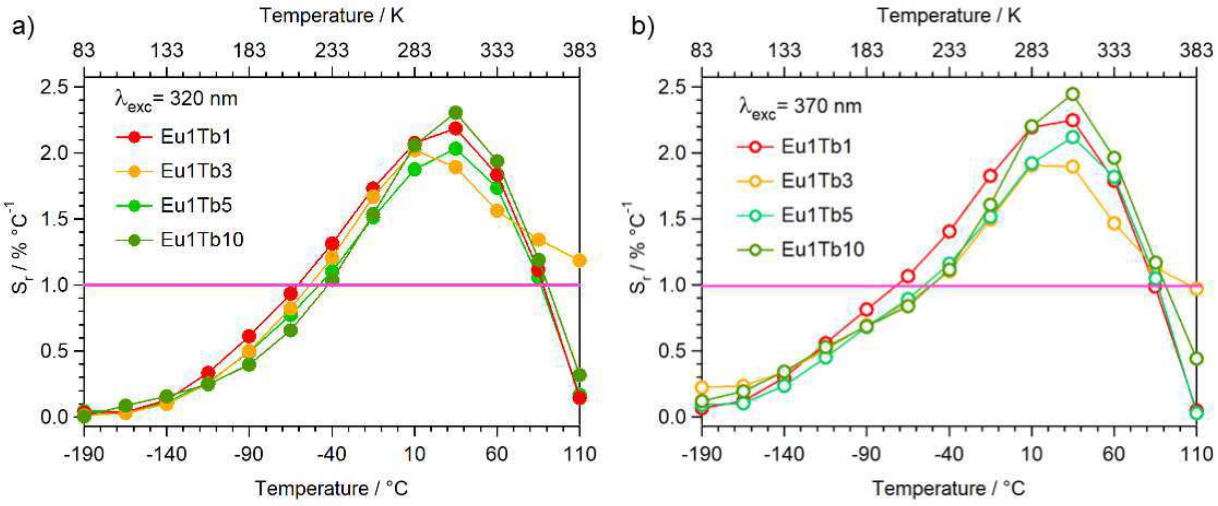

Figure 3.16: Relative thermal sensitivity of the studied samples excited at **a)** 320 nm and **b)** 370 nm.

All curves showed an asymmetric bell-shape with a S_r maximum of about 2 between 10 and 35 °C. Values of S_r greater than 1 between -50 and 100 °C define for these ratiometric thermometers the suitable temperature range for best performant applications.

Interestingly, all samples appeared promising for a large temperature range and showed excellent thermometric properties in the physiological temperature range (25-50 °C). These results are among the best reported in the literature for other Ln^{3+}-based ratiometric luminescent thermometers (see **Figure 3.17** as example).[55]

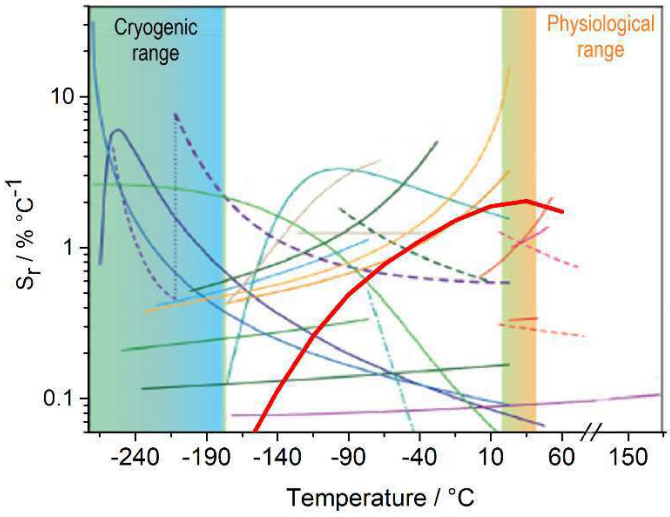

Figure 3.17: Temperature dependence of the relative thermal sensitivity (S_r) of different Ln^{3+}-based ratiometric thermometers reported in ref [55]. The S_r trend of the sample **Eu1Tb1** (λ_{exc}= 320 nm) was stacked as example (red curve). Cryogenic range T < -173 °C, physiological range 25-50 °C.

In **Table 3.2** the temperature range with S_r higher than 1, and the S_r maximum value for all samples are reported.

Sample	λ_{exc}= 320 nm		λ_{exc}= 370 nm	
	Temperature range $S_r \geq 1$	S_r max (T)	Temperature range $S_r \geq 1$	S_r max (T)
Eu1Tb1	-60 – 90 °C	2.19 (35 °C)	-70 – 90 °C	2.25 (35 °C)
Eu1Tb3	-50 – 110 °C	2.01 (10 °C)	-50 – 110 °C	1.92 (10 °C)
Eu1Tb5	-50 – 90 °C	2.03 (35 °C)	-50 – 90 °C	2.12 (35 °C
Eu1Tb10	-40 – 90 °C	2.31 (35 °C)	-50 – 90 °C	2.44 (35 °C)

Table 3.2: Temperature range with $S_r \geq 1$ and S_r maximum value (S_r max) of the studied Eu^{3+}/Tb^{3+} mixed samples at the two excitation wavelengths.

As already mentioned in **Chapter 2**, the Mott-Seitz equation (MS)[124,125] can be used to study the non-radiative deactivation pathways involved in the modulation of the luminescent properties in a luminescent thermometer. For a ratiometric thermometer the MS equation is defined as follow (see **Appendix 1** for further details):

$$\Delta = \frac{I_{Tb}}{I_{Eu}} = \frac{I_{Tb0}}{1+\sum_{i=1}^{n} \alpha_{Tb_i} \cdot exp\left(\frac{-\Delta E_{Tb_i}}{k_b \cdot T}\right)} \cdot \frac{1+\sum_{i=1}^{n} \alpha_{Eu_i} \cdot exp\left(\frac{-\Delta E_{Eu_i}}{k_b \cdot T}\right)}{I_{Eu0}} \quad \textbf{(3.1)}$$

where I_{Tb0} and I_{Eu0} are the intensities of the terbium $^5D_4 \rightarrow {}^7F_5$ and europium $^5D_0 \rightarrow {}^7F_2$ transitions at 0 K (e.g. Δ_0); ΔE_{Tb_i} and ΔE_{Eu_i} the energy required for the activation of i-th non-radiative deactivation pathway for Tb^{3+} and Eu^{3+} respectively, while α_{Tb_i} and α_{Eu_i} the ratio between the non-radiative and radiative deactivation probabilities of the considered deactivation channel; k_b the Boltzmann constant, and T the absolute temperature. In our study, since only the Tb^{3+} intensity varies with temperature while Eu^{3+} emission can be assumed almost constant the temperature range, the MS equation can be approximated:

$$\Delta = \frac{\Delta_0}{1+\sum_{i=1}^{n} \alpha_{Tb_i} \cdot exp\left(\frac{-\Delta E_{Tb_i}}{k_b \cdot T}\right)} \quad \textbf{(3.2)}$$

where $\Delta_0 = I_{Tb0}/I_{Eu0}$. It is worth to note that **Equation (3.2)** is analogous to the MS equation for a one-center intensity-based molecular thermometer (see **Chapter 2** and **4** and **Appendix 1**).

The two main mechanisms that modulate the thermometric behaviours of Tb^{3+} are the metal-to-ligand triplet level back energy transfer (BEnT) and multiphonon processes.[26] Given the absence of coordinated -OH or -NH groups, only the contribution due to the BEnT processes was considered in the MS equation. For samples excited at 320 (**Table 3.3**), the MS fit was in good agreement with the experimental data with an activation energy (ΔE_1) close to 1,400 cm^{-1} ($\Delta E_{T\text{-}Tb}$).

Compound	ΔE_1 (cm^{-1})	α_1	R^2
Eu1Tb1	1,213 ± 75	1,520	0.995
Eu1Tb3	1,261 ± 62	1,658	0.997
Eu1Tb5	1,267 ± 51	1,843	0.998
Eu1Tb10	1,347 ± 105	2,408	0.995

Table 3.3: ΔE_1 and α_1 Mott-Seitz parameters for the mixed Tb/Eu samples excited at 320 nm and the respective coefficient of determination (R^2).

Conversely, exciting the samples at 370 nm (**Table 3.4**), the use of one term in the MS did not allow a good reproduction of the experimental data. For this reason, a second term was introduced.

Compound	ΔE_1 (cm^{-1})	α_1	ΔE_2 (cm^{-1})	α_2	R^2
Eu1Tb1	1,378 ± 315	4,477	491 ± 75	10	0.996
Eu1Tb3	1,467 ± 189	4,688	366 ± 88	7	0.998
Eu1Tb5	1,595 ± 277	7,755	534 ± 143	18	0.998
Eu1Tb10	1,693 ± 337	12,500	468 ± 106	16	0.998

Table 3.4: ΔE_1, α_1, ΔE_2, and α_2 Mott-Seitz parameters for the mixed Tb/Eu samples excited at 370 nm and the respective coefficient of determination (R^2).

A possible explanation is the presence of Tb^{3+}-Tb^{3+} cross-relaxation (C-R) phenomena that are effective when excited Tb^{3+} ions are spatially close to other Tb^{3+} ions in their ground-state.[159–161] This situation can occur using 370 nm as the excitation wavelength where Tb^{3+} emission is significantly less-effectively sensitized than at 320 nm (see **Figure 3.8**). In other words, using λ_{exc}= 370 nm, the probability to have an excited Tb^{3+} ion spatially close to a Tb^{3+} ion in its ground state is much higher than at 320 nm as λ_{exc}. The C-R occurs when the energy released by a $^5D_3 \rightarrow {}^5D_4$ transition in the excited Tb^{3+} ion promotes the $^7F_6 \rightarrow {}^7F_0$ transition in a spatially close ground state ion (**Figure 3.18**). After that, both ions decay quickly through non-radiative process to their ground state $^7F_6$ level.

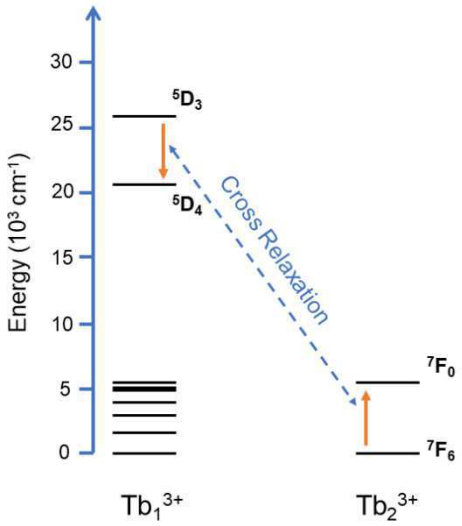

Figure 3.18: Simplified energy diagram showing the cross-relaxation process. Readapted from ref [159].

This process requires small activation energies (≈ 200 cm^{-1}) since the considered energy gaps ($^5D_3$-$^5D_4$, ≈ 5,600 cm^{-1} and $^7F_0$-$^7F_6$ ≈ 5,800 cm^{-1}) are almost isoenergetic. The optimal distance between the Tb^{3+} ions for C-R phenomena is about 10 Å[162] which is close to the Tb^{3+}-Tb^{3+} distance in our CP (12.2 Å from crystallographic data). Moreover, by plotting the trend of the two exponential terms of the MS equation (see **Figure 3.19** as example) the term associated to ΔE_2 is approximately constant in all the temperature range, in agreement with the observation that C-R is almost independent from temperature variations.[162]

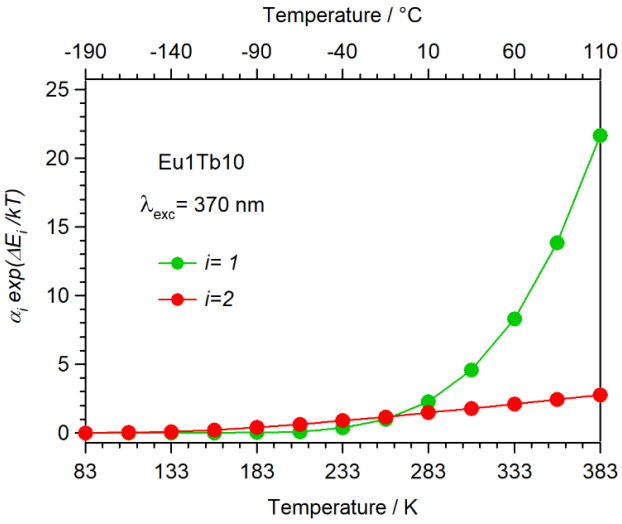

Figure 3.19: Comparison of the two exponential terms in the MS equation of **Eu1Tb10**.

Each sample showed an important and peculiar colour variation in the -140 ÷ 60 °C range depending on the excitation wavelength. The temperature-dependent chromatic variation of the samples is displayed in **Figure 3.20** through colorimetric maps.

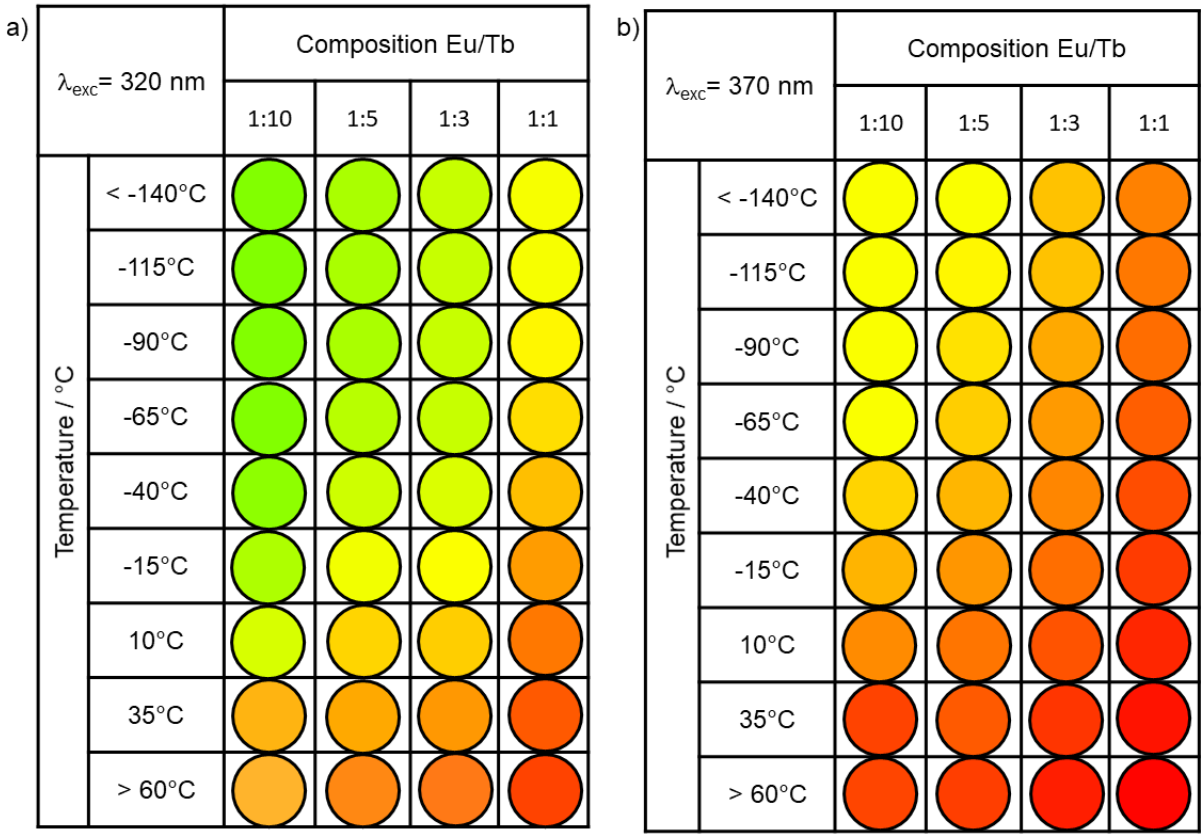

Figure 3.20: Overall chromatic variation for the studied samples excited at **c)** 320 nm and **d)** 370 nm.

Using λ_{exc}= 320 nm the colour of the emitted light changes from greenish/yellow at -140 °C, to orange/red at 60 °C, depending on the sample composition (**Figure 3.20 a**). Conversely, at 370 nm where Tb^{3+} emission is less-efficiently sensitized, the Eu^{3+} red component in the emitted light is more pronounced (**Figure 3.20 b**). The dependence between the colour of the emitted light and temperature suggests the use of these mixtures as colorimetric thermometers between -140 and 60 °C since to a given colour is associated a certain temperature range. Moreover, in principle it would be possible to distinguish narrower temperature windows by combining two or more samples thus creating a sort of bar-code colorimetric thermometers.

To conclude, the most interesting point of the photoluminescent and thermometric properties of these mixed Eu/Tb samples are summarized. The studied samples can be used as ratiometric thermometers since they show good thermometric properties in a wide temperature range, from about -50 to 100 °C, with excellent relative thermal sensitivity in the physiological temperature range (25 ÷ 45 °C). Each sample also showed an important and peculiar colour variation between -140 and 60 °C so that it can be used alone or combined with other compositions to yield a luminescent bar-code as colorimetric temperature sensor. Finally, the fact that their S_r is not influenced by the excitation wavelength is relevant from an applicative point of view. For example, the possibility to use 370 nm as excitation wavelength becomes important when the temperature sensor is shielded by a sheet of glass or dispersed in a plastic matrix since these materials strongly absorb below 350 nm.

3.3. Conclusions

The temperature dependent luminescent properties of the two homometallic 1D zig-zag $[Ln(hfac)_3(bipy)]_n$ CPs (Ln^{3+}= Eu^{3+} and Tb^{3+}) were studied in the -190 ÷ 110 °C temperature range using two excitation wavelengths, 320 and 370 nm. Independently from the excitation wavelength, the Eu^{3+} luminescent properties are sensitive to temperature variation only above 50 °C, while the Tb^{3+} compound showed a good thermometric response with S_r values higher than one above -40°C.

The Eu^{3+} and Tb^{3+} homometallic CPs were mixed in KBr to prepare a series of Eu^{3+}/Tb^{3+} ratiometric thermometers with composition **Eu1Tb1**, **Eu1Tb3**, **Eu1Tb5**, and **Eu1Tb10**. The Eu^{3+}/Tb^{3+} relative amounts and the excitation wavelength influence the emitted colour but not the S_r values of the systems. The samples showed good thermometric properties in a wide temperature range from about -50 to 100 °C and high relative thermal sensitivity in the physiological temperature range (25 ÷ 45 °C) which were among the best reported in the literature for Ln^{3+}-based ratiometric thermometers. Moreover, each sample showed a well-defined and peculiar colour variation between -140 and 60 °C so that they can be used as colorimetric thermometers. By coupling two or more samples a luminescent bar-code colorimetric thermometer can be also obtained.

The independence of the S_r values from the excitation wavelength (320 and 370 nm) allows also a good applicative flexibility for these ratiometric thermometers.

In the future, we will study the thermometric behaviour of a mixed heterobimetallic $[Eu_xTb_{1-x}(hfac)_3(bipy)]_n$ ($0 < x < 1$) CP in which the two Ln^{3+} ions are co-present in the same 1D-chain. In this case, the simultaneous presence of the two Ln^{3+} ions in the same polymeric chain could vary the thermometric properties of the system, for example introducing relevant ET phenomena between Tb^{3+} and Eu^{3+}.

4. Post-Synthesis Modifications of $[Eu_2(H_2DHT)_3(DMF)_4 \cdot 2DMF]_n$ LOF

4.1. Introduction

4.1.1. Metal Organic Frameworks

Metal Organic Frameworks (MOFs) are a class of porous inorganic-organic hybrid materials characterized by a crystalline reticular structure that can be in principle designed "*a priori*" through a proper selection of the building units.[163] Indeed MOFs are defined by the combination of an inorganic fragment (a metal center or a polynuclear aggregate), the so called secondary building unit (SBU), and a multitopic ligand with well-defined coordination modes in a self-assembling process. Generally, SBUs are well-defined molecular entities that maintain their structural integrity during the MOF growth so that the structural properties of the MOF are determined by the SBU symmetric properties.[164] For example, MOF-5 $[Zn_4O(O_2C)_6]_n$ (**Figure 4.1**), where O_2C is the carboxylate unit of the 1,4-benzenedicarboxylate ligand, is characterized by a cubic structure resulting from the assembly of SBUs with octahedral symmetry connected by the organic spacer.[165] The SBUs decorate the vertices of the cubic structure while the organic fragment expands it.

Historically, di- or poly-carboxylate ligands are the most used organic molecules employed in the MOFs synthesis for the high bond energy of their coordination to metal center. These complexes are generally synthesized by mixing the metal salt and a policarboxylic acid (with divergent carboxylic groups) at room temperature and in aerobic conditions, or *via* a solvo- or hydrothermal synthesis in autoclave. Generally, Brønsted bases are employed to facilitate the deprotonation of the carboxylic acid.[6]

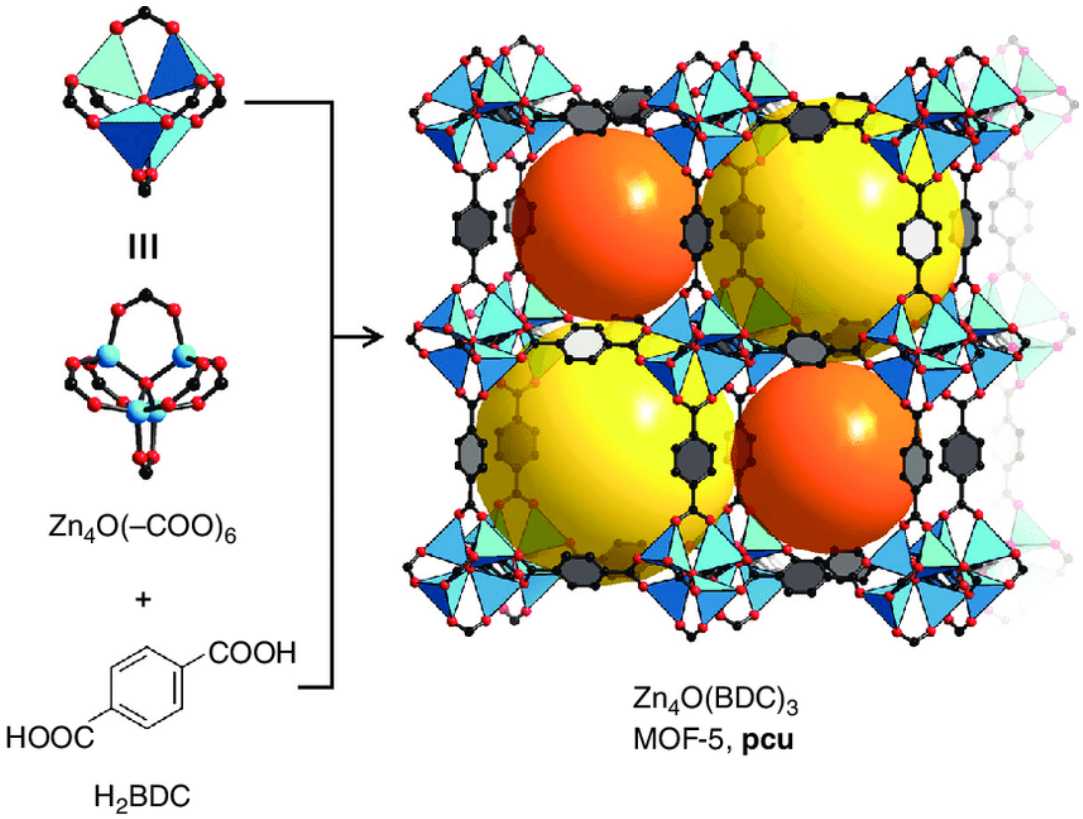

Figure 4.1: MOF-5 SBU (left) and 3D-structure (right). Zn (light blue spheres and tetrahedrons), O (red spheres), C (black spheres). The yellow and orange spheres represent the MOF cavities. Reprinted from ref. [166].

Since their discovery, MOFs have been particularly studied because of the variety of morphologies that they can assume.[167–169] Moreover, their peculiar porosity and high superficial area make MOFs appealing in several research fields as in the separation of small molecules or in gas storage,[170–173] in heterogeneous catalysis,[174] in drug delivery,[175–177] or as sensors.[178,179]

Beside the huge number of MOFs based on *d* metals, in the literature also numerous examples of Lanthanoid Organic Frameworks (LOFs) are reported.[5,6,180,181] However, differently from the *d*-metal analogues, the *"a priori"* LOF synthesis results very challenging.[182] Indeed, as previously described in **Chapter 1**, lanthanoid ions present low ligand-field stabilization energies and their coordination geometries are mainly governed by the organic ligand bulkiness. Moreover, their lability and the possibility to assume different coordination geometries allows different arrangements depending on the chemical environment (the so-called *chameleon behaviour*).[183]

One of the reasons why Lanthanoid Organic Frameworks (LOFs) are extensively studied is the possibility to create materials characterized by the luminescent properties of a lanthanoid ion (see **Chapter 1**) associated with the peculiar structural properties of a MOF. Indeed, compared to the traditional molecular approach, that uses organic molecules and coordination compounds to obtain functional luminescent materials, in the LOF approach there is an interaction among the periodically located metal centers capable to modulate the properties of the resulting material. For this reason, a variety of LOFs have been realized for applications on chemical sensing, light-emitting devices, and biomedicine over the past two decades.[6,182] More recently, in 2012, Cui and co-workers reported the first example of luminescent molecular thermometers based on the LOF $[Ln_2(DMT)_3]_n$ (Ln^{3+}= Eu^{3+} and Tb^{3+}; DMT= 2,5-dimethoxy-1,4-benzenedicarboxylate).[83] To date, LOFs are one of the most interesting substrates for the development of luminescent thermometers as highlighted by the numerous works reported in the literature.[55,78]

This interest in LOFs is certainly to be attributed to their luminescent properties that can be easily and finely tuned in many ways to create very versatile materials (see **Chapter 1**). Briefly, there are three main components in a LOF involved in luminescence phenomena: *i*) the metal ion, *ii*) the spacer, and *iii*) the guest species (organic molecules or metal ions) which generally fill the LOF cavities. In principle, all these components can be luminescent by themselves or can influence the overall emission in a certain way (e.g. through the activation of non-radiative pathways, auto absorption phenomena, etc.).

The simplest way to modulate the LOF emitting properties without altering its structure is certainly the synthesis of multi-metallic LOFs using two or more different lanthanoid ions. Indeed, since they present similar ionic radii, the LOF crystalline lattice is maintained also using mixtures of different Ln^{3+} ions. For example, Haquin and co-workers showed the possibility to modulate the colour and the brightness of the emitted light in a series of $[Tb_{2x}Eu_{2y}La_{(2-2x-2y)}(T)_3(H_2O)_4]$ LOFs (T= 1,4-

benzenedicarboxylate): in this case, the Tb/Eu molar ratio determines the resulting emitted colour which can be tuned from green (y= 0) to red (x= 0), while the La amount influences the brightness (**Figure 4.2**).[140]

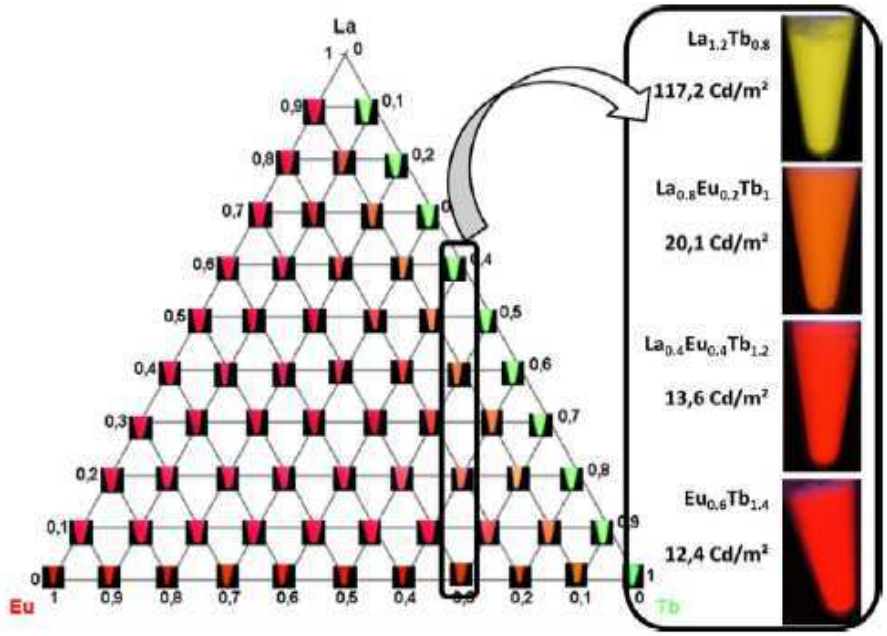

Figure 4.2: Ternary phase diagram of the $[Tb_{2x}Eu_{2y}La_{(2-2x-2y)}(T)_3(H_2O)_4]$ heterotrimetallic series with x and y ranging from 0 to 1, with the corresponding pictures and some luminance values under 0.25 W m^{-2} irradiance at 312 nm. Reproduced from ref [140]. Copyright 2013 John Wiley and Sons.

Another example of modulation of LOFs emitting properties is represented by the compound $[Eu(BTPCA)(H_2O)]$ (see **Figure 4.3**, $BTPCA^{3-}$= 1,1',1''-(benzene-1,3,5-triyl)tripiperidine-4-carboxylate)[179] which was tested versus a series of *s*, *p*, and *d* metal ions. In this case, the nature of the metal guested inside the pores determines the overall luminescent properties of the LOF because it affects how effectively the emissive states of the Eu^{3+} ion are sensitized. The changes in efficiency of the energy transfer are made responsible for quenching (e.g. using Fe^{3+}), but also for the ''turn-on'' process in the case of Zn^{2+}.[184]

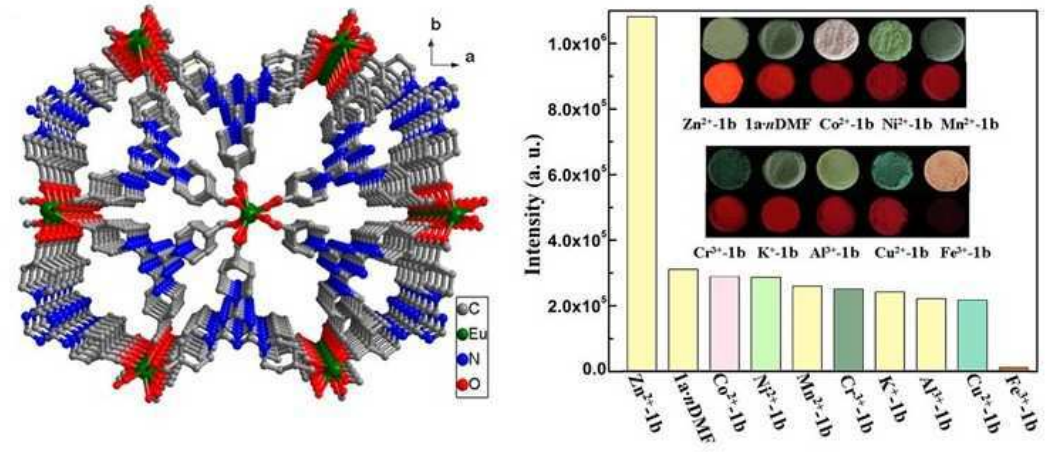

Figure 4.3: Crystal structure of the MOF [Eu(BTPCA)(H_2O)] (on the left) and the influence of metal ions on the luminescence intensity (on the right). Reproduced from ref. [185]. Copyright 2013 American Chemical Society.

If the modification of the metal ion is quite simple, that of the organic spacer is more challenging. The variation of the ligand length is a way to obtain MOFs with different porosity and luminescent properties. It is based on the principle that the MOF structure only depends on the geometry of the SBUs which is determined by the coordination properties of the metal centre and the ligand binding sites. This principle is well-described by the IRMOFs series (Iso-Reticular MOFs) developed by Yaghi starting from the MOF-5 (**Figure 4.4**).[186]

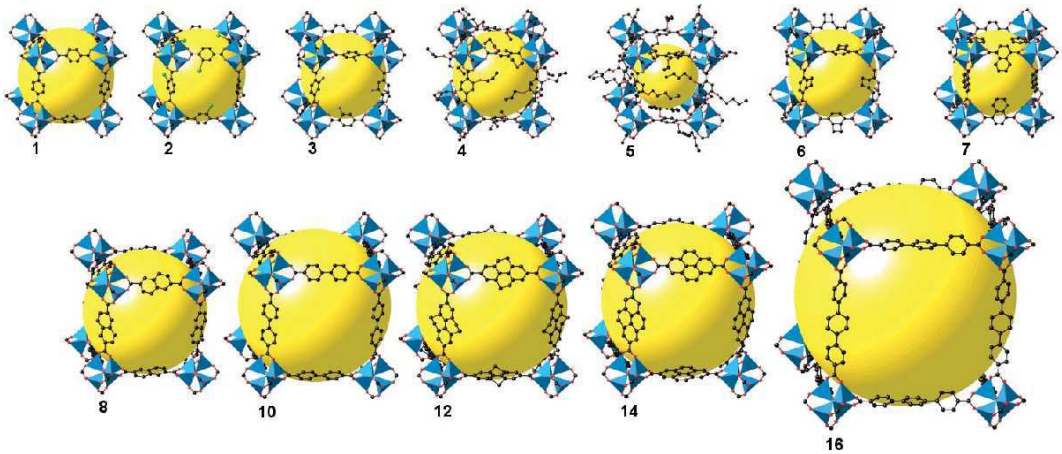

Figure 4.4: IRMOF-n (n = 1–10, 12, 14, and 16) – Zn (light blue tetrahedron), O (red), C (black), Br (green, n= 2), NH_2 (blue, n= 3). Reproduced from ref [186].

However, the introduction of ligands with reactive or thermally labile functional groups can be difficult in the reaction conditions (often solvothermal) used for the

LOFs synthesis.[187] For this reason, different methods were developed for the introduction of ligands with such kinds of functional groups.

4.1.2. Post Synthesis Modifications (PSMs)

In 2007, Wang and Cohen for the first time functionalized an amine group with an aldehyde moieties[188] introducing the term "Post Synthesis Modification" (or PSM), like the post-transduction modification employed for proteins after their synthesis.[189,190] After the PSM process, the MOF crystalline nature was unchanged retaining its original superficial area and porosity (**Figure 4.5**). Three main categories of PSMs were described by Cohen[191,192] and Burrows:[193]

1. *Desolvation*: post synthesis modification where the solvent in the channels and in the metal coordination sphere is removed creating coordinative holes that make the MOF more active in gas absorption or reactive towards coordinative molecules. This PSM is particularly used for LOFs activation because of the weak interactions with the solvent molecules.
2. *Covalent modification*: a new covalent bond is formed in the MOF architecture. Generally, this type of PSM is employed to modify the spacer ligand and it was one of the first used PSM methods.[194]
3. *Post synthesis deprotection*: in this case a chemical bond is broken to deprotect a functional group generating a material with different properties. This is the more recent and less used type of PSM. Telfer[195] showed that this method can be useful to avoid structure interpenetration which generally affects MOFs reducing the pore sizes.

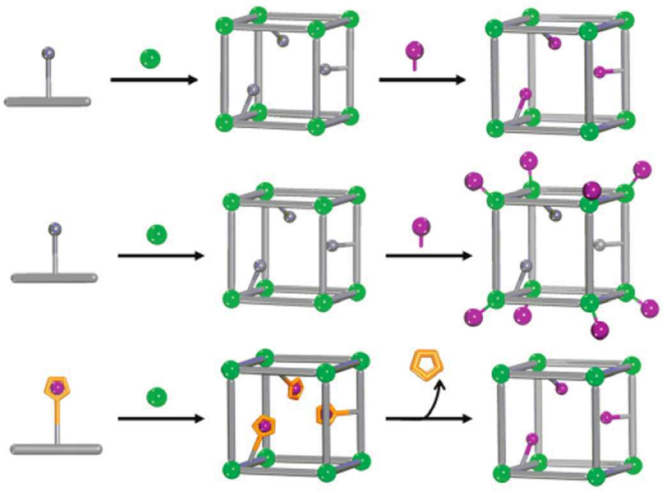

Figure 4.5: Examples of covalent Post Synthesis Modifications. Reprinted from ref [191].

More recently, the so-called "*Building Block Replacement*" (BBR) strategy was developed. BBR can be divided in three main groups:[196]

1. *Transmetallation*: a method for the incorporation of metal ions that can not be introduced in the MOF structure through conventional synthetic routes. Zhang[197] applied this PSM to substitute non-catalytic Cd^{2+} ions with active Mn^{2+} ones increasing from 7 to 75 % the yield of conversion in an epoxidation reaction (**Figure 4.6**).

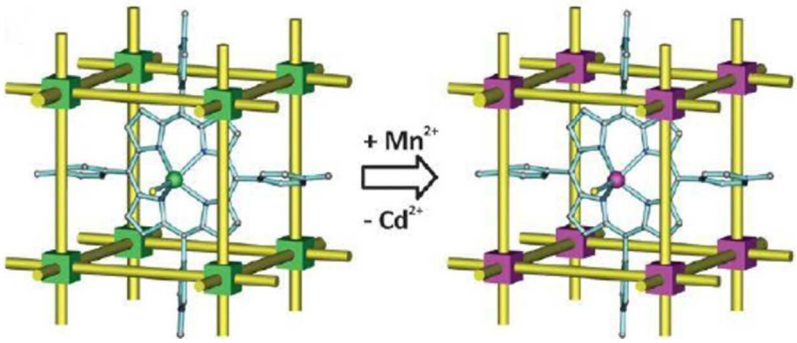

Figure 4.6: Example of transmetallation in a MOF where the Cd^{2+} ions were substituted with Mn^{2+} for catalytic purposes. Adapted from ref [197].

2. *Solvent Assisted Ligand Exchange* (SALE):[198,199] this type of modification provides the complete exchange of the ligand with another one which presents different functionalities or dimensions. When the exchange regards the solvent molecules in the MOF structure, this procedure takes the name

of *Coordinating Solvent Exchange* (CSE).[196] For example, in Rosi's work[199] it is reported an elongation of the crystallographic *c* axis in the Zn-based MOF (Bio-MOF), from 62.04 Å to 82.25 Å with this type of modification (**Figure 4.7**).

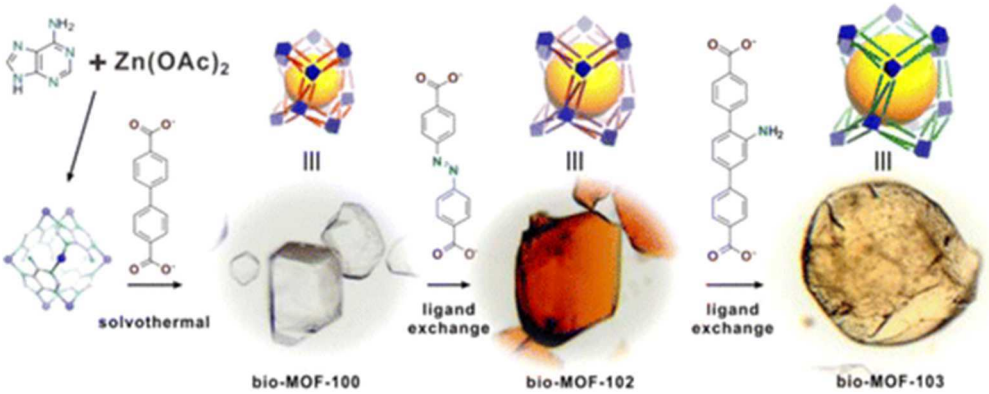

Figure 4.7: Example of solvent assisted linker exchange on the bio-MOF to increase the cell dimensions. Adapted from ref [199].

3. *Solvent-Mediated Extraction* (SME):[200] this is probably the most common method employed to remove solvent molecules from the MOF structure. The substrate is maintained in contact with a solvent (usually chloroform or toluene) which displaces the solvent molecules from the MOF pores through mass effect.

It is desirable that the PSM occurs through a single-crystal to a single-crystal transformation (SCSC) without the loss of the MOF crystalline habit. In these cases, easy to study, it has been observed that the modifications occur through the breaking and the formation of bonds between the reagents and the MOF in the solid state. No dissolution or recrystallization is present.

The advantages of the post-synthetic methodology rely in the milder reaction conditions and in a good modification efficiency at low concentrations of the used reactant. These synthetic procedures are particularly useful if the spacer ligand is sensitive, expensive, or incompatible with the reaction condition employed for the MOF direct synthesis. Moreover, these reactions allow to control the MOF pores and nodes with an engineering approach varying the volume, the channels dimensions,

and their chemical environment. For all these reasons, the PSM results a good method for tuning the LOFs properties in magnetic and luminescent materials.

4.1.3. Topic outline

Lanthanoid MOFs are good systems to study how the substitution of the guest molecules inside the 3D porous structure influences the luminescent and thermometric properties of the system (see page 15, **Chapter 1**). In particular, according to the work of Kyprianidou and co-workers,[196] small molecules such as imidazole and pyridine penetrate into the pores of a lanthanoid terephthalate MOF. Treating the europium LOF with a chloroform solution of the proper guest, the Eu^{3+} luminescent properties can be modulated. For this reason, an Eu^{3+}-LOF based on a terephthalate ligand is a good candidate to study the effect of different guest molecules on the luminescent and thermometric properties of the system.

The Eu^{3+}-based LOF $\{[Eu_2(H_2DHT)_3(DMF)_4)] \cdot 2DMF\}$ (H_4DHT= 2,5-dihydroxy-1,4-benzenedicarboxylic, DMF= *N*,*N*-dimethylformamide) was chosen as candidate for this study. Even if the H_4DHT ligand (**Figure 4.8**) chemistry has been already studied by Nayak and co-workers, who reported the synthesis of a series of isostructural LOFs with composition $\{[Ln_2(H_2DHT)_3(DMF)_4] \cdot 2DMF\}_n$ (Ln= La^{3+}, Ce^{3+}, Nd^{3+} and Gd^{3+}),[180] the Eu^{3+} derivative is not reported in the literature.

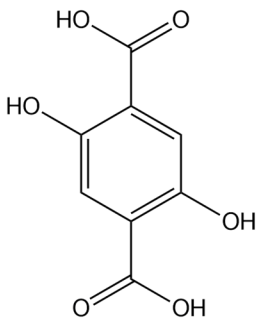

Figure 4.8: The 2,5-dihydroxy-1,4-dicarboxylic acid (H_4DHT).

As first step, the synthesis and the characterization of the $\{[Eu_2(H_2DHT)_3(DMF)_4)] \cdot 2DMF\}$ compound were performed. Then, the DMF

molecules of the $\{[Eu_2(H_2DHT)_3(DMF)_4)] \cdot 2DMF\}$ compound were substituted with different organic molecules such as chloroform ($CHCl_3$), imidazole (Im), pyridine (Py), and tetrahydrofuran (THF) using the *solvent-mediated extraction* (SME) method.[200] The resulting products were characterized through elemental analysis, infrared spectroscopy, powders and single crystal X-ray diffraction where possible. Finally, the luminescence and thermometric properties of the corresponding modified Eu^{3+}-LOFs were correlated with the structural, chemical, and physical variations imparted by the different guest molecules housed in the LOF structure after the PSM process.

4.2. Results and discussion

4.2.1. Synthesis of {[$Eu_2(H_2DHT)_3(DMF)_4$)] · 2DMF}

$Eu(NO_3)_3$ and H_4DHT were dissolved in DMF with a 2:3 stoichiometry. Subsequent heating of the system at 90 °C for 20 h in a Carius tube resulted in the formation of the air stable europium compound $\{[Eu_2(H_2DHT)_3(DMF)_4]\cdot 2DMF\}_n$ in very high yields (90 % c.a.) according to the following reaction:

$$2Eu(NO_3)_3 + 3H_4DHT + 12DMF \longrightarrow \{[Eu_2(H_2DHT)_3(DMF)_4]\cdot 2DMF\}_n + 6(H_2NMe_2)(NO_3) + 6CO \quad \textbf{(4.1)}$$

At 90 °C DMF slowly decomposes generating "*in situ*" CO and dimethylamine ($HNMe_2$). The low concentration of the amine in solution leads to the slow deprotonation of the H_4DHT. The precipitation of the $\{[Eu_2(H_2DHT)_3(DMF)_4]\cdot 2DMF\}_n$ product from the hot solution affords a crystalline solid suitable for single crystal XRD analysis.

The crucial role of the amine was also demonstrated by developing an alternative synthetic strategy at room temperature in which DMF does not act as amine source since it does not decompose. In this case a vial containing $Gd(NO_3)_3$ and H_4DHT in DMF was posed in a Schlenk tube with a heptane solution of $[NH_2Bu_2][O_2CNBu_2]$ obtained by treatment of $NHBu_2$ with CO_2 according to the following equilibrium:

$$2HNBu_2 + CO_2 \leftrightarrows [NH_2Bu_2][O_2CNBu_2] \quad \textbf{(4.2)}$$

After few days at room temperature, the slow diffusion of $NHBu_2$ originating from the $[NH_2Bu_2][O_2CNBu_2]$ solution, affords large size crystals of $\{[Gd_2(H_2DHT)_3(DMF)_4]\cdot 2DMF\}_n$ (yield higher than 90 % after one month).[201,202] The development of a room temperature synthetic procedure that affords a crystalline product is an important issue in the field of LOFs. Indeed, it can be used as a general route to intercept MOF phases that are unstable at high temperature or that require a high activation energy to proceed to more stable assemblages allowing their structural characterization.

Although the $\{[Eu_2(H_2DHT)_3(DMF)_4]\cdot 2DMF\}_n$ compound can be obtained with both the synthetic methods, the first one was used because faster than the second one.

The structure of $\{[Eu_2(H_2DHT)_3(DMF)_4]\cdot 2DMF\}_n$ was solved through single crystal X-ray studies. The Eu^{3+} compound resulted isostructural to the Gd^{3+} analogue already described in the literature (**Figure 4.9 a**).[180] Its extended structure is characterized by dinuclear SBUs linked together by terephthalate dianions. Each SBU presents two Eu^{3+} centers with coordination number of nine and a capped square antiprism geometry.

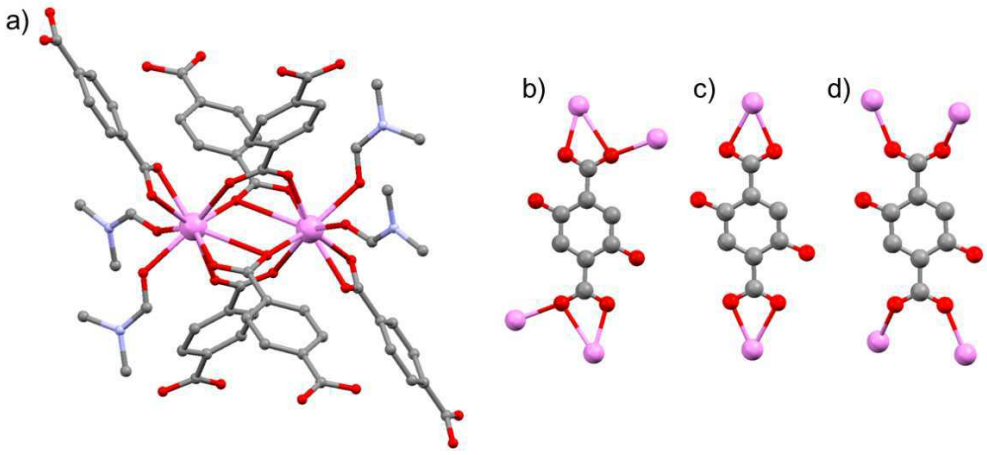

Figure 4.9: a) Asymmetric unit of $\{[Eu_2(H_2DHT)_3(DMF)_4]\cdot 2DMF\}_n$: Eu^{3+} (violet), C (grey), N (blue), and O (red). **b)**, **c)**, and **d**) H_2DHT ligand coordination modes. Hydrogen and OH groups (only in **a**) were omitted for clarity.

The two europium ions are surrounded by six H_2DHT^{2-} ligands and four coordinated DMF molecules. Each europium is bound to two H_2DHT^{2-} molecules with the **b** coordination mode, one with the **c** type, and two with the **d** one, as highlighted in **Figure 4.9**. Considering the presence of two DMF molecules coordinated through their oxygen atom, the europium total coordination number is nine.

The 3D architecture generated by the spatial repetition of the asymmetric unit is reported in **Figure 4.10**. The extended structure is characterized by 1D open channels with an almost square cross section of $9.8\cdot 8.6$ Å^2 partially filled by two DMF molecules per unit formula (one molecule per each europium center) corresponding to the 33 % of the total DMF referring to the SBU stoichiometry.

Powder-XRD measurements showed the presence of a single crystalline phase in agreement with the theoretical diffractogram calculated from the crystallographic structure of $\{[Eu_2(H_2DHT)_3(DMF)_4]\cdot 2DMF\}_n$. Henceforth, this complex will be named **Eu@DMF** for simplicity.

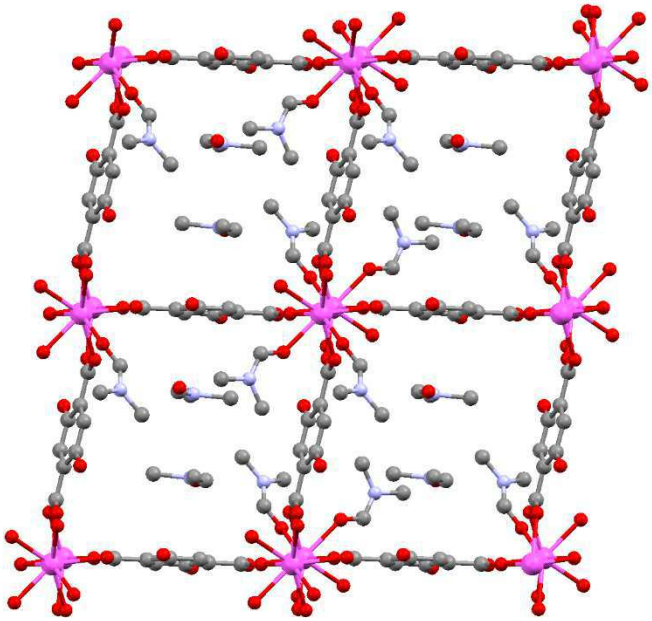

Figure 4.10: Representation of the **Eu@MOF** channels: Eu^{3+} (violet), C (grey), N (blue), and O (red). H atoms were omitted for clarity.

4.2.2. Post Synthesis Modifications

Leaving crystals of **Eu@MOF** in a chloroform solution at room temperature, it is possible to substitute two of the six DMF molecules with chloroform. The reaction can be easily followed through liquid IR spectroscopy monitoring in the organic phase, renewed daily, the intensity of the DMF peak at 1675 cm^{-1} (ν_{CO}). After seven days no DMF signals were seen in the chloroform solution indicating the completeness of the substitution. The ATR-IR spectrum recorded on the resulting crystals shows the decrease of the signals attributable to the DMF molecules in the pores (1675, 1385, and 1094 cm^{-1}) and the typical absorption of the $CHCl_3$ like the C-Cl stretching at 750 cm^{-1} (**Figure 4.11**). Elemental analysis on the air-stored product confirms the presence of chloroform in agreement with the

$\{[Eu_2(H_2DHT)_3(DMF)_4]\cdot CHCl_3\}_n$ composition. The sample will be named **Eu@CHCl₃** for simplicity.

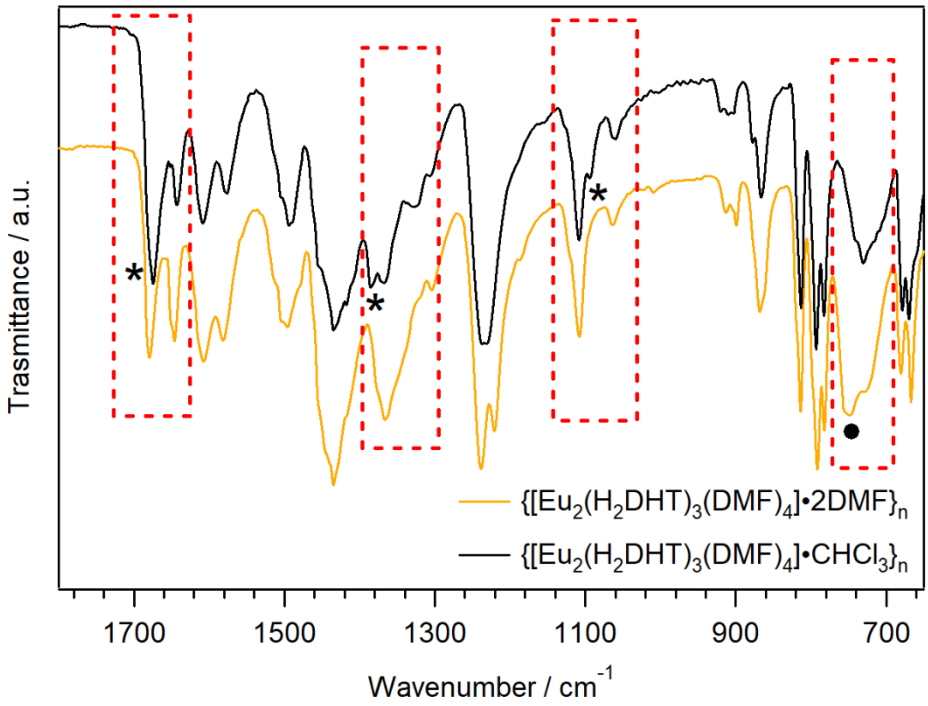

Figure 4.11: Infrared spectra comparison of of **Eu@DMF** (black) and **Eu@CHCl₃** (light-orange) compounds. Some differences are highlighted in the red dashed rectangles. The typical peaks of free DMF and $CHCl_3$ are highlighted with black asterisks and dots respectively.

The experimental powder X-ray diffractogram of **Eu@CHCl₃** showed a good agreement with that of the gadolinium analogue indicating that the two compounds are isostructural (**Figure 4.12**).

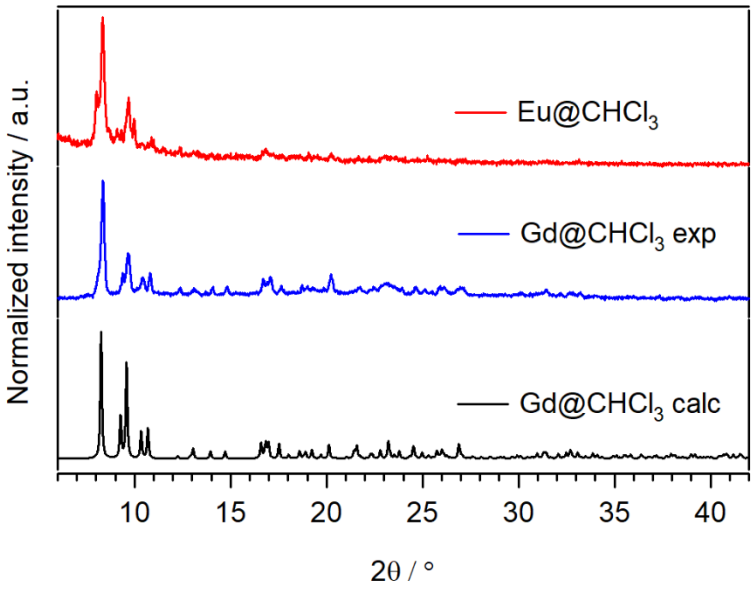

Figure 4.12: Experimental powders X-ray diffractograms of **Eu@ $CHCl_3$** (red) and **Gd@$CHCl_3$** (blue). In black, powders X-ray diffractogram calculated from **Gd@$CHCl_3$** single crystal.

Looking at the structure of **Gd@$CHCl_3$**, the substitution of the DMF molecules with chloroform generates a slight distortion in the LOF architecture which is particularly evident along the *a* crystallographic axis (**Figure 4.13**). Indeed, in **Gd@$CHCl_3$** there is a shift of the europium dinuclear units along the *b* axis that reduces the distance between two groves along the *c* axis (see the orange dashed lines and the blue arrows in **Figure 4.13** for clarity). This distortion generates smaller cavities and an interaction between the DMF molecules coordinated to two different europium dinuclear units. Powder-XRD measurements were in agreement with the theoretical diffractogram calculated from the solved structure and showed the presence of a unique crystalline phase.

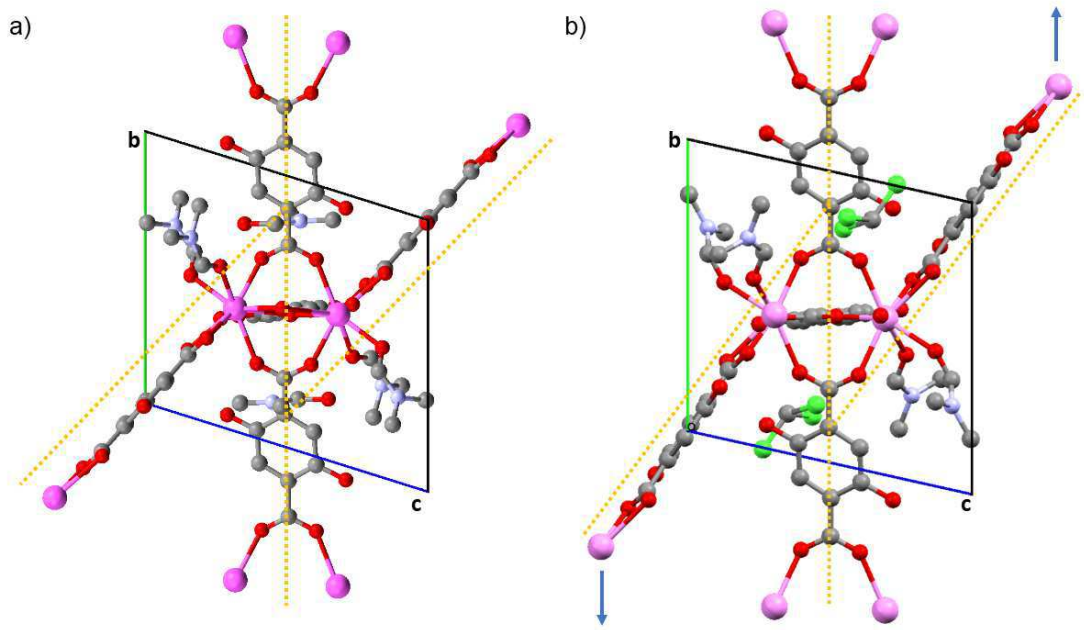

Figure 4.13: Comparison between the structure of (**a**) $\{[Eu_2(H_2DHT)_3(DMF)_4]\ 2DMF\}_n$ and (**b**) $\{[Eu_2(H_2DHT)_3(DMF)_4]\ CHCl_3\}_n$.

Encouraged by this result which afforded a single crystal to single crystal post-synthesis modification with the possibility of a full characterization of the final product, we used PSM to investigate the DMF exchange with other small molecules such as imidazole (Im), pyridine (Py) and tetrahydrofuran (THF). Chloroform was used as reaction solvent because the presence of basic sites (N- and O-sites) on the three guest candidates (Im, Py, and THF) would favour the instauration of hydrogen bonds between the guest molecules and the H_2DHT^{2-} -OH groups allowing their preferential uptake than chloroform.

Single crystals of **Eu@DMF** were posed in contact with 5 mL of an imidazole solution in chloroform (0.68 M) at room temperature for seven days. In this case the DMF release, monitored through IR spectroscopy on the liquid phase, agrees with the substitution of all the six DMF molecules in **Eu@DMF**. Also the ATR-IR spectrum of **Eu@IM** resulting crystals does not show the typical signals of DMF molecules (1675, 1643, 1385, 1094, 1063 e 660 cm^{-1}), while the presence of imidazole in the structure is associated to the bands at 1539, 1533, 1325, 1094, 1063, 935 e 659 cm^{-1} [203]

while the signal centered at 746 cm^{-1} can be attributed both to imidazole and chloroform (**Figure 4.14**).

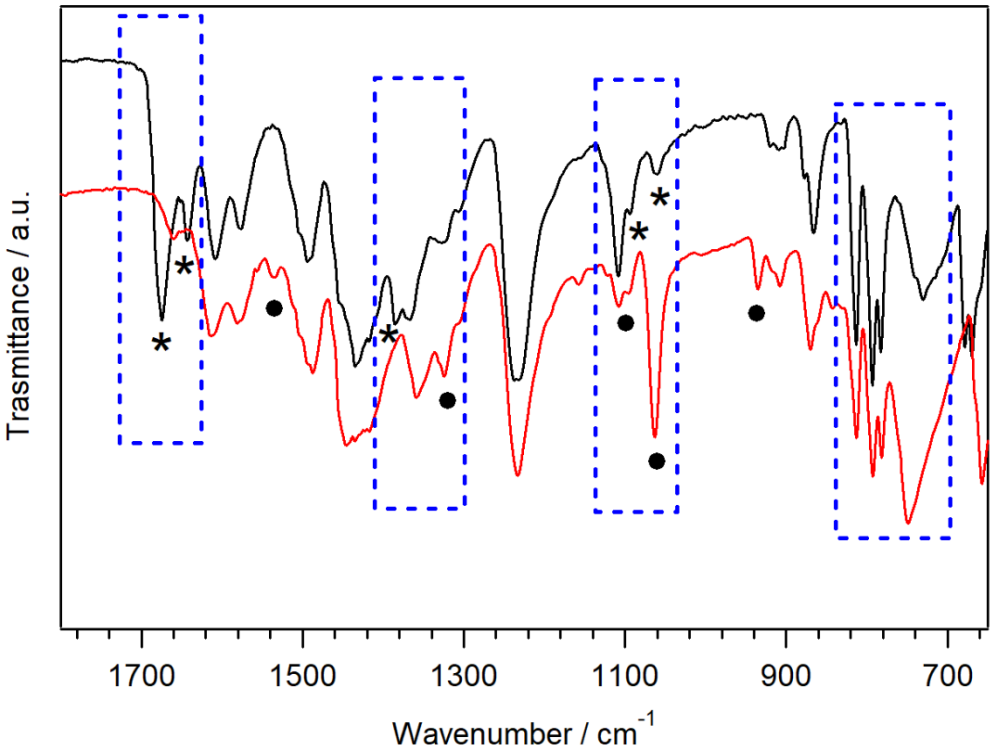

Figure 4.14: Comparison of the infrared spectra of **Eu@DMF** (black) and **Eu@IM** (red) compounds. Some differences are highlighted in the blue dashed rectangles. The typical peaks of DMF and IM are highlighted with black asterisks and dots respectively.

Also in this case, the comparison between the powder X-ray diffractograms of the resulting **Eu@IM** compounds with the experimental and calculated diffractograms of the gadolinium analogue showed that the two compounds were isostructural (**Figure 4.15**).

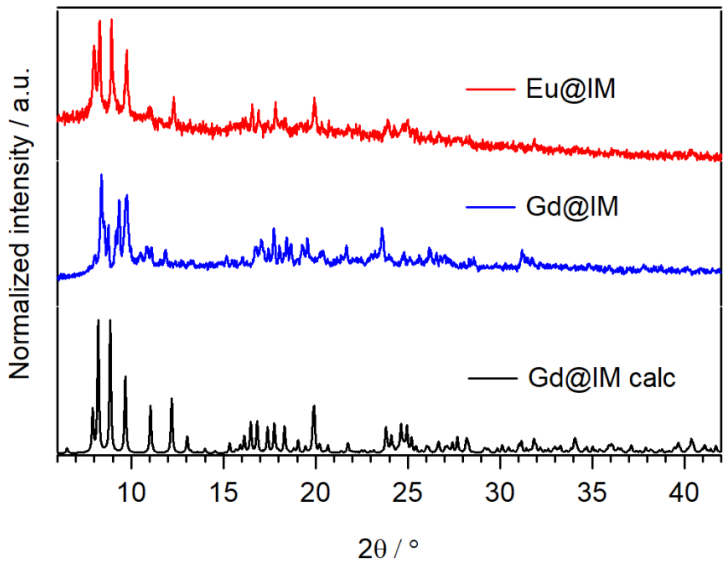

Figure 4.15: Experimental powders X-ray diffractograms of **Eu@IM** (red) compared with the **b)** experimental (blue) and calculated (black) powders X-ray diffractograms of **Gd@IM**.

Referring to the crystal structure of **Gd@IM**, the resulting compound presented two different dinuclear lanthanoid units with different compositions containing respectively (**Figure 4.16**): four coordinated imidazole ligands in the first, two imidazole ligands and two water molecules coordinated to the two Gd^{3+} centers in the second.

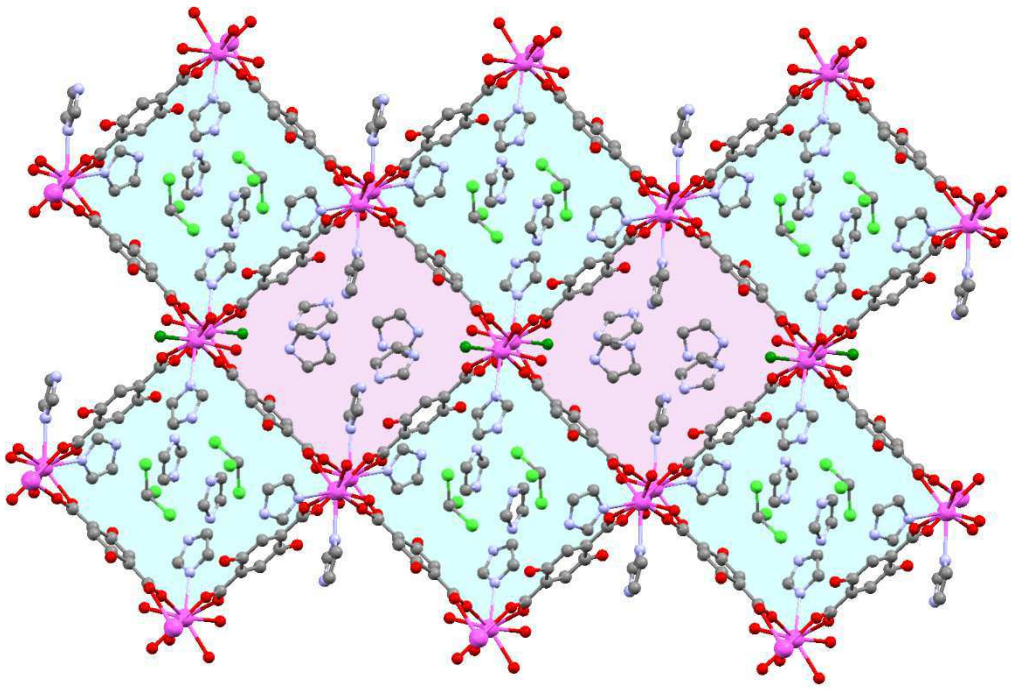

Figure 4.16: Structure of $\{[Gd_4(DHT)_6(im)_6(OH_2)_2]\cdot 6im\cdot 2CHCl_3\}_n$. Hydrogen were omitted for clarity. Coordinated water O atom is coloured in dark green. The two different types of cavities are coloured in purple and light-blue.

The molecules inside the LOF cavities are different depending on the nature of the molecules coordinated to the Gd^{3+} dinuclear units which are faced on the cavity. Referring to **Figure 4.16**, four imidazole molecules are in the cavities where water overlooks (the purple ones), while two imidazole and two chloroform molecules are in the others (the light-blue ones). It is worth to note that all the imidazole molecules inside the cavities are ordered because they interact through hydrogen bonds with water or imidazole molecules coordinated to Eu^{3+} and their position can be determined. The elemental analysis on the crystals confirmed the composition of the LOF which is $\{[Eu_4(H_2DHT)_6(im)_6(OH_2)_2]\cdot 6im\cdot 2CHCl_3\}_n$.

Using similar conditions to that employed for the DMF substitution with $CHCl_3$ and imidazole, other two tests have been performed using a chloroform solution of pyridine (5 mL; 1.24 M) and THF (5 mL, 1.23 M). In this case, monitoring the absorbance of the DMF carbonyl group at 1675 cm^{-1} through liquid IR of the surnatant solution, it was esteemed that the DMF content in solution was about 55 % of the total content for pyridine and 39 % for THF. The infrared spectra of the resulting micro-crystalline solids (**Figure 4.17**) confirmed the decrease of the DMF peak centred at 1675 cm^{-1} in both the resulting compounds.

In the sample treated with Py, the intensity of the peak at 1643 cm^{-1} diminishes while the presence in the IR spectrum of two important pyridine signals (1441 and 696 cm^{-1})[204] confirms the presence of Py in the LOF structure. The IR spectrum also coincides with that found for the corresponding Gd^{3+} derivative with the $\{[Gd_2(H_2DHT)_3(DMF)_2(H_2O)_2]\cdot 2Py\cdot 2H_2O\}_n$ analytical composition.[201] Henceforth, this complex will be named **Eu@PY** for simplicity.

On the contrary, the treatment of **Eu@DMF** with the THF solution evidences the complete substitution of the DMF molecules in the LOF channels (about 39 % of the total DMF compared to the theoretical 33 %). However, no signals ascribable to THF (e.g. 2975 cm^{-1}, 2865 cm^{-1}, and 1070 cm^{-1})[205] were detectable in the ATR-IR spectrum of the resulting compound (**Figure 4.17**).

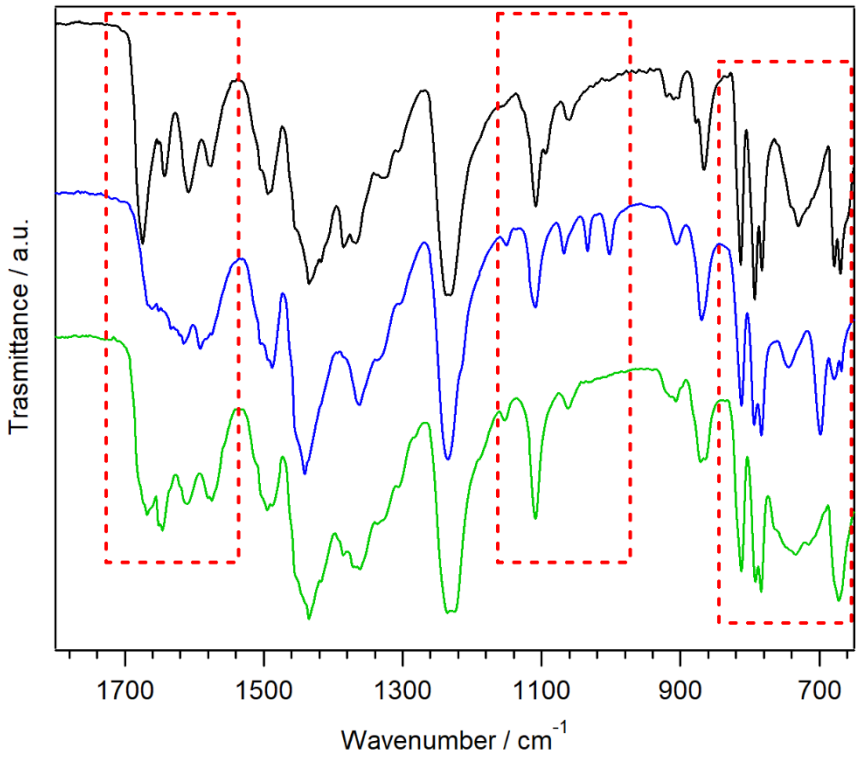

Figure 4.17: Comparison of the infrared spectra of **Eu@DMF** (black), **Eu@PY** (blue), and **Eu@THF** (green) compounds. Some differences are highlighted in the red dashed rectangles.

In this case two possible scenarios can be considered:

1. only $CHCl_3$ enters in the LOF pores forming the **Eu@CHCl₃** derivative,
2. THF substitutes the DMF molecules but it is lost during the product recovery because of its higher volatility compared to DMF.

The differences between the recorded IR spectrum and that of **Eu@CHCl₃** derivative exclude the first hypothesis and let us to conclude that THF enters in the LOF cavities but it is lost during the recovery procedure. Moreover, the IR spectrum of the solid coincided with that of its Gd^{3+} analogue with the composition $\{[Gd_2(H_2DHT)_3(DMF)_4]\cdot 0.5THF\cdot 4H_2O\}_n$.[201] This sample was labelled **Eu@THF**.

Unfortunately, in the case of **Eu@PY** and **Eu@THF**, the quality of the resulting crystals was not adequate to determine the structure through single-crystal XRD analysis. However, **Eu@PY** and **Eu@THF** powder X-ray diffractograms were appreciably different compared to that of the DMF, $CHCl_3$, and Im derivatives indicating a modification in the LOF structure attributable to the substitution of the DMF molecules after the treatment with Py and THF solutions (see **Figure 4.18**).

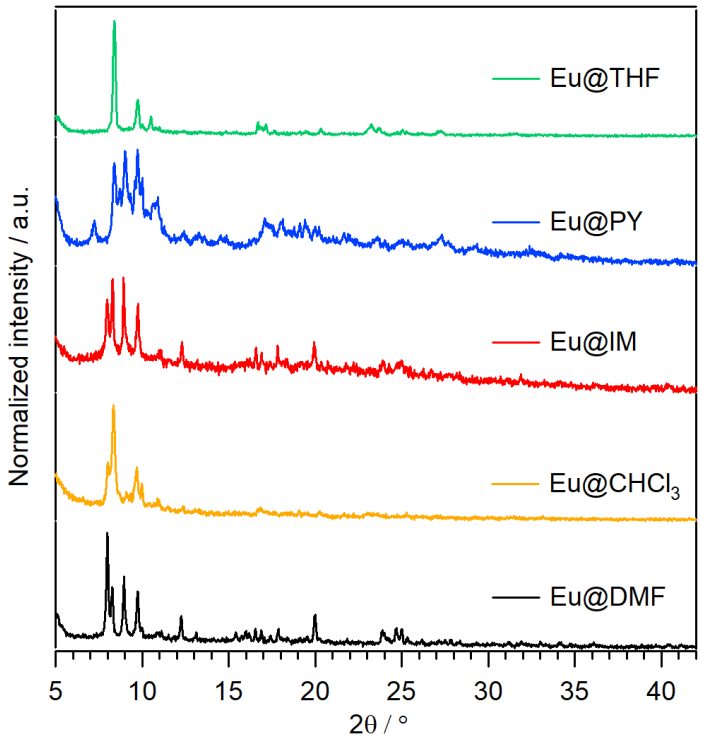

Figure 4.18: From top to bottom, experimental XRD-powder diffractograms of **Eu@THF**, **Eu@PY**, **Eu@IM, Eu@CHCl$_3$**, and **Eu@DMF**.

4.2.3. Photoluminescence studies

The diffuse reflectance (DR) spectra of the Eu^{3+} compounds (**Figure 4.19 a**) show broad bands related to ligand-centred transitions. In particular, **Eu@CHCl$_3$** and **Eu@IM** compounds are characterized by a broad absorption band up to ≈ 700 nm, whereas **Eu@DMF**, **Eu@PY**, and **Eu@THF** derivatives present only a strong absorption below 450 nm. It is worth to note that the substitution of DMF in the LOF structure with other molecules changes the colour of the resulting compound from pale yellow (**Eu@DMF**, **Eu@PY**, and **Eu@THF**) to brownish (**Eu@CHCl$_3$** and **Eu@IM**) generating new absorptions. The presence of ligand-to-metal charge transfer (LMCT) states can be a possible explanation for the different absorption properties of the studied compounds (see pages 6-7 **Chapter 1**).

A commonly employed method to reveal the presence of LMCT states is the arithmetic subtraction between the europium and gadolinium compounds reflectance spectra. Indeed, the energy difference between Gd^{3+} first excited state and the fundamental level is too high to allow the detection of a charge transfer state in the

UV/Vis range. Therefore, in the Gd^{3+} spectrum only the contributions related to ligand-cantered processes are expected to be measured (**Figure 4.19 b**).[126,127,206]

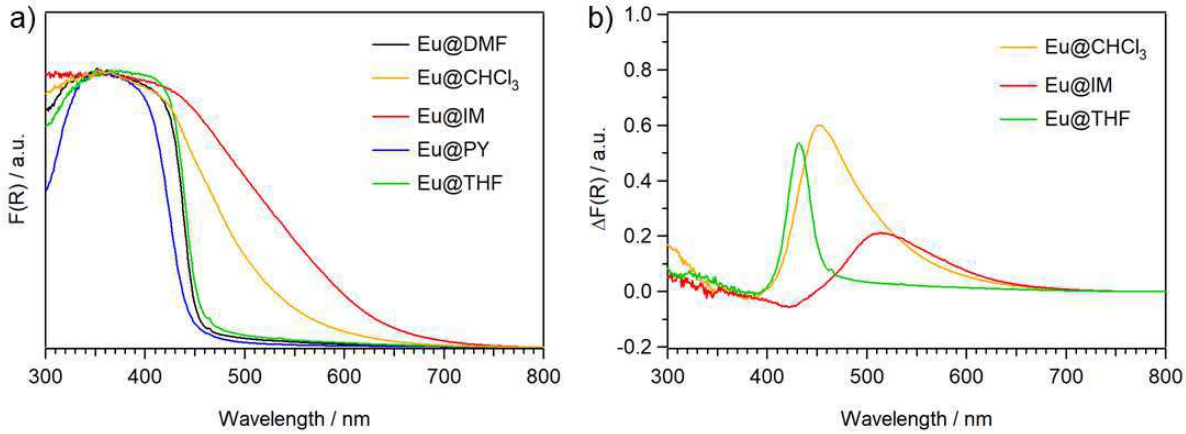

Figure 4.19: a) Diffuse reflectance spectra of **Eu@DMF**, **Eu@CHCl₃**, **Eu@IM**, **Eu@PY**, and **Eu@THF**. **b)** Differential spectrum obtained subtracting **Eu@XX** and **Gd@XX** DR spectra (**XX**= **CHCl₃**, **IM**, and **THF**).

The arithmetic subtraction revealed the presence of LMCT states with different shapes in **Eu@CHCl₃** (452 nm, 22,125 cm^{-1}), **Eu@IM** (513 nm, 19,500 cm^{-1}), and **Eu@THF** (432 nm, 23,150 cm^{-1}), while in **Eu@DMF** and **Eu@PY** low-energy LMCT bands were not observed. In all the cases, LMCT start in the visible range of the spectrum (400 – 450 nm) but their extension changes depending on the sample. In the case of **Eu@CHCl₃** and **Eu@IM** the arithmetic subtraction generates a broad peak of from 400 and 450 to 700 nm, while in **Eu@THF** a narrower peak between 400 and 450 nm is present.

The triplet (T) energy of the H_2DHT^{2-} ligand can be determined from the corresponding gadolinium analogues of the studied Eu^{3+}-LOFs.[201] Indeed, Gd^{3+} complexes are characterized by the absence of ligand-to-metal energy transfer phenomena since Gd^{3+} emitting levels are at significantly higher energy (32,000 cm^{-1}) than the triplet level reported for the more common organic ligand employed with lanthanoid ions, like the 1,4-dicarboxylate ligand and its derivatives.[37,83,196]

At room temperature, the emission spectra of **Gd@DMF**, **Gd@CHCl$_3$**, **Gd@IM**, **Gd@PY**, and **Gd@THF** LOFs are characterized by an intense broad band from 400 to ≈ 700 nm attributable to the ligand emission. The maximum is centred between 460 and 490 nm depending by the nature of the guest molecule (**Figure 4.20** full lines) which corresponds to an energy of the ligand singlet excited state (S_1) between 21,700 and 20,400 cm^{-1}.

Upon cooling the systems to liquid nitrogen temperature, no significant changes in the shape of the emission spectra were detected, except in the case of **Gd@CHCl$_3$** and **Gd@IM** where a component at higher wavelength appeared (**Figure 4.20** dashed lines).

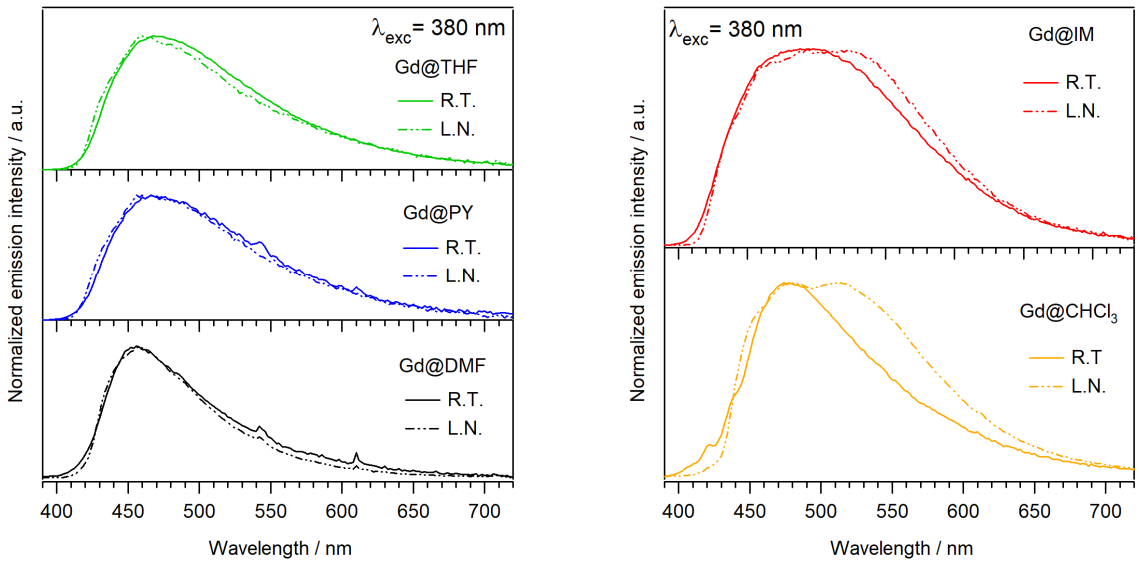

Figure 4.20: Room temperature (full line) and liquid nitrogen temperature (dashed line) emission spectra of **Gd@DMF** (black), **Gd@CHCl$_3$** (orange), **Gd@IM** (red), **Gd@PY** (blue), and **Gd@THF** (green), λ_{exc}= 380 nm

The phosphorescence spectra were recorded at -190 °C using a pulsed lamp as excitation source and introducing a time delay of 40 μs between the excitation impulse and the signal detection to eliminate the contribution of faster fluorescence phenomena (≈ 10 – 100 ns) (**Figure 4.21**). The Gd^{3+} compounds are characterized by the weak emission attributable to the radiative decay of the H_2DHT^{2-} triplet level. The energy of the triplet level is slightly affected by the guest nature: it can be

located between 17,200 – 17,550 cm^{-1} (580 and 570 nm) and it is energetically close to Eu^{3+} $^5D_0$ emissive level (17,220 cm^{-1}). Emission lines of Tb^{3+} (545 nm) and Eu^{3+} (612 nm) impurities in the samples were also detected.

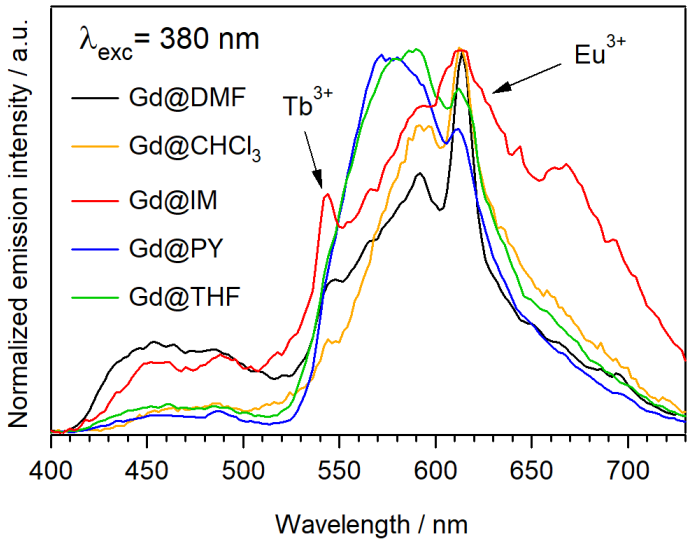

Figure 4.21: Phosphorescence spectra (λ_{exc}= 380 nm) of **Gd@DMF**, **Gd@CHCl$_3$**, **Gd@IM**, **Gd@PY**, and **Gd@THF**.

The weak phosphorescence emission can be explained considering both kinetic and thermodynamic factors. Kinetically, if a low *ISC* rate was present, the energy would be dissipated preferentially through the fluorescence radiative pathway. On the other hand, from a thermodynamic point of view, it may exist a more stable energy level which is preferentially populated than the ligand triplet state. Theoretical calculations are necessary to answer to this question.

In the case of our LOFs, the ligand triplet level is energetically close to Eu^{3+} $^5D_0$ emissive level. When the energy gap between the ligand triplet state and Eu^{3+} $^5D_0$ emissive level ($\Delta E_{T\text{-}Ln}$) is lower than 1,800 cm^{-1} metal-to-ligand back energy transfer processes are easily activated even well below room temperatures.[24,26] This feature is desirable in the development of luminescent thermometers because Eu^{3+} luminescence intensity decreases as temperature increases in presence of efficient metal-to-ligand back energy transfer processes.

At room temperature, where metal-to-ligand back-energy transfer phenomena are present, the low $\Delta E_{T\text{-}Ln}$ energy gap is reflected in the pale Eu^{3+} emission, not visible to the naked eye. The five compounds can be excited through ligand-centred transitions up to 450 nm (**Figure 4.22**). The shape of Eu^{3+} excitation spectra varies depending on the nature of the guest molecule in the LOF structure. For example, the excitation maximum moves towards higher wavelength in the order **Eu@CHCl₃**< **Eu@PY**< **Eu@THF**< **Eu@IM**< **EuDMF**. Moreover, the sample **Eu@CHCl₃** showed different excitation properties compared to the other four compounds characterized by the maximum excitation at short wavelength.

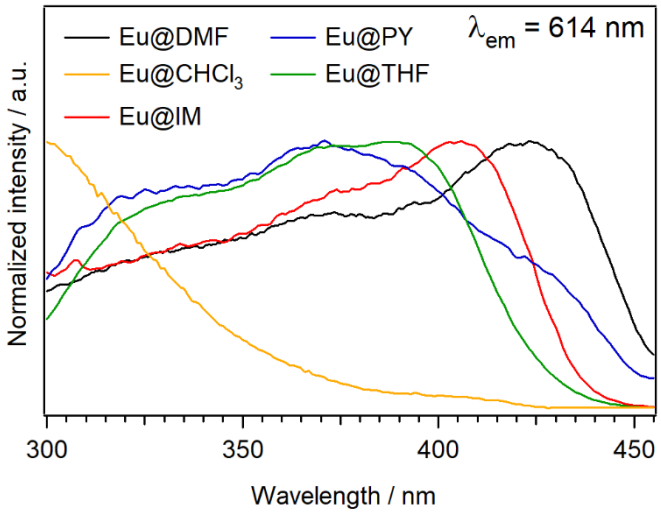

Figure 4.22: Excitation spectra of the compounds **Eu@DMF** (black), **Eu@CHCl₃** (orange), **Eu@IM** (red), **Eu@PY** (blue), and **Eu@THF** (green) recorded at 614 nm.

Comparing the excitation spectra of the studied LOFs to their absorption spectra (see **Figure 4.19 a**) some considerations can be done. For example, the sample **Eu@CHCl₃**, which has as a broad absorption up to 700 nm, shows a good excitation only at low wavelength probably due to auto-absorption phenomena. Conversely, in the other four compounds the excitation region corresponds to the ligand absorption in **Figure 4.19 a** up to ≈ 450 nm.

Room temperature emission spectra of the studied Eu^{3+}-LOFs are characterized by the typical europium transitions $^5D_0 \rightarrow {}^7F_J$ (J=1, 2, 3, and 4) centred at 592, 614, 651,

and 700 nm with the $^5D_0 \rightarrow {}^7F_2$ transition which is the predominant one in all the spectra (**Figure 4.23**). The shape of europium spectra does not vary by changing the excitation wavelength.

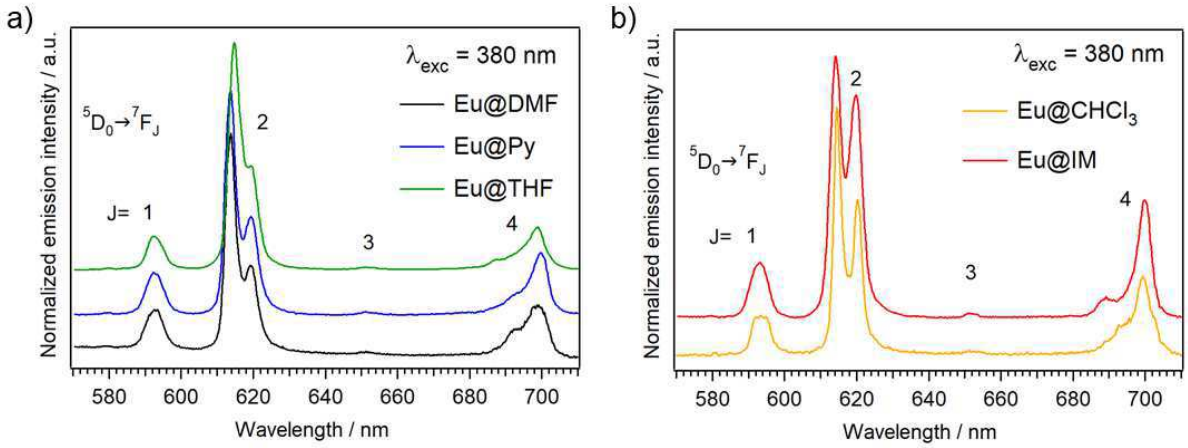

Figure 4.23: Room temperature emission spectra of **a) Eu@DMF** (black), **Eu@PY** (blue), and **Eu@THF** (green), **b**) **Eu@CHCl$_3$** (orange), **Eu@IM** (red) , λ_{exc}= 380 nm.

It is worth to note that the Eu^{3+} transitions have different shape and relative intensity especially as concerns the $^5D_0 \rightarrow {}^7F_2$ and $^5D_0 \rightarrow {}^7F_4$ transitions. Since the shape of Eu^{3+} transitions depends on the local symmetry of the metal ion first coordination sphere,[8] these variations can be explained considering the LOF structural distortion induced by the different guest molecules in the structure.

The structural data of compounds **Eu@DMF**, **Eu@CHCl$_3$**, and **Eu@IM** confirm this hypothesis. Indeed, as highlighted in **Figure 4.24**, different guest molecules induce structural modifications able to distort the Eu^{3+} coordination polyhedrons. Some differences are highlighted by the blue arrows.

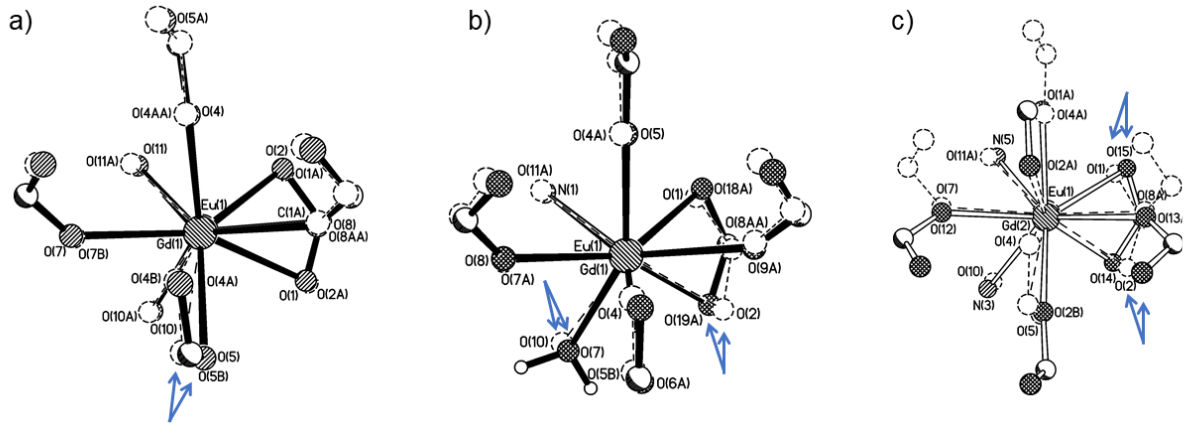

Figure 4.24: Comparison between **a) Eu@DMF** and **Eu@CHCl$_3$**, **b) Eu@DMF** and **Eu@IM$_1$** (that with coordinated water), and **c) Eu@DMF** and **Eu@IM$_2$** (that with no coordinated water) coordination polyhedra.

$^5D_0$ lifetimes (τ_{obs}) are quite similar in all the studied Eu^{3+}-LOFs (**Table 4.1**), only **Eu@PY** showed a value slightly shorter than the other compounds.[3]

Compound	τ_{obs} (ms)	τ_{rad} (ms)	Φ (%)
Eu@DMF	0.14	2.76	0.05
Eu@CHCl$_3$	0.11	2.43	0.04
Eu@IM	0.14	2.77	0.05
Eu@PY	0.09	2.51	0.03
Eu@THF	0.11	2.52	0.04

Table 4.1: Experimental lifetimes (τ_{obs}), radiative lifetimes (τ_{rad}), and intrinsic quantum yields (Φ) for the Eu^{3+}-LOFs; λ_{exc}= 380 nm.

The radiative lifetime (τ_{rad}), which corresponds to the luminescence lifetime of the $^5D_0$ level in the absence of non-radiative processes, can be derived from europium emission spectra according to **(4.3)**:[8]

$$\frac{1}{\tau_{rad}} = A_{MD,0} n^3 \left(\frac{I_{tot}}{I_{MD}}\right) \qquad \textbf{(4.3)}$$

As already said in **Chapter 2** (see page 34), in this way it is possible to achieve information on the non-radiative relaxations which correspond to the difference between the experimental excited state lifetimes (τ_{obs}) and the radiative lifetimes (τ_{rad}). In **(4.3)**, $A_{MD,0}$ is the spontaneous emission probability in vacuo of the $^5D_0 \rightarrow {}^7F_1$

transition (14.65 s^{-1}); I_{tot} and I_{MD} are the integrated areas of the whole emission spectrum and the $^5D_0 \rightarrow {}^7F_1$ transition, and n is the refractive index ($n \approx 1.55$ at the solid state).[8] In this case, all the Eu^{3+}-LOFs showed τ_{rad} values much longer than the respective τ_{obs} indicating that non-radiative quenching phenomena due to metal-to-ligand back energy transfer processes are effective at room temperature. This is also reflected in extremely low values of intrinsic quantum yields (Φ, **Table 4.1**) calculated by the ratio between the radiative and the experimental lifetimes (**4.4**):

$$\Phi = \frac{\tau_{obs}}{\tau_{rad}} \quad (4.4)$$

4.2.4. Thermometric studies

As described in **Chapter 1**, the temperature quenching of a lanthanoid ion luminescence occurs by three main mechanisms:[26,126] *i*) multiphonon relaxation, *ii*) metal-to-ligand back energy transfer (BEnT), and *iii*) ligand-to-metal charge transfer states (LMCT). However, when the energy gap between the ligand triplet level and Eu^{3+} $^5D^0$ emissive level ($\Delta E_{T\text{-}Ln}$) is lower than 1,800 cm^{-1}, BEnT processes is the most important deactivation mechanism and it is effective yet at low temperatures.[127]

Temperature dependent luminescent properties of the Eu^{3+}-LOFs were investigated in the -190/ 30 °C temperature range. This range is particularly suitable for these compounds because at low temperatures the emitted intensity in lanthanoid complexes increases due to the suppression of thermally activated metal-to-ligand back energy transfer phenomena.[27,28] In fact, while at room temperature Eu^{3+} emission is not visible to the naked eye, at -190 °C Eu^{3+} emitted light becomes visible in all the studied compounds. For example, in **Eu@DMF** the intensity of Eu^{3+} $^5D_0 \rightarrow {}^7F_2$ transition is ≈ 200 times higher than room temperature (**Figure 4.25 a**).

In this case, however, the intensity of $^5D_0 \rightarrow {}^7F_2$ transition is more or less comparable as order of magnitude with that of the other transitions (especially the $^5D_0 \rightarrow {}^7F_4$ one, see **Figure 4.25 a** as example). For this reason, we checked the intensity variation of both the total Eu^{3+} emitted light and of the $^5D_0 \rightarrow {}^7F_2$ transition in the studied

temperature range, and we normalized the curves at -190 °C. In all the samples no significant differences between the two curves were observed and the integrated intensity of the $^5D_0 \rightarrow {}^7F_2$ transition, normalized at -190 °C, was arbitrarily chosen as thermometric parameter (Δ).

Eu^{3+}-LOFs presented different temperature behaviours and the shape of their Δ curves depended on the nature of the guest species inside the LOF cavities (**Figure 4.25 b**). In particular, the Δ curves of **Eu@IM** and **Eu@THF** showed a quite similar temperature dependence as well as that of **Eu@DMF** and **Eu@CHCl₃**. Conversely, **Eu@PY** showed a different behaviour compared to the other four compounds.

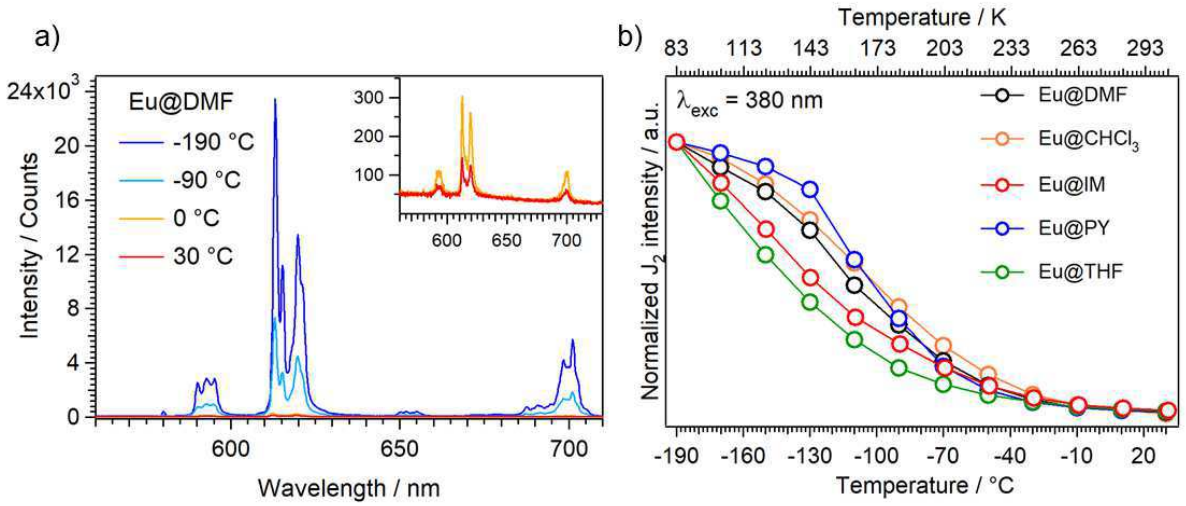

Figure 4.25: a) Emission spectra of **Eu@DMF** recorded at -190, -90, 0, and 30 °C. **b)** Temperature-dependent integrated intensity of Eu^{3+} $^5D_0 \rightarrow {}^7F_2$ transition normalized at -190 °C in **Eu@DMF**, **Eu@CHCl₃**, **Eu@IM**, **Eu@PY**, and **Eu@THF**.

The relative thermal sensitivity parameter (S_r, see **Chapter 1**) is used to compare the thermometric properties of Eu^{3+} compounds (**Figure 4.26**). As discussed in **Chapter 2**, $S_r \geq 1$ (grey line in **Figure 4.26**) was used as quality criterion to determine the applicative temperature range of the compounds. All the specimens displayed an overall good thermometric response over a wide temperature range, but two different behaviours were highlighted. The first concerns the **Eu@IM** and **Eu@THF** samples which presented $S_r \geq 1$ in all the studied temperature range. The

second behaviour is shown by the **Eu@DMF**, **Eu@CHCl$_3$**, and **Eu@PY** samples. In this case, S_r is higher than 1 only a T > -130 °C, but higher S_r maximum values (4.5 or 3.2 % °C^{-1}) were reached than in the previous two samples. In particular, **Eu@PY** was found to be the complex with the narrower operative temperature range (from -130 to 10 °C).

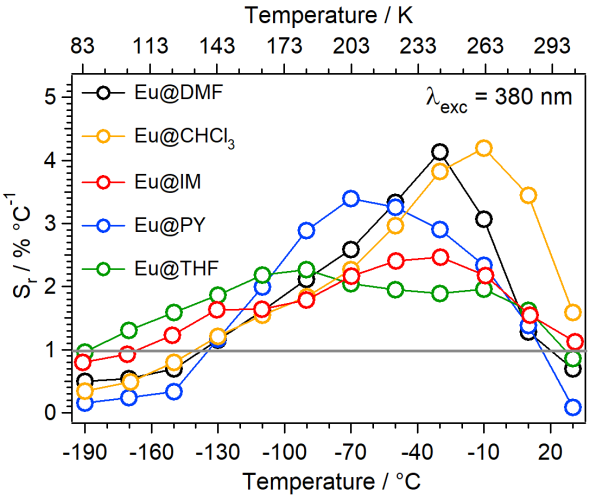

Figure 4.26: Relative thermal sensitivity (S_r) of **Eu@DMF**, **Eu@CHCl$_3$**, **Eu@IM**, **Eu@PY**, and **Eu@THF** in the -190/ 30 °C temperature range.

Moreover, it can be observed that the nature of the guest molecules not only influenced the applicative temperature range of these systems, but also the S_r maximum value and the corresponding temperature (**Table 4.2**).

Compound	S_r max	T (°C)
Eu@DMF	4.2	-30
Eu@CHCl$_3$	4.2	-10
Eu@IM	2.5	-30
Eu@PY	3.3	-70
Eu@THF	2.5	-90

Table 4.2: S_r maximum value and its corresponding temperature for the Eu^{3+}-LOFs.

Thermal and photochemical stabilities are two important parameters to be evaluated since stable compounds have longer applicative service life. Moreover, in this case,

since Δ is the integrated intensity of the $^5D_0 \rightarrow {}^7F_2$ transition (no reference transitions are used) all the phenomena that can modulate the intensity of Eu^{3+} emission, excluding temperature, are potential sources of error. To evaluate the reliability of our experimental setup, three heating/ freezing cycles were performed. All the complexes showed a good reproducibility (**Figure 4.27**), indicating that all the studied Eu-LOFs were thermally stable and that they do not suffer photochemical decomposition in these experimental conditions.

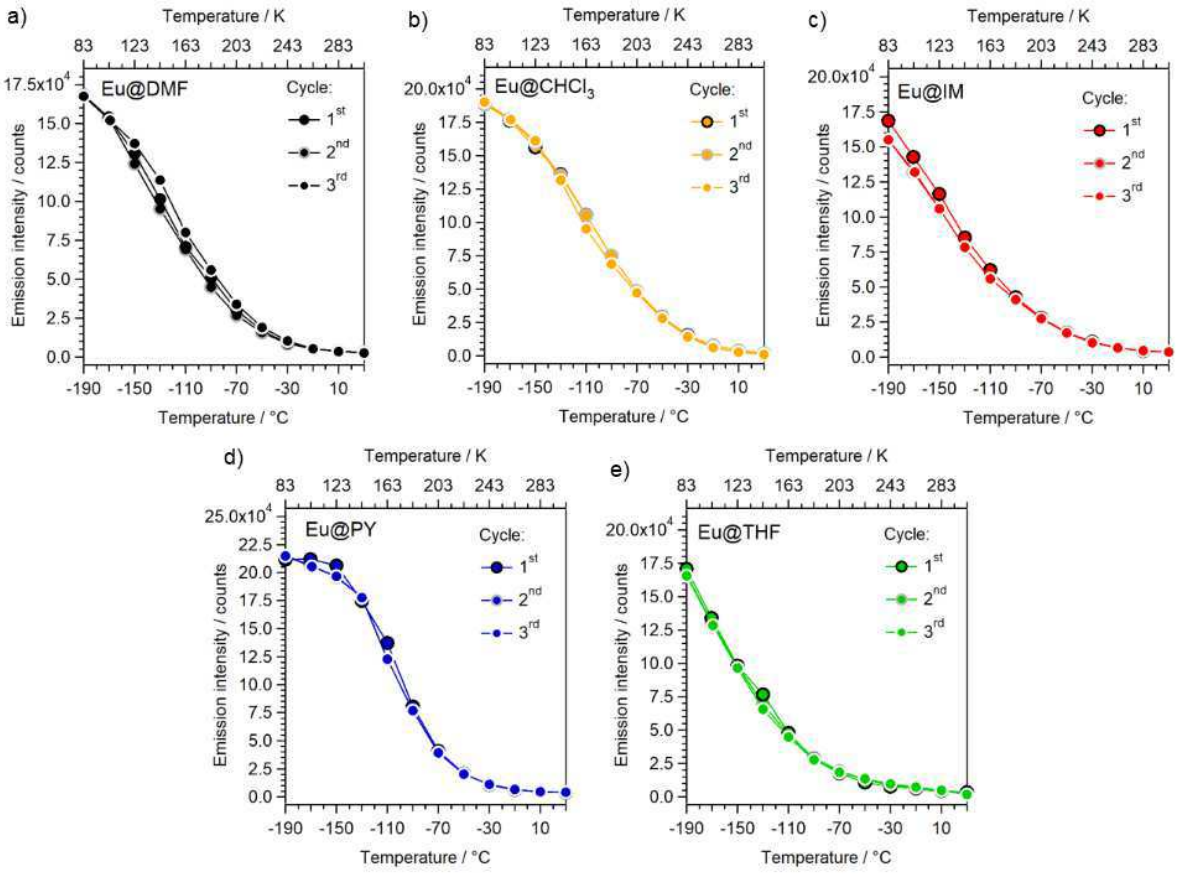

Figure 4.27: Eu^{3+} J_2 emission intensity variations in three thermal cycles for the compounds **a) Eu@DMF**, **b) Eu@CHCl$_3$**, **c) Eu@IM**, **d) Eu@PY**, and **e) Eu@THF**.

The Mott-Seitz equation (MS)[124,125] (see **Appendix 1** for further details) can be used to fit the experimental data to determine the number of non-radiative deactivation pathways which contribute to the modulation of the LOFs luminescent properties with temperature:

$$\Delta = \Delta_0 \frac{1}{1+\sum_{i=1}^{n} \alpha_i \cdot exp\left(\frac{-\Delta E_i}{k_b \cdot T}\right)} \quad (4.5)$$

Δ_0 is the extrapolated value of the thermometric parameter at 0 K, ΔE_i the energy required for the activation of i-th non-radiative deactivation pathways, α_i the ratio between the non-radiative and radiative deactivation probabilities of the considered deactivation channel, k_b the Boltzmann constant, and T the absolute temperature. As already said in previous chapters, depending on the values of ΔE_i and α_i the MS equation generates S-shaped or linear curves.[80,126,127]

When the energy gap between the ligand triplet level and Eu^{3+} $^5D_0$ emissive level ($\Delta E_{T\text{-}Ln}$) is lower than 1,800 cm^{-1}, metal-to-ligand back energy transfer processes (BEnT) is the most important deactivation mechanism.[127] In our case, the $\Delta E_{T\text{-}Ln}$ value is about 350 cm^{-1} for all the samples but considering only one term in the MS equation, the obtained curves do not well fit the experimental data. Conversely, by introducing two deactivation channels good fitting curves were obtained (see **Figure 4.28** as example). The values of the two activation energies (ΔE_1 and ΔE_2) and the corresponding probability factors (α_1 and α_2) are listed in **Table 4.3**.

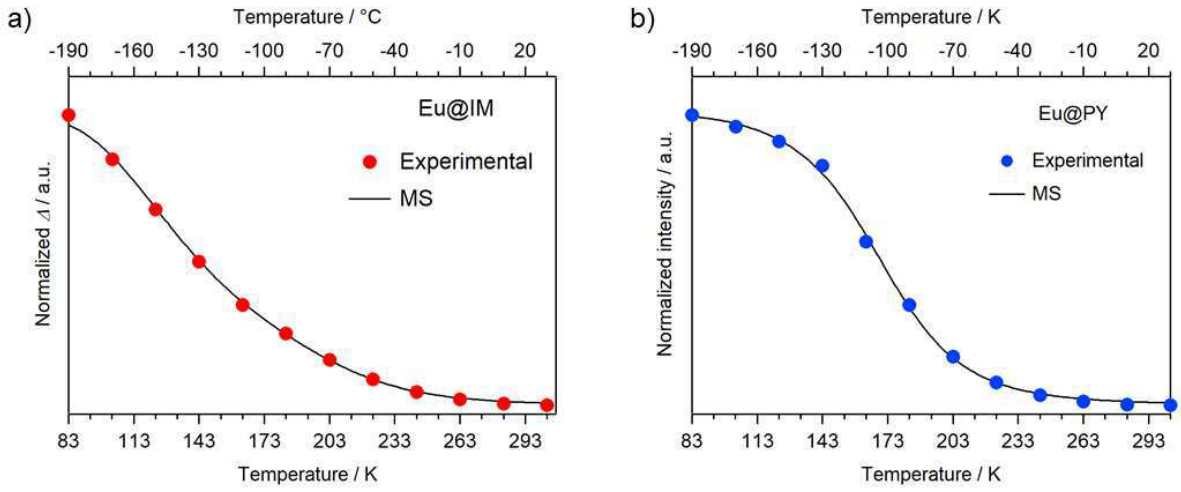

Figure 4.28: Examples of two Mott-Seitz fitting curves for samples **a) Eu@IM** and **b) Eu@PY**. The full circles represent the experimental data.

Compound	ΔE_1 (cm^{-1})	α_1	ΔE_2 (cm^{-1})	α_2	R^2
Eu@DMF	503 ± 55	81	1,731 ± 300	$4.6 \cdot 10^5$	0.999
Eu@CHCl$_3$	506 ± 40	67	1,884 ± 300	$7.2 \cdot 10^5$	0.999
Eu@IM	458 ± 30	100	1,857 ± 300	$8.1 \cdot 10^5$	0.999
Eu@PY	472 ± 80	22	1,426 ± 200	$1.1 \cdot 10^5$	0.999
Eu@THF	465 ± 40	159	1,625 ± 600	$3.3 \cdot 10^5$	0.998

Table 4.3: Calculated ΔE_n and α_n values (n=1 and 2) and coefficient of determination (R^2) for the Eu^{3+}-LOFs.

The activation energies of the first deactivation pathway (ΔE_1) in the resulting MS equation is close to the experimental $\Delta E_{T\text{-}Ln}$ value of 350 cm^{-1} in all the sample and it can be associated to the energy required for the activation of metal-to-ligand BEnT processes. The second deactivation channel could be related to ligand-to-metal charge transfer (LMCT) processes or to multiphonon relaxation.

According to the experimental data however, efficient LMCT processes can be invoked only for **Eu@IM** whose LMCT transition has an activation energy of 2,260 cm^{-1} similar to the ΔE_2 value of the MS equation (1,857 ± 300 cm^{-1}). In the case of compounds **Eu@DMF** and **Eu@PY**, in which no LMCT are present, or **Eu@CHCl$_3$** and **Eu@THF**, with high energy LMCT states (4,900 and 5,900 cm^{-1} respectively), this kind of process can not be the second deactivation channel.

As concerns the multiphonon relaxation, the considered energy gap ($\Delta E_{vib\text{-}Eu}$) is that between the 4th harmonic of the highest energy oscillator[26,133] (generally -OH groups) and 12,230 cm^{-1}, which corresponds to the energy difference between Eu^{3+} $^5D_0$ and $^7F_6$ energy levels (see **Figure 4.29** for clarity).[8]

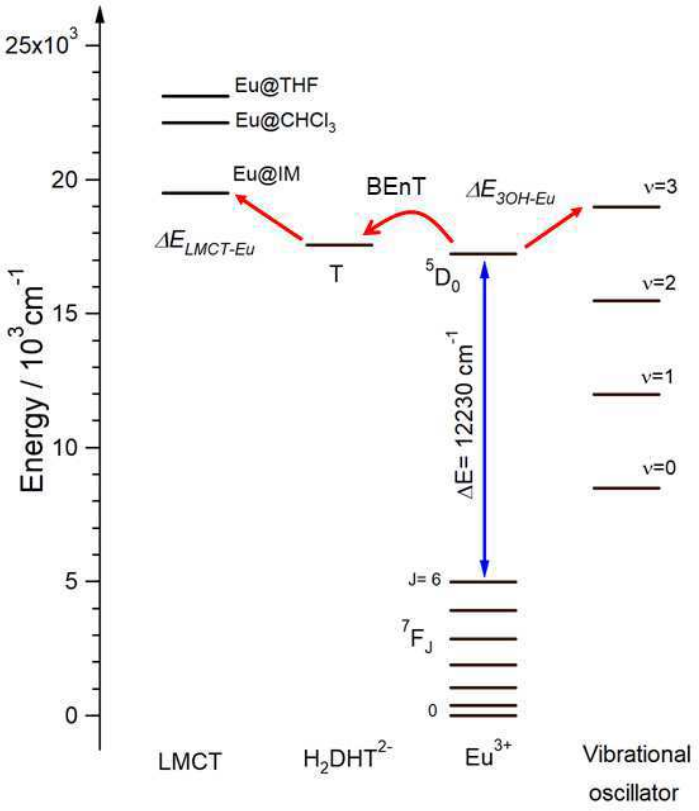

Figure 4.29: Partial energy diagram of the ligand and Eu(III) including the energy of the LMCT states and the harmonics of the stretching of the -OH stretching.

In our Eu^{3+}-LOFs the -OH stretching (νOH) is between 3,250 and 3,650 cm^{-1}. The shape of the -OH stretching depends on the nature of the compounds (see IR spectra in **Figure 4.30**). This stretching can be attributed to europium-coordinated water molecules (in **Eu@IM** and **Eu@PY**) and/or to the -OH groups of the H_2DHT^{2-} ligand that are spatially close to the Eu^{3+} centers for steric constrains as highlighted from the crystallographic data of **Eu@DMF**, **Eu@CHCl₃**, and **Eu@IM** ($d_{Eu\text{-}OH} < 5$ Å).

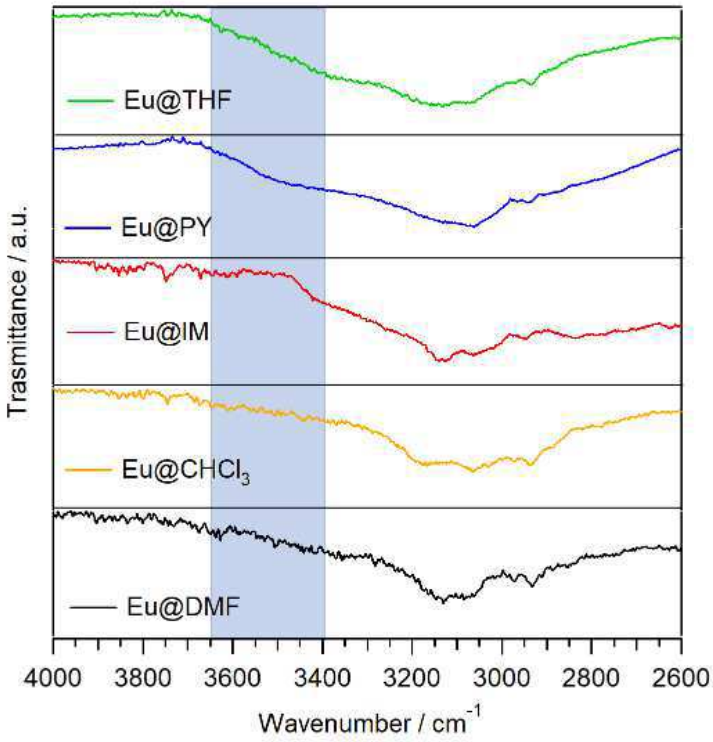

Figure 4.30: Infrared spectrum of compound **Eu@DMF** (black), **Eu@CHCl₃** (orange), **Eu@IM** (red), **Eu@PY** (blue), and **Eu@THF** (green) in the 4,000 – 2,600 cm^{-1} spectral region. The blue zone indicates the usual region of -OH stretching in phenols.

The proper determination of the -OH stretching frequency from experimental IR spectra is difficult due to the low intensity and the broadening of the bands as often occurs when -OH groups are not isolated.[207,208] However, considering the highest -OH stretching wavenumbers in the region between 3,400 and 3,650 cm^{-1}, the energy difference between the 4th -OH harmonic and the Eu^{3+} $^5D_0$ - $^7F_6$ energy gap ($\Delta E_{3OH\text{-}Eu}$) varies between 1,500 – 2,000 cm^{-1}. These values match quite well the activation energies for the multiphonon relaxation determined with the Mott-Seitz equation (**Table 4.3**).[209]

The differences in the ΔE_2 value of the MS equation and in the IR spectra of the europium LOFs can be explained considering that the introduction of different guest molecules in the LOF structure, and the consequent structural distortion, provides two possible modifications that influence the overall -OH stretching:

1. the presence of Eu^{3+}-coordinated water molecules, as in the case of **Eu@IM** and **Eu@PY**;

2. different amounts of H-bonds between the -OH groups (from coordinated water or the H_2DHT^{2-} ligand) and the guest molecules which have N- or O-sites and different polarity.

This study highlights the importance to understand and rationalize the correlations between the molecular fragments and the compounds functional response (thermometry in this case).

In the studied Eu^{3+}-LOFs for example, the metal-to-ligand back-energy transfer is the predominant mechanism which determines the temperature-dependent luminescent properties of the compounds. Indeed, since the energy gap between the ligand triplet level and Eu^{3+} $^5D_0$ level is small and almost constant ($\approx$ 350 cm^{-1}), all the Eu^{3+}-MOFs present good thermometric properties in the cryogenic up to room temperature range. Conversely, the differences in the S_r curves are related to the introduction of the different guest molecules and the consequent structural modification of the Eu^{3+}-LOFs associated to different multiphonon relaxation.

Comparing the thermometric properties of these Eu^{3+}-LOFs and that of the Eu^{3+} dinuclear compounds reported in **Chapter 2**, it is possible to see how the energy gap between the ligand triplet level and Eu^{3+} $^5D_0$ emissive level ($\Delta E_{T\text{-}Ln}$) influences the overall thermometric behaviour of the system: a good thermometric response at cryogenic temperatures is present in the Eu^{3+}-LOFs where the $\Delta E_{T\text{-}Ln}$ energy gap is small ($<$ 1,800 cm^{-1}) while in the Eu^{3+} dinuclear complexes a good thermometric response is achieved beyond room temperature since the high $\Delta E_{T\text{-}Ln}$ energy gaps ($\approx$ 3,000 cm^{-1}).

4.3. Conclusion

The synthesis of the Eu^{3+}-LOF $\{[Eu_2(H_2DHT)_3(DMF)_4]\cdot 2DMF\}_n$ (**Eu@DMF**) has been optimized: the desired compound was obtained in very high yield and in crystalline form. The compound presented europium dinuclear units linked together by H_2DHT^{2-} ligands forming a 3D-structure characterized by channels with square-like section. Four examples of post-synthesis modification of **Eu@DMF** have been investigated by substituting DMF molecules with $CHCl_3$, Im, Py, and THF. The substitution of DMF molecules occurred in different measures: only DMF molecules in the LOF channels were substituted using $CHCl_3$ and THF, while Im and Py also coordinated DMF molecules. In the case of the **Eu@CHCl$_3$** and **Eu@IM** derivatives, whose structure was solved, a structural modification in the Eu-MOF architecture due to the substitution of the DMF molecules was highlighted.

Concerning the emission properties, the europium compounds were characterized by weak emission at room temperature because of the low triplet energy of the H_2DHT^{2-} ligand. As concerns the thermometric studies, the Eu^{3+}-LOFs can be used as luminescent molecular thermometers in a wide temperature range, between -190 and 30 °C. All the complexes showed good S_r values, higher than one, in almost the whole studied temperature range, and an excellent reproducibility during three different heating cycles.

The low triplet energy of the H_2DHT^{2-} ligand sets the applicative range of these Eu^{3+}-LOFs from cryogenic up to room temperatures. Conversely, multiphonon processes cause the modulation of the resulting thermometric response of these compounds. Indeed, the structural modifications induced by the different guest molecules and their different basicity are effective in the modulation of the -OH stretching which is the highest energy oscillator involved in the multiphonon processes. In the case of **Eu@IM**, the temperature-dependent luminescent properties modulation could be also related to low-energy LMCT states.

Possible developments of this research field concern the possibility to introduce new functionalities in the studied Eu^{3+}-LOFs by exploiting the presence of the unreacted -OH groups of the H_2DHT^{2-} ligand. For example, these sites could be functionalized through the grafting reaction with different metal complexes (e.g. alkyls, alkoxides, or carbamato derivatives) introducing different metal centers with luminescent (e.g. Tb^{3+}), magnetic (Dy^{3+}, Mn^{2+}, Co^{2+}), or catalytic properties (Ti^{4+}) in order to create a multifunctional material.

As concerns the thermometric behaviour, it could be interesting to study how different functionalizations of the residual -OH groups influence the thermometric properties of the system. In this case, the ligand phenolic groups could be functionalized both with metal centers and organic fragments (e.g. acetyl groups). In the first case, different metal centers can modulate the overall luminescent properties of the LOF affecting the sensitization efficiency of the emissive states of the Eu^{3+} ion. Moreover, the use of a second luminescent metal center would allow the possibility to develop a ratiometric thermometer. In the second case, the modulation would be due to the organic fragment which alters the energy of the ligand triplet level. In this way, two possible modulation can be performed:

- create compounds with different luminescent and thermometric properties due to different substituents on the phenolic -OH group,
- modulate the compound properties by adjusting the functionalization degree of the -OH groups thus creating a series of compounds in which the organic ligand is gradually functionalized and modulating the properties of the resulting species.

5. Silica surface functionalization

5.1. Introduction

5.1.1. Materials functionalization

Surface functionalization through direct molecules bonding is a recurrent way for providing new chemical, physical, or electronic properties to a material leading to an improvement of the material itself.[210–213] For example, in (bio)chemical sensing the immobilization of the sensor system on a solid surface implies the transition from solution to the solid state which offers a convenient way to couple the sensing systems to the macroscopic worlds through read-out functions. Furthermore, immobilized sensors usually have faster response times, are easier to handle, and can be recycled. For this reason, functionalized materials are often used for the detection of different analytes[214–217] like metal ions, gases, or (bio)molecules.

Moreover, the integration of organic molecules into semiconductor-based materials and devices has a substantial impact on numerous applications, such as micro and optoelectronics, microelectromechanical machines, memory chips, Si-based biological sensors, and in the development of microelectronic computing.[29,31] For example, organic field-effect transistors (OFETs) consist in a thin-film transistor where a semiconductor π-conjugated aromatic molecule is deposited on top of the dielectric.[30]

Also lanthanoid ions have been extensively used in surface functionalization to better exploit their peculiar luminescent properties, as demonstrated by the wide literature on the topic.[36,218–220] For example, Rodrigues and co-workers recently reported a thermometric sensor based on a functionalized silicon surface. After the silicon activation with ozone, the surface was functionalized with (3-aminopropyl)triethoxysilane (APTES) and subsequently with polyethylene glycol chains bearing β-ketoester groups (acacPEGA) used as covalent sites for the coordination of lanthanoid dipicolinate (DPA) complexes (**Figure 5.1**).[221]

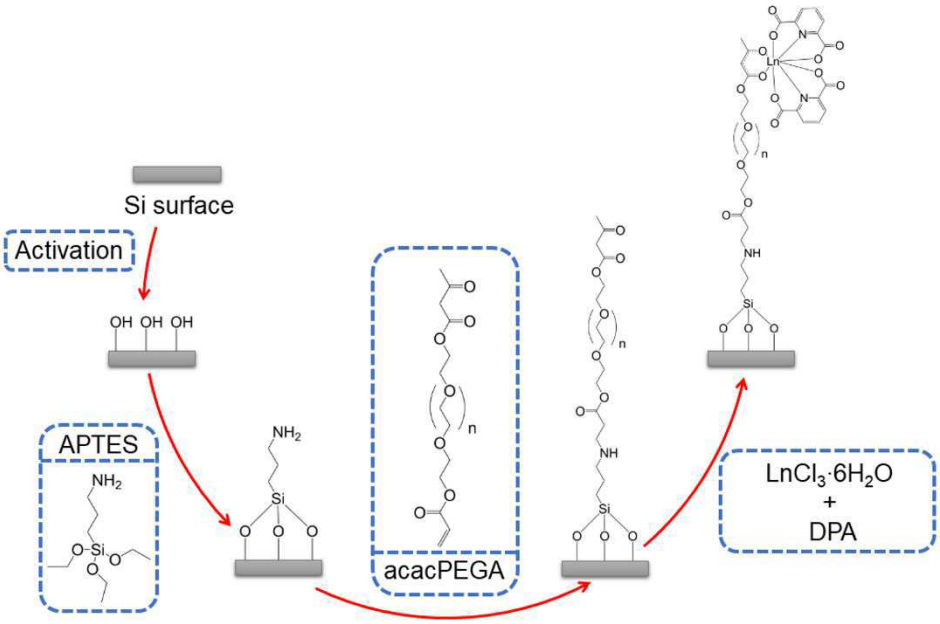

Figure 5.1: Schematic representation of the Si surface showing the activation step, the functionalization with APTES, the reaction with the PEGA polymer and the formation of the Ln^{3+} complexes. Adapted from ref. [221].

Given the importance of functional surfaces, we aimed at developing a suitable synthetic procedure for material functionalization. Starting from an inorganic substrate, our goal was to create a luminescent material by exploiting the peculiar emission properties of lanthanoid ions.

Different methodologies for the creation of functionalized materials can be employed. Four of the most widely used are: 1) the *adsorption,* 2) the *physical entrapment*, 3) the *covalent attachment*, and 4) the *smart-grafting* methods.[222] Each method has advantages and disadvantages that will be briefly discussed below.

1. The a*dsorption* method is the simplest one and it involves the physical binding of the metal complex on the surface of an inert inorganic or organic support through weak interactions such as van der Waals forces and hydrogen bonds. In this method, the support matrix and a solution containing the metal complex are left in contact until solvent removal creating a dispersion of the metal complex on the support material. This method is not convenient if the final material has to be in contact with liquids since the adsorbed complex can

be easily removed by minor changes in pH, ionic strength or temperature of the liquid medium.

2. The *physical entrapment* method is based on the "build a bottle around the ship" concept. In this case the metal complex is dissolved in a solution containing the building-blocks which will constitute the final supporting material (e.g. the oligomer of an organic polymer, nanoparticles, surfactants, etc.). After the formation of the support matrix (e.g. polymerization process, aggregation of nanoparticles, micelles formation, etc.), the metal complex is entrapped in the matrix structure. In this case, it is important that the metal complex is stable in the reaction condition used for the support formation.[148] For example, Wang and co-workers dissolved a luminescent Eu^{3+} β-diketonate complex $[Eu(BDBM)_3]$ in an acetone solution containing octyltrimethoxysilane (OTS) nanoparticles. Adding the solution to distilled water, the OTS nanoparticles change their morphology entrapping the Eu^{3+} complex within them (**Figure 5.2**).[223]

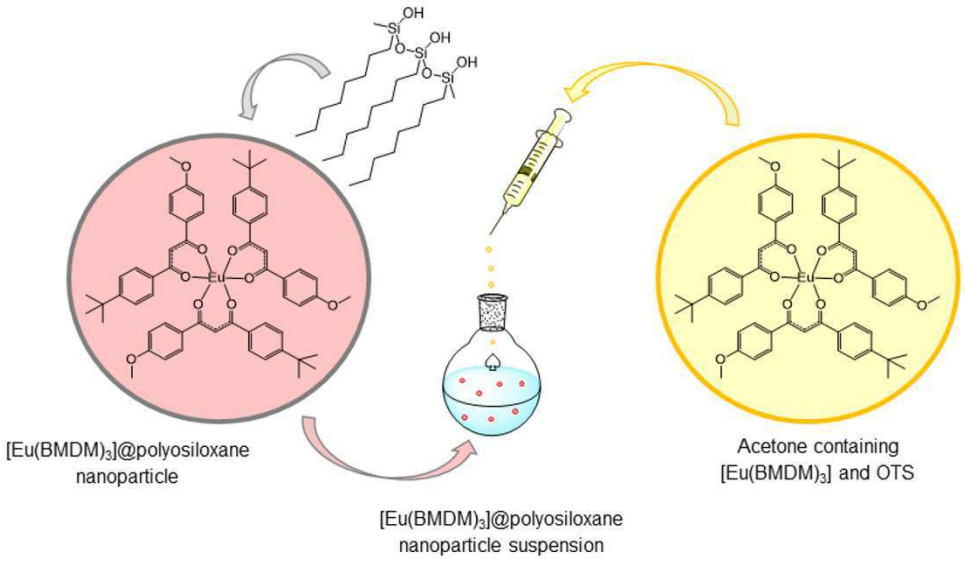

Figure 5.2: Schematic illustration of the synthesis $[Eu(BMDM)_3]$@polysiloxane nanoparticles. Readapted from ref [223].

3. The *covalent attachment method* is probably the most popular method for the creation of a functionalized material. In this case the metal complex is

covalently bound to the organic/ inorganic support through a linker (or "tether"). This method presents the advantage to be based on strong covalent bonds between the support, the linker, and the metal complex thus creating robust materials. In this case, the support matrix must be subjected to different chemical reactions for the creation of the tether linker. **Figure 5.1** reported an example of covalent attachment. In this case, three synthetic steps are required for the tether formation: the surface activation and the two sequential treatment with APTES and acacPEGA.

4. Although not used for the preparation of luminescent materials, the *smart-grafting* functionalization method is very popular for the synthesis of heterogeneous catalysts.[224,225] In this method, the acid functional groups of the support matrix (e.g. -OH in inorganic matrices or -COOH in organic polymers) are exploited to form a polar covalent metal–oxygen bond between the metal center and the support matrix without previous functionalization of the support, as it occurs in the covalent attachment.[224–226] In this case, it is necessary that the metal complex has one or more ligands able to react through an acid/ base reaction with the reactive sites of the support matrix. For this reason, metal complexes bearing strong base ligands like metallo-alkyl (R^-),[224] metal alkoxides (RO^-),[224] and metal amide (R_2N^-)[225,226] are good metal precursors in this functionalization procedure.

   The grafting reaction usually involves only a fraction of the total ligands so that the unreacted ones can be subsequently substituted by treating the material with different protic reagents bearing the desired functionality. This functionalization procedure, also called *smart grafting* through *sequential approach*, can be schemed as follows (**Figure 5.3**):

   - synthesis of the organometallic complex of the metal (M) and a first ligand (L1);

- complex anchorage on the matrix surface with partial substitution of L1 ligands;
- substitution of the residual L1 ligands with an appropriate L2 ligand depending on the final goal.

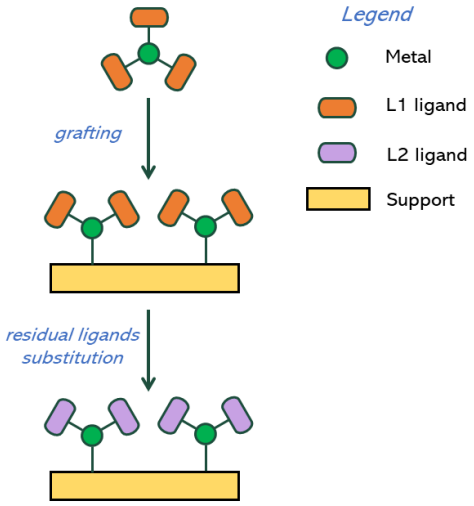

Figure 5.3: Schematization of the sequential approach smart-grafting procedure. Readapted from ref. [225].

My research group have a solid experience and know-how in the development of functional materials using the *smart-grafting* procedure, especially for catalytic purposes.[227,228] Over last years, however, we moved our interest to the possibility to use the *smart-grafting* procedure for the creation of luminescent materials based on lanthanoid ions.[229,230] For this aim, lanthanoid *N,N*-dialkylcarbamato complexes have been adopted as suitable metal precursors.

5.1.2. Lanthanoid *N,N*-dialkylcarbamato complexes as *smart-grafting* precursor

Besides the commonly used metallo-alkyl, metal alkoxides, and metal amide complexes, also *N,N*-dialkylcarbamato complexes can be exploited as alternative metal precursors in the *smart-grafting* procedure. *N,N*-dialkylcarbamato ligands, $[O_2CNR_2]^-$, where R can be an alkyl or an aril group, are anionic ligands produced by

the interaction of carbon dioxide and an amine according to the following equilibrium:[231]

$$2HNR_2 + CO_2 \rightleftharpoons [H_2NR_2][O_2CNR_2] \quad (\mathbf{5.1})$$

This equilibrium is strongly influenced by the amine nature: for dibutylamine or dibenzylamine, for example, it is quantitatively right-shifted, while for diisopropylamine only about the 15% of dialkylammonium dialkylcarbamate is formed.[232–234] The consolidated synthetic procedure of metallic *N,N*-dialkylcarbamato complexes consists in the reaction between anhydrous metal halides (MX_n), amine and CO_2 in anhydrous organic medium:[235–238]

$$MX_n + nCO_2 + 2nHNR_2 \longrightarrow [M(O_2CNR_2)_n] + nR_2NH_2X \quad (\mathbf{5.2})$$

In this reaction, the halide anion is substituted in the metal coordination sphere by the dialkylammonium dialkylcarbamato salt formed *"in situ"*. The equilibrium of this reaction is completely shifted towards the products by the formation of the R_2NH_2X salt which is insoluble in common hydrocarbon solvents. The two products can be easily separated through filtration since the metal carbamato complex is generally soluble in an amine excess due to the presence of equilibria that generate ionic species with lower nuclearities than the neutral complexes as reported in (**5.3**).

$$y/m[M(O_2CNR_2)_n] + 2xHNR_2 + xCO_2 \rightleftharpoons [R_2NH_2]_x[M_y(O_2CNR_2)]_{(ny+x)} \quad (\mathbf{5.3})$$

Numerous synthesis of $[M(O_2CNR_2)_n]$ homoleptic complexes are reported in the literature both for *p* elements and *d* transition metals.[231] First lanthanoid *N,N*-dialkylcarbamato derivatives have been synthetized through the reaction of anhydrous ytterbium (III) and erbium (III) trichlorides[239,240] with the system HN^iPr_2 /CO_2 in hydrocarbon solvent:

$$4LnCl_3 + 24HN^iPr_2 + 12CO_2 \rightarrow [Ln_4(O_2CN^iPr_2)_{12}] + 2^iPr_2NH_2Cl \quad \textbf{(5.4)}$$

(Ln= Er, and Yb)

For some early lanthanoid ions, an ethereal adduct of the halide salt is necessary probably because of its higher reactivity due to a lower nuclearity compared to the extended structure of the anhydrous halide. Starting from $LnCl_3 \cdot DME_2$, HN^iPr_2, and CO_2 a series of isostructural $[Ln_4(O_2CN^iPr_2)_{12}]$ derivatives has been prepared also for Pr^{3+}, Nd^{3+}, Eu^{3+}, Gd^{3+}, Ho^{3+}, and Lu^{3+} ions.[235]

These syntheses are performed in strictly anhydrous conditions to avoid the hydrolysis of the resulting *N,N*-dialkylcarbamato complex. Indeed, water protons can protonate the ligand oxygen atoms. The resulting M-OH group is sufficiently acid to protonate directly or indirectly, after the formation of a M-OCO_2H group, a second carbamato ligand of a different metal centre forming a μ-oxocarbamate or a carbonate-carbamate species, depending on the nature of the metal centre, the water amount, and the type of the amine R groups (**Figure 5.4**).

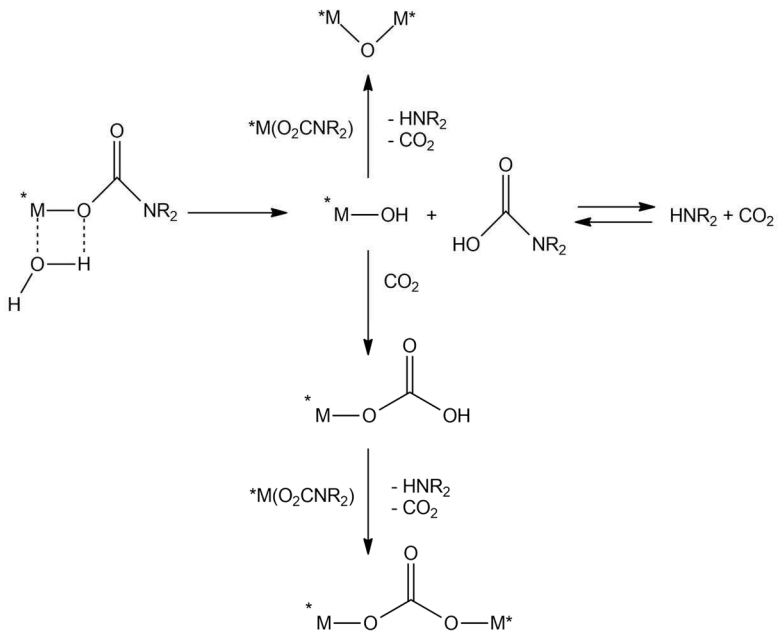

Figure 5.4: Reactivity of the carbamato ligand towards protic reagents as water.

As depicted by the systematic work of Faurholt and co-workers during the last century on the hydrolysis of dialkylammonium dialkylcarbamato species

($[R_2NH_2][O_2CNR_2]$) in aqueous medium, the hydrolysis equilibrium is strongly dependent on the amine nature:[241,242]

$$[O_2CNR_2]^- + H_2O \rightleftharpoons HNR_2 + [HCO_3]^- \quad \textbf{(5.5)}$$

Branched amines on the α carbon atom, like diisopropylamine, present an equilibrium completely shifted towards the hydrolysis product with a fast reaction rate. On the other hand, for linear amines the hydrolysis reaction is slower and less favoured.

For this reason, linear amines with a quantitative carbonatation equilibrium (eq.(**5.1**)) and lipophilic residues have been successfully used in the synthesis of *N,N*-dialkylcarbamato complexes of labile metal centers through the metal extraction from an aqueous phase to an organic one.[231] Indeed, the lipophilic nature of the dibutylamine substituents allows the preferential distribution of the formed *N,N*-dialkylcarbamato complex in the organic phase. This extraction procedure is simpler and more rapid than the anhydrous synthesis, and it has been recently optimized also for lanthanoid ions (**Figure 5.5**).[243]

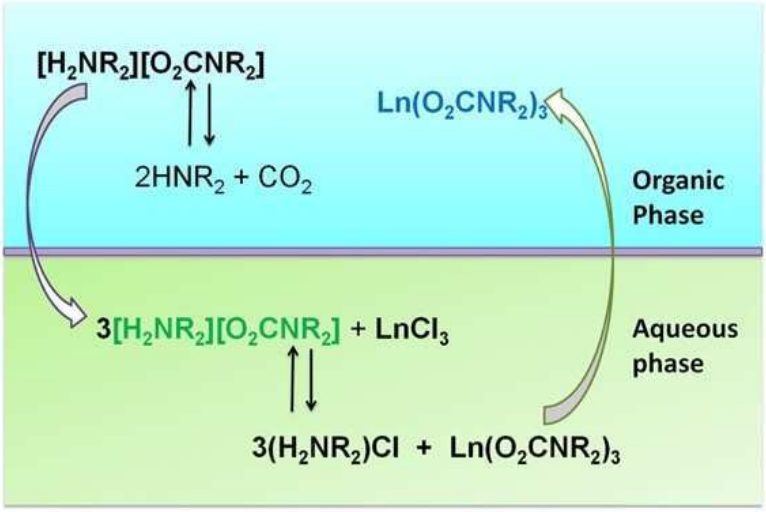

Figure 5.5: Representation of the extraction procedure for the synthesis of *N,N*-dialkylcarbamato complexes.

The resulting *N,N*-dialkylcarbamato complexes are good synthetic precursors because the carbamato ligand can be easily removed from the metal coordination sphere by Brønsted acids and protic reagents. For this reason, *N,N*-dialkylcarbamato complexes

can be used for metal centers deposition on materials with acid functionalities through the grafting procedure with the formation of a strong covalent bond between the support and the metal ion.

Commercial silica presents Si-OH groups and adsorbed water which can be removed by heating the solid at 373 K under reduced pressure.[224,244–246] Moreover, the number of silanol groups can be reduced in a very controlled way, while their complete removal can be achieved upon heating over 1273 K.[224,246] As depicted in **Figure 5.6**, there are three different type of silanol groups: (a) isolated, (b) vicinal, bonded to two different silicon atoms but close enough to give hydrogen bonding, and (c) geminal, bonded to the same silicon atom.

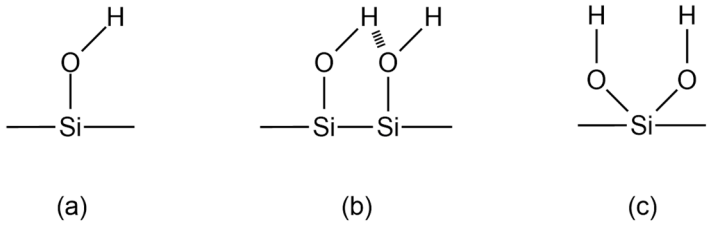

Figure 5.6: Different types of hydroxyl groups on silica surface.

Silanol groups are sufficiently acid to react with a metal carbamato complex, according to the following reaction:

$$\#SiO\text{-}H + M(O_2CNR_2)X_n \rightarrow \#SiO\text{-}MX_n + CO_2 + HNR_2 \quad (\mathbf{5.6})$$

where # represent the silica surface

Reactions of this type have been largely studied for the synthesis of transition metal-based catalyst such as Pd(II), Pt(II), Nb(III and V), Ta(V), and Au(I).[227,228,247,248] Conversely, this type of reactivity was not exploited for the preparation of luminescent materials.

Recently, we observed that the deposition of $[Tb(O_2CNBu_2)_3]$ on pre-treated commercial silica led to a homogeneous distribution of the metal on the silica surface with the evolution of CO_2 corresponding to a CO_2/Tb molar ratio of about one. This

means that, after the grafting reaction, two residual carbamato ligands are still coordinated to the lanthanoid ion. The further substitution of these ligands with the protic reagent 1,3-diphenylpropane-1,3-dione (dibenzoylmethane, Hdbm, **Figure 5.7**) affords a silica sample with interesting optical properties characterized by the typical Tb(III) green emission.[229]

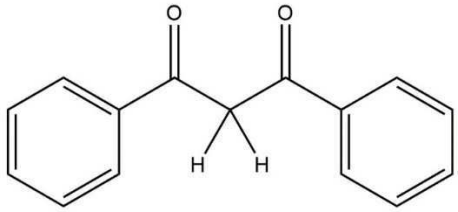

Figure 5.7: The β–diketonate ligand 1,3-diphenylpropane-1,3-dione

In the same work, we showed that starting from a mixture of $[Eu(O_2CNBu_2)_3]$, $[Tb(O_2CNBu_2)_3]$, and $[Tm(O_2CNBu_2)_3]$ derivatives in a 1:1:1 molar ratio it is possible to graft multiple metals on silica in a single step. EDX analysis on the resulting material showed that the relative amount of the three metals was maintained on silica after the grafting reaction.

Moreover, we also showed the possibility to introduce in the coordination sphere of the grafted lanthanoid ion an additional multidentate neutral ligand in case of availability of coordination sites. For example, by choosing a chiral heteroaromatic ligand like the two enantiomers of 2,6-bis(isopropyl-2-oxazolin-2-yl)pyridine (PyBox), a silica with grafted europium centers featuring highly circularly polarized luminescence was obtained (**Figure 5.8**).[230]

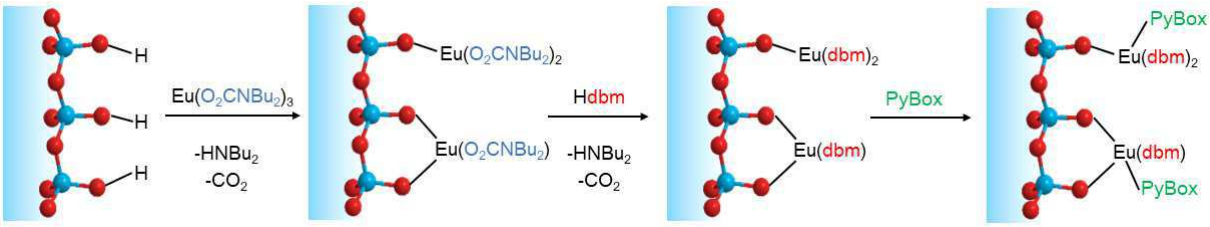

Figure 5.8: $[Eu(O_2CNBu_2)_3]$ grafting sketch of to a surface followed by further functionalizations: reaction with Hdbm and addition of PyBox. Adapted from ref. [230].

These results highlighted that the controlled step-by-step introduction of suitable ligands in the coordination sphere of an initially grafted metal center is a powerful and general route to prepare multifunctional materials. However, it is worth to note the lack of suitable methods for the structural characterization of these functionalized materials derived from the amorphous nature of the inorganic support.

5.1.3. Topic outline

To further improve this functionalization method, we explored the *smart-grafting* as possible synthetic protocol for the synthesis of sequence-dependent materials through surface functionalization of inorganic silica. As defined by Popp and Yaghi, sequence-dependent materials (SDMs) are a class of compounds characterized by a position dependent molecular formula.[249] To better understand the concept, the reader should think of natural biopolymers such as DNA, RNA, or proteins. For example, DNA is made up of four nucleotides each of which has a specific distribution along the double helix. In this case, not only the molecular formula of the DNA changes along its length, but different sequences of nucleotides are carriers of specific informations. The concept of SDM is similar: an artificial material based on the spatial repetition of different building blocks (e.g. metal complexes) where different units provide different properties to the systems or work synergistically generating new features not achievable by the individual building blocks. For this reason, these materials are particularly attractive, for example in catalysis where they could be used as multi-sites catalysts.[250] However, the synthesis of a SDM is not straightforward since the

introduction of complexity within the material is often associated to the loss of synthetic control. Moreover, SDM materials are often challenging to characterize since their intrinsic high complexity is often associated to a non-crystalline nature.[251]

An interesting example of synthesis and characterization of a SDM has been reported by Vairaprakash and co-workers who built a series of heterometallic chains based on Ru, Rh, and Pt through the progressive functionalization of a Merrifield's resin with tyrosine fragments functionalized with a chelate terpyridine.[250] The soluble tyrosine-terpyridine moiety is metallated with one of the three metal ions and then sequentially grafted on the pre-functionalized polymeric resin forming an ordered polymetallic chain (**Figure 5.9**). Cleaving the Merrifield's resin after each step, the authors were able to confirm the formation of the desired sequence through MALDI-TOF mass spectrometry.

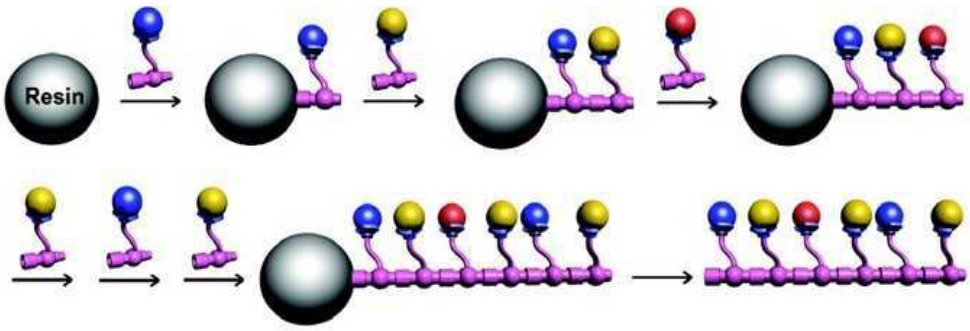

Figure 5.9: Synthetic scheme of the heterometallic chain developed by Vairaprakash. Published in ref [250]. Copyright © 2010 American Chemical Society.

Some different works are reported in literature describing the synthesis of 3*d*-metals sequence dependent materials[252–254] while, to the best of our knowledge, examples of lanthanoid-based SDMs are absent probably for the labile coordination chemistry of these metals characterized also by high coordination numbers.

Silica surface, or more generally inorganic materials surface, can be used as support for the creation of lanthanoid-based sequence dependent materials through the smart-grafting procedure following the following steps:

1. grafting of a first lanthanoid carbamate complex ($[RE_1(O_2CNBu_2)_3]$) on silica;
2. substitution of the residual carbamato moieties with a rigid divergent ligand with acidic functionalities;
3. grafting of a second metal complex ($[RE_2(O_2CNBu_2)_3]$). which can react with the residual acidic functionalities of the organic spacer.

Iteration of steps "2" and "3" leads to lengthen the sequence at will, as reported in **Figure 5.10**.

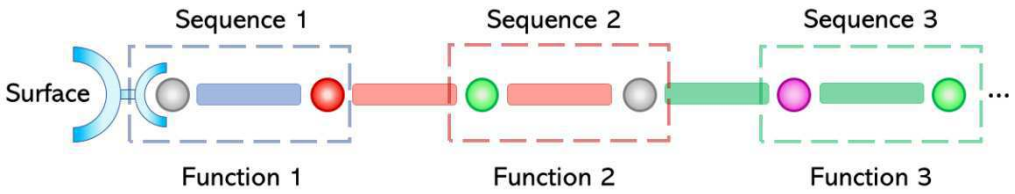

Figure 5.10: Sketch of a Sequence-Dependent Material grown on the surface of a suitable support by stepwise reaction of different building blocks endowed with different functionalities. To different colours correspond different metals/ spacer ligands.

We investigated the possibility to build an ordered heterobimetallic sequence (RE_1–Spacer–RE_2, "sequence 1" in **Figure 5.10**) endowed with luminescent properties on silica according the previous described synthetic procedure.

$[Eu(O_2CNBu_2)_3]$ and $[Tb(O_2CNBu_2)_3]$ carbamate complexes were chosen as metal precursors since these two ions are characterized by an intense red and green luminescence, respectively. Terephthalic acid (1,4-benzendicarboxilic acid, H_2T, **Figure 5.11**) has been chosen as spacer ligand because it is a rigid divergent ligand and it is also a good antenna ligand both for Eu^{3+} and Tb^{3+} ions. Moreover, the coordination chemistry of the H_2T ligand towards lanthanoid ions has been yet largely investigated for the synthesis of porous luminescent Eu^{3+} and Tb^{3+} based homo- and heterometallic LOFs.[138–140,255–259]

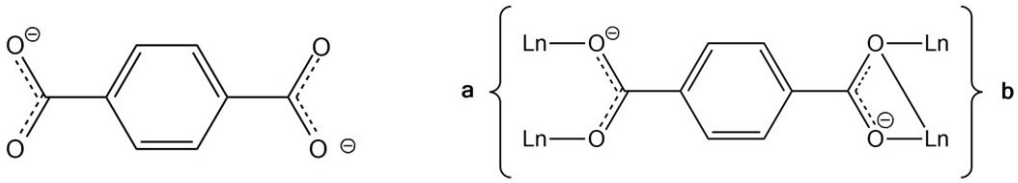

Figure 5.11: Structure of the terephthalate dianion (left) and its coordination modes (right): (**a**) bis-monodentate, and (**b**) tridentate**.**

Since maintaining the control on the arrangement of the various building blocks and characterize the functionalized surfaces is not straightforward, we exploited lanthanoid luminescent properties for the structural characterization of the resulting material. Indeed, as it will be shown, photoluminescence studies can give valuable information on the correct development of the planned synthetic sequence. In particular, Tb^{3+}-to-Eu^{3+} energy transfer can be used as molecular ruler to study the Ln^{3+} ions spatial distribution and intermetal distances which allow us to obtain data supporting the formation of the desired sequence.

5.2. Results and Discussion

Figure 5.12 (*i-iv*) reports a legend to visualize each synthetic step of the ordered heterobimetallic chain grafted on silica and to simplify the following discussion. The three synthetic steps for the creation of the heterobimetallic sequence - grafting on silica of the first carbamato derivative, substitution of the residual carbamato ligand with terephthalic acid, and grafting of the second metal complex - are summarized in the inset (***v***). The notation used to label the different samples is:

- **1RE$_1$** for a grafted metal on silica surface with residual carbamato moieties (***iii*** and ***v***),
- **2RE$_1$-TH** for a grafted metal surrounded by coordinated terephthalate ligand (***v***),
- **3RE$_1$-T-RE$_2$** for a heterobimetallic sequence where the second metal complex was reacted with the residual acidic functionalities of the organic spacer (***v***).

Below the scheme of the synthetic procedure, we report the samples that will be discussed in the text (***vi*** and ***vii***). Considering the complexity of the synthesis leading to the ordered sequence grafted on silica, we conduced preliminary studies on the solubility of terephthalic acid as well as on its reactivity towards lanthanoid carbamato complexes and free dibutylamine. (**Section 5.2.1**). Subsequently we investigated the reactivity on silica (**Section 5.2.2**) and finally we characterized the samples through photoluminescence studies (**Section 5.2.3**).

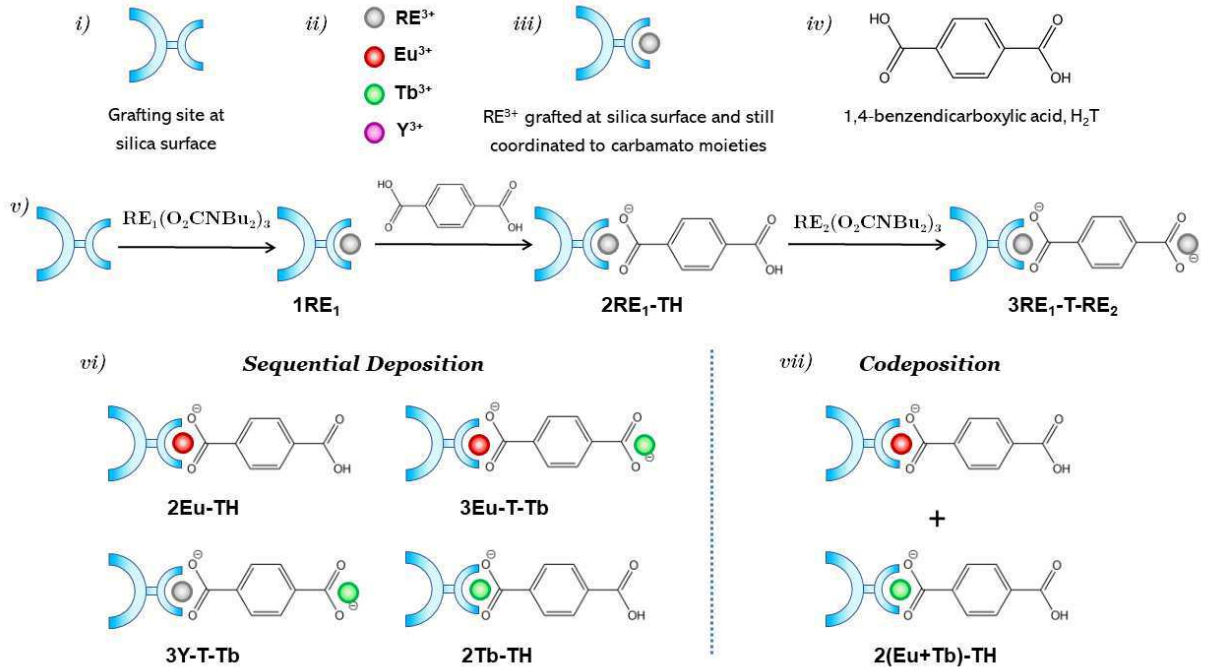

Figure 5.12: Sketch of the prepared mono and heterometallic luminescent Sequence-Dependent Materials in this work: *i-iv*) legend, *v*) general reaction scheme, *vi*) materials prepared by sequential deposition of two RE^{3+} ions interleaved with T spacers, *vii*) material obtained by simultaneous deposition of Tb^{3+} and Eu^{3+} ions. This simplified scheme reports only one terminal HT^- ligand per anchored ion.

5.2.1. Reactivity in solution

Terephthalic acid is a diprotic acid (pK_{a1}= 3.4; pK_{a2}= 4.8)[260] scarcely soluble in common organic solvents. These characteristics generate two experimental problems to be faced during the reaction conduced on the metal fragments anchored on silica (**Figure 5.12** ***v,*** step 2 and 3) such as the removal of the acid excess and the formation of reaction organic by-products. Indeed, the two pK_a values suggest that the terephthalic acid can protonate both the carbamato ligands and the resulting dibutylamine, according to the following reactions:

$$2RE(O_2CNBu_2)_{3(solv)} + 3H_2T_{(s)} \longrightarrow RE_2(T)_{3(s)} + 6HNBu_{2(l)} + 6CO_{2(g)} \quad \textbf{(5.7)}$$

$$HNBu_{2(l)} + H_2T_{(s)} \longrightarrow (H_2NBu_2)(HT)_{(s)} \quad \textbf{(5.8)}$$

$$2HNBu_{2(l)} + H_2T_{(s)} \longrightarrow (H_2NBu_2)_2(T)_{(s)} \quad \textbf{(5.9)}$$

Solubility tests showed that terephthalic acid is insoluble in most of the common organic solvents as toluene, heptane and acetonitrile, also at high temperature

because of strong intermolecular hydrogen bonds.[261] On the other hand, it is quite soluble in hot DME and soluble in DMSO and pyridine (0.6 M) at room temperature. In particular, in the literature it is reported that pyridine (Py) can break the terephthalate intermolecular hydrogen bonds forming a structurally characterized molecular adduct with composition $H_2T \cdot 2Py$.[260,262] In this adduct, the three molecules are connected through two strong N···H–O and two weak O···H–C hydrogen bonds. However, the adduct formation is a reversible process and H_2T and Py can be easily recovered from $H_2T \cdot 2Py$ under reduced pressure (10^{-2} mmHg) at room temperature. These features are desirable since Py can act as solvent for H_2T without salifying the -COOH groups during the reaction with the carbamate complex.

Conversely, dibutylammonium terephthalate salt $(H_2NBu_2)_2(T)$, equation **(5.9)**, is insoluble in pyridine and it rapidly precipitates during its formation. However, by adding to the suspension a second equivalent of H_2T and setting the dibutylamine/terephthalic acid ratio to one, a solution containing the soluble butylammonium monoacid terephthalate salt $(H_2NBu_2)(HT)$ was obtained (up to a 0.4 M solution). Single crystals suitable for X-ray analysis were obtained through slow evaporation of the solution **Figure 5.13**.

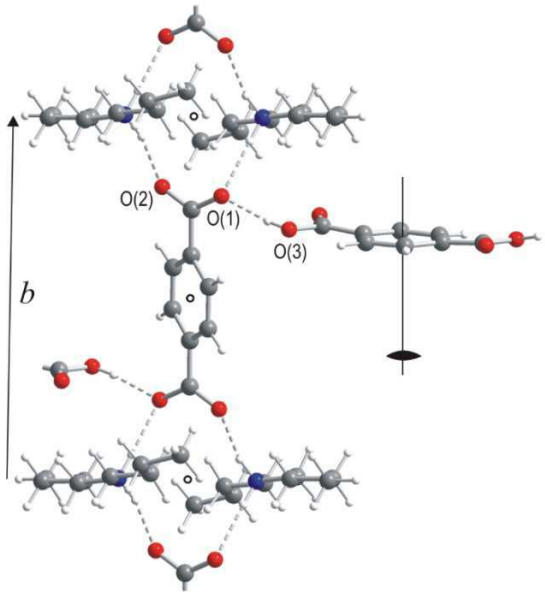

Figure 5.13: Single crystal XRD structure of the species $(H_2NBu_2)_2(T) \cdot H_2T$.

In the structure, each terephthalate dianion interacts with two dibutylammonium moieties forming a sort of double chain along the *b* crystallographic axis. Moreover, each couple of terephthalate dianions interacts with a molecule of terephthalic acid perpendicular to the chain. The salt can be described with the molecular formula $(H_2NBu_2)_2(T)\cdot H_2T$.

These results are interesting because they indicated that terephthalic acid and its butylammonium salt were soluble in pyridine leaving however residual COOH functionalities. Thinking about what might happen on silica during the reactions between the carbamato ligands and H_2T (**Figure 5.12** ***v,*** step 2 and 3), even if similar interactions are expected between pyridine and pendant COOH functionalities, they would not prevent the assembly of the RE_1–T–RE_2 sequence.

To confirm this reactivity, a reaction between $[Eu(O_2CNBu_2)_3]$ and H_2T was performed in pyridine using a H_2T/Eu^{3+} molar ratio of ten. The large excess of terephthalic acid would afford the complete substitution of the carbamato ligands and the salification of the resulting dibutylamine forming the soluble $(H_2NBu_2)(HT)$ salt instead of the insoluble $(H_2NBu_2)_2(T)$ species. The system was left under vigorous stirring at room temperature for one day. Vacuum/ dinitrogen cycles allowed to remove CO_2 shifting the reaction equilibrium towards the products and obtaining a white solid. The collected solid was washed with pyridine and dried under reduced pressure. The metal product presented a metal content in agreement with a $[Eu_2(T)(HT)_4(Py)_4]$ composition. Its ATR-IR spectrum confirms the presence of residual COOH groups as indicated by the broad band between 3,700 – 2,500 cm^{-1} ascribed to the -OH stretching, and by the -COOH stretching at 1,713 cm^{-1} and 1,692 cm^{-1} (**Figure 5.14**, red curve).

Treating the obtained compound in hot pyridine, a product with analytical composition $[Eu_2T_3(Py)_2]$ was obtained in good yields (66 %), while in the liquid phase H_2T and traces of $(H_2NBu)_2(HT)$ were detected. In this case, the IR spectrum of the obtained product is very similar to that of lanthanoid terephthalates reported

in literature:[258] the broad band of the -OH stretching disappeared as well as the -COOH stretching, while two signals ascribable to $-COO^-$ symmetric and asymmetric stretching rose up at 1,557 and 1,504 cm^{-1} respectively (**Figure 5.14**, green curve).

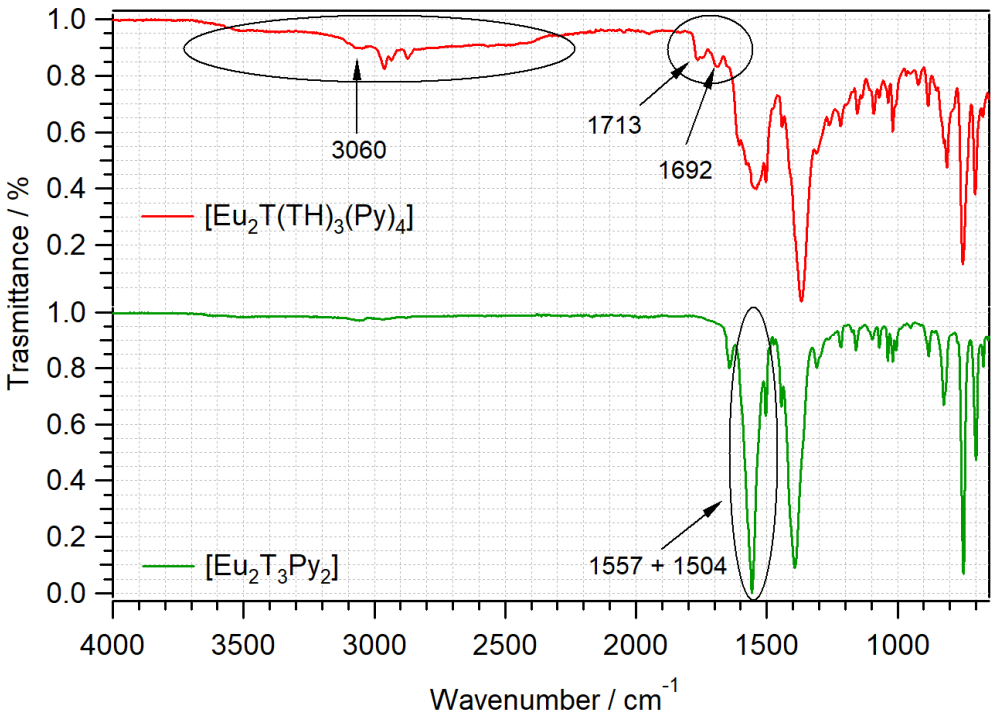

Figure 5.14: Infrared spectra of $[Eu_2T(HT)_4(Py)_4]$ (red curve) and $[Eu_2T_3Py_2]$ (green curve).

According to these studies, the formation of the three-dimensional LOF Eu_2T_3 in pyridine at room temperature is unfavoured probably for the interactions between the terephthalic acid and the solvent, while a species with residual acidic functionalities is formed. Moreover, pyridine can act as ligand which saturates the lanthanoid coordination sphere during the system evolution. Using a large excess of terephthalic acid, the easily removable $(H_2NBu_2)(HT)$ salt is also formed preventing the salification of the residual COOH groups on the metal product. These preliminary studies highlight the possibility to develop a general procedure for the creation of the ordered heterobimetallic sequence grafted on silica exploiting pyridine as reaction solvent.

5.2.2. Reactivity on silica

To help the following discussion, the synthetic scheme of **Figure 5.12** ***v*** is here reported.

The employed silica for the deposition of the metal carbamato complex is a "*crossfield*" EP17 (surface area 325 $m^2\ g^{-1}$), treated over P_4O_{10} for 24 h at 160 °C under reduced pressure (10^{-2} mmHg) to remove the physically adsorbed water. The number of silica active sites can be estimated from calcination measurements.[224] At 1,000 °C silanol groups condense together generating water and a Si-O-Si group **(5.10)** so that, from the weight loss it is possible to deduce the total number of reacted silanol:

$$2\ \text{Si-OH}_{(s)} \longrightarrow \text{Si-O-Si}_{(s)} + \text{H}_2\text{O}_{(g)} \qquad \textbf{(5.10)}$$

In our case the number of silica active sites was estimated equal to 2.02 mmol of Si-OH per gram of silica.

Silanol groups are sufficiently acid to protonate the carbamato ligands surrounding europium coordination sphere promoting the formation of a covalent bond between the metal ion and the inorganic matrix:

$$n\ \#\text{SiO-H} + [\text{Eu}(\text{O}_2\text{CNBu}_2)_3] \longrightarrow \#(\text{SiO})_n\text{-Eu}(\text{O}_2\text{CNBu}_2)_{(3-n)} + n\text{CO}_2 + n\text{HNBu}_2 \qquad \textbf{(5.11)}$$

where # represent the silica surface

We used an excess of $[\text{Eu}(\text{O}_2\text{CNBu}_2)_3]$ to reach the maximum europium loading on the surface. Indeed, to prevent the coordination of the second metal ion on silica surface, all active silanol groups must react. To drive the reaction to completeness, several vacuum/dinitrogen cycles have been performed to remove the formed CO_2. This reaction was performed in toluene according to the general protocol already

employed.[229] After 55 h stirring, the solid was filtered and dried under reduced pressure. The amount of loaded europium was assessed by titration of the unreacted metal precursor in the reaction filtrate. In this first step, it has been found a europium loading of about 0.30 mmol per gram of silica. This data was also confirmed by ICP analysis on the obtained functionalized silica sample. Infrared spectra confirm the presence of residual carbamato groups coordinated to the metal ion after the grafting on the inorganic matrix (1,550-1,500 cm^{-1}, see **Figure 5.15**). This product was labelled **1Eu**.

In the second step, the residual carbamato ligands have been completely substituted with terephthalic acid. According to past gas-volumetric analysis,[229] the number of unreacted carbamato ligands during the grafting reaction can be estimated to be about the 66 %. The addition of 4.5 equivalent of terephthalic acid per metal center was a reasonable choice to promote the complete substitution of the residual carbamato ligands and the salification of the dibutylamine generated during the reaction forming the pyridine soluble $(H_2NBu_2)(HT)$ salt:

$$\#(SiO)_n\text{-}Eu(O_2CNBu_2)_{(3-n)} + 2(3\text{-}n)\ HT \longrightarrow \#(SiO)_n\text{-}Eu(HT)_{(3-n)} + (3\text{-}n)\ CO_2 + (3\text{-}n)\ (H_2NBu_2)(HT) \quad \textbf{(5.12)}$$

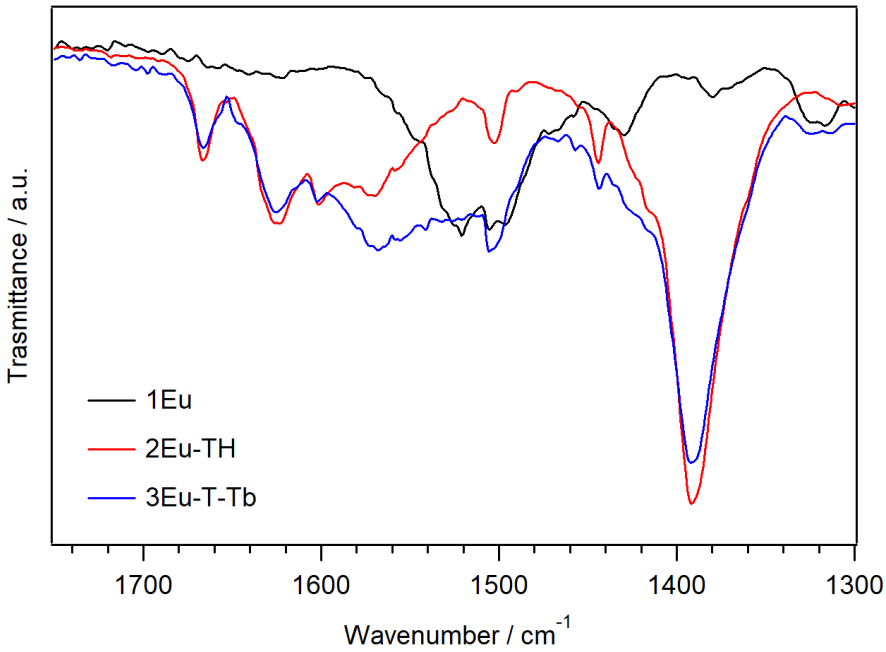

Figure 5.15: IR spectra of the **1Eu**, **2Eu-TH**, and **3Eu-T-Tb** samples in the 1,750-1,300 cm^{-1} range.

A larger excess of terephthalic acid would have favoured possible phenomena of metal leaching from the surface. On the other hand, using a defect of terephthalic acid the salification of the residual acidic functionalities by the dibutylamine could occur, preventing the HT^- reactivity in the third reaction step.

The reaction was conducted in pyridine at room temperature for about one day by repeating vacuum/dinitrogen cycles. The solid was filtrate and washed twice with fresh pyridine to completely remove the dibutylammonium salt and eventually unreacted terephthalic acid, and finally dried under reduced pressure. The ATR-IR of the product showed the complete disappearance of the carbamato groups bands and the rising of new bands attributable to terephthalate groups (1,700-1,550 cm^{-1}, see **Figure 5.15**). No traces of leached metal were found in the reaction filtrate. This product was labelled **2Eu-TH.**

In the last reaction step, [Tb $(O_2CNBu_2)_3$] complex can react only with the pendant -COOH of the HT^- ligand of **2Eu-TH** since no other acid groups are present.

$$\#(SiO)_n\text{-}Eu(TH)_{(3-n)} + (3\text{-}n)\ [Tb(O_2CNBu_2)_3] \longrightarrow \#(SiO)_n\text{-}Eu[T\text{-}Tb(O_2CNBu_2)_2]_{(3-n)} + (3\text{-}n)\ CO_2 + (3\text{-}n)\ HNBu_2 \quad \textbf{(5.13)}$$

This reaction was performed in pyridine using an excess of terbium complex to guarantee the complete reaction of the carboxylic groups. Infrared spectrum of the resulting product showed new bands ascribable to carbamato groups in addition to those already present in the previous step (see **Figure 5.15**). Analysis of the metal content in the reaction filtrate established a terbium/ europium molar ratio of about one in the functionalized silica. This value was also confirmed by EDX and ICP measurements on the silica sample. This specimen was labelled **3Eu-T-Tb**.

5.2.3. Photoluminescence studies

Photoluminescence studies support the formation of the RE-T bonds. When $[Eu(O_2CNBu_2)_3]$ is grafted on silica, the resulting material **1Eu** shows a pale red emission. Its emission spectrum (**Figure 5.16 a**) displays between 550 and 720 nm four bands associated to the $^5D_0 \rightarrow {}^7F_J$ (J= 1, 2, 3, and 4) transitions typical of Eu^{3+} centers.[8,229] The weak emission of this sample is explained considering that the carbamato ligand is not a good antenna for europium so hence Eu^{3+} emission can be sensitized only through excitation of the narrow f→f transitions (**Figure 5.16 b**).

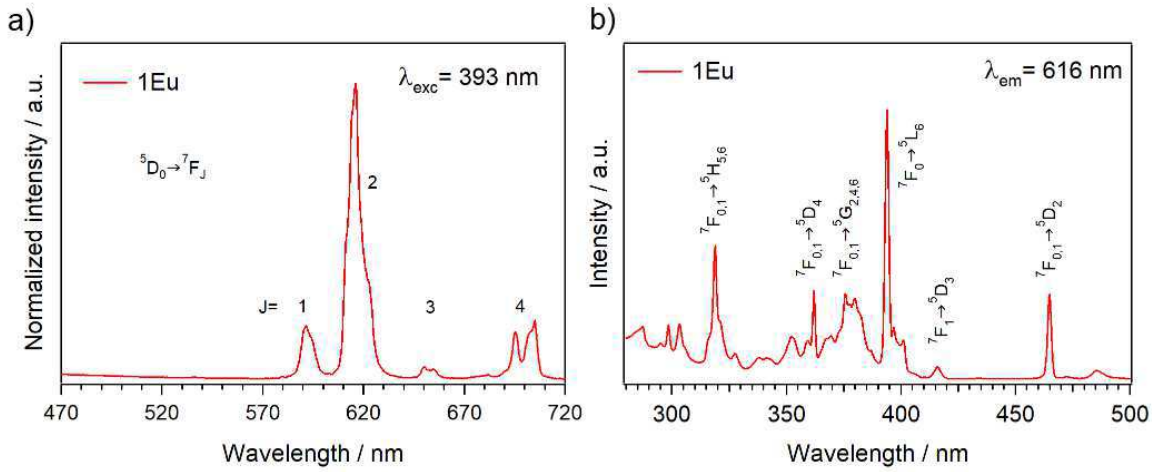

Figure 5.16: (a) Emission and **(b)** excitation spectra of the sample **1Eu.**

After the substitution of the residual carbamato ligands with terephthalic acid the sample **2Eu-TH** exhibits an intense red emission which can be also detected to the naked eye even in a lighted room. The presence of a broad band in europium excitation spectrum (**Figure 5.17 b**) associated to the HT^- ligand highlights the coordination of the terephthalate ligand to the Eu^{3+} centers. In this case, europium emission can be sensitized by both indirect and direct excitation through electronic transitions centered on the HT^- ligand and Eu^{3+} f-f transitions.

The substitution of the carbamato ligand by HT^- is also confirmed in **2Eu-TH** emission spectrum (**Figure 5.17 a**). Indeed, the coordination of the HT^- ligand generates a variation in the Eu^{3+} coordination geometry which is also reflected in the different shape of Eu^{3+} transitions.[8] For example, in **2Eu-TH** the $^5D_0 \rightarrow {}^7F_2$ transition displays a sharp and well-structured band significantly different from that of **1Eu**.

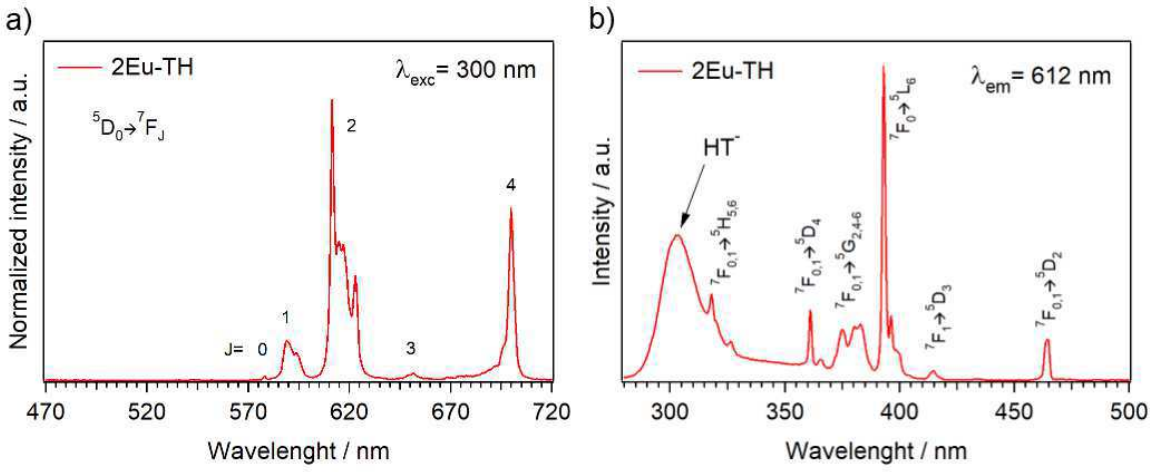

Figure 5.17: a) Emission and **b)** excitation spectra of the sample **2Eu-TH**.

Interestingly, in **2Eu-TH** an abnormal intensity for the $^5D_0 \rightarrow {}^7F_4$ transition was observed at 700 nm, which was reported in literature only in few cases.[263–268] Ferreira and co-workers have theoretically interpreted this behaviour in the terms of Judd-Ofelt ($\Omega\lambda$) intensity parameters and their dependence on the nature and local symmetry of the chemical environment around the Eu^{3+} ion.[264] In particular, highly polarizable surroundings and slightly distorted D_{4d}, D_{2d}, and D_2 coordination geometries are the factors that strongly enhance the intensity of the $^5D_0 \rightarrow {}^7F_4$

transition. Similar considerations can be applied in our case, although the complexity of the material prevents a detailed description of the system at the level of the europium coordination geometry.[229,230]

Successively, when terbium ions were grafted to the pendant carboxylic moieties of the hypodentate terephthalate ligand, the luminescence spectrum of **3Eu-T-Tb** showed the presence of terbium typical $^5D_4 \rightarrow {}^7F_J$ transitions (J= 6, 5, and 4), together with the europium ones, whose combination gives an overall orange light output (**Figure 5.18 a**). Terbium excitation spectrum consists in a single band at 300 nm due to ligand centered transitions, while Tb^{3+} f-f transitions between 330 and 390 nm are very low. This suggests the proximity of Tb^{3+} and T^{2-} supporting our synthetic scheme (**Figure 5.18 b**).

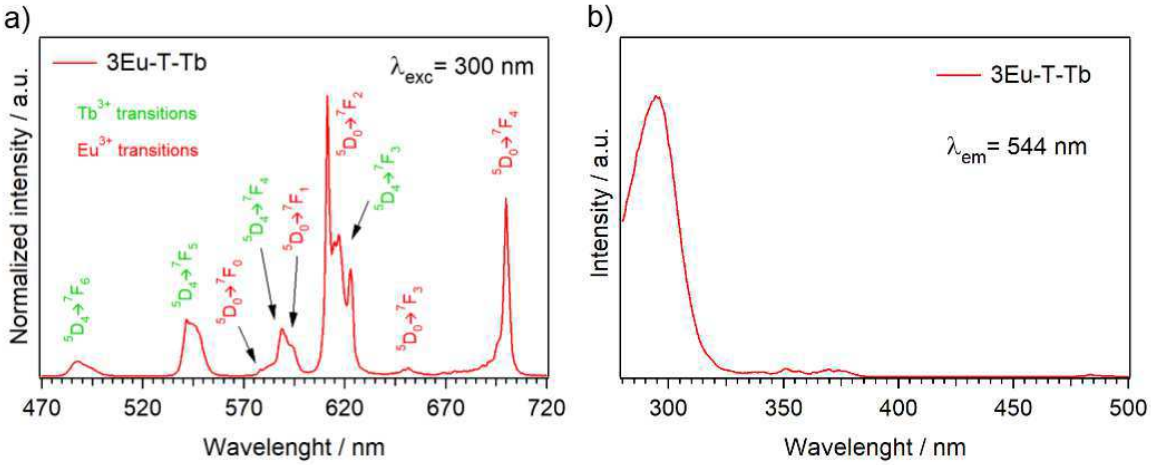

Figure 5.18: a) Overall emission and **b)** Tb^{3+} excitation spectra of **3Eu-T-Tb**. In the emission spectrum, Tb^{3+} transitions are labelled in green while Eu^{3+} transitions in red.

Although these results support the formation of RE-T bonds and RE_1-T-RE_2 sequence, they do not give detailed information on the arrangement of the two metal ions and, in particular, they do not allow to distinguish the desired sequence (**3Eu-T-Tb**) from the copresence of the two lanthanoid ions deposited on silica. Theoretically, this second possibility should be ruled out considering the excess of $[Eu(O_2CNBu_2)_3]$ used in the first grafting reaction. In this case, all the accessible silanols have been already coordinated to Eu^{3+} ions and no grafting sites are available for Tb^{3+} in the last reaction step. To confirm this hypothesis and elicit further

experimental evidence on the formation of the desired sequence, two peculiar lanthanoid luminescent properties were exploited.

The first concerns the dependency of the band shape from the metal coordination environment. Indeed, lanthanoid ions luminescence properties are largely influenced by the coordination environment[8] as it has been also shown during the discussion of the europium dimeric compounds in **Chapter 2**. It is intuitive that a lanthanoid ion directly bonded to silica or to T^{2-} and carbamato moieties can have different coordination geometries. For this reason, three further samples in which terbium was directly grafted on silica or alternatively bonded to the terephthalic acid have been prepared following the previous synthetic procedure and their emission spectra were compared with that of **3Eu-T-Tb**:

- **2Tb-TH**, where $[Tb(O_2CNBu_2)_3]$ was grafted on silica and further functionalized with terephthalic acid;
- **2(Eu+Tb)-TH**, where $[Eu(O_2CNBu_2)_3]$ and $[Tb(O_2CNBu_2)_3]$ were co-deposited on silica using the same Tb/Eu molar ratio found in the sample **3Eu-T-Tb** and then functionalized with H_2T ligand;
- **3Y-T-Tb**, a sample like **3Eu-T-Tb** in which $[Y(O_2CNBu_2)_3]$ was grafted on silica during the first step instead of europium. Yttrium was chosen because it is spectroscopically inert due to the absence of 4f electrons, but its dimension and coordination chemistry resemble that of Eu^{3+}.

For clarity, **Figure 5.12** (***vi*** and ***vii***) is here recalled giving an overview of the samples discussed henceforth.

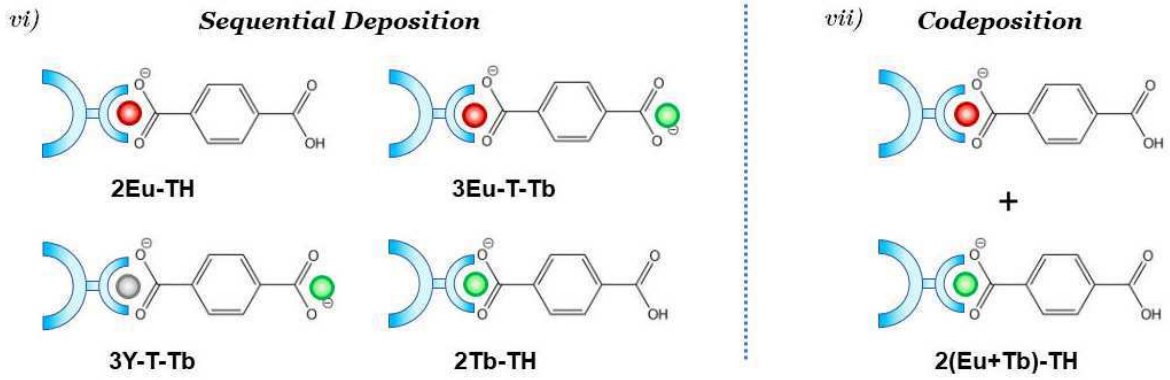

The first two samples (**2Tb-TH** and **2(Eu+Tb)-TH**) present the same IR spectrum of **2Eu-TH,** while the IR spectrum of **3Y-T-Tb** is analogue to that of **3Eu-T-Tb**. In all the samples, a metal loading of ≈ 0.30 mmol of lanthanoid ion per gram of silica was found indicating an excellent reproducibility of the smart-grafting procedure. This evidence was also supported by the Tb^{3+}/ Y^{3+} molar ratio in the sample **3Y-T-Tb** of about one as previously found for its analogue **3Eu-T-Tb**.

In **2Tb-TH** and **2(Eu+Tb)-TH**, where Tb^{3+} is directly grafted on silica and surrounded by terephthalate moieties, the $^5D_4 \rightarrow {}^7F_5$ transition has two maxima at 541.4 and 546.2 nm, whereas in **3Eu-T-Tb** these features are no longer observed and a single non-structured band is visible. These spectral differences indicate the presence of different environments around Tb^{3+} (**Figure 5.19 a**). These observations are further corroborated by considering the PL of the sample where Y^{3+} was used as neutral luminescent element to build the Y-T-Tb sequence (sample **3Y-T-Tb**). In this case, the emission spectrum closely resembles that of the terbium component in **3Eu-T-Tb** pointing out that the employed synthetic procedure reproduces an analogous environment for the second metal ion in the planned sequence (**Figure 5.19 b**).

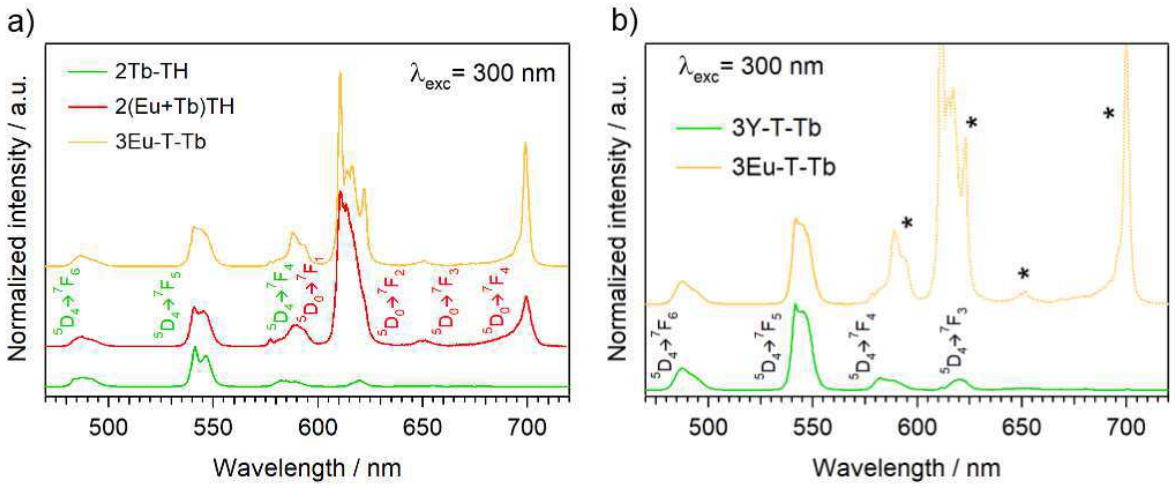

Figure 5.19: a) Emission spectra of **3Eu-T-Tb**, **2(Eu + Tb)-TH**, and **2Tb-TH** (λ_{exc} = 300 nm). **b)** Emission spectra of **3Y-T-Tb** and **3Eu-T-Tb**, europium belonging signals are faded and starred (λ_{exc} = 300 nm).

The second property is instead the presence of Tb^{3+} to Eu^{3+} energy transfer (ET) which can take place between Tb^{3+} $^5D_4$ (donor) and Eu^{3+} $^5D_0$ (acceptor) emissive levels due to the relatively small energy gap between them (3,000 cm^{-1}). Indeed, the ET extent is modulated by the intermetal distance: the shorter are the distances between the donor and the acceptor atoms, the higher is the energy transfer efficiency. In particular, high energy transfer values were reported for distances lower than 10 Å.[269]

To effectively use the distance-dependent properties of the ET processes to study the ion arrangement in our materials we need to consider both the distribution of silanols on the silica surface and the coordination modes of the T^{2-} ligand.

For the silanol density on silica surface, Zhuravlev model for amorphous SiO_2 can be used.[270] This model, developed by Zhuravlev during the last decades of twentieth century, is a physico-chemical model based on a high number of experimental data suitable to determine the properties of amorphous silica (like the amount of chemisorbed water, the number of -OH groups inside the SiO_2 skeleton per unit of surface area *etc.*) and it is commonly used in the study of silica properties.[224,246,271,272]

As previously mentioned, the silica powder used in these experiments has a surface area of 325 m^2 g^{-1} (A) and 2.02 mmol of silanols per silica gram (n_{SiOH}), corresponding to a silanol surface density (σ_{SiOH}) of 3.8 -OH nm^{-2}. The value can be easily determined according to the following equation:

$$\sigma_{SiOH} = \frac{n_{SiOH} \cdot N_A}{A} \qquad \textbf{(5.14)}$$

where N_A is the Avogadro number. To eliminate physically adsorbed water molecules form the silica surface, we treated the SiO_2 powders under vacuum at 160 °C. A similar treatment is expected to leave fully hydroxylated silica that, according to Zhuravlev model, can have a maximum of 4.9 -OH nm^{-2} on its surface.[270] Taking into account the experimental value of the silanol surface density and the Zhuravlev model, all the silanols are expected to be on the silica surface and hence available for the grafting reaction with a lanthanoid carbamato complex.

Zhuravlev model provides other useful informations about the type of silanol groups and their distribution on the silica surface that gives a sort of map of the grafting sites on silica. In particular, silica treated at temperatures lower than 190 °C presents all the three different types of silanol groups already mentioned in **Figure 5.6**: isolated (26%), geminals (13%), and vicinals (61%) with an average distance between two -SiOH groups of 2.95 and 7.60 Å for vicinal and isolated silanols, respectively.[270] On this basis, in the sample **2(Eu+Tb)-TH** (see **Figure 5.12** ***vii***) prepared by co-deposition of the two Eu^{3+} and Tb^{3+} carbamates simultaneously reacted with silica, the distance between two RE^{3+} ions will be comparable to the -SiOH separation and hence highly efficient energy transfer is compatible with similar intermetal distances. Conversely, if the desired stepwise assembly of **3Eu-T-Tb** sequence is successful (**Figure 5.12** ***vi***), the Eu^{3+}-Tb^{3+} distance will be determined by the bonding characteristics of the T^{2-} spacer. Informations on the Eu^{3+} - Tb^{3+} distance in **3Eu-T-Tb** can not be directly achieved due to the non-crystalline nature of the sample that exclude the possibility for X-ray crystallography studies. However, T^{2-} ligand has two binding sites that can be both bridging and chelating, and therefore there are different possibilities to connect two RE^{3+} ions. This aspect has been well characterized in benzendicarboxylate-based Lanthanoid Organic Frameworks (LOFs). Although these materials are quite different from out material, the behaviour of the T^{2-} ligand is the same. For this reason, the structurally characterized $Tb_2T_3(H_2O)_4$[140,255] LOF has been considered as a good model to determine the T^{2-} connectivity characteristics and estimate the possible intermetal distances in the **3Eu-T-Tb** sequence.

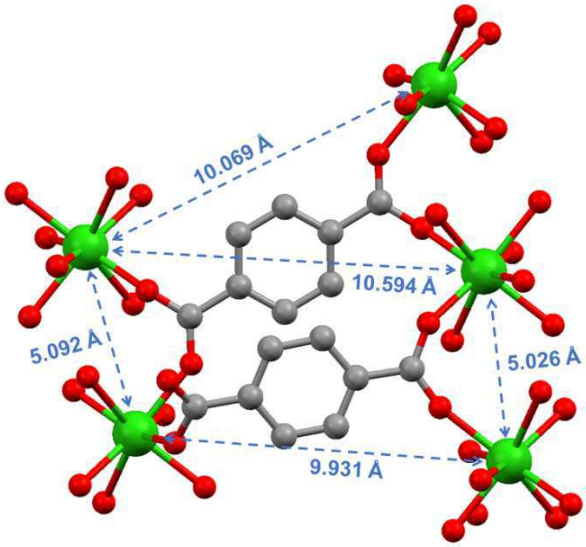

Figure 5.20: Relevant RE^{3+}-RE^{3+} distances in the crystal structure of $Tb_2T_3(H_2O)_4$ (CCDC-1241234).

Figure 5.20 reports a portion of the $Tb_2T_3(H_2O)_4$ crystal structure that evidences the binding characteristics of T^{2-} ligand. When a carboxylic group of T^{2-} acts as bridging ligand between two RE^{3+} ions, the intermetal distance is of about 5 Å. Conversely, two metal ions connected by the T^{2-} spacer through the divergent carboxylic groups are at about 10 Å. In this second case the energy transfer processes should be less efficient because of the longer intermetallic distance.[139,140,269] The energy transfer efficiency can be determined through equation (**5.15**):

$$\eta_{ET} = 1 - (\tau_{DA}/\tau_D) \qquad \textbf{(5.15)}$$

where τ_{DA} and τ_D are the experimental excited state lifetimes of the donor (Tb^{3+}) alone and in presence of the acceptor (Eu^{3+}) respectively.

For all the investigated systems, decay curves well fitted by bi-exponential functions were measured indicating the presence of multiple sites both for Tb^{3+} and Eu^{3+} ions. The efficiency of the Tb^{3+}-to-Eu^{3+} energy transfer in our sample was calculated through equation (**5.15**), by measuring the lifetime of the donor (Tb^{3+}) in absence and in presence of the acceptor (Eu^{3+}), *i.e.* in the following donor-acceptor pairs (**Figure 5.21**).:

1) **2Tb-TH** (τ_D) - **2(Eu+Tb)-TH** (τ_{DA}),
2) **3Y-T-Tb** (τ_D) - **3Eu-T-Tb** (τ_{DA}).

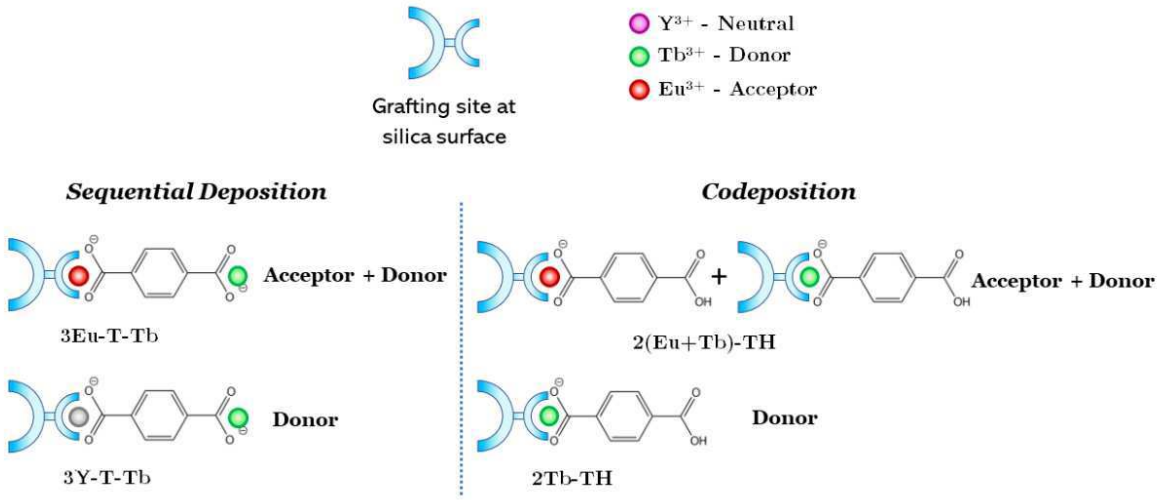

Figure 5.21: Donor and acceptor pairs used to study the ET in the sample obtained by sequential deposition and codeposition.

As reported in **Table 5.1**, low η_{ET} values (0.13) have been measured for the heterometallic sequence **3Eu-T-Tb**. Conversely, an energy transfer efficiency up to 0.62 was observed in the co-deposited sample **2(Eu+Tb)-TH**. These differences in η_{ET} values confirmed that averagely Eu^{3+} and Tb^{3+} ions are closer in **2(Eu+Tb)-TH** than in **3Eu-T-Tb**. Taking into account the constrains imposed by the -SiOH surface distributions and the connectivity characteristics of the H_2T ligand (**Figure 5.20**), these results can be explained considering the T^{2-} ligand having in **3Eu-T-Tb** one carboxylic group bonded to Eu^{3+} and the other to Tb^{3+} with the formation of the desired sequence.

	$\tau_{average}$ (ms)		
Sample	Eu^{3+}	Tb^{3+}	η_{ET}
2Eu-TH	1.96	—	—
3Y-T-Tb	—	2.06	—
3Eu-T-Tb	2.00	1.79	0.13
2Tb-TH	—	2.28	—
2(Eu-Tb)-TH	1.82	0.87	0.62

Table 5.1: Lifetime and energy transfer efficiency of the various silica samples, λ_{exc}= 300 nm.

Finally, it is interesting to compare the colour of the emitted light in the four Eu^{3+}/Tb^{3+} heterobimetallic samples reported in the chromaticity diagram of **Figure 5.22**. By using $[Eu(O_2CNBu_2)_3]$, $[Tb(O_2CNBu_2)_3]$ and H_2T under the same reaction conditions but changing the way they are reacted, *i.e.* together or stepwise, a chromatic modulation is achieved. Indeed, by changing the sequence of the building blocks we varied the spatial composition of the samples and hence their luminescent properties (e.g. the energy transfer efficiency). The reaction here employed can be generalized by modifying the nature of the metal ions and of the spacer thus providing a valuable tool for the synthesis of Sequence-Dependent Materials on the surface of inorganic and polymeric substrates.

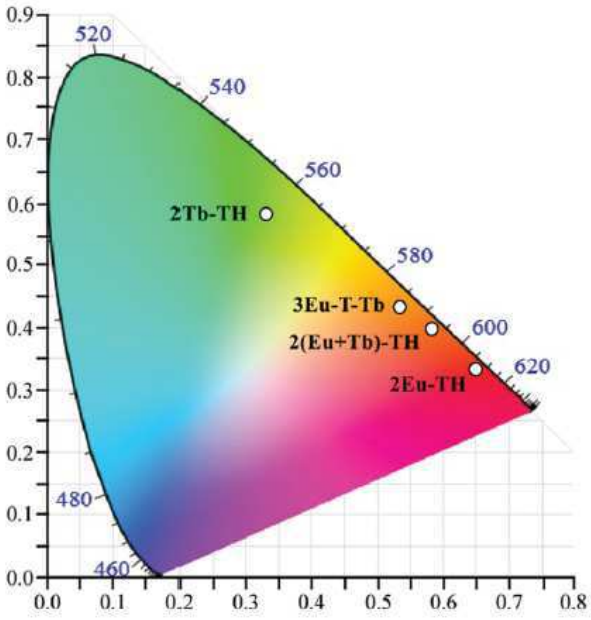

Figure 5.22: The CIE1931 colour space chromaticity diagram evidences the coordinates of the **2Eu-TH**, **2Tb-TH**, **2(Eu+Tb)-TH**, and **3Eu-T-TH**.

5.3. Conclusions

The *smart-grafting* procedure that exploits the reactivity of lanthanoid *N*,*N*-dialkylcarbamato complexes has been used for the synthesis of luminescent Sequence-Dependent Materials. A spatially ordered sequences of Eu^{3+} and Tb^{3+} connected by benzene-1,4-dicarboxylic acid as divergent rigid ligand able to sensitize the lanthanoid

emission was created onto silica surface. Silica surface can be functionalized following a stepwise synthetic path involving: *i*) the metal grafting onto SiO_2 surface by exploiting the reactivity of metal carbamato complexes $[Ln(O_2CNBu_2)_3]$ towards protic agents, and *ii*) the introduction of a suitable property-determining ligand in the Ln^{3+} coordination sphere. The resulting species, carrying a protic functionality, are successively reacted with a second metal carbamato complex allowing the growth of an ordered sequence just repeating the described steps. The use of pyridine as a solvent was crucial to obtain the desired sequence since pyridine avoids any possible contamination from free terephthalic acid or from products of H_2T with dibutylamine formed during the grafting reaction.

The light output of silica-based materials can be tuned by varying their spatial composition. The variation of the Eu^{3+} and Tb^{3+} position in the structures (**3Eu-T-Tb** and **2(Eu+Tb)-TH**) resulted particularly interesting. In fact, when they are connected through the terephthalate ligand in the **3Eu-T-Tb** sequence, the large metal ion separation (in the order of 10 Å) hampers the occurrence of efficient energy transfer processes. Conversely, high ET efficiency was detected in the co-deposited material, *i.e.* without the ordered sequence.

Noteworthy, simply by modifying the succession of the synthesis steps, it was possible to modulate the ion-ion interactions that in turn affects the material properties.

The observed results have a general importance not only in the field of luminescent materials because they show a convenient way to modulate the spatial-dependent interactions between different metal ions on materials surface, regardless of the considered property. In principle different functionalities can be introduced by changing the nature of the metal ions and of the spacer, as sketched in **Figure 5.23**.

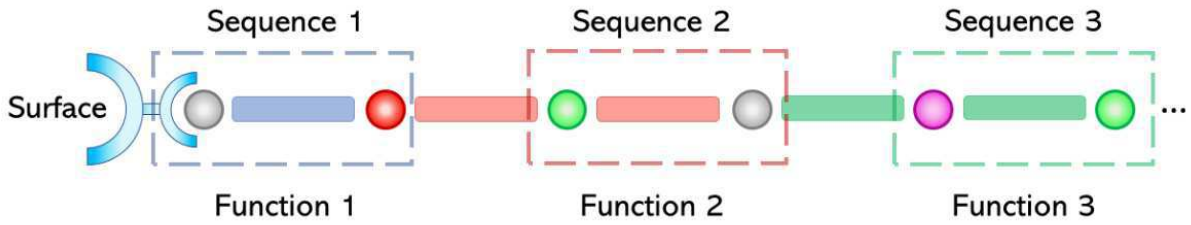

Figure 5.23: Sketch of a Sequence-Dependent Material grown on the surface of a suitable support by stepwise reaction of different building blocks endowed with different functionalities.

It was here demonstrated the general applicability of the reported synthetic protocol for the development of ordered SDMs containing any selected combination of two or more *d* or *f* metals.

In the future, it would be interesting to use the first step of this sequence (**Sequence 1** in **Figure 5.23**) as crystallization seed to build a MOF (or a LOF) on a surface. In this case the resulting MOF would be linked to the support through strong covalent bonds, while in the literature electrostatic interactions between the complex and the matrix are generally exploited.[273–275]

Another interesting outlook would be the use of this *smart-grafting* procedure for the functionalization of a flat surface (e.g. silica thin film, activated silicon, ITO glasses) to obtain functionalized materials with potential technological applications. Considering the small amount of molecular complex that would be grafted on the support, the biggest problems to be faced will be related to the sample characterization.

6. Experimental section

6.1. General procedures

If not specified elsewhere, reactions were made under dinitrogen or argon inert atmosphere; the glasswork was previously dried in an oven (T= 130°C) before use. The vacuum has been obtained using rotary oil pumps and it was in the order of 10^{-2} mbar. Aqueous solutions have been concentrated using a rotary evaporator *Buchi R-200* linked to a membrane pump *KNF Laboratori*. Solvents and other liquid reagents have been anhydrified by prolonged boiling on specific drying agents (see **Section 6.2**) and then stored under dinitrogen inert atmosphere. Solid reagents have been treated under reduced pressure to remove physically adsorbed water. H_2O means deionized water when it is used as solvent.

6.2. Organic solvents

- Toluene (Sigma-Aldrich): anhydrous, distilled over Na;
- n-Heptane (Sigma-Aldrich): anhydrous, distilled over Na;
- n-Pentane (Sigma-Aldrich): used as received;
- Pyridine (Sigma-Aldrich): anhydrous, distilled over KOH;
- $HNBu_2$ (Sigma-Aldrich): used as received;
- Chloroform (Sigma-Aldrich): anhydrous, distilled over P_2O_5;
- DMF (Sigma-Aldrich): anhydrous, distilled under reduced pressure over Al_2O_3;
- THF (Sigma-Aldrich): anhydrous, distilled over $LiAlH_4$.

6.3. Reagents

- *$Eu(O_2CNBu_2)_3$*: synthesized according to the procedure reported in literature;[243]
- *$Tb(O_2CNBu_2)_3$*: synthesized according to the procedure reported in literature;[243]
- *$Y(O_2CNBu_2)_3$*: synthesized according to the procedure reported in literature;[243]

- *Eu(dbm)₃*: synthesized according to the procedure reported in literature;[100]
- *Eu(bta)₃*: synthesized according to the procedure reported in literature;[100,276]
- *Eu(hfac)₃*: synthesized according to the procedure reported in literature;[100]
- *Eu(tta)₃*: synthesized according to the procedure reported in literature;[100]
- *4,4'-Bipyridine-N-oxide*: synthesized according to the procedure reported in literature;[102]
- *Pyrazine-N-oxide*: synthesized according to the procedure reported in literature;[277]
- *Imidazole* (Sigma-Aldrich): received as used;
- *1,4-Benzendicarboxylic acid* (Sigma-Aldrich): the commercial product has been heated at 80 °C under reduced pressure (10^{-2} mmHg) for 8 h over P_2O_5 to remove traces of physically adsorbed water and stored under inert atmosphere;
- *2,5-Dihydroxy-1,4-benzendicarboxylic acid* (Sigma-Aldrich): used as received;
- *SiO_2 Crosfield* (Grace, EP17G, superficial area 325 m^2 g^{-1}, 2.02 mmol of SiOH groups per gram) treated at 160 °C under reduced pressure (10^{-2} mmHg) for 24 h over P_2O_5 and stored under inert atmosphere.

6.4. Analytical measurements and instrumentation

Elemental analyses (C, H, N) were performed at Dipartimento di Chimica e Chimica Industriale, University of Pisa. Metal elemental analyses were carried out via EDTA titration.[278] Alternatively, metal analyses were performed in a mitten electric oven *Megawatt RO-8* heating the sample at 850 °C until constant weight was reached. The calcinated species were contained in a Pt crucible and they were treated with two drops of HNO_3 (75 %). ICP analyses were carried out with a *Quadropole X7 ICP-MS* Thermo Fisher instrument. SEM-EDX analyses were carried out with a *FEI Quanta FEG-450* microscope supplied with a Philips *XL 30* instrument. Sample disks were prepared by pressing the powders in a *Specac* manual hydraulic press.

^{1}H and ^{13}C-NMR spectra were recorded with a Bruker *Avance DRX400* spectrometer. Chemical shifts were measured in ppm (δ) from TMS by residual solvent peaks for both ^{1}H and ^{13}C nuclei.

FTIR spectra in the solid state were recorded with a Perkin-Elmer *Spectrum One* spectrometer, with ATR technique. Liquid IR spectra were recorded with a Perkin-Elmer *Spectrum 100* spectrometer. The cell sample holder has an optical path of 0.1 mm. The calibration curve for DMF in $CHCl_3$ was determined monitoring the absorbance of the C=O stretching at 1672 cm^{-1}. Seven solutions of DMF in $CHCl_3$ were prepared using concentrations between $1.55 \cdot 10^{-3}$ and $1.30 \cdot 10^{-1}$ M. A molar absorptivity of $1.34 \cdot 10^{3}$ M^{-1} cm^{-1} was esteemed and with a coefficient of determination (R^2) of 0.9996

Single crystals were glued at the end of glass fibres or sealed in glass capillaries when they lost solvent. Single-crystal X-ray Diffraction have been performed at room temperature by means of a Bruker *SMART Breeze CCD* diffractometer equipped with graphite monochromated Mo-$K\alpha$ radiation (λ = 0.71073 Å) or, alternatively, using an Oxford diffraction *Xcalibur 3 CCD* diffractometer at T = 100 K. All the structure solutions were found using the automated direct methods contained in SHELXS-97 program.[279]

Powders X-ray diffraction patterns have been collected using 2nd generation *D2 Phaser* diffractometer using the Cu(Kα) radiation and equipped with a Ni filter to exclude the Cu(Kβ) component. It has been employed a θ/ θ geometry which means that the source and the detector perform the same angular movement but in opposite directions while the sample is fixed in a horizontal position. The screen between the source and the detector present a slit of about 0.1 mm. The experimental parameter, especially the delay between two different angular increments and the explored 2θ interval, were never constant because they have been fixed after the collection of a first diffractogram.

The samples have been prepared grinding the solid powders suspended in a few drops of *n*-heptane in an Agathe mortar and then placed on a silicon monocrystal cut along the orthogonal direction of the [110] planes. The data were collected starting from appropriate θ values so that $2\,\theta > 5°$ to exclude the signal saturation due to the Si sample holder. The samples were spin with an angular speed of 15° per minute as suggested by the manufacturer.

Absorption spectra were recorded using a double-ray spectrometer *Cary 5E* with a diffuse reflectance accessory and reported as Kubelka-Munk F(R) function. The room temperature luminescence spectra were recorded in a front-face acquisition geometry with a Horiba JobinYvon *Fluorolog-3* spectrofluorimeter equipped with double-grating monochromator in both the excitation and emission sides coupled to a *R928P* Hamamatsu photomultiplier and a 450 W Xe arc lamp as the excitation source. The emission spectra were corrected for detection and optical spectral response of the spectrofluorimeter supplied by the manufacturer. The excitation spectra were corrected for the spectral distribution of the lamp intensity using a photodiode reference detector. The luminescence lifetimes in the microsecond–millisecond scales were measured by a pulsed Xe lamp with variable repetition rate and elaborated with standard software fitting procedures. The experimental uncertainty on τ values is ±10%.

Photoluminescence measurements have been usually performed on solid samples gently pressed on a KBr pellet surface. Alternatively, KBr pellets containing a dispersion of the desired sample have been prepared using the hydraulic press after grinding the sample in an Agathe mortar. IR-grade KBr (Sigma-Aldrich) previously heated at 100°C overnight to remove H_2O traces was used. Air- or moisture-sensitive samples were analysed in closed vials under dinitrogen atmosphere using optic fibres.

The modulation of samples luminescent properties with temperature were measured with a spectrometer Horiba T64000 equipped with a Peltier-cooled (Horiba Synapse) CCD detector. A Xe arc lamp (450 W) has been used as excitation source. The

diffuse radiation was collected with a 10x lens (Olympus MPLAN, 10x/ 0.25). Measurements were performed collecting the samples emission spectra each 10, 20, 25, or 30 °C depending on the width of the temperature range. Two minutes have been waited before each measurement to allow the achievement of thermal equilibrium.

6.5. Synthesis

6.5.1. Synthesis of $[Eu_2(dbm)_6(bipyMO)_2]$.

A suspension of $[Eu(dbm)_3]$ (0,300 g, 0.37 mmol)) and bipyMO (0.060 g, 0.35 mmol) in anhydrous toluene (25 mL) was refluxed for 2 h. The yellow solution was slowly cooled to -20 °C. The crystalline solid precipitated out was decanted and dried in vacuo for 4 h. Crystals lose solvent, when dried, converting to powder (0.290 g, yield 81.1% as $[Eu_2(dbm)_6(bipyMO)_2]$). El. Anal. Calcd for $[Eu_2(dbm)_6(bipyMO)_2]$, $C_{110}H_{82}Eu_2N_4O_{14}$, %: Teor: C, 66.5; H, 4.2; N, 2.8. Found: C, 66.2; H, 4.0; N, 2.6. IR-ATR (range: 1700-700 cm^{-1}): 1593m, 1548m, 1514m, 1477m, 1456m, 1411m, 1392m, 1306m, 1284w, 1259m, 1217m, 1178w, 1155w, 1066m, 1021m, 940w, 846w, 797m, 745m, 720m. Crystal suitable to single crystal X-Ray diffraction studies were obtained through diffusion of pentane vapours in a toluene solution of the product.

6.5.2. Synthesis of $[Eu_2(bta)_6(bipyMO)_2]$.

To a solution of $[Eu(bta)_3]$ (0.357 g, 0.45 mmol) in anhydrous toluene (25 mL) bipyMO (0.087 g, 0.46 mmol) was added. The pale-yellow solution was refluxed for 2 h, cooled at room temperature, concentrated under reduced pressure, and then cooled to -20 °C. The formed colorless solid was filtered and dried in vacuo for 5 h. (0.31 g, yield 59.0% as $[Eu_2(bta)_6(bipyMO)_2]$. El. Anal. Calcd for $[Eu_2(bta)_6(bipyMO)_2]$, $C_{80}H_{52}Eu_2F_{18}N_4O_{14}$, %: Teor. C, 49.6; H, 2.7; N, 2.9. Found: C, 48.3; H, 2.6; N, 2.9. IR-ATR (range: 1700-700 cm^{-1}): 1636m, 1611s, 1575m, 1537m, 1479m, 1319m, 1289s, 1239m, 1179m, 1126s, 1074m, 1024w, 944w, 847w, 816m, 764s, 734m, 716m. Crystal

suitable to single crystal X-Ray diffraction studies were obtained through diffusion of pentane vapours in a toluene solution of the product.

6.5.3. Synthesis of $[Eu_2(hfac)_6(bipyMO)_3]$.

To a suspension of $[Eu(hfac)_3]$ (0.360 g; 0.47 mmol) in toluene (25 mL) bipyMO was added (0.120 g; 0.70 mmol). The colourless mixture was refluxed for 2 h. The solution was cooled to room temperature and then at 5 °C. Precipitation of a colourless crystalline solid occurred. The suspension was filtered and the solid was dried in vacuo (0.30 g; 62.0% yield as $[Eu_2(hfac)_6(bipyMO)_3]$). El. Anal. Calcd for $[Eu_2(hfac)_6(bipyMO)_3]$, $C_{60}H_{30}Eu_2F_{36}N_6O_{15}$, %: Teor: C, 34.9; H, 1.5; N, 4.1. Found: C, 34.6; H, 1.5; N, 3.9. IR-ATR (range: 1700-700 cm^{-1}): 1663m, 1650s, 1601w, 1556m, 1530m, 1505m, 1482m, 1412w, 1349w, 1321w, 1251s, 1196s, 1134s, 1097s, 1039m, 950w, 860m, 850m, 814m, 796s, 767w, 741m, 719w. It is soluble at RT in the usual organic solvent. Recrystallization from toluene afforded crystals of $[Eu_2(hfac)_6(bipyMO)_3]$ $3C_7H_8$ suitable for X-Ray diffraction studies. The crystals were treated under N_2 atmosphere saturated with toluene to avoid collapse due to the loss of the crystallization solvent.

6.5.4. Synthesis of $[Eu_2(tta)_6(bipyMO)_2]$.

To a solution of $[Eu(tta)_3]$ (0.290 g, 0.36 mmol) in anhydrous toluene (25 mL) bipyMO (0.060 g, 0.35 mmol) was added. The yellow suspension was refluxed for 2 h and then was slowly cooled to room temperature. A small amount of solid was eliminated by filtration. The pale-yellow filtrate was treated with heptane (30 mL) and cooled to -20 °C. A finely divided colourless solid precipitated out that was dried in vacuo for 7 h (0.21 g, 60.4% yield as $[Eu_2(tta)_6(bipyMO)_2]$). El. Anal. Calcd for $[Eu_2(tta)_6(bipyMO)_2]$, $C_{68}H_{40}Eu_2F_{18}N_4O_{14}S_6$, %: Teor: C, 41.3; H, 2.0; N, 2.8. Found: C, 40.9; H, 2.0; N, 2.9. IR-ATR (range: 1700-700 cm^{-1}): 1620w, 1596m, 1537w, 1505w, 1471w, 1412w, 1355w, 1304m, 1245w, 1229w, 1180m, 1127m, 1083w, 1060w, 1036w, 1015w, 991w, 947w, 934w, 859w, 847w, 814w, 785m, 767w, 749w, 718w. Crystals

suitable to single crystal X-Ray diffraction studies were obtained through diffusion of pentane vapours in a toluene solution of the product.

6.5.5. Synthesis of $[Eu_2(dbm)_6(pyrzMO)_2]$.

A suspension of $[Eu(dbm)_3]$ (0,192 g, 0.23 mmol)) and pyrzMO (0.024 g, 0.23 mmol) in anhydrous toluene (20 mL) was heated at 60 °C for 1 h. The yellow solution was slowly cooled to -20 °C. A crystalline solid precipitated out that was decanted and dried in vacuo for 3 h. Crystals lose solvent, when dried, converting to powder (0.119 g, yield 55.3% as $[Eu_2(dbm)_6(pyrzMO)_2]$. El. Anal. Calcd for $[Eu_2(dbm)_6(pyrzMO)_2]$, $C_{98}H_{74}Eu_2N_4O_{14}$, %: Teor: C, 64.1; H, 4.0; N, 3.1. Found: C, 64.4; H, 4.0; N, 2.8. IR-ATR (range: 1700-700 cm^{-1}): 1592s, 1550s, 1515s, 1473s, 1457s, 1414s,sh, 1305m, 1261w, 1247w, 1218m, 1176w, 1156w, 1068m, 1021m, 1010m, 939w, 850m, 829m, 781w, 757s, 725s. Crystals suitable to single crystal X-Ray diffraction studies were obtained through diffusion of pentane vapours in a toluene solution of the product.

6.5.6. Synthesis of $[Eu_2(bta)_6(pyrzMO)_2]$.

To a solution of $[Eu(bta)_3]$ (0.463 g, 0.58 mmol) in anhydrous toluene (30 mL) pyrzMO (0.056 g, 0.58 mmol) was added. The pale-yellow solution was stirred at room temperature for 4 h, concentrated under reduced pressure and then cooled to -20 °C. The formed colourless solid was filtered and dried in vacuo for 7 h. (0.32 g, yield 63.0% as $[Eu_2(bta)_6(pyrzMO)_2]$. El. Anal. Calcd for $[Eu_2(bta)_6(pyrzMO)_2]$, $C_{68}H_{44}Eu_2F_{18}N_4O_{14}$, %: Teor: C, 45.7; H, 2.5; N, 3.1. Found: C, 45.7; H, 2.5; N, 3.5. IR-ATR (range: 1700-700 cm^{-1}): 1632m, 1608s, 1574m, 1532m, 1473m, 1431w, 1319m, 1292s, 1242m, 1189m, 1130s, 1077m, 1025w, 1011w, 945w, 848m, 833m, 810w, 767m, 716m, 700m. Crystals suitable to single crystal X-Ray diffraction studies were obtained through diffusion of pentane vapours in a toluene solution of the product.

6.5.7. Synthesis of $[Eu_2(hfac)_6(pyrzMO)_3]$.

To a suspension of $[Eu(hfac)_3]$ (0.766 g; 0.99 mmol) in toluene (30 mL) pyrzMO was added (0.143 g; 1.48 mmol). The colourless mixture was refluxed for 1 h. The solution

was cooled to room temperature, concentrated under reduced pressure and finally cooled to -20 °C. Precipitation of a colourless crystalline solid occurred. The suspension was filtered and the solid was dried in vacuo (0.52 g; 57.2% yield as $[Eu_2(hfac)_6(pyrzMO)_3]$). El. Anal. Calcd for $[Eu_2(hfac)_6(pyrzMO)_3]$, $C_{48}H_{22}Eu_2F_{36}N_6O_{15}$, %: Teor: C, 27.5; H, 1.0; N, 4.6. Found: C, 27.5; H, 1.4; N, 4.4. IR-ATR (range: 1700-700 cm^{-1}): 1648m, 1577w, 1533w, 1495m, 1473m, 1435m, 1253m, 1202m, 1138s, 1098m, 1012m, 848m, 801m, 734w,716w. Recrystallization from toluene afforded crystals of $[Eu_2(hfac)_6(pyrzMO)_3]\cdot 3C_7H_8$ suitable for X-Ray diffraction studies. The crystals were treated under atmosphere saturated with toluene to avoid collapse due to the loss of the crystallization solvent.

6.5.8. Synthesis of $[Eu_2(tta)_6(pyrzMO)_2]$.

To a solution of $[Eu(tta)_3]$ (0.208 g, 0.26 mmol) in anhydrous toluene (20 mL) pyrzMO (0.025 g, 0.26 mmol) was added. The yellow solution was stirred overnight at room temperature and then concentrated under reduced pressure until precipitation of a yellowish solid which was filtered and dried in vacuo for 5 h (0.15 g, 65.0% yield as $[Eu_2(tta)_6(pyrzMO)_2]$). El. Anal. Calcd for $[Eu_2(tta)_6(pyrzMO)_2]$, $C_{56}H_{32}Eu_2F_{18}N_4O_{14}S_6$, %: Teor: C, 36.9; H, 1.8; N, 3.1. Found: C, 37.9; H, 1.8; N, 3.3. IR-ATR (range: 1700-700 cm^{-1}): 1596s, 1540s, 1507m, 1471m, 1430w, 1411s, 1359m, 1303s, 1061m, 1013w, 934m, 855m, 832w, 784s, 766w, 746w, 716s. Crystals suitable to single crystal X-Ray diffraction studies were obtained through diffusion of pentane vapours in a toluene solution of the product.

6.5.9. Synthesis of $[Eu(hfac)_3(bipy)]_n$.

$[Eu(hfac)_3(H_2O)_2]$, (1.09 g; 1.35 mmol) was introduced in a weighed vial. The vial was introduced into a Schlenk tube and treated in vacuo at 50 °C for 48 h. A smooth weight loss was consistent with a complete H_2O removal. A portion of the anhydrous $[Eu(hfac)_3]$ (0.61 g; 0.78 mmol) was dissolved in toluene (90 mL) and 4,4'-bipyridine (0.13 g; 0.80 mmol) was added. After 1 h stirring at about 100 °C, the yellow solution was slowly cooled to room temperature. From the resulting suspension crystalline

solid was filtered. Single crystals suitable for X-ray diffraction studies were obtained from the filtrate. Some crystals were selected in an atmosphere saturated with toluene and sealed in capillaries to perform X-ray diffraction studies. The remaining solid was dried in vacuo; 75% total yield. El. Anal. Calc. for $[Eu(hfac)_3(bipy)]$, $C_{25}H_{11}EuF_{18}O_6N_2$: C, 32.3; H, 1.2; Eu, 16.4; N, 3.0. Found: C, 32.6; H, 1.3; Eu, 16.6; N, 2.8%. ATR IR: (range: 1700–700 cm^{-1}) 1647 (s), 1608 (mw), 1558 (mw), 1534 (m), 1461 (ms), 1418 (mw), 1251 (s), 1199 (s), 1141 (s), 1101 (s), 1069 (m), 1047 (mw), 1005 (mw), 972 (w), 951 (w), 858 (w), 800 (ms), 767 (w), 733 (m).

6.5.10. Synthesis of $[Tb(hfac)_3(bipy)]_n$.

$[Tb(hfac)_3(H_2O)_2]$, (1.04 g; 1.28mmol) was introduced in a weighted vial and treated in vacuo at 50 °C for 48 h until complete H_2O loss. $[Tb(hfac)_3]$ (1.00 g; 1.28 mmol) was dissolved in toluene (100 mL) and 4,4'-bipyridine (0.20 g; 1.28 mmol) was added. The suspension was refluxed for 1 h obtaining a yellow solution which was slowly cooled to room temperature. A suspension of a microcrystalline solid was obtained, filtered and dried in vacuo; 85% yield. El. Anal. Calc. for $[Tb(hfac)_3(bipy)]$, $C_{25}H_{11}TbF_{18}O_6N_2$: C, 32.1; H, 1.2; N, 3.0; Tb, 17.0. Found: C, 30.0; H, 1.2; N, 3.3%; Tb, 17.8. ATR IR: (range: 700-1700 cm^{-1}) 1647 (s), 1608 (mw), 1558 (mw), 1534 (m), 1461 (ms), 1418 (mw), 1251 (s), 1199 (s), 1141 (s), 1101 (s), 1069 (m), 1047 (mw), 1005 (mw), 972 (w), 951 (w), 858 (w), 800 (ms), 767 (w), 733 (m).

6.5.11. Preparation of KBr pellets containing $[Ln(hfac)_3(bipy)]_n$ (Ln^{3+}= Eu^{3+}, Tb^{3+}) complexes.

Known amounts of $[Ln(hfac)_3(bipy)]_n$ (Ln^{3+}= Eu^{3+}, Tb^{3+}) CPs were dispersed in the proper amount of KBr to obtain the desired europium/terbium molar ratio; keeping constant and equal to $1.2 \cdot 10^{-4}$ the molar fraction of the sum of the two lanthanoid ions (χ_{Ln}^{3+}) was The mixture was grinded in an agate mortar adding few drops of *n*-pentane and dried under a slight N_2 flow. The mixture was then pressed forming the pellet. Six pellets have been prepared: the samples named **Eu** and **Tb** contained only $[Eu(hfac)_3(bipy)]_n$ and $[Tb(hfac)_3(bipy)]_n$ respectively, while the samples named

Eu1Tb1, **Eu1Tb3**, **Eu1Tb5**, and **Eu1Tb10** have been prepared mixing the two complexes so that the molar ratio between the two lanthanoid ions was 1:1, 1:3, 1:5, and 1:10 respectively. The values are summarized in **Table 6.1**. The reproducibility in the sample preparation has been tested observing that replicates of **Eu1Tb3** obtained with the same experimental procedure, have room temperature emission spectra normalized at 614 nm with an experimental error about 10% on the intensity ratio between Eu^{3+} $^5D_0 \rightarrow {}^7F_2$ (614 nm) and Tb^{3+} $^5D_4 \rightarrow {}^7F_5$ (543 nm) transitions (I_{Eu}/I_{Tb}).

Sample	**$[Eu(hfac)_3(bipy)]_n$**		**$[Tb(hfac)_3(bipy)]_n$**		**KBr**	
	mg	**mmol**	**mg**	**mmol**	**mg**	**mmol**
Eu	1.49	$1.60 \cdot 10^{-3}$	//	//	151.5	1.27
Tb	//	//	1.30	$1.39 \cdot 10^{-3}$	133.6	1.12
Eu1Tb1	1.05	$1.13 \cdot 10^{-3}$	1.04	$1.12 \cdot 10^{-3}$	209.6	1.76
Eu1Tb3	0.55	$0.59 \cdot 10^{-3}$	1.65	$1.77 \cdot 10^{-3}$	222.8	1.87
Eu1Tb5	0.59	$0.64 \cdot 10^{-3}$	2.99	$3.20 \cdot 10^{-3}$	362.1	3.04
Eu1Tb10	0.28	$0.31 \cdot 10^{-3}$	2.90	$3.10 \cdot 10^{-3}$	325.3	2.73

Table 6.1: Amounts of $[Eu(hfac)_3(bipy)]_n$ and $[Tb(hfac)_3(bipy)]_n$ dispersed in KBr in the different samples.

6.5.12. Synthesis of $Ln(NO_3)_3 \cdot xH_2O$ (Ln= Gd^{3+}, Eu^{3+}).

The proper amount of Ln_2O_3 (30 mmol) was dissolved in a diluted solution of HNO_3 (2 M)[280] heated at 60 °C for 4 h. The resulting solution was led to dryness under reduced pressure obtaining a colorless solid. The solid was dissolved in distilled water and dried in vacuo to reach a solution pH value between 5 and 6. The final solid was stored under inert atmosphere to prevent water absorption. The metal content was then evaluated via complexometric titration with EDTA according to the literature procedure.[281]

6.5.13. Synthesis of $\{[Gd_2(H_2DHT)_3(DMF)_4] \cdot 2DMF\}_n$.

$Gd(NO_3)_3 \cdot 5.3\ H_2O$ (0.23 g; 0.52 mmol) and H_2DHT (0.16 g; 0.81 mmol) were dissolved in DMF (13 mL) inside a 200 mL Carius. The resulting pale-yellow solution was heated at 90 °C for 2 days. The formation and the growth of crystals of the desired product was gradually observed. The resulting yellowish crystalline solid was

air filtered and dried under reduced pressure for 4 h. (0.32 g, 90.2 % yield as $\{[Gd_2(H_2DHT)_3(DMF)_4]\cdot 2DMF\}_n$) El. Anal. Calc. for $\{[Gd_2(H_2DHT)_3(DMF)_4]\cdot 2DMF\}_n$, $C_{42}H_{58}N_6Gd_2O_{26}$, %: Teor: C 36.6; H 4.2; N 6.1. Found: C 36.7; H 4.0; N 6.4. IR-ATR (range 4000 - 650 cm^{-1}): 3200 – 3010br, 2934w, 1675s, 1643s, 1610s, 1579m, 1495s, 1435s, 1385s, 1368s, 1324m, 1307m, 1240s, 1231s, 1109m, 1094w, 1063w, 904w, 878w, 869m, 813s, 794s, 783s, 730m, 679s, 670s, 660m.

6.5.14. Synthesis of $\{[Eu_2(H_2DHT)_3(DMF)_4]\cdot 2DMF\}_n$.

$Eu(NO_3)_3\cdot 2.4\ H_2O$ (0.19 g; 0.49 mmol) and H_2DHT (0.15 g; 0.76 mmol) were dissolved in DMF (13 mL) inside a 200 mL Carius tube. The solution was heated at 90 °C for 2 days until the formation of pale-yellow crystals which were filtered and dried under reduced pressure for 4 h. (0.28 g, 87.4 % yield as $\{[Eu_2(H_2DHT)_3(DMF)_4]\cdot 2DMF\}_n$) El. Anal. Calc. for $\{[Eu_2(H_2DHT)_3(DMF)_4]\cdot 2DMF\}_n$, $C_{42}H_{58}N_6Eu_2O_{26}$, %: Teor: C 36.9; H 4.3; N 6.2. Found: C 36.4; H 4.1; N 6.2. IR-ATR (range 4000 - 650 cm^{-1}): 3200-3050br, 2937w, 1675s, 1643s, 1609s, 1578m, 1495s, 1435s, 1385s, 1368s, 1324m, 1307m, 1239s, 1109m, 867m, 813s, 793s, 783s, 730m, 679s, 670s, 660m.

6.5.15. Formation of $\{[Eu_2(H_2DHT)_3(DMF)_4]\cdot CHCl_3\}_n$.

A known amount of $\{[Eu_2(H_2DHT)_3(DMF)_4]\cdot 2DMF\}_n$ (0.16 g, 0.12 mmol) was suspended in chloroform (5 mL). The release of DMF at room temperature into the organic phase was monitored through liquid IR spectroscopy (absorption at 1672 cm^{-1}). The liquid phase was renewed daily till completeness of the extraction process which occurred after 7 d of treatment. The overall release amounting to approximately 2.0 molecule of DMF per formula unit. The light-brown solid was then filtered, dried and stored under nitrogen atmosphere (0.109 g, 64.9 % yield as $\{[Eu_2(H_2DHT)_3(DMF)_4]\ CHCl_3\}_n$). El. Anal. Calc. for $\{[Eu_2(H_2DHT)_3(DMF)_4]\cdot CHCl_3\}_n$, $C_{37}H_{41}N_4Cl_3Eu_2O_{22}$, %: Teor: C, 34.0 ; H, 3.2; N, 4.3 %. Found: C, 33.8; H, 3.3; N, 4.3. IR-ATR (range 4000 - 650 cm^{-1}): 1680m, 1646m, 1609m, 1582m, 1496m, 1435s, 1304s, 1240s, 1221s, 1107m, 1061w, 1011w, 912w, 899w,

870m, 813s, 792s, 783s, 753s, 724s, 680s, 668s. For similar precursor/solvent proportions the substitution of the hosted solvent at about 45°C was complete in 2 d.

6.5.16. Formation of $[Eu_2(H_2DHT)_3(im)_4][Eu_2(H_2DHT)_3(im)_2(H_2O)_2]$ 6Im ·2CHCl$_3$}$_n$.

{$[Eu_2(H_2T)_3(DMF)_4]$·2DMF}$_n$ (0.15 g, 0.11 mmol) was suspended in chloroform (5 mL) in a 20 mL Carius tube and the amount of DMF released into the organic phase, renewed daily, was monitored with the same frequency relying on the corresponding liquid IR spectrum. After 7 days, the overall DMF released was 0.38 mmol of DMF corresponding to about 2 molecules of DMF per formula unit. The solid phase was then treated with a solution of imidazole in chloroform (5 mL, 1.2 M). The liquid phase was renewed daily till the release of DMF reached completeness (15 d). The treatment yielded a light-brown crystalline solid which was recovered by filtration and air-dried. (0.28 g, 96 % yield as {$[Eu_2(H_2T)_3(im)_4][Eu_2(H_2T)_3(im)_2(H_2O)_2]$ · 6Im ·2CHCl$_3$}$_n$). El. Anal. Calc. for {$[Eu_2(H_2T)_3(im)_4][Eu_2(H_2T)_3(im)_2(H_2O)_2]$·6Im ·2CHCl$_3$}$_n$, $C_{43}H_{39}N_{24}Cl_3Eu_2O_{19}$, %: Teor: C, 36.4; H, 2.6; N, 11.8. Found: C, 36.5; H, 3.0; N, 11.8. IR-ATR (range 4000 - 650 cm^{-1}): 3500-2500br, 1614m, 1581m, 1488s, 1445s, 1359s, 1324s, 1233s, 1107m, 1063s, 935w, 870m, 843m, 813s, 793s, 782s, 749s, 657s. For similar reagents/solvent proportions the substitution of the coordinated DMF at about 45 °C was complete in 2 d. The product converted back to {$[Eu_2(DHBDC)_3(DMF)_4]$ · 2DMF}$_n$ when treated with hot DMF (after 12 h at 90°C) as recognized by IR and powder XRD studies.

6.5.17. Post Synthesis Modification of {$[Eu_2(H_2DHT)_3(DMF)_4)]$ · 2DMF}$_n$ with Pyridine.

{$[Eu_2(H_2DHT)_3(DMF)_4]$·2DMF}$_n$ (0.15 g, 0.11 mmol) was suspended in a chloroform solution containing Py (5 mL, 1.2 M) in a Carius tube. The mixture was heated at 45 °C for 3 d. After the treatment, a yellowish microcrystalline solid was recovered. According to liquid IR measurements, 0.38 mmol of DMF were released during the treatment (55.3 % of the total DMF molecules). IR-ATR (range 4000 - 650 cm^{-1}):

3500-2800w, 1652m, 1616m, 1574m, 1489s, 1443s, 1367s, 1304w, 1238s, 1153w, 1111m, 1067w, 1038w, 1005w, 907w, 871m, 812s, 792s, 785s, 748m, 701s, 678s. The IR spectrum coincide with that of the Gd^{3+} analogue with analytical composition $\{[Gd_2(H_2DHT)_3(DMF)_2(H_2O)_2]\cdot 2Py\cdot 2H_2O\}_n$.[201]

6.5.18. Post Synthesis Modification of $\{[Eu_2(H_2DHT)_3(DMF)_4)]\cdot 2DMF\}_n$ with THF.

$\{[Eu_2(H_2DHT)_3(DMF)_4]\cdot 2DMF\}_n$ (0.15 g, 0.11 mmol) was suspended in a chloroform solution containing THF (5 mL, 1.2 M) in a Carius tube. The mixture was heated at 45 °C for 3 d. After the treatment, a pale-yellow solid was recovered. According to IR measurements, 0.26 mmol of DMF were released during the treatment (38.6 % of the total DMF molecules). IR-ATR (range 4000 - 650 cm^{-1}): 3400-2900w, 1679m, 1652m, 1614m, 1580m, 1560w, 1551w, 1539w, 1506m, 1435s, 1364s, 1240s, 1223s, 1108m, 1063w, 900w, 870m, 834w, 813s, 793s, 783s, 728m, 680s, 671s. Also in this case, the IR spectrum coincide with that of the Gd^{3+} analogue with analytical composition $\{[Gd_2(H_2DHT)_3(DMF)_4]\cdot 0.5THF\cdot 4H_2O\}_n$.[201]

6.5.19. Solubility of H_2T in Py.

Pyridine (4 mL) was added in portions of 1 mL to H_2T (0.40 g, 2.40 mmol) until complete dissolution of the dicarboxylic acid obtaining a pale-yellow solution (0.6 M in H_2T). By cooling to -20 °C crystals of the molecular adduct $H_2T\cdot 2Py$ were obtained. The suspension was filtered at low temperature. The crystals collapsed by treatment in vacuo at room temperature with loss of pyridine. The solid residue resulted to be H_2T. IR-ATR (the most significant bands, cm^{-1}) 1676s, 1574m, 1509m, 1423m.

6.5.20. Reaction of H_2T with $NHBu_2$ in Py.

H_2T (0.80 g, 4.8 mmol) was dissolved in pyridine (12mL) and then $HNBu_2$ was added (0.81mL, 4.8mmol). For evaporation of the resulting yellow solution at room temperature colorless crystals suitable for XRD diffraction studies were obtained. Anal. Calc. for $(H_2NBu_2)(HT)$, $C_{16}H_{25}O_4N$: C, 65.1; H, 4.7; N, 8.5%. Found C, 65.2; H,

4.3; N, 8.5 %. IR-ATR (the most significant bands, cm–1): 1685m, 1623m, 1551m, 1502m, 1472m, 1372s. ^{1}H-NMR (d^{6}-DMSO), δ (ppm): 0.88 (t, 6H), 1.31 (m, 4H), 1.58 (m, 4H), 2.84 (t, 4H), 7.91ppm (s, 4H). ^{13}C-NMR (d^{6}-DMSO), δ (ppm):13.39, 19.30, 27.83, 46.33, 158.57, 167.88. Crystallographic studies allowed to establish the nature of the solid product as $(NH_2Bu_2)_2(T) \cdot H_2T$.

6.5.21. Reaction of H_2T and $[Eu(O_2CNBu_2)_3]$ in Py.

H_2T (6.02 g, 36.2 mmol) was dissolved in pyridine (60 mL) and $[Eu(O_2CNBu_2)_3]$ (2.18 g, 3.2 mmol) was added. The white suspension was stirred for 24 h at room temperature repeating several vacuum/ dinitrogen cycles. CO_2 formation was observed during the reaction. The white solid was then filtered and washed with pyridine (20 mL) under vigorous stirring for one hour and then dried under reduced pressure at room temperature for 2 days (1.89 g; 81.8 % yield as $[Eu_2(T)(HT)_4(Py)_4]$). El. Anal. Calc. for $[Eu_2(T)(HT)_4(Py)_4]$, $C_{60}H_{44}Eu_2N_4O_{26}$, %: Teor: Eu, 21.0. Found: Eu, 21.5. IR-ATR (range: 3500-700 cm^{-1}): 3300-2700 w, 2961w, 2873w, 1764 w, 1692w, 1539m, 1367s, 1217w, 1153w, 1091w, 1018w, 811m, 750s, 703m. A small fraction of $[Eu_2(T)(HT)_4(Py)_4]$ (0.55 g, 0.38 mmol) was extracted with hot pyridine (25 mL) for 9 h. The resulting colorless solid was dried under vacuum at room temperature (0.24 g; 66 % yield as $[Eu_2(T)_4(Py)_2]$). El. Anal. Calc. for $[Eu_2(T)_4(Py)_2]$, $C_{34}H_{22}Eu_2N_2O_{12}$, %: Teor: Eu, 31.8. Found: Eu, 30.9. IR-ATR (range: 3500-700 cm^{-1}): 3054w, 1643w, 1557s, 1504m, 1444m, 1392s, 1308w, 1215w, 1159w, 1096w, 1069w, 1037w, 1017w, 1005w, 823m, 748s, 700s. A white solid was recovered from the reaction filtrate whose IR spectrum coincides with that of H_2T (0.09 g; 74 % yield). Further extractions led to the recovery of small amounts of a mixture of H_2T and $(H_2NBu_2)(HT)$ characterized by IR spectroscopy.

6.5.22. Grafting of $[Eu(O_2CNBu_2)_3]$ on silica.

A pale-yellow solution of $[Eu(O_2CNBu_2)_3]$ (2.83 g, 4.25 mmol) in toluene (100 mL) was reacted under dinitrogen atmosphere with SiO_2 (6.10 g) The suspension was stirred for 55 h under dinitrogen atmosphere, repeating vacuum/dinitrogen cycles.

The solid was then filtered, washed with toluene (25 mL) and dried in vacuo at room temperature for 15 h. The product was labelled **1Eu**. IR-ATR (bands in the range 1700-1250 cm^{-1}): 1521, 1505, 1495, 1434, 1380, 1324, 1316. Analysis of the metal content of the pale-yellow filtrate could establish that about 0.30 mmol per gram of silica had been loaded.

6.5.23. Grafting of [$Tb(O_2CNBu_2)_3$] on silica.

A pale-yellow solution of $Tb(O_2CNBu_2)_3$ (2.75 g, 4.08 mmol) in toluene (100 mL) was reacted under dinitrogen atmosphere with SiO_2 (6.04g) The suspension was stirred for 55 h under dinitrogen atmosphere, repeating vacuum/dinitrogen cycles. The solid was then filtered, washed with toluene (25 mL) and dried in vacuo at room temperature for 15 h. The product was labelled **1Tb**. IR-ATR (bands in the range 1700-1250 cm^{-1}): 1521, 1505, 1495, 1434, 1380, 1324, 1316. Analysis of the metal content of the pale-yellow filtrate could establish that about 0.33 mmol per gram of silica had been loaded.

6.5.24. Grafting of [$Y(O_2CNBu_2)_3$] on silica.

A pale-yellow solution of $Y(O_2CNBu_2)_3$ (2.54 g, 4.20 mmol) in toluene (100 mL) was reacted under dinitrogen atmosphere with SiO_2 (5.47 g) The suspension was stirred for 55 h under dinitrogen atmosphere, repeating vacuum/dinitrogen cycles. The solid was then filtered, washed with toluene (25 mL) and dried in vacuo at room temperature for 15 h. The product was labelled **1Y**. IR-ATR (bands in the range 1700-1250 cm^{-1}): 1521, 1505, 1495, 1429, 1380, 1324, 1316. Analysis of the metal content of the pale-yellow filtrate could establish that about 0.30 mmol per gram of silica had been loaded.

6.5.25. Functionalization of 1Eu with H_2T.

A sample of silica functionalized with europium, **1Eu**, (5.07 g, 1.52 mmol of Eu^{3+}) was suspended in pyridine (100 mL) and reacted with H_2T (1.14 g, 6.87 mmol). After 22 h stirring, regularly repeating vacuum/dinitrogen cycles, the suspension was

filtered, washed twice with fresh pyridine (50 mL + 20 mL) and dried in vacuo for 15 h at room temperature. The product was labelled **2Eu-TH**. IR-ATR (bands in the range 1700-1250 cm^{-1}): 1658, 1621, 1599, 1567, 1503, 1444, 1384. No traces of leached metal were found in the filtrate.

6.5.26. Functionalization of 1Tb with H_2T.

A sample of silica functionalized with terbium, **1Tb**, (5.84 g, 1.93 mmol of Tb^{3+}) was suspended in pyridine (100 mL) and reacted with H_2T (1.45 g, 8.73 mmol). After 22 h stirring, regularly repeating vacuum/dinitrogen cycles, the suspension was filtered, washed twice with fresh pyridine (50 mL + 20 mL) and dried in vacuo for 15 h at room temperature. The product was labelled **2Tb-TH**. IR-ATR (bands in the range 1700-1250 cm^{-1}): 1658, 1621, 1599, 1567, 1503, 1444, 1384. No traces of leached metal were found in the filtrate.

6.5.27. Functionalization of 1Y with H_2T.

A sample of silica functionalized with yttrium, **1Y**, (5.35 g, 1.60 mmol of Y^{3+}) was suspended in pyridine (100 mL) and reacted with H_2T (1.20 g, 7.22 mmol). After 55 h stirring, regularly repeating vacuum/dinitrogen cycles, the suspension was filtered, washed twice with fresh pyridine (50 mL + 20 mL) and dried in vacuo for 16 h at room temperature. The product was labelled **2Y-TH**. IR-ATR (bands in the range 1700-1250 cm^{-1}): 1667, 1625, 1599, 1567, 1503, 1444, 1391. No traces of leached metal were found in the filtrate.

6.5.28. Deposition of $Tb(O_2CNBu_2)_3$ on 2Eu-TH.

A sample of **2Eu-TH** (3.23 g, 0.97 mmol of Eu^{3+}) was suspended in pyridine (75 mL) and reacted with $[Tb(O_2CNBu_2)_3]$ (1.65 g, 2.24 mmol). The suspension was stirred for 22 h repeating vacuum/dinitrogen cycles, filtered, washed with 30 mL of pyridine and the dried in vacuo for 13 h at room temperature. The product was labelled **3Eu-T-Tb**. IR-ATR (bands in the range 1700-1250 cm^{-1}): 1658, 1621, 1599, 1567, 1505, 1444, 1424, 1384. Analysis of the metal content of the filtrate could establish that about 1.0

mmol of Tb3+ had been loaded corresponding to an Eu/Tb molar ratio in **3Eu-T-Tb** of about 1.0. This ratio was about 1 also according to SEM-EDS measurements and 1.13 ± 0.02 according to ICP analysis.

6.5.29. Deposition of $Tb(O_2CNBu_2)_3$ on 2Y-TH.

A sample of **2Y-TH** (3.01 g, 0.86 mmol of Y^{3+}) was suspended in pyridine (75 mL) and reacted with $[Tb(O_2CNBu_2)_3]$ (1.47 g, 2.18 mmol). The suspension was stirred for 22 h repeating vacuum/dinitrogen cycles, filtered, washed with 30 mL of pyridine and the dried in vacuo for 15 h at room temperature. The product was labelled **3Y-T-Tb**. IR-ATR (bands in the range 1700-1250 cm^{-1}): 1665, 1626, 1601, 1567, 1505, 1444, 1391. Analysis of the metal content of the filtrate could establish that about 1.07 mmol of Tb^{3+} had been loaded corresponding to a Y/Tb molar ratio in **3Y-T-Tb** of 0.9.

6.5.30. Preparation of 2(Eu+Tb)-TH.

A pale-yellow solution of $Eu(O_2CNBu_2)_3$ (0.19 g, 0.29 mmol) and $Tb(O_2CNBu_2)_3$ (0.22 g, 0.33 mmol) in toluene (40 mL) was reacted under dinitrogen atmosphere with SiO_2 (0.24 g). The suspension was stirred for 24 h under dinitrogen atmosphere, repeating vacuum\dinitrogen cycles; the solid was then filtered and washed with toluene (10 mL). Analysis of the metal content of the filtrate could establish that about 0.077 mmol of (Tb^{3+} + Eu^{3+}) had been loaded corresponding to 0.32 mmol of lanthanoids per gram of silica. The functionalized silica was suspended in pyridine (40 mL) and H_2T (0.10 g, 0.6 mmol) was added. The suspension was stirred overnight and the solid was then filtered, washed with pyridine (20 mL) and dried in vacuo at room temperature. The product was tagged **2(Eu+Tb)-TH**. IR-ATR (bands in the range 1700-1250 cm^{-1}): 1660, 1621, 1599, 1501, 1444, 1384.

Appendix 1: The Mott-Seitz equation

The energy of an electronically excited state is lost by a combination of radiative and non-radiative deactivation pathways. According to the classical Mott-Seitz model,[124,125] the total transition probability (W) of an emitting level, with lifetime τ, can be described as:

$$W = W_R + W_{NR} \qquad \textbf{Equation A1.1}$$

or

$$W = \frac{1}{\tau(T)} = \frac{1}{\tau_R} + \frac{1}{\tau_{NR}} \qquad \textbf{Equation A1.2}$$

Where T is the absolute temperature, W_R and W_{NR} are the radiative and non-radiative deactivation probabilities, respectively; τ_R is the radiative lifetime, assumed to be temperature independent and equal to τ_0 (T= 0 K); and τ_{NR} is the non-radiative lifetime described by an Arrhenius type dependence:

$$\tau_{NR} = \tau_{NR}(0) \cdot \exp(\Delta E / k_b T) \qquad \textbf{Equation A1.3}$$

with ΔE the activation energy for the non-radiative deactivation pathways, k_b the Boltzmann constant, and $\tau_{NR}(0)$ the non-radiative decay time at T= 0 K.

Solving **Equation A1.2** for the total (experimentally measured) lifetime, it can be written:

$$\tau(T) = \frac{\tau_0}{1 + \alpha \cdot \exp(-\Delta E / k_b T)} \qquad \textbf{Equation A1.4}$$

where $\alpha = \tau_0 / \tau_{NR}(0) = W_{NR}^0 / W_R^0$.

The **Equation A1.4** shows the temperature dependence of the fluorophore lifetime with temperature. In more general terms, considering more than one deactivation pathways with its corresponding transition probabilities (W_{NR1}, W_{NR2}, … W_{NRn}), the Mott-Seitz equation can be written as follow:

$$\tau(T) = \frac{\tau_0}{1 + \sum_{i=1}^{n} \alpha_i \cdot \exp(-\Delta E_i / k_b T)} \qquad \textbf{Equation A1.5}$$

As concern intensity-based luminescence thermometers, the Mott-Seitz equation can be rewritten considering the relation between $\tau(T)$ and the integrated luminescence intensity, $I(T)$:[44]

$$I(T) = \frac{C \cdot \tau(T)}{\tau_0} \qquad \textbf{Equation A1.6}$$

Where C is a constant comprised of a number of physical parameters that are characteristic of the measuring system and investigated material (e.g. intensity of excitation, detection geometry, concentration of the fluorophore etc.).

Introducing **Equation A1.6** in **Equation A1.5** the Mott-Seitz equation for the luminescence intensity variation can be derived:

$$I(T) = \frac{I_0}{1 + \sum_{i=1}^{n} \alpha_i \cdot \exp(-\Delta E_i / k_b T)} \qquad \textbf{Equation A1.7}$$

where I_0 is the integrated intensity at 0 K,

In a ratiometric thermometer based on two emitters *1* and *2* (which can be also different transition of the same emitter), characterized by integrated luminescence intensities I_1 and I_2 respectively, the thermometric parameter (Δ) is defined as the ratio of the I_1 and I_2 integrated intensities.

In this case, the general temperature dependence of Δ, $\Delta(T)$, is given by (considering a single deactivation channel for both the emitters, for simplicity):

$$\Delta(T) = \frac{I_1}{I_2} = \frac{I_{01}}{1 + \alpha_1 \cdot \exp(-\Delta E_1 / k_b T)} \cdot \frac{1 + \alpha_2 \cdot \exp(-\Delta E_2 / k_b T)}{I_{02}} \qquad \textbf{Equation A1.8}$$

Where I_{01} and I_{02} are the integrated intensities at 0 K of the emitter *1* and *2*, respectively ($I_{01}/I_{02} = \Delta_0$).

The general **Equation A1.8** can be rearranged in two peculiar case: *i*) when one transition (e.g. I_2) exhibits a temperature dependence much smaller than the other; *ii*) when the exponential terms dominate the intensity of each transition ($1 << \alpha \cdot \exp(-\Delta E / k_b T)$.

In case *i*), $I_2 \approx I_{02}$ and **Equation A1.8** becomes **Equation A1.9**:

$$\Delta(T) = \frac{\Delta_0}{1 + \alpha_1 \cdot \exp(-\Delta E_1 / k_b T)} \qquad \textbf{Equation A1.9}$$

In case *ii*), when the exponential terms dominate the intensity of each transition, **Equation A1.8** may be written as **Equation A1.10**:

$$\Delta(T) = \Delta_0 \frac{1 + \alpha_2 \cdot \exp(-\Delta E_2 / k_b T)}{1 + \alpha_1 \cdot \exp(-\Delta E_1 / k_b T)} \approx \Delta_0 \frac{\alpha_2}{\alpha_1} \exp\left(-\frac{\Delta E_2 - \Delta E_1}{k_b T}\right) \qquad \textbf{Equation A1.10}$$

Appendix 2: Temperature resolution

The temperature resolution (or temperature uncertainty, δT) is the smallest temperature variation that may be measured.

Assuming that temperature uncertainty of a thermometer results only from changes of its thermometric parameter (Δ), δT can be estimated as the first term of the expansion of the temperature change with Δ:[35,44,55]

$$\delta T = \left|\frac{\partial T}{\partial \Delta}\right| \cdot \delta\Delta \qquad \textbf{Equation A2.1}$$

where $\delta\Delta$ is the uncertainty in the determination of Δ. The **Equation A2.1** can be rewritten in terms of the relative thermal sensitivity ($S_r = \frac{1}{\Delta} \cdot \left|\frac{\partial \Delta}{\partial T}\right|$, see **Equation (1.2)** page 13) in the following form:

$$\delta T = \frac{1}{S_r} \cdot \frac{\delta\Delta}{\Delta} \qquad \textbf{Equation A2.2}$$

where $\delta\Delta/\Delta$ is the relative uncertainty on Δ. In our case, $\delta\Delta$ derives from three different measurements. According to **Equation A2.2**, δT values varying between 0.001 and 0.1 °C were found in the respective applicative temperature range for all the thermometers studied in this work. These values are equal or lower than the temperature resolution of our experimental apparatus which is of 0.1 °C and therefore it would be considered as the overall system resolution.

Bibliography

1 S. Cotton, *Lanthanide and Actinide Chemsitry*, Jhon Wiley & Sons Ltd., 2006.

2 J.-C. G. Bünzli and C. Piguet, *Chem. Soc. Rev.*, 2005, **34**, 1048–1077.

3 K. Binnemans, *Handb. Phys. Chem. Rare Earths*, 2005, **225**, 111–277.

4 P. A. Vigato, V. Peruzzo and S. Tamburini, *Coord. Chem. Rev.*, 2009, **253**, 1099–1201.

5 O. Guillou and C. Daiguebonne, *Handb. Phys. Chem. Rare Earths*, 2004, **221**, 359–402.

6 P. Cheng, *Lanthanide Metal-Organic Frameworks*, Springer, 2015.

7 J.-G. Mao, *Coord. Chem. Rev.*, 2007, **251**, 1493–1520.

8 K. Binnemans, *Coord. Chem. Rev.*, 2015, **295**, 1–45.

9 X. Rao, Q. Huang, X. Yang, Y. Cui, Y. Yang, C. Wu, B. Chen and G. Qian, *J. Mater. Chem.*, 2012, **22**, 3210–3214.

10 K. Liu, H. You, Y. Zheng, G. Jia, Y. Huang, M. Yang, Y. Song, L. Zhang and H. Zhang, *Cryst. Growth Des.*, 2010, **10**, 16–19.

11 S.-L. Zhong, R. Xu, L.-F. Zhang, W.-G. Qu, G.-Q. Gao, X.-L. Wu and A.-W. Xu, *J. Mater. Chem.*, 2011, **21**, 16574–16580.

12 S. Petoud, G. Muller, E. G. Moore, J. Xu, J. Sokolnicki, J. P. Riehl, U. N. Le, S. M. Cohen and K. N. Raymond, *J. Am. Chem. Soc.*, 2007, **129**, 77–83.

13 M. D. Regulacio, M. H. Pablico, J. A. Vasquez, P. N. Myers, S. Gentry, M. Prushan, S.-W. Tam-Chang and S. L. Stoll, *Inorg. Chem.*, 2008, **47**, 1512–1523.

14 K. A. White, D. A. Chengelis, K. A. Gogick, J. Stehman, N. L. Rosi and S. Petoud, *J. Am. Chem. Soc.*, 2009, **131**, 18069–18071.

15 J.-C. G. Bünzli, *Inorg. Chim. Acta*, 1987, **139**, 219–222.

16 R. E. Whan and G. A. Crosby, *J. Mol. Spectrosc.*, 1962, **8**, 315–327.

17 G. A. Crosby, R. E. Whan and R. M. Alire, *J. Chem. Phys.*, 1961, **34**, 743–748.

18 G. A. Crosby, R. E. Whan and J. J. Freeman, *J. Phys. Chem.*, 1962, **66**, 2493–2499.

19 N. Sabbatini, M. Guardigli and J.-M. Lehn, *Coord. Chem. Rev.*, 1993, **123**, 201–228.

20 B. Chen, Y. Yang, F. Zapata, G. Qian, Y. Luo, J. Zhang and E. B. Lobkovsky, *Inorg. Chem.*, 2006, **45**, 8882–8886.

21 D. T. de Lill, A. de Bettencourt-Dias and C. L. Cahill, *Inorg. Chem*, 2007, **46**, 3960–3965.

22 D. T. de Lill, N. S. Gunning and C. L. Cahill, *Inorg. Chem*, 2005, **44**, 258–266.

23 Y. K. Park, S. B. Choi, H. Kim, K. Kim, B. Won, K. Choi, J. Choi, W. Ahn, N. Won, S. Kim, D. H. Jung, S. Choi, G. Kim, S. Cha, Y. H. Jhon, J. K. Yang and J. Kim, *Anghew. Chem. Int. Ed.*, 2007, **46**, 8230–8233.

24 A. Beeby, S. Faulkner, D. Parker and J. A. G. Williams, *J. Che. Soc. Dalton.*

Trans., 2001, **2**, 1268–1273.
25 D. Barry, D. F. Caffrey and T. Gunnlaugsson, *Chem. Soc. Rev.*, 2016, **45**, 3244–3274.
26 M. T. Berry, P. S. May and H. Xu, *J. Phys. Chem.*, 1996, **100**, 9216–9222.
27 M. L. Bhaumik, *J. Chem. Phys.*, 1964, **40**, 3711–3715.
28 S. I. Weissman, *J. Chem. Phys.*, 1942, **10**, 214–217.
29 F. F. Tao and S. L. Bernasek, *Functionalization of Semiconductor Surfaces*, John Wiley & Sons, Inc., 2012.
30 A. Facchetti, *Mater. Today*, 2007, **10**, 28–37.
31 J. E. Anthony, *Chem. Rev.*, 2006, **106**, 5028–5048.
32 T. M. I. Mahlia, T. J. Saktisahdan, A. Jannifar, M. H. Hasan and H. S. C. Matseelar, *Renew. Sustain. Energy Rev.*, 2014, 33, 532–545.
33 C. Liu, F. Li, M. Lai-Peng and H. M. Cheng, *Adv. Mater.*, 2010, 22.
34 L. Armelao, S. Quici, F. Barigelletti, G. Accorsi, G. Bottaro, M. Cavazzini and E. Tondello, *Coord. Chem. Rev.*, 2010, 254, 487–505.
35 L. D. Carlos and F. Palacio, *Thermometry at the Nanoscale: Techniques and Selected Applications*, The Royal Society of Chemistry, 2016.
36 K. Binnemans, *Chem. Rewievs*, 2009, **109**, 4283–4374.
37 O. Guillou, C. Daiguebonne, G. Calvez and K. Bernot, *Acc. Chem. Res.*, 2016, **49**, 844–856.
38 Y. Hasegawa and T. Nakanishi, *RSC Adv.*, 2015, 5, 338–353.
39 P. Atkins and J. de Paula, *Atkins' Physical Chemistry*, 10th edn., 2014.
40 C. D. S. Brites, S. Balabhadra and L. D. Carlos, *Adv. Opt. Mater.*, 2019, **7**, 1801239–1801269.
41 Grand View Research, *Temp. Sensors Mark. By Appl. (Automotive, Consum. Electron. Environ. Medical, Process Ind. Segm. Forecast to 2020.*
42 P. R. N. Childs, J. R. Greenwood and C. A. Long, *Rev. Sci. Instrum.*, 2000, **71**, 2959–2978.
43 X.-D. Wang, Wolfbeis; Otto S. and R. J. Meier, *Chem. Soc. Rev*, 2013, **42**, 7834–7869.
44 M. Dramićanin, *Luminescence Thermometry*, Elsevier, 2018.
45 C. D. S. Brites, P. P. Lima and L. D. Carlos, *J. Lumin.*, 2016, **169**, 497–502.
46 C. D. S. Brites, A. Millán and L. D. Carlos, *Handb. Phys. Chem. Rare Earths*, 2016, **49**, 339–427.
47 C. F. Chapman, Y. Liu, G. J. Sonek and B. J. Tromberg, *Photochem. Photobiol.*, 1995, **62**, 416–425.
48 C. Gota, S. Uchiyama, T. Yoshihara, S. Tobita and T. Ohwada, *J. Phys. Chem. B*, 2008, **112**, 2829–2836.
49 K. Okabe, N. Inada, C. Gota, Y. Harada, T. Funatsu and S. Uchiyama, *Nat. Commun.*, 2012, **3**, 705 1–9.
50 B. H. Peng, M. I. J. Stich, L. Yu, J.; Sun, L. H. Fischer and O. S. Wolfbeis, *Adv. Mater.*, 2010, **22**, 716–719.

51 T. Liu, B. T. Campbell, S. P. Burns and J. P. Sullivan, *Appl. Mech. Rev.*, 2009, **50**, 227–246.
52 T. Liu, in *Encyclopedia of Aerospace Engineering*, John Wiley & Sons, Ltd, 2011.
53 C. D. S. Brites, P. P. Lima, N. J. O. Silva, A. Millán, V. S. Amaral, F. Palacio and L. D. Carlos, *Nanoscale*, 2012, **4**, 4799–4829.
54 M. Quintanilla, A. Benayas, R. Naccache and F. Vetrone, *Thermometry at the Nanoscale: Techniques and Selected Applications*, The Royal Society of Chemistry, 2016.
55 J. Rocha, C. D. S. Brites and L. D. Carlos, *Chem. A. Eur. J.*, 2016, **22**, 14782-14795.
56 D. Ross, M. Gaitan and L. E. Locascio, *Anal. Chem.*, 2001, **73**, 4117–4123.
57 X. L. Guan, X. Y. Liu, Z. X. Su and P. Liu, *React. Funct. Polym.*, 2006, **66**, 1227–1239.
58 F. H. C. Wong and C. Fradin, *J. Fluoresc.*, 2011, **21**, 299–312.
59 A. Pucci, F. Signori, R. Bizzarri, S. Bronco, G. Ruggeri and F. Ciardelli, *J. Mater. Chem.*, 2010, **20**, 5843–5852.
60 R. V. de la Rosa, P. Woisel and R. Hoogenboom, *Mater. Today*, 2016, **19**, 44–55.
61 C. Pietsch, U. S. Schubert and R. Hoogenboom, *Chem. Commun.*, 2011, **47**, 8750–8765.
62 C. Gota, K. Okabe, T. Funatsu, Y. Harada and S. Uchiyama, *J. Am. Chem. Soc.*, 2009, **131**, 2766–2767.
63 L. D. Carlos, V. de Zea Bermudez, V. S. Amaral, S. C. Nunes, N. J. O. Silva, R. A. S. Ferreira, J. Rocha, C. V. Santilli and D. Ostrovskii, *Adv. Mater.*, 2007, **19**, 341–348.
64 R. Maestro, L. M.; Rodríguez, E. M.; Rodríguez, F. S.; Iglesias de la Cruz, M. C.; Juarranz, Á.; Naccache, F. Vetrone, D. Jaque, J. A. Capobianco and J. G. Solé, *Nano Lett.*, 2010, **10**, 5109–5115.
65 L. M. Maestro, P. Haro-González, M. C. Iglesias de la Cruz, F. Sanz Rodríguez, Á. Juarranz, J. G. Solé and D. Jaque, *Nanomedicine*, 2013, **8**, 379–388.
66 V. Lojpur, M. G. Nikolić and M. D. Dramićanin, *J. Appl. Phys.*, 2014, **15**, 2031061–7.
67 O. A. Savchuk, P. Haro-Gonzalez, J. J. Carvajal, D. Jaque, J. Massons, M. Aguilo and F. Diaz, *Nanoscale*, 2014, **7**, 9727–9733.
68 F. Vetrone, R. Naccache, A. Zamarrón, Á. J. de la Fuente, F. Sanz-Rodríguez, L. M. Maestro, E. M. Rodríguez, D. Jaque, J. G. Solé and J. A. Capobianco, *ACS Nano*, 2010, **4**, 3254–3258.
69 S. Balabhadra, M. L. Debasu, C. D. Brites, L. A. Nunes, O. L. Malta, J. Rocha, M. Bettinelli and L. D. Carlos, *Nanoscale*, 2015, **7**, 17261–17267.
70 A. Benayas, B. del Rosal, A. Pérez-Delgado, K. Santacruz-Gómez, D. Jaque, G. A. Hirata and F. Vetrone, *Adv. Opt. Mater.*, 2015, **3**, 687–694.

71 M. Bettinelli, L. D. Carlos and X. Liu, *Phys. Today*, 2015, **68**, 38–44.
72 L. H. Fischer, G. S. Harms and O. S. Wolfbeis, *Angew. Chemie, Int. Ed.*, 2011, **50**, 4546–4551.
73 F. Wang, C.; Zhang, *Photon Upconversion Nanomaterials, 1st ed.*, Springer, Berlin, 2015.
74 U. Rocha, K. U. Kumar, C. Jacinto, I. Villa, F. Sanz-Rodríguez, M. C. Iglesias de la Cruz, A. Juarranz, E. Carrasco, F. C. van Veggel, E. Bovero and J. G. Solé, *Small*, 2014, **10**, 1141–1154.
75 C. D. S. Brites, P. P. Lima, N. J. O. Silva, A. Millán, V. S. Amaral, F. Palacio and L. D. Carlos, *Adv. Mater.*, 2010, **22**, 4499–4504.
76 S. Uchiyama, A. P. de Silva and K. Iwai, *J. Chem. Educ.*, 2006, **83**, 720–727.
77 A. Cadiau, C. D. S. Brites, P. M. F. J. Costa, R. A. S. Ferreira, J. Rocha and L. D. Carlos, *ACS Nano*, 2013, **7**, 7213–7218.
78 Y. Cui, F. Zhu, B. Chen and G. Qian, *Chem. Commun.*, 2015, **51**, 7420–7431.
79 C. D. S. Brites, P. P. Lima, N. J. O. Silva, A. Millán, V. S. Amaral, F. Palacio and L. D. Carlos, *New J. Chem.*, 2011, **35**, 1177–1183.
80 Z. P. Wang, D. Ananias, A. Carné-Sanchéz, C. D. S. Brites, I. Imaz, D. Maspoch, J. Rocha and L. D. Carlos, *Adv. Funct. Mater.*, 2015, **25**, 2824–2830.
81 S. Sato and M. Wada, *Bull. Chem. Soc. Jpn.*, 1970, **43**, 1955–1962.
82 K. Miyata, Y. Konno, T. Nakanishi, A. Kobayashi, M. Kato, K. Fushimi and Y. Hasegawa, *Angew. Chemie - Int. Ed.*, 2013, **52**, 6413–6416.
83 Y. Cui, H. Xu, Y. Yue, Z. Guo, J. Yu, Z. Chen, J. Gao, Y. Yang, G. Qian and B. Chen, *J. Am. Chem. Soc.*, 2012, **134**, 3979–3982.
84 V. V Skopenko, V. M. Amirkhanov, T. Y. Sliva, I. S. Vasilchenko, E. L. Anpilova and A. D. Garnovskii, *Russ. Chem. Rev.*, 2004, **73**, 737–752.
85 T. N. Trieu, T. H. Dinh, H. H. Nguyen, U. Abram and M. H. Nguyen, *Zeitschrift fur Anorg. und Allg. Chemie*, 2015, **641**, 1934–1940.
86 R. G. Charles and A. Perrotto, *J. Inorg. Nucl. Chem.*, 1964, **26**, 373–376.
87 R. G. Charles and R. C. Ohlmann, *J. Inorg. Nuc.I. Chem.,* 1965, **27**, 255–259.
88 S. J. Lyle and A. D. Witts, *Inorganica Chim. Acta*, 1971, **5**, 481–484.
89 L. R. Melby, N. J. Rose, E. Abramson and J. C. Caris, *J. Am. Chem. Soc.*, 1964, **86**, 5117–5125.
90 M. F. Belian, R. O. Freire, A. Galembeck, G. F. De Sá, R. F. De Farias and S. Alves, *J. Lumin.*, 2010, **130**, 1946–1951.
91 M. Planells, E. Klampaftis, M. Congiu, R. Shivanna, K. V. Rao, O. Chepelin, A. C. Jones, B. S. Richards, S. J. George, K. S. Narayan and N. Robertson, *Eur. J. Inorg. Chem.*, 2014, 3095–3100.
92 A. I. Voloshin, N. M. Shavaleev and V. P. Kazakov, *J. Photochem. Photobiol. A Chem.*, 2000, **131**, 61–65.
93 Y. Hou, J. Shi, W. Chu and Z. Sun, *Eur. J. Inorg. Chem.*, 2013, 3063–3069.
94 C. D. S. Brites, P. P. Lima and L. D. Carlos, *J. Lumin.*, 2016, **169**, 497–502.
95 S. V. Eliseeva, D. N. Pleshkov, K. A. Lyssenko, L. S. Lepnev, J. C. G. Bünzli

and N. P. Kuzmina, *Inorg. Chem.*, 2010, **49**, 9300–9311.
96 W. R. Dawson, J. L. Kropp and M. W. Windsor, *J. Chem. Phys.*, 1966, **45**, 2410–2418.
97 H. Y. Wong, W. S. Lo, W. T. K. Chan and G. L. Law, *Inorg. Chem.*, 2017, **56**, 5135–5140.
98 M. Hu, Z. Huang, Y. Cheng, S. Wang, J. Lin, Y. Hu, D. Xu and Y. Xu, *Chinese J. Chem.*, 1999, **17**, 637–643.
99 N. M. Shavaleev, S. J. A. Pope, Z. R. Bell, S. Faulkner and M. D. Ward, *Dalt. Trans.*, 2003, 808–814.
100 L. Armelao, D. Belli Dell'Amico, L. Bellucci, G. Bottaro, L. Labella, F. Marchetti and S. Samaritani, *Polyhedron*, 2016, **119**, 371–376.
101 B. Klein and J. Berkowitz, *J. Am. Chem. Soc.*, 1959, **81**, 5160–5166.
102 H. Brunner, R. Störiko and F. Rominger, *Eur. J. Inorg. Chemsitry*, 1998, 771–781.
103 M. J. Plater, M. R. S. J. Foreman and A. M. Z. Slawin, *Inorganica Chim. Acta*, 2000, **303**, 132–136.
104 D.-L. Long, A. J. Blake, N. R. Champness, C. Wilson and M. Schroder, *Chem. Eur. J.*, 2002, **8**, 2026–2033.
105 J. Jia, A. J. Blake, N. R. Champness, P. Hubberstey, C. Wilson and M. Schröder, *Inorg. Chem.*, 2008, **47**, 8652–8664.
106 H. W. Roesky and M. Andruh, *Coord. Chem. Rev.*, 2003, **236**, 91–119.
107 W. X. Zhu and Y. He, *J. Coord. Chem.*, 2002, **55**, 251–257.
108 S.-L. Ma, W.-X. Zhu, G.-H. Huang, D.-Q. Yuan and X. Yan, *J. Mol. Strucutre*, 2003, **646**, 89–94.
109 X. Yi, G. Calvez, C. Daiguebonne, O. Guillou and K. Bernot, *Inorg. Chem.*, 2015, **54**, 5213–5219.
110 X. Yi, K. Bernot, F. Pointillart, G. Poneti, G. Calvez, C. Daiguebonne, O. Guillou and R. Sessoli, *Chem. - A Eur. J.*, 2012, **18**, 11379–11387.
111 L. Armelao, D. Belli Dell'Amico, G. Bottaro, L. Bellucci, L. Labella, F. Marchetti, C. A. Mattei, F. Mian, F. Pineider, G. Poneti and S. Samaritani, *Dalt. Trans.*, 2018, **47**, 8337–8345.
112 T. Sekine, Y. Hasegawa and N. Ihara, *J. Inorg. Nucl. Chem.*, 1973, **35**, 3968–3970.
113 G. Malandrino, O. Incontro, F. Castelli, I. L. Fragalà and C. Benelli, *Chem. Mater.*, 1996, **8**, 1292–1297.
114 G. Malandrino, C. Benelli, F. Castelli and I. L. Fragalà, *Chem. Mater.*, 1998, **10**, 3434–3444.
115 E. M. Fatila, E. E. Hetherington, M. Jennings, A. J. Lough and K. E. Preuss, *Dalt. Trans.*, 2012, **41**, 1352–1362.
116 C. F. Bernasconi, D. A. A. Ohlberg and M. W. Stronach, *J. Org. Chem.*, 1991, **56**, 3016–3020.
117 G. Manfroni, *Master Thesis*, 2018, University of Pisa.

118 L. Armelao, D. Belli Dell'Amico, L. Bellucci, G. Bottaro, S. Ciattini, L. Labella, G. Manfroni, F. Marchetti, C. A. Mattei and S. Samaritani, *Eur. J. Inorg. Chem.*, 2018, 4421–4428.
119 M. C. Das, S. Xiang, Z. Zhang and B. Chen, *Angew. Chemie - Int. Ed.*, 2011, **50**, 10510–10520.
120 J. R. Lakowicz, *Principles of fluorescence spectroscopy*, Springer, 3rd edn., 2016.
121 O. Toma, N. Mercier, M. Allain, F. Meinardi and C. Botta, *Eur. J. Inorg. Chem.*, 2017, **4**, 844–850.
122 O. Toma, N. Mercier and C. Botta, *Eur. J. Inorg. Chem.*, 2013, **7**, 1113–1117.
123 R. D. L. Gaspar, P. R. Fortes, I. O. Mazali, F. A. Sigoli and I. M. Raimundo, *ChemistrySelect*, 2018, **3**, 10491–10501.
124 N. F. Mott, *Proc. R. Soc. London. Ser. A. Math. Phys. Sci.*, 1938, **167**, 384–391.
125 F. Seitz, *Trans. Faraday Soc.*, 1939, **35**, 74–85.
126 D. A. Gálico, E. R. Souza, I. O. Mazali and F. A. Sigoli, *J. Lumin.*, 2019, **210**, 397–403.
127 A. Kovalenko, P. O. Rublev, L. O. Tcelykh, A. S. Goloveshkin, L. S. Lepnev, A. S. Burlov, A. A. Vashchenko, L. Marciniak, A. M. Magerramov, N. G. Shikhaliyev, S. Z. Vatsadze and V. V. Utochnikova, *Chem. Mater.*, 2019, **31**, 759–773.
128 W. Simmler, in *Ullmann's Encyclopedia of Industrial Chemistry*, American Cancer Society, 2011.
129 K. Tennakone and K. G. U. Wijayantha, *Appl. Catal. B Environ.*, 2005, **57**, 9–12.
130 D. shun Zhao, F. tang Li, E. peng Zhou and Z. min Sun, *Chem. Res. Chinese Univ.*, 2008, **24**, 96–100.
131 E. J. McLaurin, L. R. Bradshaw and D. R. Gamelin, *Chem. Mater.*, 2013, **25**, 1283–1292.
132 S. Wang, S. Westcott and W. Chen, *J. Phys. Chem. B*, 2002, **106**, 11203–11209.
133 M. D. Dramićanin, *Methods Appl. Fluoresc.*, 2016, **4**, 042001 1–23.
134 X. Rao, T. Song, J. Gao, Y. Cui, Y. Yang, C. Wu, B. Chen and G. Qian, *J. Am. Chem. Soc.*, 2013, **135**, 15559–15564.
135 Y. Cui, W. Zou, R. Song, J. Yu, W. Zhang, Y. Yang and G. Qian, *Chem. Commun.*, 2014, **50**, 719–721.
136 D. Jaque and F. Vetrone, *Nanoscale*, 2012, **4**, 4301–4326.
137 K. Miyata, T. Ohba, A. Kobayashi, M. Kato, T. Nakanishi, K. Fushimi and Y. Hasegawa, *Chempluschem*, 2012, **77**, 277–280.
138 C. Daiguebonne, N. Kerbellec, O. Guillou, J.-C. Bünzli, F. Gumy, L. Catala, T. Mallah, N. Audebrand, Y. Gérault, K. Bernot and G. Calvez, *Inorg. Chem.*, 2008, **47**, 3700–3708.

139 N. Kerbellec, D. Kustaryono, V. Haquin, M. Etienne, C. Daiguebonne and O. Guillou, *Inorg. Chem.*, 2009, **48**, 2837–2843.
140 V. Haquin, M. Etienne, C. Daiguebonne, S. Freslon, G. Calvez, K. Bernot, L. Le Pollès, S. E. Ashbrook, M. R. Mitchell, J.-C. Bünzli, S. V. Eliseeva and O. Guillou, *Eur. J. Inorg. Chem.*, 2013, **20**, 3464–3476.
141 Y. Wei, R. Sa, Q. Li and K. Wu, *Dalt. Trans.*, 2015, **44**, 3067–3074.
142 Y. Cui, R. Song, J. Yu, M. Liu, Z. Wang, C. Wu, Y. Yang, Z. Wang, B. Chen and G. Qian, *Adv. Mater.*, 2015, **27**, 1420–1425.
143 R. F. D'Vries, S. Álvarez-García, N. Snejko, L. E. Bausá, E. Gutiérrez-Puebla, A. De Andrés and M. Á. Monge, *J. Mater. Chem. C*, 2013, **1**, 6316–6324.
144 L. L. Wu, J. Zhao, H. Wang and J. Wang, *CrystEngComm*, 2016, **18**, 4268–4271.
145 D. Zhao, X. Rao, J. Yu, Y. Cui, Y. Yang and G. Qian, *Inorg. Chem.*, 2015, **54**, 11193–11199.
146 M. Hatanaka, Y. Hirai, Y. Kitagawa, T. Nakanishi, Y. Hasegawa and K. Morokuma, *Chem. Sci.*, 2016, **8**, 423–429.
147 K. Biradha, M. Sarkar and L. Rajput, *Chem. Commun.*, 2006, 4169–4179.
148 B. Yan, H. J. Zhang and J. Z. Ni, *Mater. Sci. Eng. B*, 2002, **52**, 123–128.
149 H. Mao, C. Zhang and H. Shi, *J. Phys. Chem. Solids*, 2011, **72**, 1230–1238.
150 C. Seward, N. X. Hu and S. Wang, *J. Chem. Soc. Dalt. Trans.*, 2001, 134–137.
151 P. R. Matthes, F. Schönfeld, S. H. Zottnick and K. Müller-Buschbaum, *Molecules*, 2015, **20**, 12125–12153.
152 P. R. Matthes, C. J. Höller, M. Mai, J. Heck, S. J. Sedlmaier, S. Schmiechen, C. Feldmann, W. Schnick and K. Müller-Buschbaum, *J. Mater. Chem.*, 2012, **22**, 10179–10187.
153 P. R. Matthes, J. Nitsch, A. Kuzmanoski, C. Feldmann, A. Steffen, T. B. Marder and K. Müller-Buschbaum, *Chem. Eur. J.*, 2013, **19**, 17369–17378.
154 C. J. Holler, M. Mai, C. Feldmann and K. Muller-Buschbaum, *Dalt. Trans.*, 2010, **39**, 337–348.
155 C. J. Höller, P. Matthes, J. Beckmann and K. Müller-Buschbaum, *Z. Anorg. Allg.Chem.*, 2010, **636**, 395–399.
156 P. R. Matthes, J. Eyley, J. H. Klein, A. Kuzmanoski, C. Lambert, C. Feldmann and K. Müller-Buschbaum, *Eur. J. Inorg. Chem.*, 2015, 826–836.
157 P. C. Andrews, B. H. Fraser, P. C. Junk, M. Massi, B. Moubaraki, K. S. Murray and M. Silberstein, *Polyhedron*, 2009, **28**, 2123–2130.
158 S. Petit, F. Baril-Robert, G. Pilet, C. Reber and D. Luneau, *J. Chem. Soc. Dalt. Trans.*, 2009, 6809–6815.
159 F. Benz, H. P. Strunk, J. Schaab, U. Künecke and P. Wellmann, *J. Appl. Phys.*, 2013, **114**, 73518.
160 W. A. Pisarski, L. Zur, M. Sołtys and J. Pisarska, *J. Appl. Phys.*, 2013, **113**, 143504 1–4.
161 P. C. Ricci, C. M. Carbonaro, R. Corpino, C. Cannas and M. Salis, *J. Phys.*

Chem. C, 2011, **115**, 16630–16636.
162 D. J. Robbins, B. Cockayne, B. Lent and J. L. Glasper, *Solid State Commun.*, 1976, **20**, 673–676.
163 H. Furukawa, K. E. Cordova, M. O'Keeffe and O. M. Yaghi, *Science (80-.).*, 2013, **341**, 1230444–1230457.
164 J. Kim, B. Chen, T. M. Reineke, H. Li, M. Eddaoudi, D. B. Moler, M. O'Keeffe and O. M. Yaghi, *J. Am. Chem. Soc.*, 2001, **123**, 8239–47.
165 S. S. Kaye, A. Dailly, O. M. Yaghi and J. R. Long, *J. Am. Chem. Soc.*, 2007, **129**, 14176–14177.
166 A. Schoedel and O. M. Yaghi, in *Macrocyclic and Supramolecular Chemistry: How Izatt–Christensen Award Winners Shaped the Field*, ed. R. M. Izatt, John Wiley & Sons, Ltd, 1st edn., 2016, pp. 200–219.
167 G. Férey, *Chem. Soc. Rev.*, 2008, **37**, 191–214.
168 M. Eddaoudi, D. B. Moler, H. Li, B. Chen, T. M. Reineke, M. O'Keeffe and O. M. Yaghi, *Acc. Chem. Res.*, 2001, **34**, 319–30.
169 D. Bradshaw, J. B. Claridge, E. J. Cussen, T. J. Prior and M. J. Rosseinsky, *Acc. Chem. Res.*, 2005, **38**, 273–282.
170 N. L. Rosi, J. Eckert, M. Eddaoudi, D. T. Vodak, J. Kim and O. M. Yaghi, *Science (80-.).*, 2003, **300**, 1127–1129.
171 S. Zheng, T. Wu, J. Zhang, M. Chow, R. A. Nieto, P. Feng and X. Bu, *Angew. Chemie - Int. Ed.*, 2010, **49**, 5362–5366.
172 D. X. Xue, A. J. Cairns, Y. Belmabkhout, L. Wojtas, Y. Liu, M. H. Alkordi and M. Eddaoudi, *J. Am. Chem. Soc.*, 2013, **135**, 7660–7667.
173 R. E. Morris and P. S. Wheatley, *Angew. Chemie - Int. Ed.*, 2008, **47**, 4966–4981.
174 L. Ma, J. M. Falkowski, C. Abney and W. Lin, *Nat. Chem.*, 2010, **2**, 838.
175 X. Meng, B. Gui, D. Yuan, M. Zeller and C. Wang, *Sci. Adv.*, 2016, **2**, e1600480 1-7.
176 B. Illes, P. Hirschle, S. Barnert, V. Cauda, S. Wuttke and H. Engelke, *Chem. Mater.*, 2017, **29**, 8042–8046.
177 X. Chen, R. Tong, Z. Shi, B. Yang, H. Liu, S. Ding, X. Wang, Q. Lei, J. Wu and W. Fang, *ACS Appl. Mater. Interfaces*, 2018, **10**, 2328–2337.
178 X. Zhou, H. Li, H. Xiao, L. Li, Q. Zhao, T. Yang, J. Zuo and W. Huang, *Dalt. Trans.*, 2013, **42**, 5718–5723.
179 Q. Tang, S. Liu, Y. Liu, J. Miao, S. Li, L. Zhang, Z. Shi and Z. Zheng, *Inorg. Chem.*, 2013, **52**, 2799–2801.
180 S. Nayak, H. P. Nayek, C. Pietzonka, G. Novitchi and S. Dehnen, *J. Mol. Struct.*, 2011, **1004**, 82–87.
181 K. L. Gurunatha, S. Mohapatra, P. A. Suchetan and T. K. Maji, *Cryst. Growth Des.*, 2009, **9**, 3844–3847.
182 S. Roy, A. Chakraborty and T. K. Maji, *Coord. Chem. Rev.*, 2014, **273**, 139–164.

183 F. Le Natur, G. Calvez, S. Freslon, C. Daiguebonne, K. Bernot and O. Guillou, *J. Mol. Struct.*, 2015, **1086**, 34–42.
184 Z. Liu, W. He and Z. Guo, *Chem. Soc. Rev.*, 2013, **42**, 1568–1600.
185 C. Wang, S.-Y. Lin, W. Shi, P. Cheng and J. Tang, *Dalt. Trans.*, 2015, **44**, 5364–5368.
186 W. Lu, Z. Wei, Z.-Y. Gu, T.-F. Liu, J. Park, J. Park, J. Tian, M. Zhang, Q. Zhang, T. Gentle III, M. Bosch and H.-C. Zhou, *Chem. Soc. Rev.*, 2014, **43**, 5561–5593.
187 P. Deria, J. E. Mondloch, O. Karagiaridi, W. Bury, J. T. Hupp and O. K. Farha, *Chem. Soc. Rev.*, 2014, **43**, 5896–5912.
188 Z. Wang and S. M. Cohen, *J. Am. Chem. Soc.*, 2007, **129**, 12368–12369.
189 R. Uy and F. Wold, *Science (80-.).*, 1977, **198**, 890–896.
190 C. T. Walsh, S. Garneau-Tsodikova and G. J. Gatto, *Angew. Chemie - Int. Ed.*, 2005, **44**, 7342–7372.
191 K. K. Tanabe and S. M. Cohen, *Chem. Soc. Rev.*, 2011, **40**, 498–519.
192 S. M. Cohen, *Chem. Rev.*, 2012, **112**, 970–1000.
193 A. D. Burrows, eds. F. L. I. Xamena and J. Gascon, The Royal Society of Chemistry, 2013, pp. 31–75.
194 Y. H. Kiang, G. B. Gardner, S. Lee, Z. Xu and E. B. Lobkovsky, *J. Am. Chem. Soc.*, 1999, **121**, 8204–8215.
195 R. K. Deshpande, J. L. Minnaar and S. G. Telfer, *Angew. Chemie - Int. Ed.*, 2010, **49**, 4598–4602.
196 E. J. Kyprianidou, T. Lazarides, S. Kaziannis, C. Kosmidis, G. Itskos, M. J. Manos and A. J. Tasiopoulos, *J. Mater. Chem. A*, 2014, **2**, 5258–5266.
197 Z. Zhang, W. Y. Gao, L. Wojtas, S. Ma, M. Eddaoudi and M. J. Zaworotko, *Angew. Chemie - Int. Ed.*, 2012, **51**, 9330–9334.
198 M. Gharib, L. Esrafili, A. Morsali and P. Retailleau, *Dalt. Trans.*, 2019, **48**, 803–8814.
199 T. Li, M. T. Kozlowski, E. A. Doud, M. N. Blakely and N. L. Rosi, *J. Am. Chem. Soc.*, 2013, **135**, 11688–11691.
200 J. E. Mondloch, O. Karagiaridi, O. K. Farha and J. T. Hupp, *CrystEngComm*, 2013, **15**, 9258–9264.
201 J. De Bellis, *Master Thesis*, 2018, University of Pisa.
202 J. De Bellis, D. Belli Dell'Amico, G. Ciancaleoni, L. Labella, F. Marchetti and S. Samaritani, *Inorganica Chim. Acta*, 2019, **495**, 118937 1–10.
203 M. J. Wójcik, J. Kwiendacz, M. Boczar, L. Boda and Y. Ozaki, *Chem. Phys.* , 2010, **372**, 72–81.
204 *Spectr. Database Org. Compd.*, **No.518**, RN 110-86-1.
205 *Spectr. Database Org. Compd.*, **No.: 497**, RN 109-99-9.
206 J. A. Fernandes, R. A. Sá Ferreira, M. Pillinger, L. D. Carlos, I. S. Gonçalves and P. J. A. Ribeiro-Claro, *Eur. J. Inorg. Chem.*, 2004, 3913–3919.
207 J. Coates, in *Encyclopedia of Analytical Chemistry*, John Wiley & Sons, Ltd,

2006.
208 M. Silverstein, Robert, X. Webster, Francis and D. J. Kiemls, *Spectrometric Identification of Organic Compounds*, John WIley & Sons, 7th edn., 1963.
209 C. Doffek, J. Wahsner, E. Kreidt and M. Seitz, *Inorg. Chem.*, 2014, **53**, 3263–3265.
210 E. Southern, K. Mir and M. Shchepinov, *Nat. Genet.*, 1999, **21**, 5–9.
211 S. F. Bent, *Surf. Sci.*, 2002, **500**, 879–903.
212 S. Onclin, B. J. Ravoo and D. N. Reinhoudt, *Angew. Chemie - Int. Ed.*, 2005, **44**, 6282–6304.
213 T. Zhou, R. T. Anderson, H. Li, J. Bell, Y. Yang, B. P. Gorman, S. Pylypenko, M. T. Lusk and A. Sellinger, *Nano Lett.*, 2015, **15**, 3657–3663.
214 A. Bianco, F. Gasparrini, M. Maggini, D. Misiti, A. Polese, M. Prato, G. Scorrano, C. Toniolo and C. Villani, *J. Am. Chem. Soc.*, 1997, **119**, 7550–7554.
215 A. A. Tomchenko, G. P. Harmer, B. T. Marquis and J. W. Allen, *Sensors Actuators B Chem.*, 2003, **93**, 126–134.
216 D. S. Wilson and S. Nock, *Angew. Chem. Int. Ed.*, 2003, **42**, 494–500.
217 J. H. Chua, R.-E. Chee, A. Agarwal, S. M. Wong and G.-J. Zhang, *Anal. Chem.*, 2009, **81**, 6266–6271.
218 A. Bettencourt-Dias, *Luminescence of Lanthanide Ions in Coordination Compounds and Nanomaterials*, John Wiley and Sons, Ltd, 2014.
219 G. Blasse and B. C. Grabmaier, *Luminescent materials*, Springer, 1994.
220 Hartmut Yersin, *Highly Efficient OLEDs with Phosphorescent Materials*, Wiley-VCH Verlag GmbH & Co. KGaA, 2008.
221 M. Rodrigues, R. Piñol, G. Antorrena, C. D. S. Brites, N. J. O. Silva, J. L. Murillo, R. Cases, I. Díez, F. Palacio, N. Torras, J. A. Plaza, L. Pérez-García, L. D. Carlos and A. Millán, *Adv. Funct. Mater.*, 2016, **26**, 200–209.
222 R. Anwander, in *Handbook of Heterogeneus Catalysis*, ed. Wiley-VCH Verlag GmbH, Weinheim, 2nd edn., 2008, vol. 8, pp. 583–614.
223 X. Wang, S. Zhou and L. Wu, *Mater. Chem. Phys.*, 2012, **137**, 644–651.
224 C. Copéret, A. Comas-Vives, M. P. Conley, D. P. Estes, A. Fedorov, V. Mougel, H. Nagae, F. Núñez-Zarur and P. A. Zhizhko, *Chem. Rewievs*, 2016, **116**, 323–421.
225 Y. Liang and R. Anwander, *Dalt. Trans.*, 2013, **42**, 12521–12545.
226 R. Anwander, *Chem. Mater.*, 2001, **13**, 4419–4438.
227 D. Belli Dell'Amico, F. Calderazzo, C. Ciofi, F. Garbassi, L. Grande and G. Masciarelli, *J. Clust. Sci.* , 1998, **9**, 473–485.
228 L. Abis, L. Armelao, D. Belli Dell'Amico, F. Calderazzo, F. Garbassi, A. Merigo and E. A. Quadrelli, *J. Chem. Soc., Dalt. Trans.*, 2001, **0**, 2704–2709.
229 L. Armelao, D. Belli Dell'Amico, L. Bellucci, G. Bottaro, L. Labella, F. Marchetti and S. Samaritani, *Inorg. Chem.*, 2016, **55**, 939–947.
230 L. Armelao, D. Belli Dell'Amico, L. Bellucci, G. Bottaro, L. Di Bari, L. Labella, F. Marchetti, S. Samaritani and F. Zinna, *Inorg. Chem.*, 2017, **56**,

7010–7018.
231 D. Belli Dell'Amico, F. Calderazzo, L. Labella, F. Marchetti and G. Pampaloni, *Chem. Rev.*, 2003, **103**, 3857–3897.
232 D. B. Dell'Amico, F. Calderazzo, S. Farnocchi, L. Labella and F. Marchetti, *Inorg. Chem. Commun.*, 2002, **5**, 848–852.
233 D. Boschi, *Master Thesis*, 1998, University of Pisa.
234 M. Politi, *Master Thesis*, 1997, Univeristy of Pisa.
235 U. Baisch, D. Belli Dell'Amico, F. Calderazzo, L. Labella, F. Marchetti and A. Merigo, *Eur. J. Inorg. Chem.*, 2004, 1219–1224.
236 A. Belforte, F. Calderazzo and P. F. Zanazzi, *J. Chem. Soc., Dalt. Trans.*, 1988, **0**, 2921–2926.
237 E. Agostinelli, D. Belli Dell'Amico, F. Calderazzo, D. Fiorani and G. Pelizzi, *Gazz. Chim. Ital.*, 1988, **118**, 729–740.
238 A. Belforte, D. Belli Dell'Amico, F. Calderazzo, M. Devillers and U. Englert, *Inorg. Chem.*, 1993, **32**, 2282–2286.
239 D. Belli Dell'Amico, F. Calderazzo, F. Marchetti and G. Perego, *J. Chem. Soc., Chem. Commun.*, 1979, **0**, 1103–1105.
240 D. Belli Dell'Amico, F. Calderazzo, F. Marchetti and G. Perego, *J. Chem. Soc., Dalt. Trans.*, 1983, **0**, 483–487.
241 M. B. Jensen, E. Jørgensen and C. Faurholt, *Acta Chem. Scand.*, 1954, **8**, 1137–1140.
242 A. Jensen, M. B. Jensen and C. Faurholt, *Acta Chem. Scand.*, 1954, **8**, 1129–1136.
243 L. Armelao, D. Belli Dell'Amico, P. Biagini, G. Bottaro, S. Chiaberge, P. Falvo, L. Labella, F. Marchetti and S. Samaritani, *Inorg. Chem.*, 2014, **53**, 4861−4871.
244 H. Gilman, R. A. Benkeser and G. E. Dunn, *J. Am. Chem. Soc.*, 1950, **72**, 1689–1691.
245 C. E. Bronnimann, R. C. Zeigler and G. E. Maciel, *J. Am. Chem. Soc.*, 1988, **110**, 2023–2026.
246 A. Rimola, D. Costa, M. Sodupe, J. F. Lambert and U. Ugliengo, *Chem. Rewiew*, 2013, **113**, 4216–4313.
247 L. Abis, D. Belli Dell' Amico, C. Busetto, F. Calderazzo, F. Garbassi and A. Tomei, *J. Mater. Chem.*, 1998, **8**, 2855–2861.
248 C. Forte, G. Pampaloni, C. Pinzino and F. Renili, *Inorganica Chim. Acta*, 2011, **365**, 251–255.
249 T. O. M. Popp and O. M. Yaghi, *Acc. Chem. Res.*, 2017, **50**, 532–534.
250 P. Vairaprakash, H. Ueki, K. Tashiro and O. M. Yaghi, *J. Am. Chem. Soc.*, 2011, **133**, 759–761.
251 M. Che and J. C. Védrine, *Characterization of Solid Materials and Heterogeneous Catalysts - From Structure to Surface Reactivity*, Wiley-VCH Verlag GmbH & Co. KGaA., 2012.

252 A. M. Fracaroli, K. Tashiro and O. M. Yaghi, *Inorg. Chem.*, 2012, **51**, 6437–6439.
253 K. Sajna, A. M. Fracaroli, O. M. Yaghi and K. Tashiro, *Inorg. Chem.*, 2015, **54**, 1197–1199.
254 K. Isozaki, Y. Haga, K. Ogata, T. Naota and H. Takaya, *Dalt. Trans.*, 2013, **42**, 15953–15966.
255 T. M. Reineke, M. Eddaoudi, M. Fehr, D. Kelley and O. M. Yaghi, *J. Am. Chem. Soc.*, 1999, **121**, 1651–1657.
256 M. Gustafsson, A. Bartosaewicz, B. Martin-Matude, J. Sun, J. Grins, T. Zhao, Z. Li, G. Zhu and X. Zou, *Chem. Mater.*, 2010, **22**, 3316–3322.
257 R. Cao, D. Sun, Y. Liang, M. Hong, K. Tatsumi and Q. Shi, *Inorg. Chem.*, **2002**, 2087–2094.
258 C. Daiguebonne, N. Kerbellec, K. Bernot, Y. Gérault, A. Deluzet and O. Guillou, *Inorg. Chem.*, 2006, **45**, 5399–5406.
259 Z. Wang, Y. Yang, Y. Cui, Z. Wang and G. Qian, *J. Alloy. Compd.*, 2012, **510**, L5–L8.
260 S. Mohamed, D. A. Tocher, M. Vickers, P. G. Karamertzanis and S. L. Price, *Cryst. Growth Des.*, 2009, **9**, 2881–2889.
261 M. Bailey and C. J. Brown, *Acta Crystallogr.*, 1967, **22**, 387–391.
262 S. H. Dale, M. R. J. Elsegood, M. Hemmings and A. L. Wilkinson, *CrystEngComm*, 2004, **6**, 207–214.
263 L. Armelao, G. Bottaro, S. Quici, C. Scalera, M. Cavazzini, G. Accorsi and M. Bolognesi, *ChemPhysChem*, 2010, **11**, 2499–2502.
264 R. A. S. Ferreira, S. S. Nobre, C. M. Granadiero, H. I. S. Nogueira, L. D. Carlos and O. L. Malta, *J. Lumin.*, 2006, **121**, 561–567.
265 M. Bettinelli, V. Speghini, F. Piccinelli, A. N. C. Neto and O. L. Malta, *J. Lumin.*, 2011, **131**, 1026–1028.
266 D. Ananias, F. A. Almeida Paz, D. S. Yufit, L. D. Carlos and J. Rocha, *J. Am. Chem. Soc.*, 2015, **137**, 3051–3058.
267 G. Bottaro, F. Rizzo, M. Cavazzini, L. Armelao and S. Quici, *Chem.-Eur. J.*, 2014, **20**, 4598–4607.
268 S. Quici, A. Casoni, F. Foschi, L. Armelao, G. Bottaro, R. Seraglia, G. Bolzati, N. Salverese, D. Carpanese and A. Rosato, *J. Med. Chem.*, 2015, **58**, 2003–2014.
269 M. Back, R. Marin, M. Franceschin, N. Sfar Hancha, F. Enrichi, E. Trave and S. Polizzi, *J. Mater. Chem C*, 2016, **4**, 1906–1913.
270 L. T. Zhuravlev, *Colloids Surfaces A*, 2000, **173**, 1–38.
271 E. R. Cruz-Chu, A. Aksimentiev and K. Schulten, *J. Phys. Chem. B*, 2006, **110**, 21497–21508.
272 J. J. Adams, *Energy & Fuels*, 2014, **28**, 2831–2856.
273 D. Zacher, O. Shekhah, C. Wöll and R. A. Fischer, *Chem. Soc. Rev.*, 2009, **38**, 1418–1429.

274 O. Shekhah, J. Liu, R. A. Fischer and C. Wöll, *Chem. Soc. Rev.*, 2011, **40**, 1081–1106.
275 A. Bétard and R. A. Fischer, *Chem. Rev.*, 2012, **112**, 1055–1083.
276 M. Ismail, S. J. Lyle, J. E. Newbery, I. T. Moeller, D. F. Martin, L. C. Thompson, R. Ferrus, G. R. Feistel and W. J. Randall, *J. Inorg, Nucl. Chem.*, 1969, **31**, 1715–1724.
277 C. F. Koelsch and W. H. Gumprecht, *J. Org. Chem.*, 1958, **23**, 1603–1606.
278 H. A. Flaschka, *EDTA Titrations; An Introduction to Theory and Practice*, Pergamon Press, 1964.
279 G. M. Sheldrick, *Acta Crystallogr., Sect. A*, 2008, **64**, 112–122.
280 V. S. Sastri, J.-C. G. Bünzli, V. Ramachandra Rao, G. V. S. Rayudu and J. R. Perumareddi, *Modern Aspects of Rare Earths and Their Complexes*, Elsevier, 2003.
281 I. M. Kolthoff and P. J. Elving, *Treatise on Analytical Chemistry*, New York, 1963, vol. 8.

Acknowledgements

I would like to express my deepest gratitude to Prof. Lidia Armelao from the University and ICMATE-CNR institute of Padova, for supervising my Ph.D. project and for the idea to strengthen the already existing collaboration between the University of Padua and the University of Pisa where I performed part of this work.

A special thanks goes to Dr. Gregorio Bottaro from the ICMATE-CNR institute of Padova and Prof. Luca Labella form the University of Pisa, for their continuous support and guidance throughout these three years.

I would like also to thank Prof. Fabio Marchetti form the University of Pisa, for the X-Ray diffraction studies and Prof. Valerio Causin from the University of Padova, for thermogravimetric analysis.

Thanks go also to Prof. Daniela Belli dell'Amico and Prof. Simona Samaritani form the University of Pisa and Dr. Marzio Rancan from the ICMATE-CNR institute of Padova for the helpful discussion.

Finally, I want to thank Prof. Leonard J. Prins from the University of Padova, for the work done as coordinator of the Ph.D. course in molecular science.